MAX-PLANCK-INSTITUT FÜR RADIOASTRONOMIE
BONN

Small Molecules, Big Impact

Investigating Hydrides in the Interstellar Medium

Arshia Maria Jacob

2021

MAX-PLANCK-INSTITUT FÜR RADIOASTRONOMIE
BONN

Small Molecules, Big Impact
Investigating Hydrides in the Interstellar Medium

Dissertation

zur

Erlangung des Doktorgrades (*Dr. rer. nat.*)

der

Mathematisch-Naturwissenschaftlichen Fakultät

der

Rheinischen Friedrich–Wilhelms–Universität Bonn

vorgelegt von

Arshia Maria Jacob

aus

Trivandrum, India

Bonn 2021

Angefertigt mit Genehmigung der Mathematisch-Naturwissenschaftlichen Fakultät der Rheinischen Friedrich–Wilhelms–Universität Bonn
Prepared with the permission from the Faculty of Mathematics and Natural Sciences of the University of Bonn

1. Referent / *First Referee*: Prof. Dr. Karl M. Menten
2. Referent / *Second Referee*: Prof. Dr. Pavel Kroupa

Tag der Promotion / *Conferral Date*: 4th June, 2021
Erscheinungsjahr / *Year of Publication*: 2021

RHEINISCHE FRIEDRICH–WILHELMS–UNIVERSITÄT BONN

Abstract

by Arshia Maria Jacob

for the degree of

Doctor rerum naturalium

This thesis investigates hydride molecules in the interstellar medium (ISM) and their use as diagnostics of different phases of the ISM. Particular emphasis is given to the central CH radical, a probe of diffuse and translucent molecular clouds, including those not traced by the otherwise common CO. We discuss our searches for the rare isotopologues of CH and address questions regarding the origin of another molecule, CH_2, which despite being chemically associated with the ubiquitous CH, has largely remained elusive. In addition, the molecular ion, ArH^+, a tracer for diffuse atomic gas is studied.

Whilst the 9 cm ground state radio lines of CH are widely observed, their excitation has been poorly understood as their intensities have long been found to be inconsistent with the assumptions of local thermodynamic equilibrium (LTE). We present the first interferometric observations of these CH lines using the *Karl G. Jansky* Very Large Array (VLA) and provide constraints on the physical and excitation conditions traced by these lines, through non-LTE radiative transfer models which invoke the effects of far-infrared (FIR) line overlap. Furthermore, by taking advantage of the synergies between the FIR and radio transitions of CH we constrain our models using reliable column densities determined from the FIR lines of CH at 149 μm observed using the high spectral resolution upGREAT receiver on board the Stratospheric Observatory for Infrared Astronomy (SOFIA). Our results reveal that the physical conditions traced by CH are consistent with those found within the warm layers of photodissociation regions (PDRs), which along with astrochemical considerations suggest that CH may be formed via the dissipation of turbulence, possible even in dark clouds. This analysis establishes the use of the widely observed ground state transitions of CH as a powerful tool to probe the diffuse and translucent ISM at radio wavelengths.

By further exploiting the unique capabilities provided by SOFIA, we discuss our search for, and successful detection, of ^{13}CH in the ISM for the first time. Combined with observations of its main isotopologue we highlight its use as a potentially unbiased tracer of the ^{12}C/^{13}C isotopic ratio, an important diagnostic tool for probing the nucleosynthesis history of the Galaxy.

Based on early observations of high energy level transitions of CH_2 between 68 and 71 GHz toward the hot cores in Orion and W51, astronomers associated the observed emission as arising from dense, hot environments. The subsequent non-detection of these lines toward the archetypal Orion-KL hot core in high resolution observations

have raised questions regarding the molecule's origin. To address this, we conducted new observations of these transitions toward the Orion region and other star-forming regions. Our data, with the aid of ancillary carbon recombination line data and radiative transfer models, establishes CH_2's association with warm but dilute PDR gas layers. Additionally, we find that for the physical conditions derived, the observed CH_2 lines show level inversion and acts as a weak maser.

Finally, we extend the view of the chemistry of argonium (ArH^+) using observations carried out with the Atacama Pathfinder EXperiment (APEX) 12 m telescope. Combined with archival observations of OH^+ and H_2O^+, we determined the properties of the gas traced by ArH^+ by analysing the steady-state chemistry. Our results confirm the role of ArH^+ as a tracer of atomic gas, probing regions with an extremely low average molecular fraction of 8.8×10^{-4}. Furthermore, by comparing the abundance and molecular fraction traced by ArH^+ and by atomic gas tracers OH^+ and H_2O^+ and molecular gas tracers CH or HF, we study the transition from the diffuse atomic to the diffuse and translucent molecular clouds in the ISM.

To my family, whom I love so dearly

The truth may be puzzling. It may take some work to grapple with. It may be counter-intuitive. It may contradict deeply held prejudices. It may not be consonant with what we desperately want to be true. But our preferences do not determine what's true.

Carl Sagan,
Pulitzer Prize winner for General Non-Fiction, 1978

List of publications

Publications related to this thesis

1. Fingerprinting the effects of hyperfine structure on CH and OH far infrared spectra using Wiener filter deconvolution
   A. M. Jacob, K. M. Menten, H. Wiesemeyer, M-Y. Lee, R. Güsten and C. A. Durán, A&A, 632, A60 (2019), DOI: 10.1051/0004-6361/201936037 [arxiv:1911.00393]

2. First detection of ^{13}CH in the interstellar medium
   A. M. Jacob, K. M. Menten, H. Wiesemeyer, R. Güsten, F. Wyrowski and B. Klein, A&A, 640, A125 (2020), DOI: 10.1051/0004-6361/201937385 [arXiv:2007.01190]

3. Extending the view of ArH^+ chemistry in diffuse clouds
   A. M. Jacob, K. M. Menten, F. Wyrowski, B. Winkel, and D. A. Neufeld, A&A, 643, A91 (2020), DOI: 10.1051/0004-6361/202039197 [arXiv:2010.02258]

4. Hunting for the elusive methylene radical
   A. M. Jacob, K. M. Menten, Y. Gong, P. Bergman, M. Tiwari, S. Brünken, and A.O.H. Olofsson, A&A, in press (2021), DOI: 10.1051/0004-6361/202039906 [arXiv:2101.02654]

5. The CH radical at radio wavelengths: Revisiting emission in the 3.3 GHz ground state lines
   A. M. Jacob, K. M. Menten, H. Wiesemeyer, and G. N. Ortiz-León, A&A submitted (2021)

Other publications

1. Unveiling the chemistry of interstellar CH. Spectroscopy of the 2 THz $N = 2 \leftarrow 1$ ground state line
   H. Wiesemeyer, R. Güsten, K. M. Menten, C. A. Durán, T. Csengeri, **A. M. Jacob**, R. Simon, J. Stutzki, F. Wyrowski, A&A, 612, A37 (2018), DOI: 10.1051/0004-6361/201731810 [arXiv:1804.04707]

2. The magnetic field in the dense photodissociation region of DR 21
   A. Koley, N. Roy, K. M. Menten, **A. M. Jacob**, T. G. S. Pillai, and M. R. Rugel, MNRAS, 501(4), 4825-4826 (2021), DOI: 10.1093/mnras/staa3898 [arXiv:2012.08253]

3. SOFIA FEEDBACK survey: exploring the kinetics of the stellar wind driven shell of RCW 49
   M. Tiwari, R. Karim, M. Pound, M. Wolfire, **A. Jacob**, C. Buchbender, R. Güsten, C. Guevara, S. Kabanovic, C. Pabst, N. Schneider, R. Simon, J. Stutzki, and A. G. G. M. Tielens, ApJ, submitted (2020)

Contents

List of Figures

List of Tables

Chapter 1

Introduction

They cannot scare me with their empty spaces
Between stars - on stars where no human race is.
I have it in me so much nearer home
To scare myself with my own desert places.

Robert Frost, Desert place, American Mercury, 1934

Overview

While the space between the stars may seem empty to the naked eye as *Robert Frost* states in his poem *Desert place*, in reality, interstellar space is not completely empty. It contains gas and dust in the form of clouds or more diffuse material permeated by energetic particles and exposed to radiation. This is illustrated in Fig. 1.1 that, in near infrared (NIR) light, displays as an example, the star cluster RCW 38 together with the dusty interstellar clouds that surround it. The hot an luminous stars of the cluster irradiate the surrounding gas clouds, which makes them glow in colours, predominantly in tints of blue. The dark shades in black, red, and orange represent dust that is interspersed through the bright core of this region. Therefore, just from this impressive example alone it is evident that interstellar space is not in a state of complete vacuum.

One of the first pieces of evidence for the existence of gaseous material between stars, collectively known as the interstellar medium (ISM), came more than one and a half centuries ago, with the discovery of spectral lines in the optical spectra of emission nebula (Huggins & Miller 1864; Huggins & Huggins 1889). Furthermore in the early 1930s with better resolution spectroscopic studies it was inferred that the ISM is not homogeneous and in the late 1970s it was found that the ISM was rather comprised of a variety of phases with widely varying physical and excitation conditions (McKee & Ostriker 1977). The interplay between the different phases and constituents of the ISM plays a fundamental role in the formation of stars and for the evolution of galaxies, making the study and understanding of the ISM pivotal for many fields of astronomy.

One of the main scientific goals of this thesis, is to demonstrate the use of hydrides (molecules containing covalently bound H atoms of the type XH_n and XH_n^+) as diagnostic tools of the different phases of the neutral ISM. Therefore, this introductory chapter presents the background information necessary to appreciate the scientific context of this thesis, starting with a description of the ISM, its structure and the interactions between its different phases with particular emphasis on the cold neutral medium. The general references used in this chapter are reviews by Grenier et al. (2005), Snow & McCall (2006), and Gerin et al. (2016)

and more comprehensive references on the physics and chemistry of the ISM are the books by Draine (2011) and Tielens (2005), unless stated otherwise.

Figure 1.1: Near-infrared image of the RCW 38 star cluster observed using the High Acuity Wide-field K-band Imager (HAWK-I) instrument on the European Space Organisation's (ESO's) Very Large Telescope, highlighting the gas and dust between stars. Credit: ESO/ K. Muzic.

1.1 The interstellar medium

The ISM is composed of gas predominantly in the form of hydrogen and helium with trace amounts of heavier elements ('metals') as a result of primordial and stellar nucleosynthesis, as well as dust grains that were formed out of molecules. The ISM is permeated by electromagnetic radiation, magnetic fields and also by electrons and cosmic rays, protons and atomic nuclei, all moving at relativistic velocities. Constituting approximately 10% of the visible (baryonic) matter in galaxies with low particle densities on average, the ISM represents an enthralling laboratory that facilitates the study of a wide range of astrophysical phenomena that include the formation of molecules and their chemistry, the processes by which stars form, stellar nucleosynthesis and the structure and evolution of galaxies. Therefore, the ISM plays a

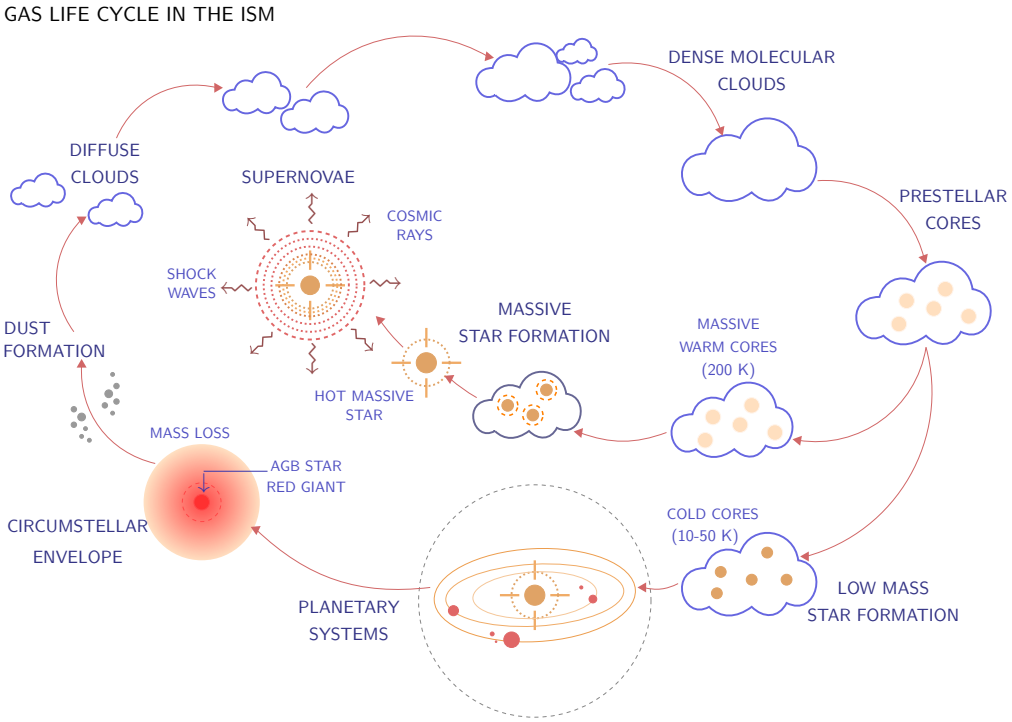

Figure 1.2: The life cycle of stars, gas and dust in the ISM. Illustration adapted from Verschuur (1992).

crucial role in many aspects of astronomy, particularly because it is an essential link between phenomena at stellar and galactic scales. Stars form via gravitational collapse of the compact core regions of molecular clouds that represent the densest parts of the ISM.

As stars evolve over time, they produce elements in their cores via nuclear fusion and eventually expel this matter and energy back into the ISM through outflows and stellar winds, thereby replenishing it. Therefore, stars cannot form without molecules, and most molecules cannot form without stars. This re-cycling of material between stars and the constituents of the ISM is illustrated in Fig. 1.2.

1.1.1 Energy balance in the ISM

As mentioned in the previous sections, the ISM is conventionally described in terms of a number of distinct environments, commonly called ‘phases’. This is a consequence of the fact that a balance between its different heating and cooling processes, at a given pressure, can often be achieved at more than one temperature. The general properties of the material encompassing the different phases are governed and influenced by the radiation, turbulence, and magnetic fields at play. We briefly summarise the energy balance in the ISM and the properties of the different contributing forces. The discussion below is based on reviews by Lequeux (2005) and Klessen & Glover (2016), and we refer the reader to the same for a more detailed account of the subject.

The first is the interstellar radiation field (ISRF) which encompasses radiation from all

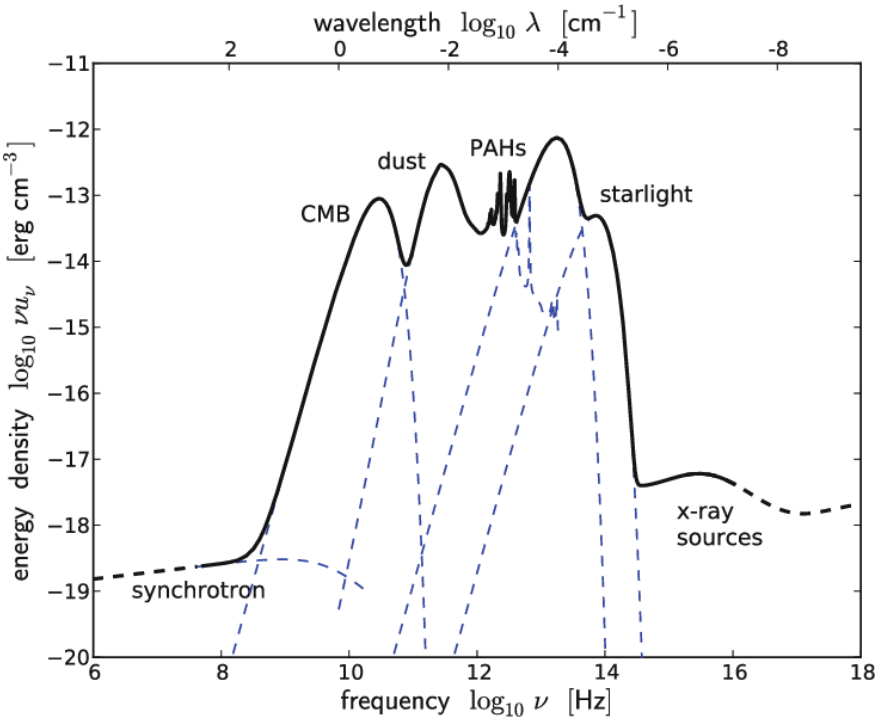

Figure 1.3: Schematic sketch of the energy density of the interstellar radiation field at different frequencies. Taken from Klessen & Glover (2016).

wavelengths of the electromagnetic spectrum. Its main components are the cosmic microwave background (CMB), synchrotron emission from relativistic electrons, starlight, infrared (IR) and far-infrared (FIR) emission from dust grains illuminated by starlight, free-free, bound-free, and bound-bound emission from ionised plasma, and X-rays. In Fig. 1.3 we display a schematic of the spectral energy distribution (SED) of the ISRF as a function of wavelength (and frequency). From this example we see that the CMB dominates the SED at radio wavelengths and thermal dust emission at IR wavelengths, while starlight dominates the optical and UV regimes.

Another source of pressure and ionisation at play even in the very densest environments of the ISM, are cosmic rays. They are high-energy, relativistic particles ($\sim$99% small nuclei and $\sim$1% electrons) with energies spanning from 100 MeV to $\geq$1 TeV (Fig. 1.4).

Comic rays propagate through gas with sparse interactions, except at low energies, at which their energy spectrum is least explored. Therefore, most present day estimates of the cosmic ray ionisation rate, a key quantity of astrochemistry are made indirectly through chemical constraints. The cosmic rays are strongly coupled to the magnetic fields by Lorentz forces and by strong scattering off field irregularities. The strength of the magnetic field is on average 5 μG and is essential in providing a net pressure over large scales, responsible for balancing the self-gravity of the gas.

And lastly, hot luminous massive stars, through their winds and the supernova explosions they end in, deposit mechanical energy into the ISM and drive supersonic motions and turbulence. Turbulence plays a key role in the transport and mixing of new elements. These

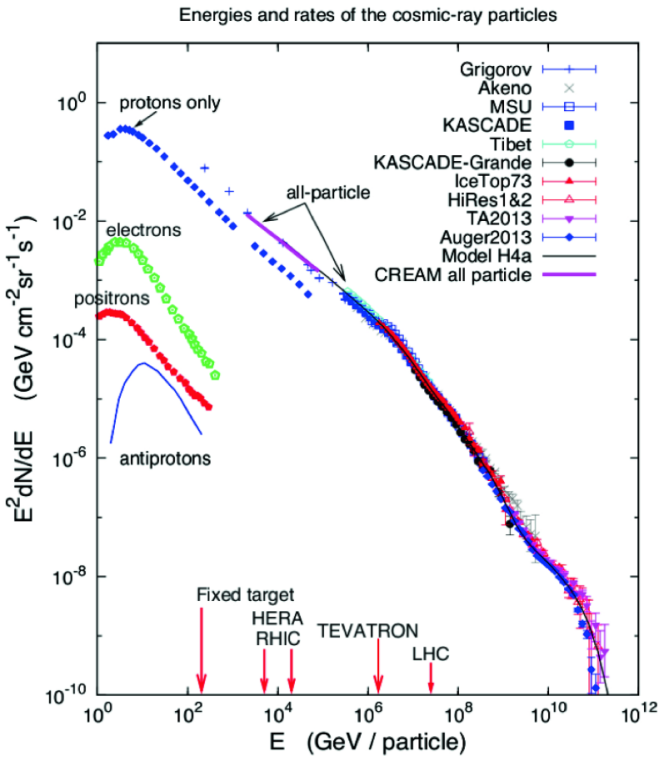

Figure 1.4: Energy spectrum of cosmic rays as observed with different instruments and telescopes. Taken from Blasi (2014).

cycled elements become parts of molecules and thus participate in star formation as illustrated in Fig. 1.2. Moreover, the pressure resulting from the velocity dispersion also plays a role in stabilising against gravitational instabilities present in the region. It is remarkable that the energy densities of the different components discussed, are similar up to an order of magnitude between 0.2, and 2 eV cm^{-3} (see Table 1.5 of Draine (2011) for a complete list of energy densities) for the conditions prevalent in the local ISM. Only partly coincidental, this equivalence reflects the efficient transfer of energy between the different forces at play. Therefore, it is imperative to include or take into account the interplay between the different sources of energy present in the ISM, particularly when studying its dynamics, but also its chemistry.

1.1.2 Phases of the interstellar medium

The earliest of the many models characterising the multi-phase ISM was put forth by Field et al. (1969), who postulated the existence of a two phase ISM assuming that the atomic gas in the ISM is in thermal equilibrium. The two phases were referred to as the cold, and warm neutral media (CNM, and WNM). As their names suggest, the former represents dense gas at low temperatures (~ 100 K) while the latter corresponds to warm (10^4 K) but diffuse gas. This schematic of the two phase ISM was extended by McKee & Ostriker (1977) to include 'coronal' gas with temperatures in excess of 10^6 K primarily formed from ionised bubbles created in supernovae explosions. This phase of the ISM came to be known as the hot ionised medium (HIM) and observationally manifests itself through its X-ray emission. While this gas fills a significant volume fraction it only represents a small fraction of the total gas mass. Thus an additional phase was invoked, the so-called warm ionised medium (WIM), which is a

Table 1.1: Typical properties of the different phases of the ISM. The values are adapted from Draine (2011) and Snow & McCall (2006).

ISM phase		Temperature [K]	Density [cm^{-3}]	Volume filling factor [%]
HIM		$10^{5.5}$–10^{7}	0.004	50
WIM		$\sim 10^{4}$	0.3	10
WNM		~ 5000	0.6	40
CNM	Diffuse atomic	30–100	10–100	0.01
	Diffuse molecular	30–100	100–500	0.001
	Translucent	15–50(?)	500–5000(?)	0.001(?)
	Dense molecular	10-50	$> 10^{4}$	10^{-4}

widespread component whose constituent material is predominantly ionised by radiation from massive stars of stellar types O and B. The physical conditions traced by the different phases are tabulated in Table 1.1, as determined from large scale surveys of neutral, ionised and coronal material.

1.1.3 Structure and dynamics of the cold neutral ISM

The cloud components comprising the CNM can be further classified into diffuse atomic, molecular, translucent and dense molecular clouds, respectively. The gas in these cloud layers is considered to be neutral with reference to the ionisation state of hydrogen as most of its volume lacks Lyman continuum photons (with energies > 13.6 eV) that can ionise it. However, the CNM is not neutral in the strictest sense because species with ionisation potentials lower than that of hydrogen (> 13.6 eV) can still be ionised (for example the ionisation potential of atomic carbon is 11.26 eV). Furthermore, cosmic rays are can freely penetrate and (partially) ionise gas in dense clouds that are well shielded from other sources of ionisation like UV and X-ray photons. As we will see later in this work, this process enables the chemistry of exothermic ion-neutral reactions. This classification of the CNM described above, is illustrated through a chemical model in Fig. 1.5.

Diffuse atomic clouds

Diffuse atomic clouds are entirely exposed to ISRFs, as a consequence of which the molecules formed in these layers readily undergo photo-dissociation. However, since the different cloud components are well mixed without distinct boundaries, the neutral gas in consideration here, is not *purely* atomic. Therefore, this phase is characterised not only by its large abundance of neutral atomic hydrogen but also its low molecular fraction, f_{H_2}, typically < 0.1. The molecular fraction defines the amount of molecular material along a given sight line over the total gas fraction sampled. It is either expressed as a ratio between volume densities as $f^{n}_{H_2} = 2n(H_2)/n(H)$ or in terms of their column densities as $f^{N}_{H_2} = 2N(H_2)/N(H)$. Hence, the majority of the properties of these cloud layers are naturally inferred from observations of the 21 cm line of atomic hydrogen (HI). This transition arises from the small ground state hyperfine

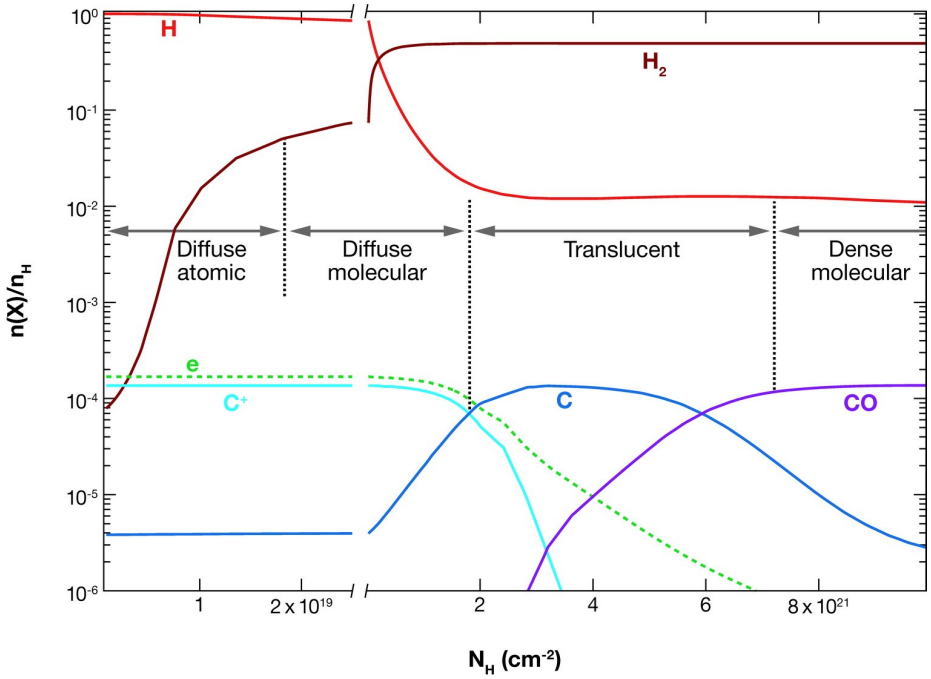

Figure 1.5: Photodissociation region (PDR) model with $n_{\rm H} = 100\,{\rm cm}^{-3}$ and $\chi_{\rm UV} = 1$, illustrating the classification of the CNM. Taken from Snow & McCall (2006).

structure (HFS) splitting of the hydrogen atom caused by the interaction between the magnetic moments of the proton and electron within the atom. In the ISM, this famous 21 cm line is most widely observed in emission, but may also appear in absorption against a background radio continuum source. While HI observations can map the distribution of gas in galaxies (although not without uncertainty), it can also be used to measure orbital motions of the gas to determine the rotation curves of these galaxies. An application in which observations of the HI 21 cm line are used to measure heliocentric distances is briefly discussed in Chapter 7.

In addition to atomic hydrogen, diffuse atomic clouds can also be probed by the fine-structure lines of neutral and ionised metals[1], most notably of carbon (CI, CII), nitrogen (NI, NII) and oxygen (OI, OII, OIII) at FIR wavelengths, which are important coolants. These fine-structure transitions arise from interactions between the orbital angular momentum of the electrons in an atom and the total spin state of the atom. However, despite being the most abundant elements in diffuse atomic gas, both hydrogen and helium are very weak coolants because they do not emit photons through collisional excitation, at the low gas temperatures of these regions. In recent years, ArH^+ whose chemistry is initiated by the ionisation of Ar by cosmic-rays, has proven to be an excellent tracer of the diffuse atomic gas. In Chapters 7 and 8 we discuss in more detail the capabilities of this molecule or rather molecular ion in tracing the diffuse atomic gas layers.

[1]In astronomical parlance, the term metal is used for all atoms heavier than helium.

Diffuse molecular clouds

The diffuse molecular clouds present in the CNM has a substantial molecular fraction ($f_{H_2} > 0.1$), which subsequently initiates interstellar chemistry. Within such clouds, molecular hydrogen, H_2, is formed on bare dust grains that consist of amorphous silicates or carbonaceous material. Upon colliding with a dust grain, there is a probability that the incoming H atom can get adsorbed onto the grain surface. The adsorbed H atoms diffuse across the surface of the grain either by thermal hopping or by tunnelling. When two such H atoms encounter each other on the surface they (may) form H_2. It should be noted that the formation of H_2 in the gas phase is simply impossible because the excess energy produced in the synthesising the excited H_2^* complex cannot be efficiently radiated away owing to the lack of an electric dipole moment. Wakelam et al. (2017) presents a detailed summary of our current understanding of the formation of H_2 from the stand point of theory, observations and experiments and models.

The chemical composition of the diffuse molecular clouds is still regulated by the ionising ISRF and therefore many molecules are not sufficiently protected from dissociating UV radiation within these cloud layers. It is for this reason, that the main reservoir of carbon in these clouds is in the form of C^+ and not CO.

Translucent clouds

Translucent clouds form an intermediary cloud type with properties in between those of diffuse, and dense molecular clouds. Coined by van Dishoeck & Black (1989), the term 'translucent' explicitly refers to clouds with a certain range of visual extinction, A_V. Its definition has since been expanded to comprise a transition layer in which the dominant state in which carbon exists is no longer C^+ but C, and is not yet CO. Exposed to lesser amounts of irradiation than the diffuse molecular clouds, the decreasing abundance of C^+ and of the electron fraction in these cloud layers causes an increase in the abundance of neutral atomic carbon and subsequently (to a smaller degree) results in an increase in the abundance of carbon-bearing molecules like CO. Moreover, a major part of the analysis presented in this thesis probes the diffuse molecular and translucent layers of the CNM using the CH and CH_2 radicals, see Chapters 4 and 6, respectively.

Dense molecular clouds

Almost completely shielded against the ISRF, the dense molecular clouds form the densest cloud component of the CNM with densities $> 10^4$ cm^{-3}. With only a small fraction of free electrons, carbon predominantly resides in the form of CO, making it the second most abundant molecule after H_2. These regions have been the central focus of very many studies not only because they host a rich chemistry but also because portions of dense molecular clouds can undergo (or are actually undergoing) gravitational collapse to form stars. High-mass stars formed this way then emit intense ultraviolet (UV) radiation thereby heating and ionising the surrounding ISM. Large regions of cold and dense molecular clouds are often referred to as giant molecular clouds (GMCs). With masses up to $10^6\,M_\odot$, GMCs can perturb gravitational effects on stars in the disks of galaxies and are most commonly found in the spiral arms. The complexities of star formation will not be dealt with here in this thesis but we point the reader

to reviews by Larson (2003), Kennicutt & Evans (2012), and references therein, for more information.

1.2 Challenges in observing molecular hydrogen

Despite being the most abundant molecular species, molecular hydrogen has traditionally been very difficult to observe. Lacking strong transitions in the visible wavelength regime of the electromagnetic spectrum (3500–7500 Å) that could be observed from the ground, astronomical signatures of this most abundant molecule were first detected by Carruthers (1970), who observed the Lyman resonance absorption bands of H_2 between 1000 and 1100 Å using the Aerobee-150 rocket toward the luminous stars ε Persei and ξ Persei. Searches for cosmic H_2 at different wavelengths followed, aided by advancements in detector technology, theory and laboratory experiments (see review by Williams 1999). The electronic transitions of H_2 produce spectral lines typically found at far-UV wavelengths but are limited to observations in the diffuse ISM in which the bright UV light of background stars is little affected by effects of interstellar dust extinction.

Since for redshifts, z, $\gtrsim 3$, the Lyman resonance lines are shifted into the visual part of the electromagnetic spectrum, using high spectral resolution instruments like the Ultraviolet and Visible Echelle Spectrograph (UVES) at the European Southern Observatory's Very Large Telescope, astronomers have directly detected H_2 in the far Universe in the spectra of quasars or γ-ray bursts (see, e.g., Ledoux et al. 2006).

While molecular hydrogen itself is practically unobservable in the general ISM, we mention that the rotational energy levels in the vibrationally excited states of H_2 can be excited under special conditions, either by collisions in interstellar shock waves, which create the high temperatures required, or by UV resonance. Indeed, the resulting *emission* in the (primarily) observed lines from the $v = 1 - 0$ vibration-rotation band at wavelengths around 2.2 μm are frequently observed in shocked regions, like the outflows from young stellar objects in the first case and in photodissociation regions (PDRs) in the latter (see, e.g. Shull & Beckwith 1982).

Since H_2, being a homo-nuclear and symmetric molecule does not possess a permanent dipole moment, its excited rovibrational states will only radiate through a weak quadrupole transition at $\sim$28 μm ($h\nu/k_\mathrm{B} \sim 500$ K). Therefore, sans transitions at radio wavelengths and only quadrupole transitions at near- and mid-IR wavelengths which cannot be excited in the cold gas phases associated with star formation, astronomers are, ironically unable to directly probe the coldest and densest parts of the ISM that are primarily composed of H_2. Fortunately, observational astronomers are able to overcome this hurdle by using other associated chemical species (including dust) as surrogates for H_2. The most commonly used proxy for measuring the total molecular reservoir in both local and high redshift galaxies is the 2.6 mm (115.27 GHz) $J = 1 - 0$ transition of CO, whose integrated intensity is scaled to that of molecular hydrogen by an empirical CO-to-H_2 conversion factor X(CO). The value of X(CO) most commonly adopted in studies of the Milky Way is 2×10^{20} cm^{-2} (K km s^{-1})$^{-1}$, with a $\pm$30 % uncertainty (see Bolatto et al. 2013b, and references therein). There is convincing evidence that the X(CO) factor displays a gradient with Galactocentric distances with its value at the Galactic centre being smaller than that in the disk by factors up to ten, which is also reaffirmed by observations

toward the centres of external galaxies. We refer the reader to Bolatto et al. (2013b) for a thorough discussion on the varied efforts to measure X(CO) in both the Milky Way and external galaxies, the uncertainties in the computed values, and the validity and assumptions involved in prescribing to a single value. Therefore a key question that naturally arises is, how reliable the measurements of CO are, in reproducing the total reservoir of molecular gas present in different galaxies?

1.2.1 CO-dark molecular gas – a new phase of the CNM

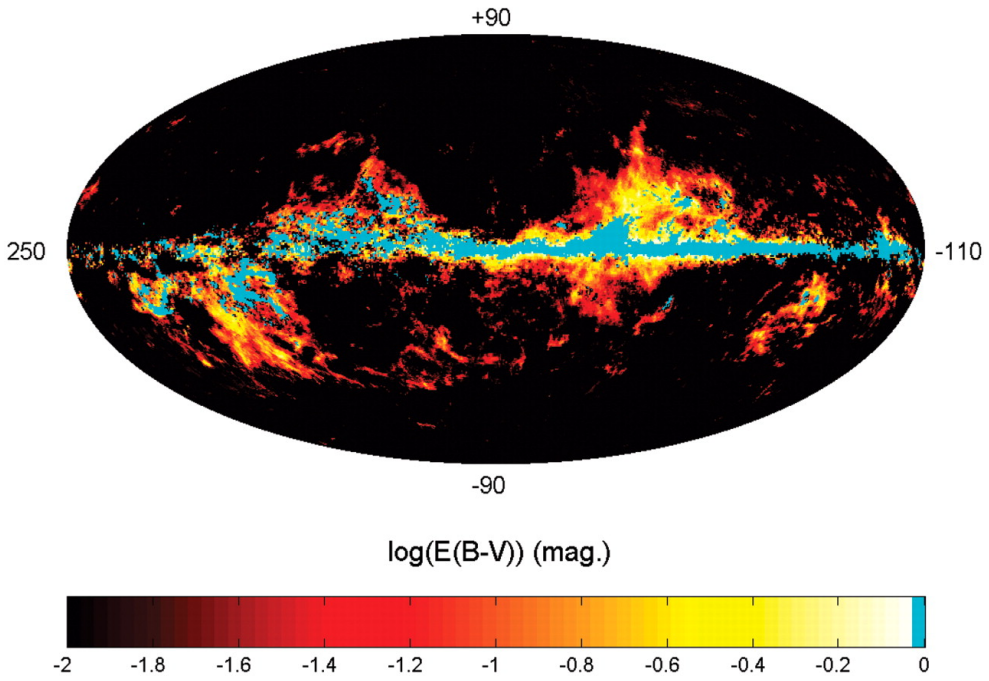

Figure 1.6: Example illustrating the CO-dark molecular gas component. Map, in Galactic coordinates centred on $l = 70°$, of the excess dust reddening found above that linearly correlated with the integrated HI and CO line intensities. The 94 GHz emission map shows the same excesses. CO intensities above $4\,\mathrm{K\,km\,s^{-1}}$ are overlaid in cyan. The dust excesses form extended halos around all CO clouds, the bright ones as well as the fainter CO cloud-lets that are not overlaid. This dust spreads in a dark gas, not seen in HI and CO but detected in γ rays. Figure taken from Grenier et al. (2005).

From the previous sections, one may conclude that the combination of the neutral hydrogen (HI) traced by the 21 cm line and H_2 traced using the CO ($J = 1 - 0$) transition can be used to account for the total hydrogen column density. However, when compared with large scale, spectrally resolved surveys made using other tracers of the total gas column density such as the γ-ray flux (EGRET, Grenier et al. 2005) and the sub-mm dust optical depth (*Planck,* Planck Collaboration et al. 2016), an excess of gas was inferred (see for example Fig. 1.6). This excess gas, invisible in emission from HI and CO can be attributed to either the saturation of the HI emission profile or the inability of CO to act as a proxy for H_2, in regions of low

dust column densities (or visual extinction). Hence, this component of the neutral gas is termed as 'CO-dark' molecular gas (DMG). While the main constituent of this gas is sight line dependent, studies have shown that the excess dark gas is primarily molecular (Liszt et al. 2018). The atomic gas content that is unaccounted for, can be understood using HI absorption measurements while the molecular gas content missed by CO requires the use of additional H_2 tracers. While CO seems to trace the bulk of the molecular material in the ISM, in diffuse and translucent regions it is less efficiently self-shielded than H_2 and is readily photodissociated by the surrounding ISRF. Therefore, in such regions exposed to irradiation where carbon primarily resides in either its atomic or ionised forms, a substantial amount of molecular hydrogen is left undetected. Therefore this gas component found outside CO-emitting regions is often referred to as 'CO-dark' molecular gas. Since knowledge of the physical and excitation properties of the DMG is vital for our understanding of the chemical evolution and diversity of the ISM, it is of great importance to investigate the nature and composition of this dark gas.

The most widely studied chemical tracers of the dark neutral gas is C^+, a chemical precursor of CO within the diffuse and translucent regions of the ISM. The C^+ 158 μm line, a major cooling line in the ISM, has been used to extensively study the properties of the CO-dark gas in the Galactic plane under the Galactic Observations of Terahertz C+ (GOTC+; Pineda et al. 2013) survey using the Hershel telescope. However, since C^+ emission traces both atomic as well as molecular gas it is necessary to compare these results with those from other tracers in order to better constrain the physical properties of the molecular gas in these clouds. For this reason, astronomers have sought the use of other molecules and their signatures to not only investigate DMG but also the other phases of the CNM. However, with a wealth of molecules and molecular ions to choose from, ranging from the simplest diatomic molecules to complex organic and polycyclic aromatic hydrocarbons, astronomers are spoilt for choice. In this thesis we approach this problem bottom-up, by precisely characterising the properties of small molecules which in-turn have a big impact on the molecular complexity of the ISM as they form the building blocks from which increasingly more complex species are formed.

1.2.2 The diagnostic power of hydrides

This thesis focuses on hydrides and hydride ions of the form XH_n and XH_n^+, respectively, and aims to investigate the properties of different phases of the CNM, with particular emphasis on diffuse (and translucent) clouds. Not only are diffuse clouds key contributors to the total mass of the ISM, they also form essential links in the stellar gas life-cycle (as shown in Fig. 1.2), making them a reservoir for heavy elements and ideal laboratories for the study of astrochemistry.

From a historical perspective, hydrides were the first gas-phase molecules detected in the ISM, through the detection and successful identification of the optical bands of CH and CH^+ near 4300 Å, along with that of CN by Swings & Rosenfeld (1937); Douglas & Herzberg (1941). While it was the transitions of OH at 18 cm that became the first molecular signature to be detected in the ISM at radio wavelengths by Weinreb et al. (1963), not too long after the discovery of the HI 21 cm line. From an astrochemical perspective, hydrides are of paramount importance as they are the first molecules formed at the root of interstellar chemistry.

Apart from H_2, which is formed on dust grains (Gould & Salpeter 1963), the chemical

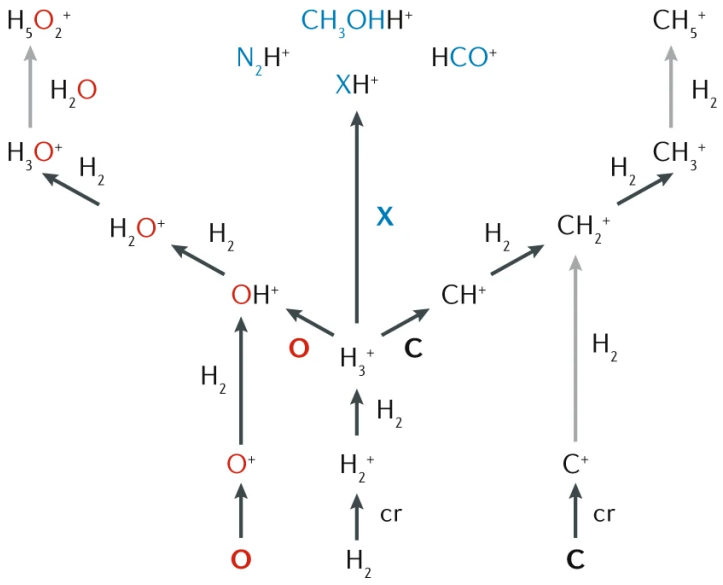

Figure 1.7: Network displaying the main astrochemical reactions stemming from the H_3^+ cation. The colours and thicknesses of the arrows depict different reaction mechanisms that occur depending on the astrophysical environment. Taken from McGuire et al. (2020).

composition of interstellar gas is largely determined by an ion-molecule chemistry, pioneered by Herbst & Klemperer (1973) and Watson (1974). The key molecular ion at the heart of interstellar ion-molecule chemistry is H_3^+, which is formed by the cosmic ray induced ionisation of H_2 (Geballe & Oka 1996). Figure 1.7 illustrates the fundamental role played by H_3^+ and in turn its first by-products i.e., the first metal hydrides in initiating the chemistry of oxygen-, and carbon-bearing species. Of the various gas-phase chemical pathways that are described by ion-molecule chemistry, that pertaining to carbon chemistry is of particular interest for the work presented in this thesis. In the following we summarise the chemical formation and destruction pathways of carbon-bearing species most relevant. One starts with the proton transfer reaction between neutral atomic carbon and H_3^+:

$$\mathrm{C} \xrightarrow{\mathrm{H_3^+}} \mathrm{CH^+} \xrightarrow{\mathrm{H_2}} \mathrm{CH_2^+} \xrightarrow[\mathrm{H_3^+}]{} \mathrm{CH_3^+}$$

Alternatively, in the presence of sufficient amounts of ionised carbon, as in regions dominated by UV radiation, carbon chemistry is driven by the hydrogenation of ionised carbon by successive reactions with vibrationally excited H_2:

$$\mathrm{C^+} \xrightarrow{\mathrm{H_2}} \mathrm{CH_2^+} \xrightarrow{\mathrm{H_2}} \mathrm{CH_3^+} \xrightarrow{\mathrm{e^-}} \mathbf{CH}$$
$$\xrightarrow{\mathrm{e^-}} \mathbf{CH_2}$$

The carbon chain cations are mainly destroyed via reactions with H_2 to from the corresponding protonated cation: $C_n^+ + H_2 \rightarrow C_nH^+ + H$ which can then undergo dissociative recombination to form neutral carbon chain molecules or radicals. Here, n counts the number of carbon atoms. This forward reaction for $n = 1$ presents another formation route for CH via CH^+ that is highly endothermic requiring energies 4640 K i.e., $C^+ + H_2 \rightarrow CH^+ + H$. For a long time, the high CH^+ abundances observed in diffuse molecular clouds have puzzled astrochemists. As a plausible solution, the supersonic motions of shock waves driven by supernovae and

protostellar outflows were invoked, which heat and compress the ambient gas, meeting the requirements of the endothermicity of the formation of CH^+ (Elitzur & Watson 1978; Flower & Pineau des Forets 1998). Alternately, but perhaps complementary, Godard et al. (2009) have proposed that the required energy is provided by the dissipation of interstellar turbulence and find that the 'turbulence dissipation regions' (TDRs) they model can reproduce the CH^+ column densities observed in diffuse clouds.

Once formed, the extremely reactive CH^+ readily undergoes hydrogen abstraction reactions to form CH_2^+ which then forms CH and CH_2 via dissociative recombination.

Both CH and CH_2 are primarily destroyed via reactions with atomic oxygen as follows:

$$\mathbf{CH} \xrightarrow{\mathrm{O}} HCO^+ + e^-$$
$$\mathbf{CH_2} \xrightarrow{\mathrm{O}} HCO + H$$

These reactions further initiate organic chemistry and the formation of a large fraction of the molecules present in the ISM. Since the formation and destruction and in turn the abundance and excitation of these species are determined by radiative and collisional processes coupled to the physical conditions of the gas they reside in, they form excellent diagnostics for the same. The analysis of the physical and excitation conditions traced by certain transitions of CH and CH_2 presented in Chapters 4 and 6 are aided by our understanding of their chemical network.

Moreover, recent advancements in sub-mm and FIR technology have opened up new access to explore the FIR sky (described in more detail in Sect. 2.1.2), whose interstellar spectrum is shaped by the rotational transitions of hydrides. Therefore, by taking timely advantage of these developments, we study the transitions of hydrides at sub-mm/FIR and radio wavelengths, the specific details of which are discussed in Chapter 2.

1.3 Scientific goals and outline of this thesis

While the primary goal of this thesis is clearly stated in the previous section, in the following paragraphs we describe the specific scientific objectives of this work. The scientific contents of this thesis is broadly divided into four parts the first of which pertains to the use of hydrides in probing the diffuse and translucent molecular phases of the ISM, while the second part concentrates on the search for methylidyne isotopologues, the third part aims to study the elusive methylene radical and lastly, the fourth part is aimed at probing the diffuse atomic ISM.

Part I: Probing the diffuse and translucent molecular ISM

- As discussed in Sect. 1.2.1, while CO has been historically used as a tracer for molecular hydrogen, which largely remains invisible in the quiescent conditions of the ISM (as it lacks a permanent dipole moment), there is mounting evidence that indicates the existence of a missing gas component unaccounted for by CO. One of the goals of this thesis is to establish the use of the methylidene radical, CH, as a tracer for H_2 in the diffuse regions of the ISM.

CH stands out from other hydride tracers because it has a tight correlation with H_2 as established by Federman & Willson (1982); Sheffer et al. (2008); Weselak (2019). Moreover, it is seen in widespread unsaturated absorption in the optical and FIR wavelength regimes which deems the determination of its column densities straightforward. Therefore in Chapter 3, we present upGREAT/SOFIA observations of the supra-Terahertz rotational transitions of CH and analyse its absorption spectra in the context of CO-dark molecular gas. We also explore the relation between CH and another widely studied tracer of the DMG component, the hydroxyl radical, OH (Li et al. 2018; Engelke & Allen 2018).

- While the absorption spectra of the sub-mm and FIR wavelength transitions of CH provide robust tools for measuring column densities, their observations are limited and, moreover, expensive because they require space- or air-borne instrumentation. This turns our attention toward other viable transitions of CH and in particular the three radio wavelength (9 cm) HFS lines between the Λ-doublet components of its rotational ground state. Observed for the first time by Rydbeck et al. (1973), the radio lines of CH were soon extensively observed across the Galaxy toward both HII regions and dark clouds, alike. The excitation conditions of this ubiquitously observed component were found to be inconsistent with assumptions of local thermodynamic equilibrium (LTE) and further complicated by level inversion. Therefore, the excitation properties of this weak maser have not been well understood.

  In Chapter 4, we aim to provide new constraints on both the excitation as well as the physical conditions traced by the CH ground state radio lines, 'anchoring' them with accurate column densities provided by its FIR CH rotational lines, whose HFS transitions share a common lower energy level with the HFS lines in the rotational ground state of CH. The results of our effort will greatly validate the use of the easily observable ground state HFS lines of CH as a powerful radio-wavelength probe of the diffuse and translucent ISM, alongside the 21 cm HI, the 18 cm OH, and the 6 cm H_2CO lines.

Part II: Methylidene isotopologues

- While CH has been studied across a wide range of frequencies, there is very little known about its isotopologues, ^{13}CH and CD, in the ISM. Chapter 5 details our search for ^{13}CH in the ISM, with the aim of providing additional constraints on the $^{12}C/^{13}C$ ratio over Galactic scales, a quantity that traces the degree of nuclear processing present within a Galaxy. Unsaturated and free from isotope selective effects which preferentially favour the production of one isotope over the other, CH presents a new, potentially unbiased candidate to probe the $^{12}C/^{13}C$ Galactic gradient. Turning to another isotopologue, CD, investigating the degree of fractionation in CD, inferred from the CD/CH ratio, will help unravel its formation chemistry and association with CH_2D^+ – one of the primary deuterated ions responsible for deuterium fractionation in carbon-bearing species in the ISM.

Part III: The elusive methylene radical

- As an early product of ion-molecule gas phase chemistry, the methylene radical, CH_2 similar to CH, plays an important role in interstellar chemistry. But in spite of its astrophysical importance and large predicted abundance (comparable to that of CH) there have been very few known and unambiguous detections of this molecule till date. This is partly due to its widely spaced energy levels, which have rendered its low-energy lines inaccessible from the ground. The 68–71 GHz ortho-CH_2 lines were first detected towards the Orion and W51 star-forming regions by Hollis et al. (1995). Given their high energies above the ground (225 K) they were thought to arise in dense, hot regions near newly formed stars, contrary to expectations from chemistry.

  In Chapter 6, we address this question and clarify the nature of CH_2's emission particularly toward the Orion GMC, but also discuss our successful searches towards other sources.

Part IV: Probing the diffuse atomic ISM with a molecule

- Thus far, our scientific goals have primarily focused on the diffuse *molecular* and translucent parts of the ISM but, what about the diffuse *atomic* clouds? As discussed in Sect. 1.1.3 and seen from Fig. 1.5, neither are the diffuse clouds purely atomic nor does the 21 cm HI line strictly trace regions of atomic gas alone. Tracing cloud components with varying amounts of molecular material from 0.1% up to 50%, paradoxically, HI does not selectively trace only atomic gas. One of the surprises of the Herschel mission was the detection of ArH^+ towards the Crab Nebula in emission and in absorption towards strong Galactic background sources. The analysis of the latter suggested that ArH^+ ubiquitously and exclusively probes the diffuse atomic regions of the ISM. This conclusion was drawn from observations, which showed almost no absorption toward the envelopes of the observed star-forming regions. Moreover, ArH^+ must reside in low-density gas as it would otherwise be readily destroyed via proton transfer reactions with H_2. Furthermore, the chemistry of ArH^+ is initiated via the ionisation of Ar to Ar^+ by cosmic rays which makes ArH^+ a good tracer of not only diffuse atomic gas but also of the cosmic ray ionisation rate present in these regions.

  Therefore, in Chapters 7 and 8 we study ArH^+ alongside other diffuse gas tracers like OH^+, and H_2O^+ and the molecular gas tracer CH (and HF) toward seven sight lines within the Milky Way and toward the central regions of two nearby external galaxies, with the aim of providing an observational probe for the transition from primarily diffuse *atomic* gas to translucent *molecular* gas by constraining the molecular fraction.

Finally, Chapter 9 summarises the main findings of this work together with an outlook on future projects. In the next chapter, we present an overview of observational astronomy and the general methods employed for data analysis.

Chapter 2

Observations and data analysis

So remember to look up at the stars and not down at your feet. Try to make sense of what you see and hold on to that childlike wonder about what makes the universe exist.

Stephen William Hawking, theoretical physicist, cosmologist

Overview

With their eyes, humans have looked at the stars forever. For decades astronomers have studied, and continue to study, the universe through observations of media other than visual light, by detecting radiation over the whole electromagnetic spectrum, particles, and most recently, gravitational waves. A multi-wavelength endeavour, modern astronomy relies on the synthesis of data collected at a variety of wavelengths in order to form an accurate and coherent picture of the universe. However, the techniques used to explore the different wavelength bands are vastly different, and in this thesis we concentrate on observations made in the sub-millimetre and radio ranges. Therefore, this chapter aims to introduce to the reader essential aspects of the different observational techniques employed, alongside methods of data analysis that are most relevant to the contents of this thesis. The general references used in this chapter are Wilson et al. (2012), Burke & Graham-Smith (2014), and Thompson et al. (2017) while a detailed description of the specifics related to the observations is given in each individual chapter.

2.1 Introduction

2.1.1 A brief history

While, early attempts to detect solar radio waves were unsuccessful, it was in 1931 that the first radio waves from the Milky Way were detected by the physicist and radio engineer Karl G. Jansky. Employed at that time, by the Bell telephone laboratories it was upon investigating the origins of radio wavelength interference, that he was able to show that the source of the excess radiation he observed at $\nu = 20.5\,\mathrm{MHz}$ ($\lambda = 14.6\,\mathrm{m}$) arose from outside of the solar system. Intrigued by the detection of 'noise' from the sky, this work was followed up, and extended by Grote Reber who carried out the first sky survey of the Galactic plane at radio wavelengths in 1938, using a parabolic dish reflector that he built by himself (Reber 1944). The surprise discovery by Jansky and pioneering efforts by Reber and others, along with advancements in technology during and post World War II, led to the birth of radio astronomy, a field that has been evolving ever since.

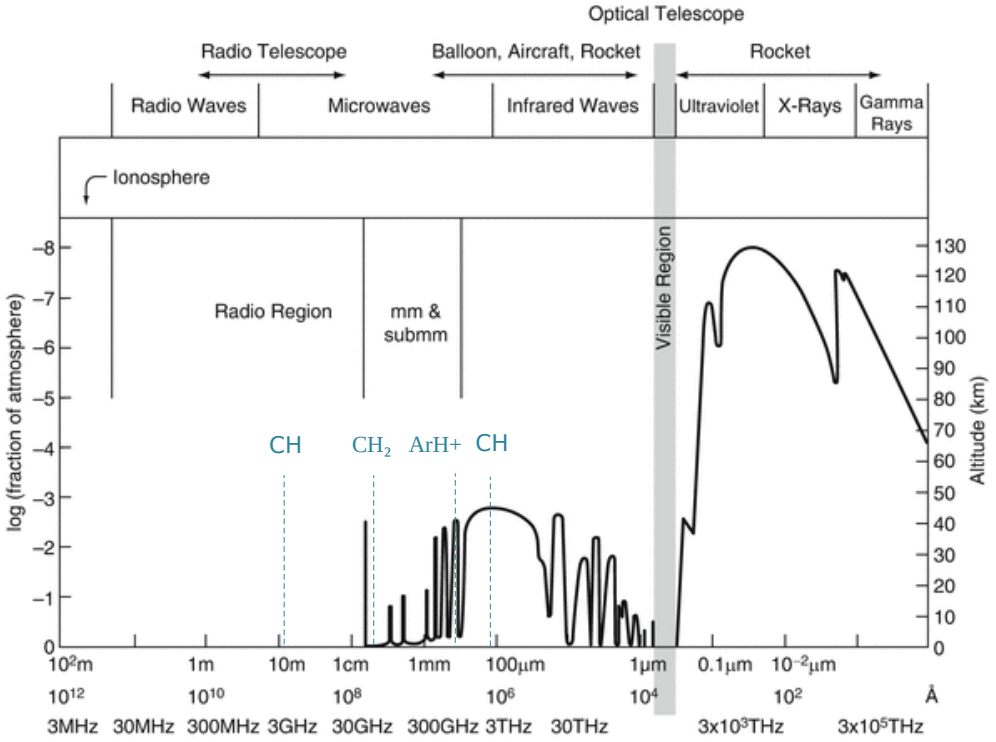

Figure 2.1: Schematic of the transmission through the Earth's atmosphere across the electromagnetic spectrum plotted as a function of wavelength (*upper x-axis*) and frequency (*lower x-axis*). Some of the main transitions studied in this thesis are highlighted by the dashed blue lines. The black curve represents the fraction of the atmosphere (*left-axis*) and the altitude (*right-axis*) needed to reach a transmission of 0.5. Image adapted from Wilson et al. (2012).

Astronomy at millimetre (mm) and sub-millimetre (sub-mm) wavelengths however, began only in the 1960's, accessing a part of the electromagnetic spectrum between the infrared and radio wavelengths. The mm/sub-mm wavelength interval provides a unique range for probing cold molecular gas and observing highly excited lines from ions and molecules. Together, over the past sixty odd years, astronomers have used both mm/sub-mm as well as radio observations to explore everything from the atmospheres of planets in the solar system to energetic phenomena in the hearts of nearby and even high redshift galaxies.

2.1.2 The atmospheric window

Combined, the mm/sub-mm and radio wavelength band extends from, $\lambda = 10$ m down to 0.3 mm ($\nu = 30$ MHz $-$ 1 THz) and radiation coming in from space is constrained by the absorption, emission and refraction of radiation through the Earth's atmosphere as shown in Fig. 2.1. The lower limit of the radio window near $\sim$30 m ($\nu = 10$ MHz) determined by the Earth's ionosphere whose charged particles reflect radio waves (with λ>30 m) back into space. The high-frequency limit, at far-infrared (FIR) wavelengths is set by the absorption at $\sim$1 THz by molecules in the Earth's atmosphere, such as O_2 and O_3, with H_2O contributing by far the

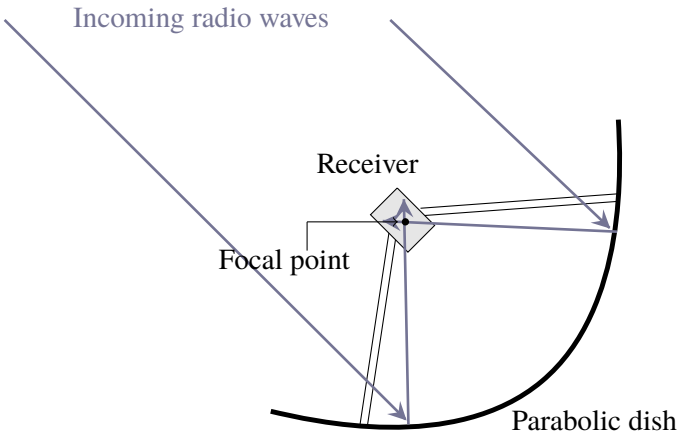

Figure 2.2: Schematic of the frontend components of a single-dish radio telescope.

most.

Since the atmosphere is not or only moderately transparent over a large part of this wavelength range, much of it cannot be easily accessed from the ground. Still, observations in certain wavelength intervals called the 'sub-mm windows' are possible, since the atmospheric transmission varies with altitude and the weather conditions present (i.e., precipitable water vapour, pwv). Therefore, such windows are typically observed from high mountain sites with dry conditions like the Atacama desert in Chile for $\lambda < 0.2\,\mathrm{mm}$ (frequency 1.5 THz). Higher frequency sub-mm/FIR observations are only possible with air-borne telescopes, balloons, and spacecrafts. Moreover, ground-based observations can be carried out either using a single-dish telescope or an interferometer or both in conjuncture, depending on the scientific goals.

2.2 Observables and telescope properties

2.2.1 Telescope fundamentals

The simplest observing instrument is a single-dish telescope comprising of a parabolic mirror or antenna, as shown in Fig. 2.2. The parabolic-shape of the antenna reflects and directs the electromagnetic waves entering the dish to the focal point of the mirror where it is collected using a receiver (feed). Despite focusing radiation from the telescope-pointing direction, the reflecting surface is not perfectly directional as it is still sensitive to radiation from all other directions, making directivity an important property of a radio telescope.

Radio telescopes are therefore characterised by their power pattern, $P_\mathrm{n}(\theta, \phi)$, which measures the response of the telescope to a point source. For a parabolic mirror, the power pattern in the focal plane is represented by the classical two-dimensional diffraction spectrum known as the *Airy pattern*. Fig. 2.3 displays the typical power pattern of a radio telescope. The largest lobe is known as the main beam and the smaller lobes are called sidelobes. This undesirable stray radiation is, a.o., the result of blockage by the structures holding the feed and irregularities of the surface of the telescope dish.

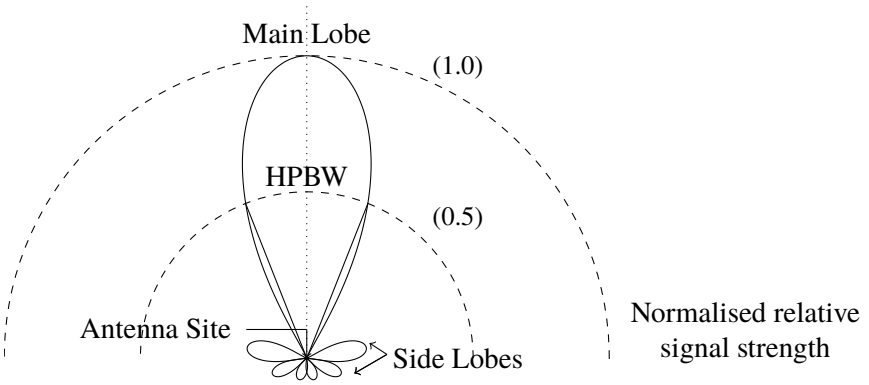

Figure 2.3: Normalised 2-dimensional antenna power pattern in linear scales.

It is hence clear that, in practice, the equivalent area over which the dish effectively collects and reflects radiation is not the same as the geometric area ($A_{\rm geo}$) of the dish. The effective collecting area, $A_{\rm eff}$, can be expressed in terms of the total beam solid angle, $\Omega_{\rm A}$, as,

$$A_{\rm eff} = \frac{\lambda^2}{\Omega_{\rm A}}\,, \tag{2.1}$$

where λ is the wavelength of the incident radiation. The ratio between $A_{\rm eff}$, and $A_{\rm geo}$ of a dish is called the aperture efficiency ($\eta_{\rm A}$) and forms a fundamental calibration parameter.

The beam solid angle can be defined as the solid angle subtended by an ideal isotropic beam,

$$\Omega_{\rm A} = \iint_{4\pi} P_{\rm n}(\theta,\phi)\,{\rm d}\Omega\,, \tag{2.2}$$

where $P_{\rm n}$ is the antenna power pattern normalised with respect to its peak. If Eq. 2.2 is integrated over only the main lobe, then we obtain an expression for the main beam solid angle, $\Omega_{\rm MB}$. This motivates the definition of the main beam efficiency, $\eta_{\rm MB}$, which describes the fraction of the effective solid angle that lies within the main beam,

$$\eta_{\rm MB} = \frac{\Omega_{\rm MB}}{\Omega_{\rm A}}\,. \tag{2.3}$$

Furthermore, if we characterise the main beam lobe by using a Gaussian function, then its width at half power (half power beam width, HPBW, or full width at half maximum, FWHM), defines the angular resolution, or capability of the telescope to separate two nearby point sources. The resolution, $\theta_{\rm HPBW}$, is well known from the optics of the instrument and is proportional to λ/D, where D is the diameter of the telescope and the proportionality factor is of the order of unity and depends on the illumination of the (sub-)reflector. Note that the minimum angular resolution of a telescope is considered to be its diffraction limit.

Another important antenna property is the type of antenna mount used, which, a.o., determines the accuracy of a telescope's pointing behaviour. The mechanical principles of different steerable mount designs will not be discussed in this text but we refer the reader to the detailed summary presented in Baars & Kärcher (2018). While increasing the size of the telescope can increase the resolution achieved, realistically, the size of the largest fully steerable dish

with acceptable performance is limited to $D = 100$–$110\,\mathrm{m}$. Moreover, because of technical limitations the larger the telescope the less accurate is its surface and so, the highest angular resolutions achieved by single-dish telescopes at sub-mm wavelengths is $\sim 10''$. Higher angular resolution can be attained with radio interferometry, which was pioneered in the 1950s and at mm wavelengths in the 1980s. By using an array of smaller single-dish telescopes working in unison, interferometry can achieve the resolving power (but not the sensitivity) of a fictional large dish with a diameter equal to the largest separation between the unit telescopes. The properties of interferometers will be discussed in more detail in Sec. 2.2.3.

The electromagnetic radiation collected by a telescope, is converted into measurable quantities that describe the strength of the observed radiation. Therefore, the following section appropriately introduces the basic terminology associated with measuring radiation.

2.2.2 Measuring radiation

Flux density

The power received by an antenna from an element of the solid angle of the sky, for each polarisation per unit frequency is given by,

$$P_\nu = \frac{1}{2} A_{\mathrm{eff}} \int_\Omega B(\theta,\phi) P_{\mathrm{n}}(\theta,\phi)\,\mathrm{d}\Omega \quad [\mathrm{W\ Hz^{-1}}], \tag{2.4}$$

where, $B(\theta,\phi)$ is the sky brightness distribution and the factor of 1/2 accounts for polarisation (the incoming radiation is generally, assumed to be unpolarised). For a discrete radio source observed using an antenna with a power pattern $P_{\mathrm{n}}(\theta,\phi)$, the integral of the product between the brightness distribution and the beam pattern of the antenna, measures the flux density, S_ν of the source and is given as follows:

$$S_\nu = \iint_{\mathrm{source}} B(\theta,\phi) P_{\mathrm{n}}(\theta,\phi)\,\mathrm{d}\Omega \quad [\mathrm{W\ m^{-2} Hz^{-1}}]\,. \tag{2.5}$$

If the size of the observed source is small in comparison to that of the beam, then $P_{\mathrm{n}}(\theta,\phi) \approx 1$. However, if the source is extended and much larger than the beam pattern, then Eq. 2.5 reduces to,

$$S_\nu(\theta_{\mathrm{o}},\phi_{\mathrm{o}}) = B(\theta_{\mathrm{o}},\phi_{\mathrm{o}}) \iint_{\mathrm{source}} P_{\mathrm{n}}(\theta,\phi)\,\mathrm{d}\Omega = B(\theta_{\mathrm{o}},\phi_{\mathrm{o}})\,\Omega_{\mathrm{A}} \quad [\mathrm{W\ m^{-2} Hz^{-1}}] \quad (\text{using Eq. 2.2})\,. \tag{2.6}$$

Owing to the large distances of the radio sources, the measured radio emission is weak. Therefore, the standard unit adopted for flux density is defined as $10^{-26}\,\mathrm{W\,m^{-2}\,Hz^{-1}}$ and is called Jansky [Jy], named after *Karl G. Jansky* the pioneer of radio astronomy.

Antenna and brightness temperature

Using *Planck's law* for radiation, the brightness, $B(\theta,\phi)$, of a black body radiator at a temperature, T, is given by,

$$B = \frac{2h\nu^3}{c^2} \frac{1}{\mathrm{e}^{h\nu/k_{\mathrm{B}}T} - 1} \quad [\mathrm{W\ m^{-2} Hz^{-1} sr^{-1}}], \tag{2.7}$$

where, h is Planck's constant, k_B is Boltzmann's constant and c is the velocity of light. Over the radio frequency range, for which $h\nu \ll k_B T$, the brightness can be approximated using the *Rayleigh-Jeans* (RJ) approximation as:

$$B = \frac{2k_B T\nu^2}{c^2}\,. \tag{2.8}$$

Under the RJ approximation, substituting Eq. 2.2 and 2.8 in Eq. 2.4 yields,

$$P = k_B T \quad [\,\mathrm{WHz}^{-1}]\,, \tag{2.9}$$

which represents the *Johnson-Nyquist theorem* (1928). This equation can be used to relate the power per unit frequency received by the antenna and its temperature, T. This equivalent temperature is the measured antenna temperature, T_A, of a radio source and can be expressed using Eq. 2.4 as,

$$T_A = A_{\rm eff}\frac{\nu^2}{c^2}\int_\Omega T(\theta,\phi)P_n(\theta,\phi)\,\mathrm{d}\Omega = \frac{1}{\Omega_A}\int_\Omega T(\theta,\phi)P_n(\theta,\phi)\,\mathrm{d}\Omega\,. \tag{2.10}$$

Assuming that the temperature is uniform across the solid angle, then,

$$T_A = \frac{1}{\Omega_A}T\int_\Omega P_n(\theta,\phi)\,\mathrm{d}\phi = T \quad \text{(using Eq. 2.2)}\,. \tag{2.11}$$

This implies that, in the RJ limit, the antenna temperature measured when observing an extended source of uniform brightness is equivalent to this temperature and independent of the size of the antenna. This temperature is defined as the brightness temperature, T_B. Note that, outside of the RJ regime, RJ equivalent temperatures are to be used.

Receiver noise and sensitivity

The total amount of radiation collected by a receiver system is a combination of energy received from the radio source itself (T_A) as well as additive noise from the receiver system. This noise is influenced by many factors and is collectively called the system noise temperature or system temperature ($T_{\rm sys}$). Therefore, the system temperature can be expressed as a linear combination of noise from different sources:

$$T_{\rm sys} = T_{\rm atm} + T_{\rm bg} + T_{\rm gr} + T_{\rm rec} + \ldots\,, \tag{2.12}$$

where, $T_{\rm atm}$, $T_{\rm bg}$, $T_{\rm gr}$, and $T_{\rm rec}$ account for radiation from (mostly) water vapour present in the Earth's atmosphere (which significantly contributes to $T_{\rm sys}$ at mm wavelengths), general contributions from the microwave and galactic backgrounds, noise contributed by radiation from the ground (spillover and scattering), and electronic noise temperature generated by the amplifiers in receivers, to name a few sources of noise.

Typically, $T_{\rm sys} \gg T_A$, therefore, in order to detect the signal, it is essential that σ, the root-mean-square (rms) noise of $T_{\rm sys}$ is smaller than the T_A level of signal one aims to detect. In a heterodyne receiver, the stability requirements needed for (sub-)mm astronomical observations

are met by down-converting the incoming signal frequencies to a passband at lower (radio) frequencies, which is achieved by non-linear mixing with a suitable local oscillator signal tuned to the target frequency. Fundamentally, Dicke (1946) showed that for such a 'square-law detector', σ is given by

$$\sigma = T_{\rm sys}\,\sqrt{2}/\,\sqrt{N}\,, \tag{2.13}$$

for N independent samples. The integration time over which the samples are averaged, $t_{\rm avg}$, is related to the elementary integration time step, Δt, by

$$t_{\rm int} = N\Delta t\,. \tag{2.14}$$

The critical sampling of the bandwidth-limited signal is given by the *Nyquist* sampling rate, $1/\delta t = 2f_{\rm max}$. In order to achieve a spectral resolution $\Delta\nu$, $N_{\rm c}$ spectral channels are required such that,

$$\Delta\nu = \frac{f_{\rm max}}{N_{\rm c}} = \frac{1}{2N_{\rm c}\delta t} = \frac{1}{2\Delta t} \tag{2.15}$$

Using Eqs. 2.14 and 2.15 to express the relationship between σ and $T_{\rm sys}$ (2.13) in terms of $\Delta\nu$ and $t_{\rm int}$, yields the radiometer sensitivity equation:

$$\sigma = \frac{T_{\rm sys}}{\sqrt{\Delta\nu\, t_{\rm int}}}\,. \tag{2.16}$$

In practice, $\Delta\nu$ is related to the spectral resolution by a factor close to unity which depends on the shape of an individual spectral channel. For a single-dish telescope, the contributions of the sky background and of the receiver itself are eliminated by a differential measurement on and off the astronomical target, such that,

$$\sigma = \frac{T_{\rm sys}}{\sqrt{\Delta\nu\, t_{\rm int}}} = \frac{T_{\rm sys}}{\sqrt{\Delta\nu\, t_{\rm ON+OFF}}}\,, \tag{2.17}$$

if equal amounts of time have been spent on both positions. For practical reasons, the smallest change in antenna temperature that can be reliably detected is typically defined as being at least three times the rms noise. Therefore a line is said to be securely detected if its peak line intensity is $>3\sigma$. This condition is particularly important in designing detection experiments of weak lines such as those reported in Chapters 5 and 6.

2.2.3 Interferometers

As discussed earlier, interferometry is a technique that combines incident radiation simultaneously collected by antennas that are widely separated. The relative phase of the signal received by each antenna varies because of the rotation of the Earth as well as due to differences in the path length between the source and each antenna. Therefore, when combined, the data received from each antenna produces an interference fringe pattern, which is later reconstructed to form an image of the observation.

The angular resolution in this case is proportional to λ/B, where B is the baseline length or projected distance between any two antenna-pairs as seen from the source. While, interferometers have the advantage that they can provide angular resolutions far higher than single-dish

receivers, they often filter out the response from extended sources, ($\theta_s \gg \theta_b$), a problem that is referred to as, missing short spacings. Therefore, an interferometer is sensitive to only a range of angular sizes that lies between λ/B_{max} and λ/B_{min}, where B_{min} and B_{max} represent the shortest and longest baselines, respectively. This loss of the source flux density information is often accounted for with the aid of additional single-dish measurements.

The spatial correlations of signals from various baselines recorded by an interferometer project positions with coordinates (u, v) on a plane perpendicular to the line of sight known as the *(u,v)* plane. They are related to the distribution of brightness in the sky via the Fourier Transform (FT). The mathematical formalism and the technicalities are significantly more involved and will not be discussed here in this thesis and for a comprehensive description refer the reader to Thompson et al. (2017).

For an interferometer system with N identical receivers there are $N(N-1)/2$ individual baselines and $N(N-1)$ independent samples. The radiometer equation (Eq. 2.16) for such a system then becomes,

$$\sigma = \frac{T_{sys}}{\sqrt{N(N-1)\Delta\nu t}} \,. \tag{2.18}$$

The corresponding rms noise in the measured brightness temperature, $\sigma_{(T_B)}$, in the RJ limit is given by,

$$\sigma_{(T_B)} = \frac{2k_B T_{sys}}{A_{eff}\Omega_B \sqrt{(N(N-1)\Delta\nu\, t)}} \,. \tag{2.19}$$

where, Ω_B is the beam solid angle. For a Gaussian beam it is given by $\Omega_B = 1.133\ \theta^2_{HPBW}$.

2.3 Telescopes used in this thesis

This section briefly introduces the main instruments used to collect the data presented in this thesis. The specifics pertaining to the different observations and the subsequent data reduction is described in greater detail in the corresponding chapters, in which also references are given.

The Atacama Pathfinder EXperiment 12 m telescope (APEX)

The APEX 12 m diameter telescope is located on the high plateau (5100 m above sea level) around the Chajnantor summit in Chile and operates at mm and sub-mm wavelengths. It is a modified prototype of a large fraction of the antennas comprising the Atacama Large Millimetre/submillimetre Array (ALMA). Two Nasmith cabins have been added to accommodate receivers for both coherent (heterodyne) and incoherent detection, as well as equipment suitable for single dish observations, in particular large area imaging. The telescope houses several instruments covering a wide range of frequency windows between (presently) ∼157 and 850 GHz, with receivers working around 1.0, 1.2 and 1.4 THz in the past and the future.

Figure 2.4: APEX 12 m telescope on Llano de Chajnantor. Credits: Laura Busch.

It thus covers all the sub-mm windows from 2 to 0.2 mm accessible from the ground (see, `http://www.apex-telescope.org/ns/instruments/` for a complete instrumentation overview). In Chapters 7 and 8 of this thesis, we present data collected using the Swedish-ESO PI (SEPIA660) receiver, which operates at frequencies from 578 to 738 GHz, and the now decommissioned MPIfR 1.05 THz receiver which operated at frequencies from 1000 to 1080 GHz. In addition, in Chapter 6, we discuss data collected using the dual-frequency instrument First Light APEX Submillimetre Heterodyne (FLASH) which can observe the 0.65 mm (460 GHz) and 0.87 mm (345 GHz) atmospheric windows, simultaneously.

The Effelsberg 100 m radio telescope

Located in the Eifel area in the western part of Germany, the Effelsberg radio telescope with a 100 m parabolic primary mirror and a 6.5 m elliptical secondary mirror, is one of the largest fully steerable telescopes in the world. Together, the prime and secondary focus receivers are capable of covering radio frequencies from 0.3 to 96 GHz. The different receiver systems cater to a broad range of scientific goals from spectral line and continuum, to pulsar observations and is even used for Very Long Baseline Interferometry (VLBI) experiments. We conducted our spectral line observations with the S20mm double beam receiver in the secondary focus, which covers a frequency range from 12–18 GHz as discussed in Chapter 6. For more details, see `https://www.mpifr-bonn.mpg.de/en/effelsberg`.

Figure 2.5: Effelsberg 100 m telescope in the Eifel valley. Credits: `https://www.radionet-org.eu/`.

The Onsala 20 m telescope

Located on the western coast of Sweden in Onsala near Göteborg, the Onsala 20 m telescope is enclosed in a radome which protects its structure from the (often harsh) weather. The telescope is equipped to observe at mm wavelengths with two channels, one at 3 mm, operating between 85 and 116 GHz and the other one at 4 mm operating between 67 and 86 GHz. Chapter 6 details our use of the 4 mm receiver channel of the Onsala 20 m telescope in our efforts to explain the elusive nature of the methylene radical. In addition to spectroscopic studies the telescope is also widely used for both astronomical and geodetic VLBI experiments (see, `https://www.chalmers.se/en/researchinfrastructure/oso/radio-astronomy/20m/Pages/default.aspx`).

Figure 2.6: The Onsala 20 m telescope inside the radome at the Onsala Space Observatory in Sweden. Credits: Peter Krantz.

The Stratospheric Observatory for Infrared Astronomy (SOFIA) telescope

Figure 2.7: SOFIA soaring over the snow-covered Sierra Nevada mountains with its telescope door open during a test flight. Credits: NASA/Jim Ross.

SOFIA is an airborne observatory, operating a 2.7 m reflecting telescope (with a 2.5 m effective aperture) mounted on a modified Boeing 747SP aircraft, designed to observe the universe at infrared wavelengths. It hosts a suite of instruments suitable for imaging, spectroscopy and polarimetry (for an overview, see, `https://www.sofia.usra.edu/science/sofia-overview`). Observations made using the German REceiver for Astronomy at Terahertz frequencies (GREAT) instrument onboard SOFIA have been widely used across this thesis. GREAT is a heterodyne receiver for high spectral resolution, and has six frequency channels, of which up to five can be used simultaneously.

For the observations carried out in this thesis (Chapters 3 and 5) we use the configuration between the low- and high-frequency arrays of the upGREAT receiver which cover frequency ranges from 1.81 to 2.07 THz and 4.74 THz, respectively.

The Karl G. Jansky Very Large Array (VLA)

Figure 2.8: Some of the 27 antennas that comprise the Very Large Array in the plains of San Agustin, in New Mexico. Credits: Magsud Aliyev.

Operated by the US National Radio Astronomy Observatory (NRAO), the VLA is an interferometer array with 27 active 25 m antennas (plus a spare), located on the San Agustin plains, northwest of Socorro in the United States covering frequencies between 1 and 50 GHz. The antennas are configured across three arms, with nine antennas in each arm, such that in alignment they form a 'Y' shape. The VLA offers four configurations of varying angular resolutions that are realised by moving the antennas relative to each other along the lengths of the arm; these are termed A, B, C, and D (in decreasing order of resolution). For more details see, `https://public.nrao.edu/telescopes/vla/`. In Chapter 4, we discuss the radio wavelength 3.3 GHz 'S-band' data collected using the VLA in D-configuration.

2.4 Interpretation of molecular line observations

Nikola Telsa had once remarked that, "*if you want to find the secrets of the Universe, think in terms of energy, frequency and vibration*". A majority of our knowledge and understanding of astronomical objects comes from the electromagnetic radiation received from it, in the form of spectral line features which may appear in absorption and/or emission. The following sections review the basic concepts of spectroscopy and radiative transfer theory necessary for interpreting the incoming radiation in terms of energy and frequency (and vibration).

2.4.1 Spectroscopy

The observed characteristics of the studied spectral lines features reflect the physical state and the chemical composition of the regions in which they originate. For every line, the frequency of the absorbed or emitted photons corresponds to discrete quantum mechanical upper and lower energy levels of the electronic, vibrational, rotational and/or fine-, and hyperfine-structure transitions of atoms, ions or molecules. Supplemented with theoretical and/or laboratory

measurements of spectroscopic parameters, the observed spectra can be used to determine physical properties of the gas such as the its density, temperature, and ionisation state.

Since transitions from different carriers can have similar frequencies, the unambiguous identification and assignment of spectral lines to a given species requires detailed laboratory measurements of the spectra of astronomically interesting species that (may) occur in the interstellar/circumstellar medium or planetary atmospheres. The laboratory efforts of generations of spectroscopists have measured the frequencies of lines for many hundreds of species and assigned them to energy levels. The results are catalogued and curated by several spectroscopic groups, prominently in the Cologne Database for Molecular Spectroscopy (CDMS, Müller et al. 2005) and the Jet Propulsion Laboratory catalogue (JPL, Pickett et al. 1998), to name the most important for radio and (sub-)mm astronomy.

The profiles of the spectral line profiles contain invaluable information on the gas dynamics along the line-of-sight (LOS). Typically described using Gaussian profiles, the centroid of the line profile provides, via the Doppler effect, the mean velocity, while its width and amplitude provide information on the velocity dispersion (often characterised by the FWHM) and the line intensity. The observed line widths are broadened as a result of the thermal (random) motions of atoms, ions or molecules in the gas or through non-thermal and turbulent motions associated with the local fluid dynamics of the regions they arise in.

In order to interpret observations of atomic and molecular lines in terms of the ambient physical conditions in the ISM, it is essential to calculate the population of the species in question in different energy levels of their quantum mechanical system. Therefore in the next sub-section we describe the processes responsible for exciting and de-exciting the different transitions.

2.4.2 Radiative and collisional processes

The different energy levels of bound and multi-level atomic or molecular systems are populated via collisions with the most abundant colliders in the ISM (e^-, H, H_2, He) or through radiative processes. Additionally, excitation can also result from recombination, or from chemical reactions ('chemical pumping'). Radiation can excite atoms or molecules to higher energy levels via the absorption of external radiation and can de-excite them to lower levels through the emission of a photon either spontaneously or through stimulation by an external radiation field.

Quantitatively, the population density of a two level system labelled l and u under statistical equilibrium (time-independent distribution that is, $\mathrm{d}n_i/\mathrm{d}t$=0 for every level i), is determined via the detailed balance between the different excitation processes to, and the de-excitation processes from a given energy level. Hence, for a two level system labelled l and u with population densities n_l and n_u, the detailed balance is given as follows,

$$n_l \left(B_{lu}\bar{J}_\nu + C_{lu}\right) = n_u \left(A_{ul} + B_{ul}\bar{J}_\nu + C_{ul}\right) , \tag{2.20}$$

where, $\bar{J}_\nu$ is the specific intensity averaged over all directions and over the line profile ($\bar{J}_\nu = 1/4\pi \iint I_\nu \phi(\nu)\, \mathrm{d}\nu \mathrm{d}\Omega$). The A and B coefficients introduced by Einstein in a seminal paper, Einstein (1917) characterise the *radiative* processes between a lower, l, and an upper, u, energy level. Namely A_{ul} (in s^{-1}), B_{lu} (in $\mathrm{cm}^2\mathrm{erg}^{-1}\mathrm{s}^{-1}\mathrm{sr}$) and B_{ul} (in $\mathrm{cm}^2\mathrm{erg}^{-1}\mathrm{s}^{-1}\mathrm{sr}$)

quantify spontaneous emission, absorption, and stimulated emission, respectively. In addition, the level populations are affected by *collisions*, which are described by the rates for collisional transitions, C_{lu} and C_{ul} (in s^{-1}). For a fixed set of physical conditions say, gas density, gas temperature and radiation field, the level populations are determined using the above equation. As the radiation field itself depends upon the level populations, this is a non-linear equation, which can be extended to multi-level systems.

Obeying detailed balance, the three Einstein coefficients are related such that the values of all three coefficients can be determined given the value of any one of them. The Einstein relations are as follows,

$$g_l B_{lu} = g_u B_{ul} \quad \text{and} \quad A_{ul} = \frac{2h\nu^3}{c^2} B_{ul}\,, \tag{2.21}$$

where g_l and g_u represent the statistical weights of the two levels.

The collisional excitation rates are expressed as the product between the density of the collision partner, $n_{\rm col}$ and the rate coefficient, which is the average velocity-integrated cross-section, γ (in $cm^3 s^{-1}$). Moreover, being only dependent on the quantum mechanical properties of the collision partners and independent of the equilibrium conditions, the upward and downward collisional rates are related by

$$C_{lu} = \frac{g_u}{g_l} C_{ul} \left(e^{-h\nu/k_B T}\right)\,. \tag{2.22}$$

The collisional rate coefficients are either measured directly from reaction rates in the laboratory which is a difficult task at very low temperatures or, most frequently, are computed quantum-chemically (see, e.g., the book by Flower 1990). The collisional rate coefficients for some of the most common interstellar species are listed on the website of the Leiden Atomic and Molecular Database (LAMDA; van der Tak et al. 2020).

Upon ignoring the effects of both internal and external radiation fields ($\bar{J}_\nu = 0$) under the optically thin limit and re-arranging the terms, Eq. 2.20 reduces to,

$$\frac{n_u}{n_l} = \frac{C_{lu}}{(C_{ul} + A_{ul})} = \frac{1}{(1 + A_{ul}/C_{ul})} \frac{g_u}{g_l} e^{-h\nu/k_B T} \quad \text{(using Eq. 2.22)}\,, \tag{2.23}$$

$$\frac{n_{\rm crit}}{n_{\rm col}} = \frac{A_{ul}}{C_{ul}} \quad \Rightarrow \quad n_{\rm crit} = \frac{A_{ul}}{\gamma_{ul}} \because C_{ul} = n_{\rm col}\gamma_{ul}\,, \tag{2.24}$$

where, $n_{\rm crit}$, the so-called critical density is an important parameter used to describe the dominant de-excitation process. Therefore, $n_{\rm crit}$ defines the density at which the rates of collisional de-excitation are equally as important as the rates of radiative de-excitation. This implies that at densities above $n_{\rm crit}$, collisional excitations are efficient enough to compensate for the losses in n_u through de-excitation by spontaneous emission. Therefore, species with higher critical densities can be used to probe denser regions.

If $n_{\rm crit} < n_{\rm col}$, then de-excitation via collisions dominate and the transition is said to be thermalised and the ratio of the level populations follows the Boltzmann distribution,

$$\frac{n_u}{n_l} = \frac{g_u}{g_l} e^{-h\nu/k_B T}\,. \tag{2.25}$$

Furthermore, if the excitation properties of the atoms/molecules given by the excitation temperature, $T_{\rm ex}$, can be determined by local excitation conditions of the gas namely, the kinetic temperature, $T_{\rm kin}$, then this state is known as *local thermodynamic equilibrium* (LTE). Therefore, under conditions of LTE the measured intensities of all transitions will give the kinetic temperature of the gas, regardless of their abundance.

On the contrary, if $n_{\rm crit} > n_{\rm col}$, then radiative processes dominate the de-excitation of the atom/molecule. In this case, the transitions are said to be sub-thermally populated and their relative populations can be described by $T_{\rm ex}$ such that $T_{\rm ex} < T_{\rm kin}$. The excitation in this case is governed by the radiation temperature which takes into account effects of dust heating by external radiation which may not affect the ambient gas and conversely there maybe effects such as the propagation of shocks which heat the gas which are not reflected by the dust. At very high densities, the contributions from gas and dust are coupled such that the level populations can be described by a single temperature. However this is not the case for most interstellar conditions encountered, particularly in the diffuse and translucent regions of the ISM which are the main regions of interest in this thesis. Therefore one would have to solve Eq. 2.20 for a given set of physical conditions in order to determine both the level populations as well as the line radiation. One should be cautioned that the notion of the critical density only qualifies for rough estimates because its definition is based on a two-level system, and not a more realistic multi-level one.

2.4.3 Radiative transfer

Radiative transfer theory describes the exchange of energy as electromagnetic radiation propagates through, and interacts with matter. These interactions can often modify the intensity of incoming radiation and primarily occurs via the emission, absorption and scattering of photons. Consider a beam of radiation with a specific intensity I_ν emitted at a frequency ν, propagating through matter in a given direction. Neglecting the effects of scattering, the change in the amount of radiation received along a path length, ds, can be described as follows,

$$\mathrm{d}I_\nu = j_\nu \mathrm{d}s - I_\nu \kappa_\nu \mathrm{d}s \,. \tag{2.26}$$

Eq. 2.26 comprises a source term, j_ν, otherwise known as the emissivity (emission coefficient), which increases the emission along the path with the addition of photons and a sink term, κ_ν, which attenuates the intensity via the absorption of photons known as the absorption coefficient or opacity.

The ability of a photon to penetrate an absorbing medium along a given path is characterised by the optical depth, τ_ν, which is given by $\mathrm{d}\tau_\nu = \kappa_\nu \mathrm{d}s$. Therefore, if $\tau \gg 1$ then the medium is said to be optically thick to the incident radiation and conversely, if $\tau \ll 1$ then it is optically thin. Furthermore, *Kirchoff's law* states that, the ratio of j_ν/κ_ν, known as the source function, S_ν, of a body, is independent of the nature of the radiating body and is dependent only on the frequency of the radiation and its absolute temperature. In terms of the Einstein coefficients

j_ν, κ_ν and thus S_ν can be written as,

$$j_\nu = \frac{h\nu_{ul}}{4\pi} n_u A_{ul} \phi_\nu \,, \tag{2.27}$$

$$\kappa_\nu = \frac{h\nu_{ul}}{4\pi} \left(n_l B_{lu} \phi_\nu - n_u B_{ul} \phi_\nu\right) \,, \tag{2.28}$$

$$S_\nu = \frac{n_u A_{ul}}{(n_l B_{lu} \phi_\nu - n_u B_{ul} \phi_\nu)} = \frac{2h\nu^3}{c^2} \left(\frac{g_u n_l}{g_l n_u} - 1\right)^{-1} \quad \text{(using Eq. 2.21)}, \tag{2.29}$$

where ϕ_ν, is the line profile function which describes the distribution of the emitting or absorbing atoms or molecules at a frequency ν. Re-writing Eq. 2.26 in terms of optical depth yields,

$$\mathrm{d}I_\nu = S_\nu \mathrm{d}\tau_\nu - I_\nu \mathrm{d}\tau_\nu \,. \tag{2.30}$$

If the nature of $S_\nu(\tau_\nu)$ is known along each element ds of the path, then the formal solution of Eq. 2.30 is given by,

$$I_\nu(\tau_\nu) = I_\nu(0)\mathrm{e}^{-\tau_\nu} + \int_0^{\tau_\nu} S_\nu(\tau'_\nu) e^{-(\tau_\nu - \tau'_\nu)} \, \mathrm{d}\tau'_\nu \,. \tag{2.31}$$

If the radiation is assumed to propagate through a uniform medium, under conditions of LTE then, the intensity of the radiation entering ($I_\nu(0)$), and emerging (I_ν) from the medium, can be approximated by blackbody radiation at $T_{\rm bg}$ (corresponding to the background temperature) and $T_{\rm ex}$, respectively, as per *Planck's law* discussed in Sect. 2.2.2. Therefore, at a constant excitation temperature Eq. 2.31 can be written as,

$$I_\nu(\tau_\nu) = B_\nu(T_{\rm bg})\mathrm{e}^{-\tau_\nu} + B_\nu(T_{\rm ex}) \left(1 - \mathrm{e}^{-\tau_\nu}\right) \,. \tag{2.32}$$

Described in terms of the brightness temperature following Eq. 2.8, the above solution of the radiative transfer equation can be re-written as,

$$T_{\rm B}(\tau_\nu) = T_{\rm bg}(0)\mathrm{e}^{-\tau_\nu} + T_{\rm ex}(\tau_\nu) \left(1 - \mathrm{e}^{-\tau_\nu}\right) \,. \tag{2.33}$$

For the case of absorption spectroscopy, Eq. 2.33 reduces to only the first term which makes it straightforward to estimate the optical depth from the observed line intensities and subsequent column density measurements. For emission spectroscopy, if the emission is optically thin ($\tau_\nu \ll 1$) then, $T_{\rm B} = \tau_\nu T_{\rm ex}$ but in the case of optically thick emission ($\tau_\nu \gg 1$) then, $T_{\rm B} = T_{\rm ex}$.

2.4.4 Non-LTE radiative transfer

As discussed above, under conditions of LTE, $T_{\rm ex}$ is approximated to be equal to the kinetic temperature, $T_{\rm kin}$, which is the temperature that characterises the average kinetic energy of the particles in the gas, and the level populations can be determined using Eq. 2.25. Since LTE does generally not attain, it is necessary to solve the rate equations Eq. 2.20 for statistical equilibrium where different excitation temperatures are typically required to characterise the relative population of different energy levels. Therefore, under non-LTE conditions solving the radiative transfer equations forms a non-linear and non-local coupled problem, difficult even for highly symmetric systems that in general will require a numerical treatment. While,

conserving the number of particles and charges involved, closes the system of equations, solving them via complete linearisation is cumbersome and not accurate enough, especially in two- and three-dimensional models. Therefore, numerical methods are used to iteratively solve the system of equations that govern the non-LTE radiative transfer problem. While various numerical schemes have been developed to solve these coupled equations, we summarise the methods most relevant to this thesis below. See Rybicki & Lightman (1979); Kalkofen (1984) or Cannon (1985) for detailed treatments of this topic.

Lambda iteration

Lambda iteration (LI) presents the most straightforward method for solving the non-LTE radiative transfer problem. It simply iterates between solving for the mean intensity, $\bar{J_{lu}}$ from the source function, S_{lu}, and the Λ_{lu} operator ($\bar{J_{lu}} = \Lambda_{lu}[S_{lu}]$) and computing $\bar{J_{lu}}$ from the level populations, until the relative change in the value of $\bar{J_{lu}}$ between successive iterations is lower than a pre-defined threshold. It is an attractive method because it defines the local response of the radiation field to changes in the level population by computing matrices of size $M \times M$ (at most), where M is the number of energy levels involved in the calculation. However, it has the disadvantage that it may often be slow. This is especially true for the case of optically thick lines which get trapped and subsequently require a large number of iterations before converging to a solution.

This drawback is overcome by using *accelerated* lambda iteration (ALI; Rybicki & Hummer 1991), a method that separates the local and external radiation contributions of the Λ-operator. The local part accounts for the radiation emitted by any given cell and its nearest neighbours, is represented by the tridiagonal part of the Λ operator which when directly inverted removes issues of self-coupling within the cell. Not requiring any iteration, the local problem is solved directly, leaving behind only the external component, whose radiation perturbs the level populations, to be solved iteratively. It is possible to further accelerate the convergence by using linear combinations of successive iterations instead of only the last one to obtain an improved set of initial values for the next iteration (Auer 1987).

Escape probability

Another commonly used method for simplifying the statistical equilibrium equations is the so-called *escape probability* (EP) method (Rybicki 1985). The EP formalism decouples radiative transfer from the rate equations. This is particularly useful in overcoming effects that hamper the transport of energy (photons) as is the case for optically thick transitions as discussed above. Therefore it is important to determine the various ways by which radiation can escape. The radiation escapes mainly either through multiple scattering or through the line wings of a transition. In the EP method, the transfer process is characterised using the escape probability, β, which defines the probability of an emitted photon to escape from a cloud with a certain optical depth. Therefore, the probability for a photon emitted at a frequency, ν, to escape a medium of optical depth, τ_ν, over the entire line profile, $\phi(\nu)$, is

$$\beta = \int \frac{1 - \mathrm{e}^{\tau_\nu}}{\tau_\nu} \phi(\nu) \mathrm{d}\nu, \quad \ni 0 < \beta < 1 \,. \tag{2.34}$$

Thus, the Λ operator discussed in the previous section is related to β by, $\Lambda_{lu} = (1 - \beta_{lu})$. Substituting β_{lu} into the statistical equilibrium equation (Eq. 2.20) yields,

$$n_l \left(B_{lu}(1 - \beta_{lu})S_{lu} + C_{lu}\right) = n_u \left(A_{ul} + B_{ul}(1 - \beta_{ul})S_{ul} + C_{ul}\right) . \tag{2.35}$$

Using Eq. 2.29 leads to,

$$\beta_{ul} n_u A_{ul} + n_u C_{ul} - n_l C_{lu} = 0 . \tag{2.36}$$

Therefore, with a good estimate of β_{ul} one can determine the level populations. The caveat is that Eq. 2.34 is only an approximation and one should in fact account for the probability of the photon escaping in all directions which changes Eq. 2.34 to,

$$\beta = \frac{1}{4\pi} \oint \frac{1 - \mathrm{e}^{\tau_\nu(\boldsymbol{i})}}{\tau_\nu(\boldsymbol{i})} \, \mathrm{d}\Omega \quad \text{where,} \quad \tau_\nu(\boldsymbol{i}) = \int_0^{\inf} \alpha_\nu(\boldsymbol{x} + s\boldsymbol{i}, \boldsymbol{i}) \mathrm{d}s \tag{2.37}$$

represents ray tracing along an infinitely long path from the point of interest, $\boldsymbol{x}$, along each direction $\boldsymbol{i}$.

In this thesis we have made use of two non-LTE radiative transfer codes namely, MOLPOP-CEP (Asensio Ramos & Elitzur 2018) and RADEX (van der Tak et al. 2007) in Chapters 4 and 6, respectively. Both codes are one-dimensional non-LTE radiative transfer codes, that compute the rate equations using the escape probability formulation assuming an isothermal and homogeneous medium with the option of using different geometries. Additionally, the MOLPOP-CEP code is also capable of providing an exact solution to the multi-line problem by computing coupled escape probabilities (CEP). It considers the source to be divided into zones that are coupled through terms resembling the standard escape probability expressions discussed above, resulting in a set of coupled algebraic equations for level populations that are self-consistent with the line radiation generated (see Asensio Ramos & Elitzur 2018, for more details).

2.4.5 Other lines and line radiative transfer phenomena

2.4.5.1 Masers

In a three-level system, it is possible to create an overpopulation in the second level if the radiative decay from the highest energy level is faster toward the second one than the lowest one. This requires collisional or radiative pumping mechanisms to ensure the population of the highest level. The subsequent cascade may lead to relative populations between the two lower levels that are far from LTE and can even result in *level inversion* such that,

$$n_u B_{ul} - n_l B_{lu} < 0 \quad \text{for} \quad u > l . \tag{2.38}$$

This leads to both a negative excitation temperature as well as a negative optical depth and the resulting amplified emission for a medium with a sufficient velocity coherence, is referred to as *maser* (microwave amplification by stimulated emission of radiation) emission. The highly non-linear nature of this process makes it difficult to model numerically. The weak masing action of important CH and CH_2 lines is discussed in Chapters 4 and 6, respectively. We refer the reader to the review by Elitzur (1982) and the books by Elitzur (1992) and Gray (2012) for thorough treatments of maser theory and phenomenology.

2.4.5.2 Recombination lines

When atoms get ionised by radiation from a hot source like O-B type stars, then recombination can take place to the higher energy levels in the atom that do not usually get thermally excited. The cascade down from these high levels can result in emission even at relatively low gas temperatures. These emission lines when observed at radio frequencies are called *radio recombination lines* (RRLs) and are most often observed in atoms of hydrogen, helium and carbon. We discuss the use of CRRLs as tracers for PDR layers in Chapter 6. Extensive information on RRLs can be found in the review by Brown et al. (1978) and the book by Gordon & Sorochenko (2002).

Part I

Probing the diffuse and translucent molecular ISM

Chapter 3

CH as a tracer for diffuse H_2

The visible and near-ultraviolet emission spectrum of the CH radical has been known ever since spectra of an ordinary Bunsen burner have been taken.

Gerhard Herzberg, Nobel Prize in Chemistry, 1971.

Overview

Despite being a commonly observed feature, the modification of the velocity structure in spectral line profiles by hyperfine structure complicates the interpretation of spectroscopic data. This is particularly true for observations of simple molecules such as CH and OH toward the inner Galaxy, which show a great deal of velocity crowding. A method to evaluate the influence of hyperfine structure splitting on complex spectral lines, was developed during the course of my Master thesis (see, Jacob 2017) based on the theory formulated by *Norbert Wiener* (Sect. 3.2). In this chapter, we present high spectral resolution observations of the rotational ground state transitions of CH near 2 THz seen in absorption toward several strong FIR-continuum sources. The observed line profiles of CH were deconvolved from the imprint left by the lines' hyperfine structures using the Wiener filter deconvolution. The quantitative analysis of the deconvolved spectra first entails the computation of CH column densities. Reliable N(CH) values are of importance owing to the status of CH as a powerful tracer for H_2 in the diffuse regions of the interstellar medium. The goal of this chapter is to further emphasise the use of CH as a tracer for H_2 particularly in 'CO-dark' regions, to investigate the radial distribution of its column densities across the Galactic plane, and to subsequently use it as a surrogate for H_2 to determine the abundance of the other molecules, like in this case OH. This chapter is published in *Astronomy & Astrophysics* as a paper titled, 'Fingerprinting the effects of hyperfine structure on CH and OH far infrared spectra using Wiener filter deconvolution', Jacob et al. (2019)[1], with changes made only in order to adapt it to the layout of this thesis.

3.1 Introduction

Hyperfine structure (HFS) splitting is a commonly observed phenomenon in spectroscopy that arises from interactions between unfilled electron shells and the nuclear spin magnetic moment of atoms or molecules. It leaves a unique imprint on the spectrum of a given chemical species and transition, much like fingerprints. Over the years, knowledge of HFS in atoms and molecules has served both atomic-, molecular-, and astro-physicists alike in interpreting

[1]Jacob et al. A&A, 632, A60, 2019, reproduced with permission ©ESO

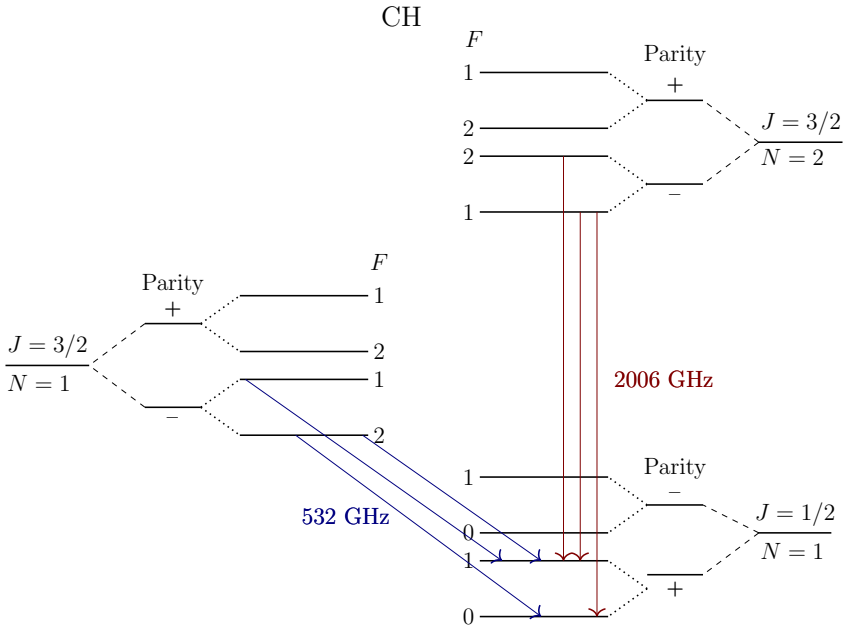

Figure 3.1: Low-lying energy level structure of CH. The $N, J = 2, 3/2 \rightarrow 1, 1/2$ HFS transitions of CH near 2006 GHz that were observed using SOFIA are represented in red while the $N, J = 1, 3/2 \rightarrow 1, 1/2$ HFS transitions near 532 GHz observed with *Herschel*/HIFI are displayed in blue.

observations. The effects of such splitting, despite being small, leads to energy differences that are typically of the order of ~ 0.03 K in terms of temperature. Since HFS interactions broaden, shift, and even alter the shape of spectra (Booth & Blackwell 1983), not taking them into consideration might lead to erroneous interpretations of astrophysical quantities. Overall, taking HFS splitting into account makes it possible to precisely model and resolve the underlying spectral line shapes, since the observed integral line profile is a superposition of the various HFS components. In recent years, the onset of improved observational techniques with greater sensitivity and higher spectral resolution have paved the way for rigorous spectroscopic studies and abundance measurements, in particular in the sub-millimetre and far-infrared (FIR) regions. Observations made between 2010 and 2013 with the Herschel-High Frequency Instrument for the Far-Infrared (HIFI, de Graauw et al. 2010), later followed by the German REceiver at Terahertz frequencies (GREAT, Heyminck et al. 2012) on board of the Stratospheric Observatory for Infrared Astronomy (SOFIA, Young et al. 2012) have resulted in high resolution (down to 10^{-7}) absorption spectra of a plethora of light hydride molecules of which the study is important for various reasons (for an overview see Gerin et al. 2016). In many cases, the background sources reside far away in the inner Galaxy. Thus the differential Galactic rotation causes complex velocity crowding, which is further complicated by the HFS of many of these molecules, including CH and OH, which are studied here. All this requires advanced techniques of analysis of the observed line profiles. Several different approaches

have previously been used to fit the HFS of various spectral lines through techniques ranging from simulated annealing algorithms (Wiesemeyer et al. 2016) and Monte Carlo approaches that use genetic algorithms (Estalella 2017) to direct deconvolution (Gerin et al. 2010), and multi-Gaussian fitting techniques (Neufeld et al. 2015a; Persson et al. 2016). In this paper, we introduce a technique that decomposes the contributions of HFS from astrophysical spectra, based on the theory developed by Wiener (1949). A linear and time-invariant method, the Wiener filter theory has found its application in practical signal reconstruction scenarios. It stands out from other filtering techniques because it provides the maximum a posteriori estimate of the unknown signal through a simple least squares analysis. Consequently, the Wiener filter has also found its application in astronomy as a tool that aids in cleaning contaminated images retrieved by aperture synthesis techniques (Caprari et al. 2000). In cosmological studies, deconvolution using the Wiener filter has been employed to accurately decompose the observed polarisation of the cosmic microwave background (CMB) radiation into maps of pure polarisation for its two components: E and B (Bunn & Wandelt 2017). Given the proven capability of the Wiener filter deconvolution as a method of choice for decomposition, we decided to adapt it for a novel application, the deconvolution of HFS from astrophysical spectra.

Concentrating for most of this paper on the transitions of a single molecule, we illustrate the working of the Wiener filter algorithm on spectra that are of astrophysical importance, through the spectroscopy of the $N, J = 2, 3/2 \rightarrow 1, 1/2$ ground state rotational transitions of CH, the methylidene radical. CH was amongst the first molecules detected in the interstellar medium (ISM) by Dunham (1937), and identified by Swings & Rosenfeld (1937). Being the simplest organic carbyne and one of the lightest hydrides, CH initiates the formation of a large fraction of the molecules present in the ISM, thereby playing a pivotal role in both the physics and chemistry of interstellar gas clouds. CH has been widely studied in various spectral regimes to infer the thermal, chemical and dynamical evolution of diffuse and translucent cloud regions (Rydbeck et al. 1973; Turner & Zuckerman 1974; Stacey et al. 1987). Moreover, the advent of space- and air-borne telescopes like *Herschel* and SOFIA have established the use of CH alongside other interstellar hydrides as tracers for H_2 in the diffuse regions of the ISM (Gerin et al. 2010; Wiesemeyer et al. 2018). Figure 3.1 shows the low-lying energy level structure of the ground electronic state of the CH molecule, abiding by Hund's case b. The total angular momentum states labelled J splits into a pair of Λ-doublet levels of opposing parity ($\pm\Lambda$). Each of these are further split into hyperfine levels given by $F = J \pm I$, where I is the nuclear spin of the H atom, I(H) = 1/2.

The outline of this paper is as follows: In Sect. 3.2.1, we develop the theory behind the working of the Wiener filter, and in Sect. 3.2.2, we detail our procedure for spectral line analysis: the Wiener filter algorithm. Having motivated our astronomical case study on the $N, J = 2, 3/2 \rightarrow 1, 1/2$ HFS transitions of CH, in Sect. 3.3, we describe our observations. In Sect. 3.4, we present the implementation of the Wiener filter on the absorption spectra and its analysis, while the results obtained are discussed in Sect. 3.5, in which we also compare the distribution of CH with that of OH, and explore the usefulness of CH as a tracer for H_2. We conclude this work in Sect.3.6.

3.2 Theory

Convolution is a formal mathematical operation used to describe the interaction between an input signal, $f(\nu)$, and an impulse response function, $h(\nu)$, to produce an output signal, $g(\nu)$, in a linear system. In spectroscopic terms, the input and output signals are analogous to the original and observed spectra while the impulse response in this case arises from the HFS splitting. For a discrete sample, such a convolution model can be mathematically formulated as follows:

$$g(\nu) = f(\nu) \circledast h(\nu) = \sum_{\nu'=-\infty}^{+\infty} f(\nu')h(\nu - \nu')\,. \tag{3.1}$$

With astrophysical observations, one is posed with the inverse problem of convolution, which is deconvolution, wherein the output spectrum is known, while its main constituent, the original spectrum, remains unknown. The convolution theorem renders this task trivial, as it reduces the operations of both convolution and deconvolution into those of simple multiplication and division, in Fourier space, given a priori knowledge of $g(\nu)$ and $h(\nu)$. Hence, in Fourier space, Eq. 3.1 becomes

$$\begin{aligned} G(\tilde{\nu}) &= F(\tilde{\nu}).H(\tilde{\nu}) \quad \text{Convolution;} \\ F(\tilde{\nu}) &= \frac{G(\tilde{\nu})}{H(\tilde{\nu})} \quad \text{Deconvolution}\,, \end{aligned} \tag{3.2}$$

where $G(\tilde{\nu})$, $F(\tilde{\nu})$ and $H(\tilde{\nu})$ represent the Fourier transforms (FTs) of $g(\nu)$, $f(\nu)$ and $h(\nu)$, respectively. However, such a point-wise division of the Fourier transforms is sufficient to obtain an estimate of $f(\nu)$, only as long as the transform of the response function remains non-zero over all frequencies. Moreover, realistic systems are influenced by noise, $n(\nu)$, which further degrades the observed spectrum, $d(\nu)$. This additive noise is often amplified when directly deconvolved, because it acts as a low-pass filter and gives rise to faux features in the reconstructed signal. Such issues of sensitivity are often tackled by using filters, and in the following sections, we introduce and employ one such filter, namely the Wiener filter.

3.2.1 Wiener filter deconvolution

Wiener's theory formulated a linear tool, the Wiener filter (hereafter WF) for additive noise reduction aimed to resolve the signal restoration problems (singularities) faced by direct deconvolution. The WF model assumes all signals to be stationary[2], and modelled by linear stochastic processes with a signal-independent noise. The WF output in the Fourier or inverse frequency domain, $\hat{F}(\tilde{\nu})$ is the product of the (noise) degraded observed spectrum, $D(\tilde{\nu})$, and the frequency response of the filter, $W(\tilde{\nu})$:

$$\hat{F}(\tilde{\nu}) = D(\tilde{\nu})W(\tilde{\nu}) \quad \Rightarrow \quad \hat{F}(\tilde{\nu}) = \left[F(\tilde{\nu})H(\tilde{\nu}) + N(\tilde{\nu})\right] W(\tilde{\nu}) \tag{3.3}$$

The filter further models the input signal by implementing a minimum mean square error

[2]Time invariant in first and second order statistics.

(MSE) ε^2 constraint on the deconvolution:

$$\varepsilon^2 = \sum_{\tilde{\nu}} \left|F(\tilde{\nu}) - \hat{F}(\tilde{\nu})\right|^2 \tag{3.4}$$

$$= \sum_{\tilde{\nu}} \left|F(\tilde{\nu}) - \left[F(\tilde{\nu})H(\tilde{\nu}) + N(\tilde{\nu})\right] W(\tilde{\nu})\right|^2 \tag{3.5}$$

$$= \sum_{\tilde{\nu}} \left|F(\tilde{\nu})[1 - H(\tilde{\nu})W(\tilde{\nu})] - N(\tilde{\nu})W(\tilde{\nu})\right|^2 \tag{3.6}$$

Expanding the quadratic term in Eq. 3.6,

$$\begin{aligned}\varepsilon^2 = \sum_{\tilde{\nu}} &\left([1 - H(\tilde{\nu})W(\tilde{\nu})]\,[1 - H(\tilde{\nu})W(\tilde{\nu})]^*\right)|F(\tilde{\nu})|^2 \\ &- [1 - H(\tilde{\nu})W(\tilde{\nu})]\,W(\tilde{\nu})^*\,(F(\tilde{\nu})N(\tilde{\nu})^*) \\ &- W(\tilde{\nu})\,[1 - H(\tilde{\nu})W(\tilde{\nu})]^*\,(N(\tilde{\nu})F(\tilde{\nu})^*) + |W(\tilde{\nu})|^2|N(\tilde{\nu})|^2\,.\end{aligned} \tag{3.7}$$

We assume that $N(\tilde{\nu})$ is independent of $F(\tilde{\nu})$, therefore $(F(\tilde{\nu}).N(\tilde{\nu})^*) = (N(\tilde{\nu}).F(\tilde{\nu})^*) = 0$. This reduces Eq. 3.7 to,

$$\varepsilon^2 = \sum_{\tilde{\nu}} |F(\tilde{\nu})|^2\,|1 - H(\tilde{\nu})W(\tilde{\nu})|^2 + |N(\tilde{\nu})|^2\,|W(\tilde{\nu})|^2\,. \tag{3.8}$$

The derivative of the MSE, ε^2 with respect to $W(\tilde{\nu})$ yields

$$\frac{\partial \varepsilon^2}{\partial W(\tilde{\nu})} = |F(\tilde{\nu})|^2\,[2(1 - W^*H^*)(-H)] + |N(\tilde{\nu})|^2\,[2W^*]\,, \tag{3.9}$$

using $\frac{\partial(zz^*)}{\partial z} = 2z^*$ (property of conjugates), where the asterisk represents the complex conjugate. Minimising $\partial\varepsilon^2/\partial W(\tilde{\nu})$ by equating Eq. 3.9 to zero and solving for $W(\tilde{\nu})$ results in the general form of the Wiener filter,

$$W(\tilde{\nu}) = \frac{H^*(\tilde{\nu})}{|H(\tilde{\nu})|^2 + \left|\frac{N(\tilde{\nu})}{F(\tilde{\nu})}\right|^2}\,.$$

Since the exact forms of both $N(\tilde{\nu})$ and $F(\tilde{\nu})$ are model-dependent, they remain as unknowns for most practical systems. However, for additive white noise that is independent of the signal, the $\frac{F(\tilde{\nu})}{N(\tilde{\nu})}$ ratio can be approximated by the signal-to-noise ratio (S/N), or some form of normalised noise variance, $\sigma_{\tilde{\nu}}$, characterised by the system noise. Rearranging the terms to fit the inverse filter formulation, the Wiener filter and restored spectra are given as:

$$W(\tilde{\nu}) = \frac{1}{H(\tilde{\nu})}\frac{|H(\tilde{\nu})|^2}{|H(\tilde{\nu})|^2 + \left|\frac{1}{\mathrm{S/N}}\right|^2} \qquad \text{and} \tag{3.10}$$

$$\hat{F}(\tilde{\nu}) = \underbrace{\frac{D(\tilde{\nu})}{H(\tilde{\nu})}}_{\text{Inverse filter}}\ \underbrace{\frac{|H(\tilde{\nu})|^2}{|H(\tilde{\nu})|^2 + \left|\frac{1}{\mathrm{S/N}}\right|^2}}_{\text{Kernel}}\,. \tag{3.11}$$

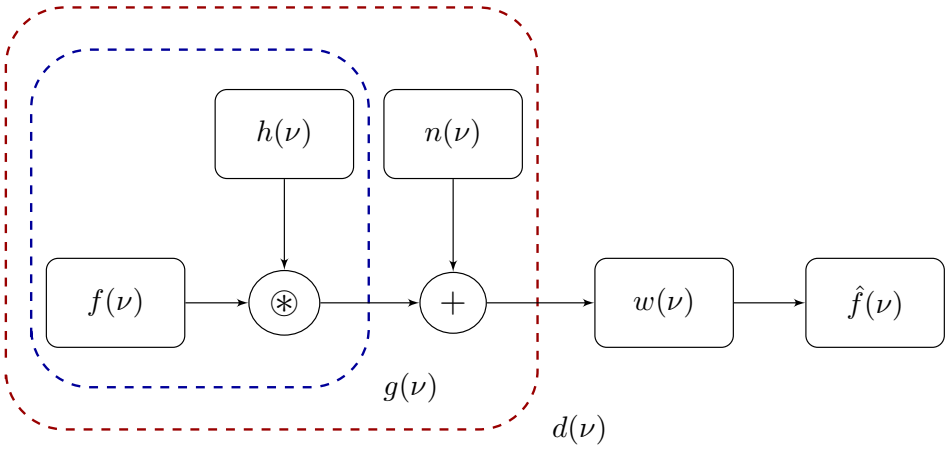

Figure 3.2: Schematic diagram showcasing working principle of the Wiener filter in frequency space.

Figure 3.2 illustrates the idea behind the WF deconvolution algorithm as expressed in Eq. 3.11. Therefore, a reliable estimation of the "original", underlying spectrum using the WF deconvolution is dependent upon the assumptions made in determining the kernel term, $W(\tilde{\nu})$, of the filter (Eq. 3.11). The kernel term is dependent on the noise of the system and on the response function, which in this case is tailored to address the effects of HFS splitting. The following section details the kernel estimation, as well as the adopted algorithm.

3.2.2 WF algorithm

This section features a brief description of our WF fitting and deconvolution algorithm written in python, based on the mathematical formulation discussed in Sect. 3.2.1. The WF algorithm uses the radiative transfer equation to express the observed line profile, T_l, of a given molecular transition containing n_HFS hyperfine components in terms of optical depths, τ. This is done under the assumption of local thermodynamic equilibrium (LTE) and unsaturated absorption. The formal solution of the radiative transfer equation for a constant excitation temperature reads:

$$T_\mathrm{l} = \Phi_\mathrm{l} T_\mathrm{ex}(1 - \mathrm{e}^{-\tau}) + \Phi_\mathrm{c} T_\mathrm{c} \mathrm{e}^{-\tau}, \tag{3.12}$$

where the excitation temperature, T_ex and the background continuum, T_c are expressed as Rayleigh-Jeans equivalent temperatures, and Φ_l and Φ_c are the beam filling factors of the line and continuum emission, respectively. For the specific case of absorption spectroscopy of far-infrared ground state transitions in low-excitation gas ($h\nu \gg kT_\mathrm{ex}$), we can neglect the first term and recast the radiative transfer equation displayed in Eq. 3.12 as $T_\mathrm{l} = \Phi_\mathrm{c} T_\mathrm{c} \mathrm{e}^{-\tau}$. In cases where we cannot neglect the emission term, particularly in the immediate environment of the continuum source, a realistic description needs to account for an excitation gradient, and therefore requires a full non-LTE solution, which is outside the scope of this paper.

The next step of the algorithm determines the kernel term, which constitutes the hyperfine response and the noise term. Hence, the quality of the restored spectrum relies both on the impulse response of the HFS and an accurate representation of the system noise. The effects

of HFS splitting are characterised by using weighted impulses in the frequency domain. The impulse response of each hyperfine component is represented by a Dirac-δ function, weighted by the relevant spectroscopic parameters. The weighting function, $\Omega_{(\mathrm{HFS})}$, accounts for the fraction of the specified species in the upper energy level, E_u (in Kelvin) of a given transition that has an upper-level degeneracy, g_u and Einstein A coefficient, A_{E} as follows:

$$\Omega_{(\mathrm{HFS})} = \frac{g_u A_{\mathrm{E}}}{Q(T_{\mathrm{rot}})} \exp\left(\frac{-E_u}{T_{\mathrm{ex}}}\right) . \tag{3.13}$$

For a given hyperfine transition, all of the above spectroscopic terms remain constant, except for the partition function, Q, which itself is a function of rotation temperature, T_{rot}, which in our case (LTE) is equal to the excitation temperature, T_{ex}. When deriving the formulation of the WF, in Sect. 3.2.1, the noise term was approximated to be the inverse of the S/N. While this serves as an acceptable choice for the noise contribution, it can be further refined and expressed explicitly as a function of the receiver system, which we will not discuss here in this paper.

The WF kernel is then determined following Eq. 3.10, and the algorithm then fits the spectrum. The standard deviation of the residual distribution is used to measure the quality of the spectral fit, and based on this, the algorithm carries out deconvolution following Eq. 3.11. In the last step, the WF algorithm applies an inverse FT to convert the modelled spectrum $\hat{F}(\tilde{\nu})$ into $\hat{f}(\nu)$ in frequency space. The deconvolved optical depth signature, τ_{decon} is then converted to molecular column density values using

$$\left(\frac{\mathrm{d}N}{\mathrm{d}v}\right)_i = \frac{8\pi\nu_i^3}{c^3\Omega}\left[\exp\left(\frac{h\nu_i}{k_{\mathrm{B}}T_{\mathrm{ex}}}\right) - 1\right]^{-1} (\tau_i)_{\mathrm{decon}} , \tag{3.14}$$

for each velocity channel, i, since, the backend provides the frequencies (and the velocities) as a discrete sequence of data, which was further smoothed by us to a useful spectral resolution as explained in Sect. 3.3 and where Ω represents the mean HFS weight. Having established the general scheme of the WF algorithm, the following sections detail its functioning on spectra that are of astrophysical importance.

3.3 GREAT observations and data reduction

The observations presented here were performed using upGREAT[3]/LFA (Risacher et al. 2018), on board SOFIA over its cycle 5 and 6 campaigns, in a number of the observatory's flights (on 26 June and 6 July in 2017, and 20 and 22 June in 2018). Our source selection consists of several far-infrared bright hot cores from the ATLASGAL[4] survey (Csengeri et al. 2017) and Sgr B2 (M). The observed sources, whose strong far-infrared dust continuum emission serves as background for our absorption measurements, are listed in Table. 3.1.

[3]upGREAT, an extension of the German REceiver for Astronomy at Terahertz frequencies, is a development by the MPI für Radioastronomie and KOSMA/Universität zu Köln, in cooperation with the MPI für Sonnensystemforschung, and the DLR Institut für Optische Sensorsysteme.

[4]APEX Telescope Large Area Survey of the GALaxy (ATLASGAL)

Table 3.1: Continuum source parameters.

Continuum Source	R.A. (J2000) [$^{h\,m\,s}$]	Dec. (J2000) [$^\circ\ '\ ''$]	l [°]	b [°]	D [kpc]	v_{LSR} [km s^{-1}]	T_c [K]
AGAL010.624−00.384 (G10.62)	18:10:28.69	−19:55:50.0	10.624	−0.383	4.9	−2.9	8.2
AGAL034.258+00.154 (G34.26)	18:53:18.49	+01:14:58.7	34.257	+0.153	1.6	+58.5	7.5
AGAL327.293−00.579 (G327.29)	15:53:08.55	−54:37:05.1	327.292	−0.578	3.1	−44.7	2.5
AGAL330.954−00.182 (G330.95)	16:09:53.01	−51:54:55.0	330.954	−0.183	9.3	−91.2	11.7
AGAL332.826−00.549 (G332.83)	16:20:10.65	−50:53:17.6	332.825	−0.549	3.6	−57.1	7.7
AGAL351.581−00.352 (G351.58)	17:25:25.03	−36:12:45.3	351.580	−0.352	6.8	−95.9	5.2
Sgr B2 (M)	17:47:20.16	−28:23:04.5	0.667	−0.036	8.3	+64.0	15.1

Notes: Columns are, left to right, source designation, equatorial coordinates, Galactic coordinates, heliocentric distance, LSR velocity, and signal band continuum brightness temperature derived by means of a DSB calibration.

References: For the heliocentric distances: AGAL010.624−00.384: Sanna et al. (2014), AGAL034.258+00.154: Zhang et al. (2009), AGAL327.293−00.579: Urquhart et al. (2014), AGAL330.954−00.182: Urquhart et al. (2012), AGAL332.826−00.549: Moisés et al. (2011), AGAL351.581−00.352: Green & McClure-Griffiths (2011), Sgr B2 (M): Reid et al. (2014).

Table 3.2: Spectroscopic parameters for $N, J = 2, 3/2 \rightarrow 1, 1/2$ hyperfine transitions of CH.

Transition		Frequency	$A_{\rm E}$	E_u
Parity	F	[GHz]	$10^{-2}\times$ [s^{-1}]	[K]
$- \rightarrow +$	$1 \rightarrow 1$	2006.74892	1.117	96.31
	$1 \rightarrow 0$	2006.76263	2.234	
	$2 \rightarrow 1$	2006.79912	3.350	
$+ \rightarrow -$ $^{(*)}$	$1 \rightarrow 1$	2010.73859	1.128	96.66
	$1 \rightarrow 0$	2010.81046	2.257	
	$2 \rightarrow 1$	2010.81192	3.385	

Notes: Columns are quantum number information, frequency, Einstein A coefficient and upper level energy; all taken from the Cologne Database for Molecular Spectroscopy (Müller et al. 2005). The frequencies were determined by Davidson et al. (2001). $^{(*)}$ - indicate the transitions that are not observed in this experiment.

The receiver configuration is comprised of the (7+7) pixel low frequency array (LFA) receiver on upGREAT, in dual polarisation. Only one set of HFS transitions near 2006 GHz (Table. 3.2) was observed, because the atmospheric transmission along some sight lines was affected by telluric ozone absorption lines. The wavelengths of the ozone features at 149.1558 μm and 149.7208 μm originating from the signal band coincide with the CH hyperfine transitions at 2010 GHz. These ozone lines, despite having relatively narrow spectral features, contaminate the CH absorption measurements made toward the strong continuum sources. Therefore, the receivers were tuned to 2006.7 GHz in the upper side band mode.

Both atmospheric as well as systematic fluctuations arising from the instrumental set-up were removed by using a double beam chop-nod mode. The secondary mirror chopped at a rate of 2.5 Hz with a chop amplitude of 60″ and 105″ for the observations carried out in 2017 and 2018. An advanced version of the MPIfR-built Fast Fourier transform spectrometer (dFFTS4G) (Klein 2017) was used as the backend to carry out the spectral analysis of the procured data. A velocity resolution of 0.036 km s^{-1} was achieved by using a 4 GHz bandwidth per pixel, with a channel spacing of 244 kHz over 16384 channels for almost all the 2006 GHz spectra. The spectra were further calibrated using the KALIBRATE program (Guan et al. 2012) with an underlying forward efficiency of 0.97 and a main-beam efficiency of 0.68. The fully calibrated spectra were subsequently analysed using the GILDAS-CLASS software[5]. The spectra were smoothed to 0.36 km s^{-1}-wide velocity bins, and up to a second order polynomial baseline was removed. After baseline subtraction, the continuum level determined by using a double-sideband (DSB) calibration, was added back to the spectra to obtain the correct line-to-continuum ratio. Based on the instrumental performance and atmospheric transmission, we assume a 5% error in the calibration of the continuum level. The relative sideband gain

[5]Software package developed by IRAM, see `https://www.iram.fr/IRAMFR/GILDAS/` for more information regarding GILDAS packages.

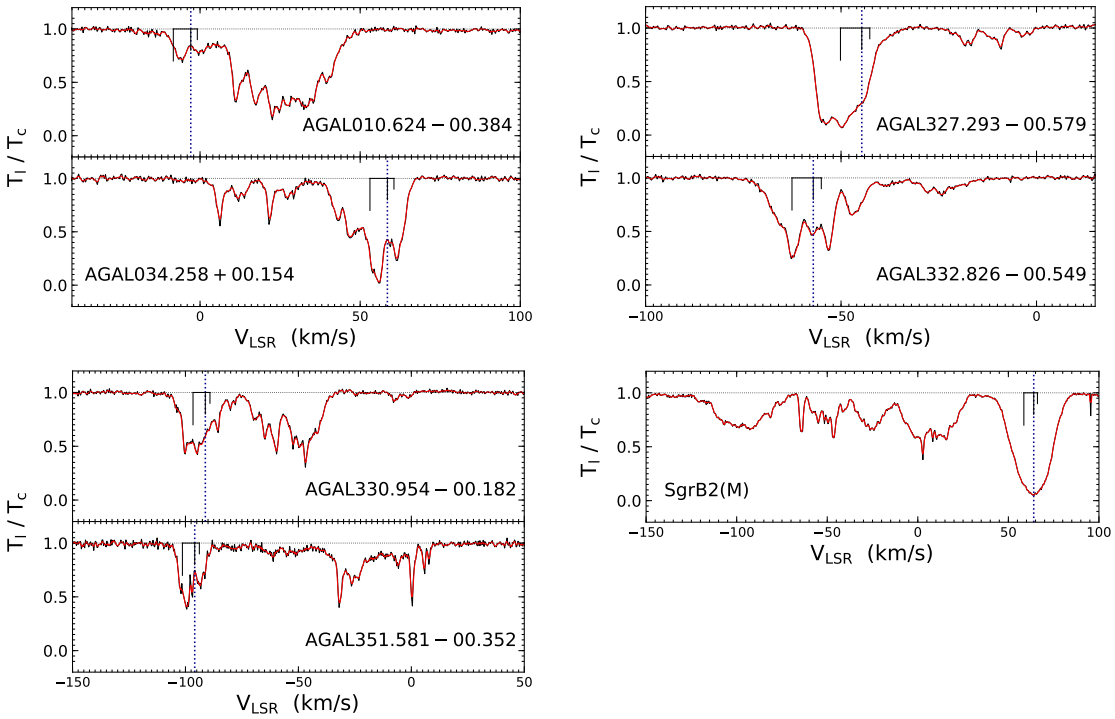

Figure 3.3: CH ($N, J = 2, 3/2 \rightarrow 1, 1/2$) hyperfine transition spectra observed toward (*from top*) AGAL010.624−00.384, AGAL034.258+00.154, AGAL327.293−00.579, AGAL332.826−00.549, AGAL330.954−00.182, AGAL351.581−00.352, and Sgr B2 (M) using GREAT/SOFIA. Each spectrum is normalised with respect to its continuum level. The WF fits are overlaid in red and include the HFS structure. The positions and relative intensities of the HFS structure are displayed in black. Sources with similar velocity distributions were grouped to display the absorption features along the LOS, in detail. The systemic velocities of the sources are represented by the dotted blue lines.

is calibrated by assuming a signal-to-image band gain ratio of unity, as determined by Kester et al. (2017) for all bands of the HIFI instrument, with an accuracy between 1 and 4%. Hence, even for the upGREAT instrument sharing the same receiver technology as that of HIFI bands 6 and 7, we assume that there is no significant departure in the band gain ratio from unity.

The CH spectra are detected in deep, yet unsaturated absorption toward each individual sight line, even at velocities corresponding to star forming regions (SFRs) as shown in Fig. 3.3. This is because almost all of the CH molecules are expected to remain in the ground state within dilute envelopes and diffuse clouds, surrounding the denser hot-core regions. The observed absorption features correspond to the radial velocities expected for different spiral arms, and are broadened by the kinematic structure of the intervening absorbing medium.

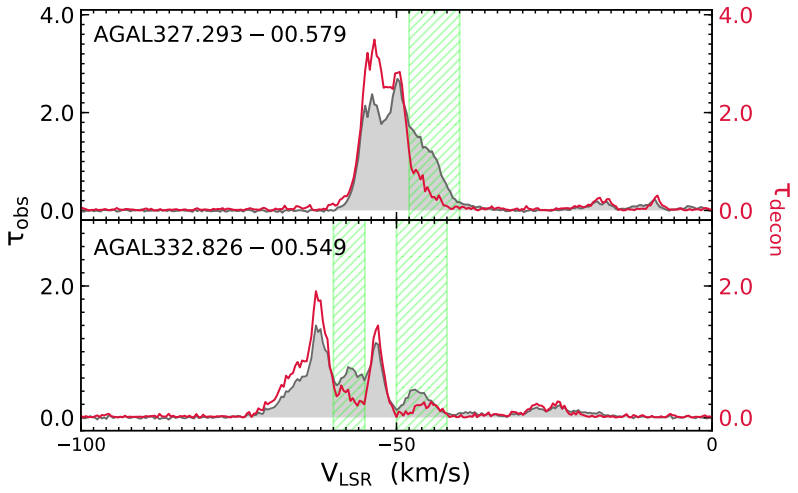

Figure 3.4: Example illustrating effects of HFS splitting. The grey-filled area represents the observed spectra toward AGAL327.293−00.579 (*top*) and AGAL332.826−00.549 (*bottom*) in terms of optical depth, while their WF deconvolved spectra are displayed in red. The green hashed regions indicate velocity intervals where we observe line broadening due to HFS splitting.

3.4 Line profile analysis

3.4.1 WF deconvolution

In Fig. 3.3, we display how the WF fits to the CH spectra observed towards the different lines of sight (LOS), following the algorithm described in Sect. 3.2.2. In Appendix A.1, we illustrate how the observed degraded spectrum is the convolution product of the deconvolved spectrum and the hyperfine weights. For two sources, we compare the line profiles of the observed spectrum with those of the deconvolved one in Fig. 3.4. The column densities determined from the former will be systematically larger over velocity intervals corresponding to the molecular clouds due to the line broadening effect of the HFS splitting, as evidenced from the differences between the two line profiles. While the extent of these variations are sight line-dependent, we find the column densities of CH determined from the observed spectra (prior to deconvolution) to be on average 24.8% larger than those determined post deconvolution, for the molecular cloud features. The quality of the WF fit toward the varied sight lines are assessed prior to deconvolution by means of the fit residuals (see Appendix A.2). Furthermore, we discuss the efficiency of the WF fit and deconvolution in Appendix A.3.

The column densities are derived following Eq. 3.14 by assuming an excitation temperature of ∼3.1 K, which is close to the temperature of the cosmological blackbody radiation (2.738 K), and was found to represent contributions of the Galactic interstellar radiation field (Gerin et al. 2010), and integrated over velocity intervals thought to be characteristic of spiral-arm and inter-arm features, based on the spiral-arm structure of the Milky Way presented by Reid et al. (2014), and consistent with those used by Godard et al. (2012) and Wiesemeyer et al. (2016).

The ground state occupation assumption at LTE ($T_{ex} = T_{rot} = 3.1$ K) is valid for the physical conditions that prevail over diffuse and translucent regions, and is questionable only within the molecular cloud components themselves. The dense envelopes of these molecular clouds can result in higher values of T_{ex} as a consequence of collisional excitation of CH. The consequences of determining column densities by assuming a single excitation temperature component along each LOS is briefly discussed in Appendix A.4. Upon modelling the absorption features associated with the dense molecular environments of our continuum sources, we find the derived column densities of CH increase by $\sim 15\%$ at $T_{ex} = 10$ K, and up to $< 50\%$ at $T_{ex} = 30$ K. This further indicates that the uncertainties in our column density estimates at velocity intervals corresponding to those of the molecular cloud components predominantly arise from our assumption of a single excitation temperature. Hence, the column densities derived over their associated velocity components represent a lower limit on the N(CH) values. The derived column densities for each sight line are summarised in Table. 3.3. The CH column densities per velocity component are found to vary between $\sim 10^{12}$ and 1.2×10^{14} cm^{-2} along inter-arm and spiral-arm clouds along the different sight lines. We inspect the reliability of the column densities derived using the WF by comparing them with other techniques in Sect. 3.4.2.

As the optical depths are computed from the line-to-continuum ratio, uncertainties in the continuum level give rise to systematic errors in the derived column densities. The uncertainties are partly due to the receiver-gain ratio between the signal and the image band, possibly deviating from unity. For the mixer technology (hot-electron bolometers) used by upGREAT, this quantity is difficult to measure without re-tuning the receiver. For the HIFI bands employing the same technology and closest to our tuning, a dedicated study (Kester et al. 2017) provides typical deviations of 1 to 4%. At this level, given the available sensitivity and typical optical depths ranging from 0.1 to 1, the impact of the continuum uncertainty on the derived column densities is difficult to disentangle from that of the thermal noise in the absorption profile. However, following the DSB error estimation presented in Wiesemeyer et al. (2018), we account for the uncertainties present in the continuum level that will subsequently lead to errors in the optical depths and derived column densities. Further, the errors in the WF computed column densities are determined by sampling a posterior distribution of the deconvolved optical depths[6]. We sampled 5000 artificial spectra, each generated by adding a pseudo-random noise contribution with the same standard deviation as the line free part of the continuum, to the absorption spectra prior to applying the WF fit and deconvolution, over each iteration. The deconvolved optical depths and subsequently derived column densities (per velocity interval) sample a point in the channel-wise distribution of the column densities across all spectra. The empirical spread of these distributions yield the asymmetric errors in the computed column densities. However, the column densities are not always normally distributed, and often showcase skewed distributions, as normality is not imposed. For this reason, the profiles of the distributions are best described by using the median and inter-quartile range from which the sample mean and standard deviation are derived following Wan et al. (2014). This is done so as to remove any biases introduced in the determination of the mean due to the asymmetry of the distribution. The new mean and standard deviation are then used

[6]The error in the derived column densities (per velocity interval) scale with the deconvolved optical depths by a constant value. This constant is a function of the spectroscopic parameters that govern the transition and the excitation temperature.

Table 3.3: CH $N, J = 2, 3/2 \rightarrow 1, 1/2$ absorption line analysis using WF deconvolution algorithm and comparison of column densities with OH.

$v_{\rm min}$–$v_{\rm max}$ [km s^{-1}]		$R_{g,\rm min}$–$R_{g,\rm max}$ [kpc]		Remark$^{(b)}$	N(CH) [10^{13} cm^{-2}]	N(H$_2$)$^{(c)}$ [10^{21} cm^{-2}]	N(OH)$^{(d)}$ [10^{14} cm^{-2}]
AGAL010.624−00.384							
−11	−2	8.9	11.6	MC	> 4.82	–	> 3.42
−2	+2	8.1	8.9	MC	> 4.84	–	> 10.21
+2	+7	7.2	8.1	Norma	$7.78^{+0.22}_{-0.05}$	2.22	$5.68^{+0.17}_{-0.03}$
+7	+15	6.2	7.2	Sgr	$15.70^{+0.05}_{-0.01}$	4.48	$6.54^{+0.09}_{-0.02}$
+15	+20	5.7	6.2		$25.26^{+0.17}_{-0.08}$	7.21	$14.45^{+0.10}_{-0.05}$
+20	+31	4.8	5.7	Scu/Per	$27.31^{+0.06}_{-0.02}$	7.80	$17.67^{+0.14}_{-0.06}$
+31	+36	4.5	4.8		$22.63^{+0.10}_{-0.00}$	6.46	S
+36	+51	3.7	4.5	Sgr	$5.31^{+0.19}_{-0.01}$	1.51	S
AGAL034.258+00.154							
+0	+16	7.5	8.5		$1.65^{+0.28}_{-0.33}$	0.47	$2.71^{+0.11}_{-0.03}$
+16	+32	6.8	7.5	Sgr	$1.51^{+0.20}_{-0.17}$	0.43	$1.81^{+0.08}_{-0.11}$
+32	+38	6.5	6.8		$0.76^{+1.37}_{-0.84}$	0.22	$0.48^{+0.82}_{-0.61}$
+38	+68	5.5	6.5	MC	> 9.35	–	S
AGAL327.293−00.579							
−61	−32	7.4	9.5	Scu, MC	> 9.68	–	S
−32	−25	9.5	10.2		$0.22^{+0.38}_{-0.41}$	0.06	$0.05^{+0.71}_{-0.38}$
−25	−14	10.2	11.5		$1.10^{+0.50}_{-0.09}$	0.31	$0.52^{+0.25}_{-0.15}$
−14	−6	11.5	12.6		$0.82^{+1.10}_{-0.05}$	0.23	$0.98^{+0.24}_{-0.18}$
−6	,+3	12.6	14.2		$0.22^{+0.85}_{-1.08}$	0.06	$0.42^{+0.30}_{-0.15}$
AGAL330.954−00.182							
−115	−75	4.1	5.0	MC	> 2.96	–	S
−75	−55	5.0	5.6		$3.80^{+0.05}_{-0.12}$	1.09	$1.23^{+0.05}_{-0.02}$
−55	−30	5.6	6.6	Norma	$3.66^{+0.01}_{-0.02}$	1.04	S
−30	−10	6.6	7.7	Scu	$0.19^{+1.31}_{-1.07}$	0.05	$0.04^{+0.70}_{-0.51}$
−10	+4	7.7	8.8	Norma	$0.45^{+0.36}_{-0.31}$	0.12	$0.09^{+0.03}_{-0.02}$
AGAL332.826−00.549							
−81	−50	4.7	5.6	Norma, MC	> 5.00	–	S
−50	−40	5.6	6.0		$1.12^{+0.02}_{-0.02}$	0.32	$5.20^{+0.09}_{-0.02}$
−40	−32	6.0	6.4		$0.34^{+0.60}_{-0.52}$	0.09	$3.94^{+0.13}_{-0.01}$
−32	−8	6.4	7.8	Sgr	$0.72^{+0.75}_{-0.67}$	0.20	$2.57^{+0.11}_{-0.01}$

Table 3.3: Continued.

v_{min}–v_{max} [km s^{-1}]		$R_{g,min}$–$R_{g,max}$ [kpc]		Remark[b]	N(CH) [10^{13} cm^{-2}]	N(H_2)[c] [10^{21} cm^{-2}]	N(OH)[d] [10^{14} cm^{-2}]
AGAL351.581−00.352							
−109	−88	2.0	2.3	MC	> 3.65	–	S
−88	−68	2.3	2.7		$0.45^{+0.30}_{-0.25}$	0.13	$0.20^{+0.10}_{-0.03}$
−68	−42	2.7	3.7	Sgr	$0.81^{+0.31}_{-0.23}$	0.23	$0.94^{+0.05}_{-0.01}$
−42	−14	3.7	6.0	Norma	$2.69^{+0.06}_{-0.04}$	0.76	S
−14	−12	6.0	6.2		$0.90^{+0.24}_{-0.20}$	0.25	$0.15^{+1.06}_{-0.08}$
−12	−3	6.2	7.7	Sgr	$1.80^{+0.11}_{-0.07}$	0.51	$0.18^{+0.26}_{-0.08}$
−3	+3	7.7	9.4	Scu	$2.99^{+0.06}_{-0.04}$	0.85	S
+3	+12	9.4	13.5		$0.44^{+0.40}_{-0.24}$	0.12	$0.28^{+0.02}_{-0.01}$
Sgr B2 (M)							
−124	−67				$27.81^{+0.01}_{-0.02}$	7.94	–
−67	−38				$3.16^{+0.10}_{-0.13}$	0.90	–
−38	−12			3 kpc	$3.60^{+0.09}_{-0.08}$	1.30	–
−12	+8			GC	$6.28^{+0.01}_{-0.02}$	1.79	–
+8	+29			Sgr	$4.57^{+0.11}_{-0.11}$	1.31	–
+29	+40			Scu	$0.89^{+0.61}_{-0.49}$	0.25	–
+40	+90			MC	> 73.02	–	–

Notes: [a] The galactocentric distances for each velocity interval is computed using, $R_G = R_0 \frac{\Theta(R_G)\sin(l)\cos(b)}{v_{lsr}+\Theta_0\sin(l)\cos(b)}$, with R_0 = 8.3 kpc, Θ_0 = 240 km s^{-1} and assuming a flat Galactic rotation curve, i.e, $\Theta(R_G) = \Theta_0$. Note that we do not account for the non-circular motion of the 3 kpc arm (Dame & Thaddeus 2008).[b] The positions of the four main spiral arms and the local arms have been inferred from the spiral arm characteristics presented in Reid et al. (2014) and the velocities corresponding to the molecular cloud envelopes are indicated by MC. [c] $N(H_2)$ is derived from [CH]/[H_2] = 3.5×10^{-8} given by Sheffer et al. (2008). [d] S denotes velocity components with saturated absorption line profiles.

to determine the asymmetric errors through positive and negative deviations. While errors in the deep absorption features corresponding to spiral-arm velocities arise from imperfections in the fit, the errors in the inter-arm gas features are dominated by uncertainties in the true continuum.

3.4.2 Comparison of WF algorithm with other procedures

In this section, we briefly compare column densities of the CH molecule inferred using the WF algorithm with those obtained from other commonly used techniques. To carry out an unbiased analysis, we performed the WF algorithm on the $N = 1, J = 3/2 \rightarrow 1/2$ HFS spectra of CH near 532 GHz, obtained using *Herschel*/HIFI toward Sgr B2 (M) as a part of the

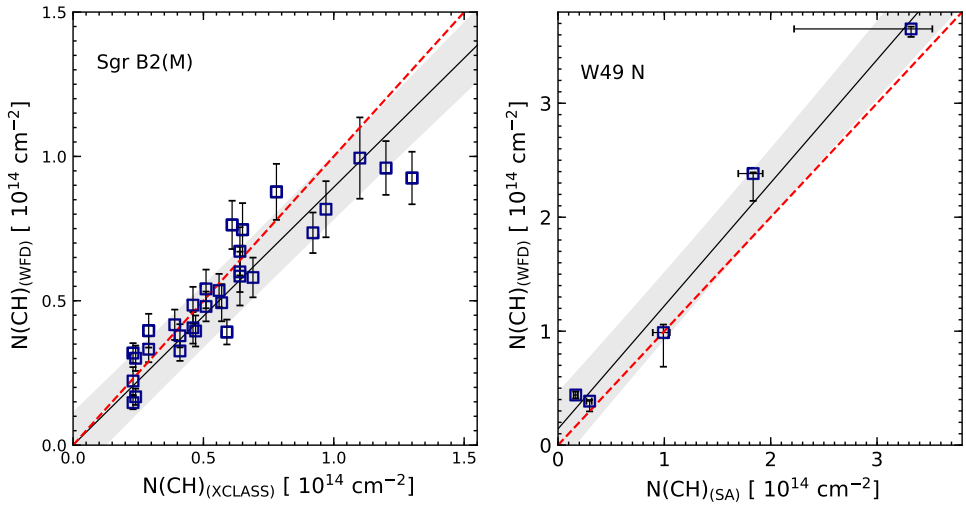

Figure 3.5: *Left*: Comparison of $N = 1, J = 3/2 \rightarrow 1/2$ CH column densities derived using WF deconvolution and the XCLASS software presented in Qin et al. (2010). *Right*: Comparison of $N, J = 2, 3/2 \rightarrow 1, 1/2$ CH column densities derived using WF deconvolution and the simulated annealing algorithm presented in Wiesemeyer et al. (2018). The black solid line represents the weighted fit to the data, while the red dashed line represents a ratio of one. The data points that lie within 1σ intervals of the weighted linear regression are indicated by the grey-shaded regions.

HEXOS[7] survey toward Sgr B2 (M). The spectroscopic parameters of these HFS transitions are summarised in Table. A.1. The LOS toward Sgr B2 (M) was chosen because of its complex spectral line profile which contains an amalgamation of narrow and broad features, alike. Qin et al. (2010) modelled the CH spectra by using XCLASS (Möller et al. 2017) and the automated fitting routine provided by MAGIX[8] for an excitation temperature of 2.73 K. Assuming LTE, XCLASS solves the radiative transfer equation with an underlying Gaussian brightness profile to model the observed spectral line profile. Using the WF algorithm, we derived the column densities of the CH HFS transitions near 532 GHz, integrated over the same velocity intervals as those specified in Table. 1 of Qin et al. (2010). The errors were computed as before, but with the assumption of a 20% error in the continuum level.

A comparison between the CH column densities derived using the WF algorithm and the XCLASS fits is displayed in Fig. 3.5 for all absorption features along the LOS except, for the strong absorption from the envelope of the Sgr B2 (M) molecular cloud, which traces denser gas. The weighted regression at lower column densities systematically follows a one-to-one correlation while at larger column densities the values derived using the WF algorithm are almost always smaller than those computed using XCLASS, with an overall ratio of

[7]The guaranteed time key project, *Herschel*/HIFI observations of EXtra-Ordinary Sources(HEXOS) (Bergin et al. 2010) was aimed to investigate the chemical composition of several sources in the Orion and Sgr B2 star-forming regions.

[8]See `https://magix.astro.uni-koeln.de/` for more information about the MAGIX software.

$N(\mathrm{CH})_{\mathrm{WFD}}/N(\mathrm{CH})_{\mathrm{XCLASS}} = 0.76 \pm 0.06$. The deviations may arise due to the intrinsically different means by which the two methods account for HFS splitting, an effect that is particularly prominent at the larger column density values. Additionally, inconsistencies in the post-processing of the *Herschel*/HIFI data (baseline fitting, etc) also contribute to the observed deviations. Nonetheless, the CH abundances determined using both methods are in agreement within the systematic uncertainties.

In addition, we also compare the column densities obtained using the WF deconvolution with those obtained by Wiesemeyer et al. (2018) when using simulated annealing (SA) to the $N, J = 2, 3/2 \rightarrow 1, 1/2$ hyperfine transitions of CH toward W49 N. The column densities derived using both methods have a tight relation with a slope of, $N(\mathrm{CH})_{\mathrm{WFD}}/N(\mathrm{CH})_{\mathrm{SA}} = 1.08 \pm 0.08$. The column densities derived using the two methods deviate in value only within the inter-arm gas components and the overall concordances between the two methods further validates the use of the non-iterative WF deconvolution scheme.

3.5 Results

In Sect. 3.5.1, we investigate the correlation between the column densities of CH with values determined for another widely studied light hydride, hydroxyl (OH), and evaluate its abundance using CH as a proxy for H_2. To further appreciate the global characteristics of the CH molecule as a surrogate for H_2 within the Milky Way, in Sect. 3.5.2, we study its radial distribution across the Galactic plane.

3.5.1 CH versus OH column density

For quite some time, CH has been used as a tracer for H_2 in the diffuse regions of the ISM based on its observed correlation with H_2 (Federman & Willson 1982; Mattila 1986; Sheffer et al. 2008). As a precursor to the formation of CO, OH has also gained recognition as a promising tracer for the “CO-dark" component (Grenier et al. 2005) of molecular gas in the ISM (Tang et al. 2017; Li et al. 2018; Engelke & Allen 2018; Rugel et al. 2018). In Table 3.3, we present column densities of H_2 estimated using the $N(\mathrm{CH})/N(\mathrm{H_2}) \sim 3.5^{+2.1}_{-1.4} \times 10^{-8}$ relation derived by Sheffer et al. (2008). This correlation was established using optical observations of the $A^2\Delta$ - $X^2\Pi$ system of CH at 4300 Å and the (2-0), (3-0), and (4-0) bands of the Lyman B-X transitions of H_2 toward 37 bright stars. Akin to the CH observations presented in our study, the optical CH and UV H_2 lines presented by Sheffer et al. (2008) are seen in absorption toward sight lines that probe molecular clouds in the local diffuse ISM ($10^{19} < N(\mathrm{H_2}) < 10^{21}$ cm^{-2}).

In order to carry out a comparison between N(OH) and N(CH), we use data published in Wiesemeyer et al. (2016) of the $^2\Pi_{3/2}$, $J = 5/2 \rightarrow 3/2$ ground-state transitions of OH, procured using GREAT/SOFIA as a part of the observatory’s cycle 1 campaign. The spectroscopic parameters of these OH transitions are summarised in Table. A.1. For this preliminary search, observations were carried out toward all the sight lines discussed in this paper, except for Sgr B2 (M). The OH spectra are saturated at velocities corresponding to the SFR-related molecular cloud components (that provide the background continuum emission) themselves,

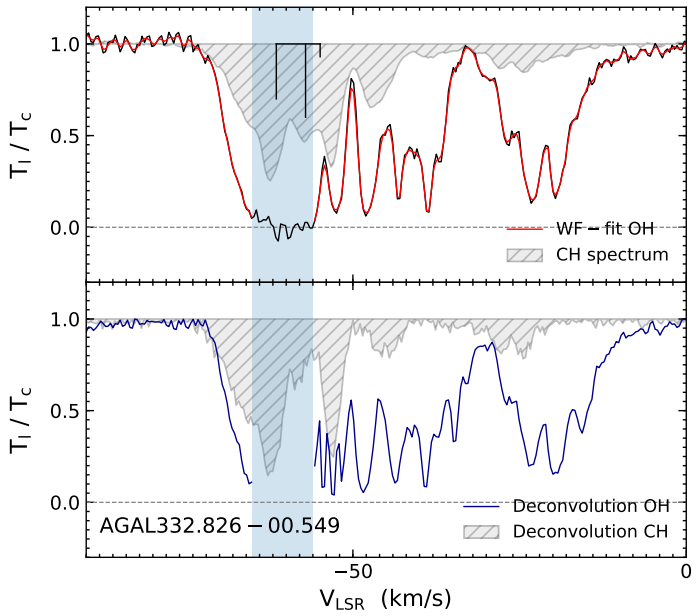

Figure 3.6: *Top*: Normalised line profile and HFS structure of OH near 2514 GHz (in black) overlaid with WF fit in red toward AGAL332.826−00.549. The WF fit avoids velocity intervals of the OH spectrum that show saturation between -65 < $v_{\rm lsr}$ <-56 km s^{-1}, bounded by the blue-shaded regions. The grey shaded and hatched region displays the CH absorption profile toward the same source for comparison. *Bottom*: Normalised WF deconvolved line profile of OH (avoiding the saturated region) in blue, and corresponding deconvolved spectrum of CH displayed by the shaded and hatched grey region.

as shown in Fig. 3.6. The saturated absorption features of the OH spectra arising in the envelopes of the hot cores of these star-forming regions are indicative of the fact that a complete ground-state occupation assumption is no longer valid (Csengeri et al. 2012). Moreover, from Fig. 3.6, it can be seen that most of the observed OH absorption features have corresponding features in the CH spectrum with notable differences at velocity intervals between −13 and −21 km s^{-1}, and from −36 to −42 km s^{-1}, in this example. The WF fit and deconvolution is applied to the OH spectra with a $T_{\rm ex}$ = 3.1 K (for consistency), and integrated over the same velocity intervals as those used for CH. Our assumption of a complete ground-state occupation for OH is broken down for spectral features associated with the dense molecular clouds. The WF faces singularities when $T_{\rm l}$ tends to zero and thus avoids the OH features arising from these regions because they showcase saturated absorption. Therefore, the use of a lower excitation temperature does not affect our analysis.

The derived CH and OH column densities are presented in Fig. 3.7. The used data correspond to column densities based on values computed within the velocity intervals used in Table. 3.3. The plotted data points represent values re-sampled to 1 km s^{-1} wide velocity

bins (except towards the velocity intervals corresponding to the molecular clouds, as well as those contaminated by outflows). The N(CH)-N(OH) correlation plots for the individual sources are presented in Appendix A.6. Across the different sight lines, we obtained a range of N(OH)/N(CH) values between one and 10. Moreover, almost all the sources, except AGAL351.581−00.352 and AGAL332.826−00.549, have significant correlation coefficients between 0.46 and 0.75 with false-alarm probabilities below 5% (summarised in Table. A.2) within the spiral arm data, while there is no remarkable correlation observed in the inter-arm regions. The lack of, or weak correlations present in the above mentioned sources can be attributed to the fact that the OH spectra toward these two sources showcase more saturated features along the LOS than in the remainder of the sources.

Fitting a linear regression to the combination of all the sight lines yields N_v(OH)/N_v(CH) = (3.85 ± 0.15), with a Pearson's correlation coefficient of 0.83 (false-alarm probability below 1%) for velocity intervals of 1 km s^{-1}. The functional form of the regression was chosen after comparing the standard error of a regression fit through the origin with that of an ordinary least square regression, both of which yielded best fit slopes that are consistent with one another (within a 5% error). From Fig. 3.7, we find that this relation spans roughly two orders of magnitude between 0.1 and 10, with a majority of the ratios lying between one and 10. We noted that those data points with N(OH)/N(CH) > 10 correspond to the broad line wings of saturated OH features, while those with N(OH)/N(CH) < 1 have larger errors in the determined N(OH) arising from their continuum-level uncertainties. Since the spectral features arising from star-forming regions are unsaturated in the case of the CH molecule, its effective broadening into the inter-arm regions is less. We further extend this analysis by combining our data set with optical observations[9] of the CH B-X transitions at 3886 and 3890 Å, and OH A-X transitions at 3078 and 3082 Å presented toward 20 bright OB-type stars at low Galactic latitudes ($-17° < b < +23°$) from Weselak et al. (2010). Moreover, Weselak et al. (2010) show that the LOS toward these stars probe physical conditions (gas densities, n(H) = 250-600 cm^{-3} and temperatures, $T_{kin} = 20 - 30$ K) that are typical for diffuse molecular clouds (Snow & McCall 2006) similar to those of our data set, and report a N(OH)/N(CH) value of 2.52 ± 0.35. The revised abundance ratio (combining both sets of data) displayed in Fig. 3.8 follows N(OH)/N(CH) = (3.14 ± 0.49). Using this abundance ratio and the Sheffer et al. (2008) relation, we derive the OH abundance using CH as a surrogate for H_2 to be $X_{OH} = N(OH)/N(H_2) = (1.09 \pm 0.27) \times 10^{-7}$. This result is consistent with the column density ratios presented by Liszt & Lucas (2002), and is in the range of theoretical predictions presented by Albertsson et al. (2014). When using a N(CH)/N(H_2) ratio of $\sim 4.97 \times 10^{-8}$ as derived by Weselak (2019), we find the corresponding OH abundance to be $X(OH) = 1.56 \times 10^{-7}$.

3.5.2 Radial distribution of CH

The azimuthally-averaged CH column densities obtained toward all the sight lines in this study, except Sgr B2 (M), are plotted as a function of galactocentric distances, R_G, in Fig. 3.9. The

[9]These observations were made using the UVES spectrograph at the European Southern Observatory (ESO) Paranal in Chile.

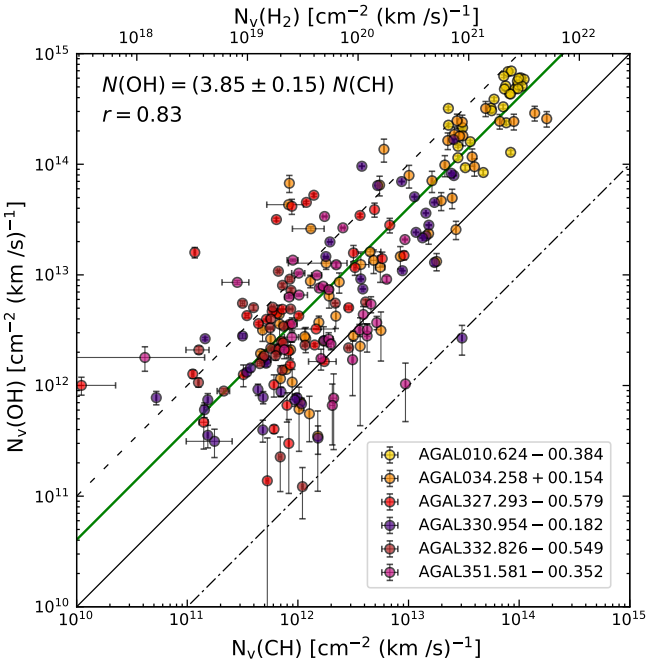

Figure 3.7: N(OH) vs. N(CH), per unit velocity interval derived using WF algorithm. The different coloured data points represent contributions from the different sources. The black dashed, solid, and dotted-dashed lines indicate N(OH)/N(CH) ratios of 10, 1, and 0.1, respectively while the linear regression fit to the data, N(OH) = (3.85 ± 0.15) N(CH) is displayed in green.

galactocentric distances to the different spiral arm features were computed assuming a flat rotation curve, with the distance of the Sun from the Galactic centre given by R_0 = 8.3 kpc, and an orbital velocity of Θ_0 = 240 km s^{-1} of the Sun, with respect to the Galactic centre (Reid et al. 2014). The uncertainties in the CH column densities are typically of the order of a few 10^{12} cm^{-2}(km s^{-1})$^{-1}$, and are too small to be visible in some parts of the plot. This analysis is limited to a small number of strong background continuum sources, distributed at low Galactic latitudes, which lie close to the Galactic plane.

We find that the CH column densities peak at galactocentric distances between 4 and 8 kpc. LOSs within the l = 0-180° range dominate contributions toward the first column density peak observed around 5 kpc, while the second peak near 7 kpc originates from LOSs in the l = 180-360° range. The column density peak near 5 kpc is associated with absorption arising from a combination of the Perseus and Norma spiral-arm crossings, and the 7 kpc peak may be attributed to the intersection of the Scutum-Crux spiral-arm crossing along the sight lines. The higher observed column densities peaking near these spiral arms can be attributed to the larger (mass) molecular content that is present at these galactocentric radii. Owing to the larger error bars, the significance of a third peak near 9 kpc is unclear. However, it is in line with contributions that may arise from the Scutum- and Sagittarius-arm far side crossings. Due to a lack of data points at galactocentric distances smaller than 2 kpc, the nature of the CH molecular gas distribution there remains unknown. We do not include contributions

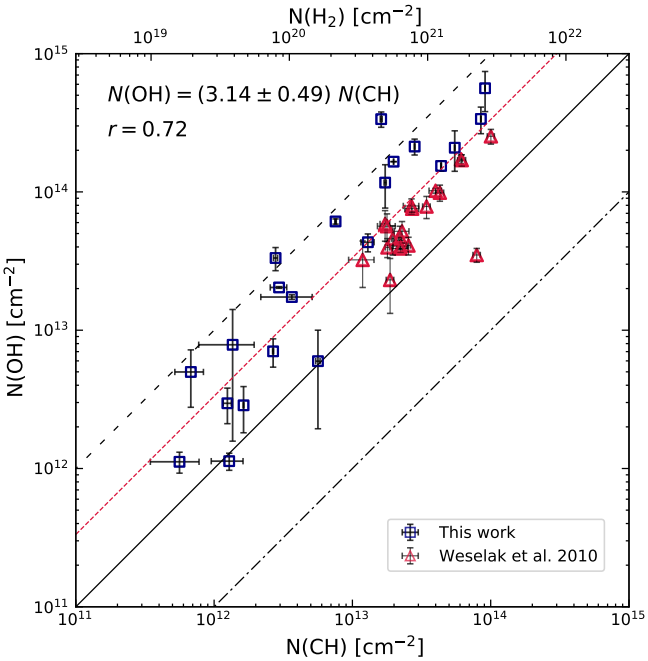

Figure 3.8: Correlation plot between column densities of the CH, and OH molecules, integrated over broad velocity intervals as per Table. 3.3. The red triangles and blue squares represent column density measures from Weselak et al. (2010) and this work, respectively. The black dashed, solid, and dotted-dashed lines indicate N(OH)/N(CH) ratios of 10, 1, and 0.1, respectively while the linear regression fit to the data, N(OH) = (3.15 ± 0.49) N(CH) is displayed by the red dotted line.

from the sight line toward Sgr B2 (M) in this analysis, because in the Galactic centre direction, it is difficult to assign the CH absorption to different components based on their LSR velocities.

A similar dual-peaked radial distribution profile has been reported by both Pineda et al. (2013), and Velusamy & Langer (2014) for the cold neutral medium (CNM) component of [CII] emission. [CII] is a proficient tracer that is sensitive to various evolutionary stages of the ISM, but by taking advantage of differing densities, Pineda et al. (2013) were able to decompose contributions of the [CII] emissivity from the different phases of the ISM, excluding the warm ionised medium (WIM) for sources in the Galactic plane, $b = 0°$. Despite the smaller sample size, our results broadly resemble the shape of the [CII] integrated intensity distribution profile.

The framework of carbon chemistry in the diffuse regions, which is initiated by the radiative association of the ground vibrational state of H_2 with ionised carbon, explains the observed correspondence between CH and [CII] radial profiles (Gerin et al. 2016). Peaking at the same R_G values as those of HI (see Fig. 12 in Pineda et al. (2013)), suggests that CH likely traces the more diffuse regions of the CNM between [CII] and the extended HI emission. Upon comparing the distribution of H_2 column densities derived from CH (using the Sheffer et al. (2008) relation) with those derived from both CO (CO-traced H_2 gas) and [CII] (CO-dark H_2

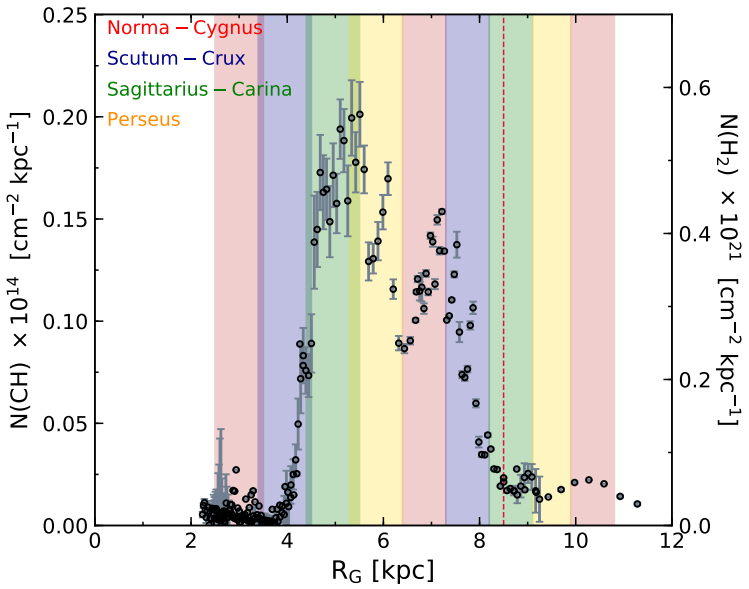

Figure 3.9: Radial distribution of CH column densities toward lines of sight probed in this study except Sgr B2 (M). The column density values for each distance interval are averages over the underlying distribution. The secondary y-axis display $N(H_2)$ values computed using the Sheffer et al. (2008) relation. The dashed red vertical line indicates the galactocentric distance to the Sun. The spiral arm locations typical for a fourth quadrant source, are plotted with spiral arm widths of 0.85 kpc.

gas) by Pineda et al. (2013) (their Fig. 18) we find that: (1) at $R_G < 2$ kpc, we cannot comment on the behaviour of the distribution due to the lack of data points, (2) 2 kpc $< R_G <$ 8 kpc, the CH-traced H_2 column density is comparable to the [CII]-traced H_2 column density, while being smaller than the CO-traced H_2 column density and, (3) $R_G > 8$ kpc, despite attaining a constant level at these distances, similar to the CO-dark H_2 gas traced by [CII], the column density distribution of H_2 obtained using CH is lower than that traced by [CII]. The general agreement between the column density of the CO-dark gas traced by [CII] and the H_2 column densities traced by CH at galactocentric distances < 8 kpc, is a good indicator of the usefulness of CH as a tracer for the CO-dark component of molecular gas.

3.6 Conclusions

In this paper, we presented the analysis of SOFIA/GREAT observations of the $N, J = 2, 3/2 \rightarrow 1, 1/2$ transitions of CH detected in absorption toward strong, FIR-bright continuum sources by using the Wiener filter algorithm. Although it has previously not been used as a conventional tool for spectral line analysis, we find the WF deconvolution algorithm to be a self-consistent concept that sufficiently alleviates biases manifested in spectra with close hyperfine spacing, provided that the transitions are optically thin. The absorption features along each LOS are broadly classified into contributions arising from different spiral arm and inter-arm regions

based on the spiral arm model of the Milky Way presented by Reid et al. (2014). Using the WF as the basis for our spectral analysis, we derived a linear relationship between CH and OH, $N(\mathrm{OH})/N(\mathrm{CH}) = 3.85 \pm 0.15$ that is consistent with previous work. Upon increasing the number of sight lines in this analysis by including those studied by Weselak et al. (2010), we derived a revised relationship with a $N(\mathrm{OH})/N(\mathrm{CH}) = 3.14 \pm 0.49$. By subsequently using CH as a surrogate for tracing H_2, we derived an OH abundance of $X(\mathrm{OH}) = (1.09 \pm 0.27) \times 10^{-7}$. It is important to note that this result pivots on the validity of the $N(\mathrm{CH})$-$N(H_2)$ relation used. We find the radial distribution of the CH abundances of our sample to peak between 4 and 8 kpc. In addition to the tight correlation that exists between the CH and H_2 established by Sheffer et al. (2008), the likeness of the CH abundance distribution to that of [CII] , a well known tracer, of the CO-dark H_2 gas, lends credence to its use as tracer for H_2 in these regions. Furthermore, this work may initiate follow-up observational studies, investigating a larger sample of sources covering a wide range of physical conditions at varying galactocentric distances to study the Galactic distribution of CH. This will reinforce its use as a tracer for H_2 in regions where hydrogen is molecular, and carbon may be both neutral or ionised, but not traced by CO, over Galactic scales.

Chapter 4

The CH radical at radio wavelengths

An attempt has been made to compute the numbers
of certain molecules in interstellar space ...
A search for the bands of CH, OH, NH, CN and C_2
would appear to be promising

P Swings and L Rosenfeld, 1937

Overview

The detection and identification of the first molecules in interstellar space by (Swings & Rosenfeld 1937) and others, provoked great interests in the field of astrochemistry and perhaps presents the first attempts at modelling interstellar chemistry. CH, one of the first molecules to have been detected by these has been widely observed since. In this Chapter we discuss the excitation conditions of the three hyperfine structure transitions between the Λ-doublet components of the rotational ground state of CH, the contents of which has been submitted as a paper titled, 'The CH radical at radio wavelengths: Revisiting emission in the 3.3 GHz ground state lines' to *Astronomy & Astrophysics*.

The intensities of the three widely observed radio-wavelength hyperfine structure (HFS) lines between the Λ-doublet components of the rotational ground state of CH are inconsistent with local thermodynamic equilibrium (LTE) and indicate ubiquitous population inversion. While this can be qualitatively understood assuming a pumping cycle that involves collisional excitation processes, the relative intensities of the lines and in particular the dominance of the lowest frequency satellite line has not been well understood. This has limited the use of CH radio emission as a tracer of the molecular interstellar medium.

We aim to investigate the nature of the (generally) weak CH ground state masers by employing synergies between the ground state HFS transitions themselves and with the far-infrared lines, near 149 μm (2 THz) (studied in Chapter 3), that connect these levels to an also HFS split rotationally excited level. We interpret our data with the help of non-LTE statistical equilibrium calculations that employ recently calculated collisional rate coefficients.

We present the first interferometric observations, with the *Karl G. Jansky* Very Large Array, of the CH 9 cm ground state HFS transitions at 3.264 GHz, 3.335 GHz, and 3.349 GHz toward the four high mass star-forming regions (SFRs) Sgr B2 (M), G34.26+0.15, W49(N), and W51. We combine this data set with our high spectral resolution observations of the $N, J = 2, 3/2 \rightarrow 1, 1/2$ transitions of CH near 149 μm observed toward the same sources made

with the upGREAT receiver on SOFIA, which share a common lower energy levels with the HFS transitions within the rotational ground state.

Toward all four sources, we observe the 3.264 GHz lower satellite line in enhanced emission with its relative intensity higher than its expected value at LTE by a factor between 4 and 20. We perform statistical equilibrium calculations with the non-LTE radiative transfer code MOLPOP-CEP in order to model the excitation conditions traced by the ground state HFS lines of CH and to infer the physical conditions in the emitting regions. The models account for effects of far-infrared line overlap with additional constraints provided by reliable column densities of CH estimated from the 149 μm lines.

The derived gas densities indicate that the CH radio emission lines (and the far-infrared absorption) arise from the diffuse and translucent outer regions of the SFRs' envelopes as well as in such clouds located along the lines of sight. We infer temperatures ranging from 50 to 125 K. These elevated temperatures, together with astrochemical considerations, indicate that the observed CH is likely formed in cloud layers heated by the dissipation of turbulence. The excitation conditions we derive reproduce the observed level inversion in all three of the ground state HFS lines of CH over a wide range of gas densities with a value of ~ -0.3 K, consistent with previous theoretical predictions.

4.1 Introduction

The 4300.3 Å electronic transition of the methylidyne radical, CH, was one of the first three molecular lines detected in the interstellar medium (ISM; Dunham 1937; Swings & Rosenfeld 1937; McKellar 1940). Since then, CH has been extensively observed in a wide range of wavelength regimes, from the radio at 9 cm (3.3 GHz) (Rydbeck et al. 1973), over the sub-millimetre (sub-mm) and far-infrared (FIR) ranges to the far-ultraviolet (FUV) regime at 1369.13 Å (Watson 2001). The CH radical has also been detected in a variety of environments, hosting different physical and excitation conditions from diffuse, and translucent interstellar clouds to dark clouds, outflows, and shocks at the edges of dense molecular clouds, and even in external galaxies (for example, Lang & Wilson 1978; Whiteoak et al. 1980; Mattila 1986; Sandell et al. 1988; Magnani et al. 1992; Magnani & Onello 1993).

As the simplest carbyne, CH is an important intermediary in the gas phase chemistry of carbon bearing molecules, initiating the formation of larger and more complex species in the ISM. In addition, studies using high resolution optical spectroscopy were able to reveal a tight correlation between the derived column densities of CH, and those of H_2 (or the visual extinction) in diffuse and translucent clouds (Federman 1982; Sheffer et al. 2008; Weselak 2019). However, such optical absorption studies are limited to nearby clouds (a few kpc) as they require visually bright ($V < 10$ mag) background stars. Fortunately, the advent of space- and air-borne telescopes like Herschel and SOFIA, respectively, have not only renewed interests in CH and other light hydrides, but have also extended their studies over Galactic scales. Measurements of absorption in the generally optically thin rotational transitions of CH at 532/536 GHz (560 μm) (Gerin et al. 2010) and 2006/2010 GHz (149 μm) (Wiesemeyer et al. 2018; Jacob et al. 2019) against the continuum emission from distant star-forming regions (SFRs) in spiral arms and the Galactic centre region, yielding column densities, have further emphasised its use as a tracer

Table 4.1: Spectroscopic properties of the CH ground state HFS transitions. The columns are (from left to right): the transition as described by the hyperfine quantum number (F), the frequency of the transition, the Einstein A coefficient and the relative line intensities at LTE.

Transition $F' - F''$	Frequency [MHz]	$A_{\rm E}$ $\times 10^{-10}$ [s^{-1}]	Relative Intensity
$0^- - 1^+$	3263.793447	2.876	1.0
$1^- - 1^+$	3335.479356	2.045	2.0
$1^- - 0^+$	3349.192556	1.036	1.0

Notes: The frequencies were measured by Truppe et al. (2014) with uncertainties of 3 Hz.

for H_2 in diffuse and translucent clouds.

In the early days of molecular radio astronomy, Rydbeck et al. (1973) first detected the hyperfine structure (HFS) lines between the Λ-doublet levels of the rotational ground state of CH at 3.3 GHz (9 cm). At frequencies near 3.264 GHz, 3.335 GHz, and 3.349 GHz (see Table 4.1), they were always detected in (generally quite weak) emission. Extensive single dish surveys across the Galaxy found the CH radio emission to be very widespread in the general molecular ISM in regions ranging from quiescent dark clouds to the environment of HII regions (example, Zuckerman & Turner 1975; Rydbeck et al. 1976; Genzel et al. 1979).

That always emission was observed, even toward continuum sources, and that the relative populations of the three HFS lines often deviate from their expected values at local thermodynamic equilibrium (LTE), which are $I_{3.264} : I_{3.335} : I_{3.349} = 1 : 2 : 1$ (see Table 4.1), suggested that the populations of the CH ground state Λ-doublet HFS levels must be inverted. The observed ubiquitous inversion of these CH transitions across sources for which one might assume varying physical conditions suggest that there must exist a general pumping mechanism that preferentially populates the upper HFS levels of the ground state Λ-doublet independent of the prevailing physical conditions within a region. The level inversion, leading to weak maser action in the ground state HFS line of CH was initially thought to be excited through collisional processes (involving collisions with atomic or molecular hydrogen) to the first rotational level (Bertojo et al. 1976; Elitzur 1977). However, Bujarrabal et al. (1984) have shown that collisions alone cannot explain the observed excitation anomalies. In particular, the $F' - F'' = 0^- - 1^+$ satellite line at 3.264 GHz is seen in enhanced emission while the $F' - F'' = 1^- - 1^+$ main line may sometimes, but very rarely, appear in absorption against the strong continuum of background sources. Excitation by collisions alone cannot be solely responsible for the observed 'enhancement' in the relative intensity of the lower satellite line, and necessitates the inclusion of radiative processes in order to explain the observed line strengths of the CH ground state transitions in SFRs.

In this work, we aim to investigate the excitation mechanism causing the ubiquitous weak masering effects in the CH ground state lines. Our analysis is aided by recently calculated collisional rate coefficients determined for inelastic collisions of CH with H, H_2, and He by Dagdigian (2018b) and Marinakis et al. (2019). Moreover, the use of accurate column density measurements determined from the high angular resolution observations of the

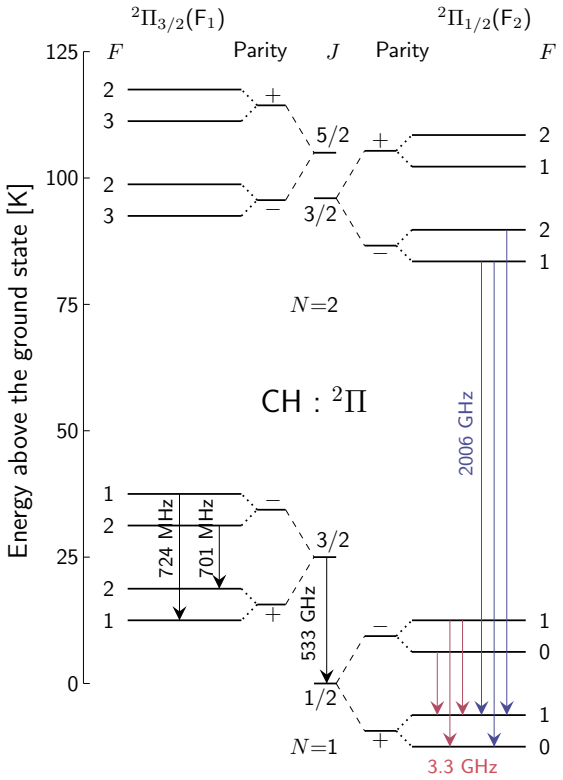

Figure 4.1: Lowest rotational energy levels of CH. The relevant transitions are labelled with their transitions marked using arrows, with the HFS splitting of the ground state energy level of CH as well as the rotational transition from the $N, J = 2, 3/2 \rightarrow 1, 1/2$ highlighted in magenta and blue, respectively. Note that the Λ-doublet and HFS splitting level separations are not drawn to scale.

$N, J = 2, 3/2 \rightarrow 1, 1/2$ FIR transitions of CH near 149 μm (2006 GHz) observed using the upGREAT instrument (Risacher et al. 2016) on board the Stratospheric Observatory for Infrared Astronomy (SOFIA; Young et al. 2012), whose HFS components have a common lower energy level with the CH radio ground state lines (see Fig. 4.1), will provide new constraints on our non-LTE models. In principle, such a comparison between the 2006 GHz transitions of CH observed using the 91.4 cm telescope onboard the Kuiper Airborne Observatory (KAO) and the 3.264 GHz ground state line, was previously carried out by Stacey et al. (1987) towards Sgr B2 (M). While the analysis presented by these authors attributes the level inversion to excitation effects and subsequently estimates the excitation temperature, the accuracy of their estimations is limited by the coarse spectral resolution of their FIR observations. The higher spatial and spectral resolution of our data allows us to estimate the column densities of CH and broadly assign contributions as arising from different spiral-arm and inter-arm regions for any given sight line.

We present here, the first interferometric observations of CH using the NRAO[1] *Karl G. Jansky* Very Large Array (VLA) in New Mexico toward four well known high-mass SFRs, namely, Sgr B2 (M), G34.26+0.15, W49(N), and W51. In Sect. 4.2 we detail the excitation

[1]The National Radio Astronomy Observatory (NRAO) is operated by Associated Universities Inc., under a collaborative agreement with the US National Science Foundation.

mechanism of the CH ground state and describe the observational setup in Sect. 4.3. We present the resulting line profiles, and introduce our non-LTE models in Sect. 4.4 and discuss the subsequently obtained physical and excitation conditions in Sect. 4.5 and finally in Sect. 4.6 we summarise the main conclusions derived from this work.

4.2 Excitation mechanism of the CH ground state Λ-doublet

The ground electronic state of the CH radical, with an unfilled π electron in its valence shell, exists in a $^2\Pi$ state. Following Hund's case b coupling, the spin-orbit interactions ($\boldsymbol{L.S}$) of the unpaired π electron splits each principal quantum level, N, into two orbital manifolds – $^2\Pi_{1/2}(F_2)$ and $^2\Pi_{3/2}(F_1)$, respectively, as displayed in Fig. 4.1. For CH, unlike in the case for OH, the $^2\Pi_{3/2}$ ladder is above the $^2\Pi_{1/2}$ ladder, i.e. the absolute ground state is in the $^2\Pi_{1/2}, J = 1/2$ level. The spatial orientation of the electron's orbital momentum axis relative to the axis of the molecule's rotation, splits the rotational levels, J, into Λ-doublet states. The Λ-doublet levels are distinguished based on their parity denoted by either + or −. Interactions between the total angular momentum and the nuclear spin of the hydrogen atom ($I_{\rm H} = 1/2$) further split each Λ-doublet level into two HFS levels with hyperfine quantum numbers, F. In general, for the $^2\Pi_{1/2}(F_2)$ ladder, the energies of the HFS levels are ordered with increasing values of F while for the $^2\Pi_{3/2}(F_1)$ ladder the opposite holds for all HFS levels, except for the lowest.

As briefly discussed in Sect. 4.1, the widely observed level inversion in CH can be qualitatively understood by invoking a simple pumping cycle. The pumping cycle involves the collisional excitation of CH (via collisions with atomic hydrogen, H_2 and/or He) to the first rotational state, $^2\Pi_{3/2}(F_1), J = 3/2$, followed by radiative decay back to the ground state (Bertojo et al. 1976; Elitzur 1977). Moreover, in order for collisions to produce a level inversion, the excitation cross-sections of the lower level of the $^2\Pi_{3/2}(F_1), J = 3/2$ Λ-doublet level must be larger than that of its upper level such that the preferential population of this level will create a level inversion after it cascades to the ground state. This difference in the collisional cross-sections within pairs of Λ-doublets is referred to as 'parity discrimination' (see, Dixon & Field 1979a, for a detailed description). In terms of parity discrimination, the pumping cycle works such that collisions between the + parity components of the Λ-doublet levels, corresponding to the $^2\Pi_{1/2}(F_2), J = 1/2$ and $^2\Pi_{3/2}(F_1), J = 3/2$ levels, are more probable than collisions between their − components. The radiative cascade that subsequently follows ($+ \rightarrow -$ and $- \rightarrow +$) will therefore tend to overpopulate both HFS levels of the − parity component of the ground state Λ-doublet relative to the + parity components HFS levels.

Theoretical considerations by Bertojo et al. (1976) and Dixon & Field (1979b,a) have shown that the effects of parity discrimination-induced level inversion varies depending on the collisional partner considered. Both studies were in agreement that, with a smaller reduced mass, collisions between CH and atomic hydrogen effectively invert the ground state HFS levels, but they disagreed on the role played by collisions with H_2. While Bertojo et al. (1976) suggest that collisions of CH with H_2 will tend to follow a similar parity discrimination as those

for the case of H, Dixon & Field (1979b) suggest an inverse propensity for collisions with H_2, where the collision between the $- \rightarrow -$ levels dominate. The latter contradicts observations of the ground state transitions of CH toward SFRs which show anomalous excitation effects at velocities corresponding to the envelopes of molecular clouds which are mainly comprised of molecular material. Taking all things into consideration the models we discuss in Sect. 4.4.3 do not specifically take into account parity discrimination effects but rather weigh contributions from different collision partners based on the molecular fraction (f_{H_2}) of the clouds considered.

Following selection rules, the ground state level of CH displays three transitions as the result of HFS splitting, at 3.264 GHz, 3.335 GHz, and 3.349 GHz, respectively (the spectroscopic properties of which are summarised in Table 4.1). Because it has twice the theoretical (LTE) intensity of the two other lines, the 3.335 GHz transition corresponding to the $F' - F'' = 1^- - 1^+$ is referred to as the main HFS line, while the other two transitions corresponding to $F' - F'' = 0^- - 1^+$ and $F' - F'' = 1^- - 0^+$ at 3.264 GHz, and 3.349 GHz are known as the lower, and upper satellite lines, respectively. While the collisional pumping model discussed above describes the framework for the level inversion observed in the ground state of CH, it does not account for the relative line strengths between its different HFS components, more specifically that of the enhanced intensity observed in the lower satellite line, which generally is the strongest of the three. As discussed in Zuckerman & Turner (1975) and Bujarrabal et al. (1984), the HFS lines' relative intensities are influenced by effects of line overlap of transitions to higher rotational levels. This can occur either through thermal broadening of the lines or via bulk velocity gradients in the gas, both of which are capable of bringing different sets of transitions into resonance with one another. With a typical line width between 2 km s^{-1} (for line-of-sight (LOS) components) and $\geq$6 km s^{-1} (at the envelope of the molecular cloud), there maybe partial or total line overlap from the HFS lines from the + parity component of the Λ-doublet levels of the first rotationally excited states of both orbital manifolds of CH at $^2\Pi_{3/2}(F_1), J = 3/2$ and $^2\Pi_{1/2}(F_2), J = 3/2$. Therefore, it is essential to take into account effects of line overlap as they significantly alter the amount of radiative trapping between the two Λ-doublet levels of the ground state.

4.3 Observations

Observations of the HFS lines between the Λ-doublet of the ground state level of CH near 3.3 GHz, were carried out on 2017 March 3, 5, 16, and 23 using the radio 'S-band' receivers of the VLA in the D-configuration (project id: 17A-214) for a total observing time of 1.3 hours per source. A total of eight well known SFRs as well as an active galactic nucleus (AGN) were observed across the four observational epochs mentioned above, however in this first paper we present the results and analysis toward only four of these sources, namely, Sgr B2 (M), G34.26+0.15, W49(N), and W51. This subset of sources, all of which are characterised by strong mm and FIR continuum emission, were selected in particular, not only because the physical conditions toward them have been extensively studied but, importantly, also because complementary observations of the FIR $N, J = 2, 3/2 \rightarrow 1, 1/2$ HFS transitions of CH at 2006 GHz toward them had been made with the upGREAT receiver on board SOFIA. The main properties of the sources discussed in our study are summarised in Table 4.2.

The VLA WIDAR correlator was configured to allow three spectral setups consisting of a 4 MHz wide sub-band or 2048 channels, centred at the frequency of each of the three CH lines, the spectroscopic parameters of which are summarised in Table 4.1. This setup corresponds to a native spatial resolution of 1.953 kHz (corresponding to 0.18 km s^{-1}). We also carry out broad band continuum observations over a total bandwidth of 2 GHz between 1.98 and 3.98 GHz, in 16 spectral windows, each of which are 128 MHz wide. The quasar 3C286 was used as both the bandpass as well as the flux calibrator, while J1751−2524, J1830+0619, J1924+1540, and J1925+2106 were used as phase calibrators for the different epochs in which Sgr B2 (M), G34.26+0.15, W49(N), and W51 were observed. In addition to the three CH spectral setups, there were eight spectral window setups used to observe hydrogen radio recombination lines (HRRLs) with principal quantum numbers, n, between 123-130. However, since this work mainly concentrates on the CH ground state transitions, the HRRLs will not be discussed here.

The data was calibrated and imaged using the Common Astronomy Software Applications (CASA) package with a modified version of the VLA pipeline[2].Then, the calibrated visibilities were CLEANed with a pixel size of $3''$ and an image size of $15' \times 15'$. Continuum subtraction was performed to the visibility data using the task `uvcontsub`, for which we exclude channels with line emission or absorption. To allow a meaningful comparison with the SOFIA data, the VLA images were restored with circular beams of full-width at half-maximum (FWHM) $\theta_{\rm B}$ with areas identical to those of the elliptical beams synthesised by CASA, i.e., $\theta_{\rm B} = \sqrt{\theta_{\rm maj} \times \theta_{\rm min}}$, where $\theta_{\rm maj}$ and $\theta_{\rm min}$ are, respectively, the major and minor FWHM axes of the synthesised beam. Values for $\theta_{\rm B}$, $\theta_{\rm maj}$ and $\theta_{\rm min}$ are given in Table 4.2 following the sources' positions and other attributes. For the analysis that follows, the intensity scales were converted from specific brightness, S, to brightness temperature, $T_{\rm B}$, using the Rayleigh-Jeans relation,

$$T_{\rm B} = \frac{Sc^2}{\nu^2\, k_{\rm B}\, \Omega} = \frac{1.222 \times 10^6 \text{ K}}{\nu^2 \text{ (GHz)}\, \theta_{\rm B}^2('')} S \text{ (Jy beam}^{-1}), \tag{4.1}$$

where $k_{\rm B}$ is the Boltzmann constant, c the speed of light, ν the frequency and Ω the beam solid angle. The second expression allows for convenient units to obtain $T_{\rm B}$ in K, from S measured in Jy beam^{-1}, observed at a frequency ν (in GHz) with a circular beam with a FWHM beam size of $\theta_{\rm B}$ in arc seconds. For $\nu = 3.3$ GHz and our average $\theta_{\rm B} = 23''$, $T_{\rm B}/S = 212$ K/Jy.

[2]https://science.nrao.edu/facilities/vla/data-processing/pipeline

Table 4.2: Summary of source parameters. The columns are (from left to right): the source designation, the equatorial source coordinates, the heliocentric distances, distance reference, systemic velocity of the source, FWHM of the synthesised beams ($\theta_{\rm maj} \times \theta_{\rm min}$), position angles (P.A.), and FWHM of the restored circular beams ($\theta_{\rm FWHM}$) and the root-mean-square (rms) noise levels of the line and continuum maps, respectively.

Source	Coordinates (J2000)		d	Ref	$\upsilon_{\rm LSR}$	$\theta_{\rm maj} \times \theta_{\rm min}$	P.A.	$\theta_{\rm B}$	$\rm rms_{line}$	$\rm rms_{cont}$
	α [hh:mm:ss]	δ [dd:mm:ss]	[kpc]		[km s^{-1}]	[$'' \times ''$]	[°]	[$''$]	[mJy/beam]	[mJy/beam]
Sgr B2 (M)	17:47:20.50	−28:23:06.00	8.3	[1]	64.0	35.3×15.0	169.7	23.0	2.5	2.7
G34.2+0.15	18:53:18.70	+01:14:58.00	1.6	[2]	59.0	22.3×18.8	−26.7	20.5	2.0	1.1
W49 (N)	19:10:13.20	+09:06:11.88	11.4	[3]	11.8	20.5×18.6	−32.2	19.5	2.6	4.1
W51 E	19:23:43.90	+14:30:31.00	5.4	[4]	62.0	33.2×23.2	−48.5	27.7	3.2	3.1

References: For the heliocentric distances:[1] Reid et al. (2019); [2] Zhang et al. (2009); [3] Zhang et al. (2013); [4] Sato et al. (2010)

The spectra of the 3.3 GHz CH lines were extracted from a region encompassing the same area as that by the FWHM beam width of the central pixel of the upGREAT/SOFIA (13.5″) and centered at the same positions toward which the 2006 GHz observations were carried out. These pointing positions coincide with the centres of the map, the corresponding positions of which, toward the different sources is tabulated in Table 4.2. The spectra were further post-processed and analysed using Python packages numpy (van der Walt et al. 2011) and scipy (Jones et al. 2001). The spectra of the CH transitions near 2006 GHz presented in the following sections do not represent the actually observed spectra but rather the line profiles resulting from the deconvolution of its HFS splitting. The HFS is deconvolved following the Wiener filter algorithm discussed in Jacob et al. (2019) with the local standard of rest (LSR) velocity scale set by the strongest HFS component of the 2006 GHz transition.

4.4 Results

In Figs. 4.2 and 4.3 we present the calibrated and baseline subtracted spectra of all three ground state HFS transitions of CH near 3.3 GHz toward Sgr B2 (M), G34.26+0.15, W49(N), and W51 E, respectively. Alongside these ground state lines we also display the corresponding HFS deconvolved spectra of the CH $N, J = 1, 1/2 \rightarrow 2, 3/2$ transitions near 2006 GHz presented in Wiesemeyer et al. (2018) and Jacob et al. (2019) observed using upGREAT/SOFIA. In Figs. 4.4 to 4.7 we compare the distribution of the 3.3 GHz continuum emission and the integrated intensities of the ground state HFS lines of CH (integrated over the velocity dispersion of each source) with that of the emission traced by the cold, dense dust at 870 μm observed as a part of the ATLASGAL survey (Schuller et al. 2009).

4.4.1 Spectral line profiles

The $N, J = 2, 3/2 \rightarrow 1, 1/2$ CH spectrum shows deep absorption profiles not only at velocities corresponding to the LOS features arising from the different spiral-, and inter-arm crossings but also toward the envelope of the molecular clouds. However, the lower satellite line of the ground state is always seen in emission, both toward the molecular cloud as well as along the LOS, while both the main and upper satellite lines show either absorption, emission or a mixture of both. Surprisingly, in the case of the latter two lines, we do not detect significant absorption or emission along the LOS which makes it difficult to constrain the physical conditions of these regions (except toward Sgr B2 (M)).

Furthermore, we observe a blend of several components toward the systemic velocities of these sources which can be attributed to different foreground, and background layers of the envelope surrounding these regions with possible contributions also arising from nearby HII regions, as well. Therefore, prior to carrying out our non-LTE analysis, we first decompose the contributions from the different cloud components associated with each of the molecular clouds. A similar decomposition of the envelope components was carried out for the sight lines toward Sgr B2 and W51 by Genzel et al. (1979) for the CH ground state lines observed using the Effelsberg 100 m telescope with a 4′ Gaussian beam. We characterise the different components using Gaussian profiles with velocities and line widths set by using the spectra of the $N, J = 1, 3/2 \rightarrow 1, 1/2$ HFS transitions of CH near 532 GHz presented in Gerin et al.

(2010), Qin et al. (2010) or retrieved from the Herschel archives[3] pointed toward the same positions as our study, as templates. The spectra of the 532 GHz lines of CH toward our sample of sources are quite complex, showing a combination of foreground absorption and emission corresponding to the velocity of the molecular cloud. These velocities are further cross-checked using position-velocity diagrams and the line widths were compared to the line profile properties of other related interstellar species like CN. Additionally, the spectral line properties are derived by fitting Gaussian components, simultaneously to all three of the ground state lines of CH such that the intrinsic line width and velocities are consistent with one another. The Gaussian fits to the 2006 GHz lines represent the same components from which the column densities are determined from, which will be later used as an important constraint in our non-LTE analysis. The subsequently derived peak intensities, FWHM and velocities with respect to $\upsilon_{\rm LSR}$ for the 3.3 GHz lines are tabulated in Table 4.3. In the following sections we present a qualitative description of the observed line profiles toward each source.

Sgr B2 (M)

Located close to the Galactic centre (GC), at a heliocentric distance of $\sim$8.15 kpc (Reid et al. 2019), the LOS toward the Sgr B2 giant molecular cloud (GMC) intersects several spiral-arm and inter-arm clouds. The most prominent features arise from the Sagittarius, Scutum, 4 kpc, and 3 kpc arms at LSR velocities of +8, +22, −22, and −45 km s^{-1}, respectively, with contributions from clouds near the GC (at a distance <2 kpc from it) at velocities near 0 km s^{-1} (Greaves & Williams 1994). LSR velocities between $\approx$ +60 and +70 km s^{-1} indicate material associated with the Sgr B2 region itself.

The Sgr B2 GMC contains two main protoclusters hosting a prodigious degree of star formation activity –and has been termed a 'mini-starburst' – namely, Sgr B2 North (N) and Sgr B2 Main (M) which are themselves surrounded by a number of smaller hot cores (Bonfand et al. 2017; Sánchez-Monge et al. 2017) and HII regions (De Pree et al. 2015, and references therein), all embedded in a $\sim$19 pc wide low-density envelope ($\sim 10^3$ cm^{-3}; Schmiedeke et al. 2016). Marked in the 3.3 GHz continuum emission maps presented in Fig. 4.4 are the positions of the Sgr B2 (M) and Sgr B2 (N) hot cores along with that of a position North-East of (M) labelled (L) which corresponds to an ultra compact (UC) HII. The FIR transitions of CH near 2006 GHz were observed toward the Sgr B2 (M) position, which hosts, compared to (N), stronger continuum emission at sub-mm wavelengths, ideal for absorption spectroscopy. Therefore, the analysis of the ground state HFS lines of CH, carried out in the remainder of this paper concentrates exclusively on the Sgr B2 (M) position. From panel (a) in Fig. 4.4 we see that both the 3.3 GHz continuum as well as the CH line emission (and absorption) distributions are offset from the 870 μm dust emission peaks which traces the densest parts of the HII region, which corroborates the association of CH with cloud populations of lower gas densities.

[3]See, `http://archives.esac.esa.int/hsa/whsa/`

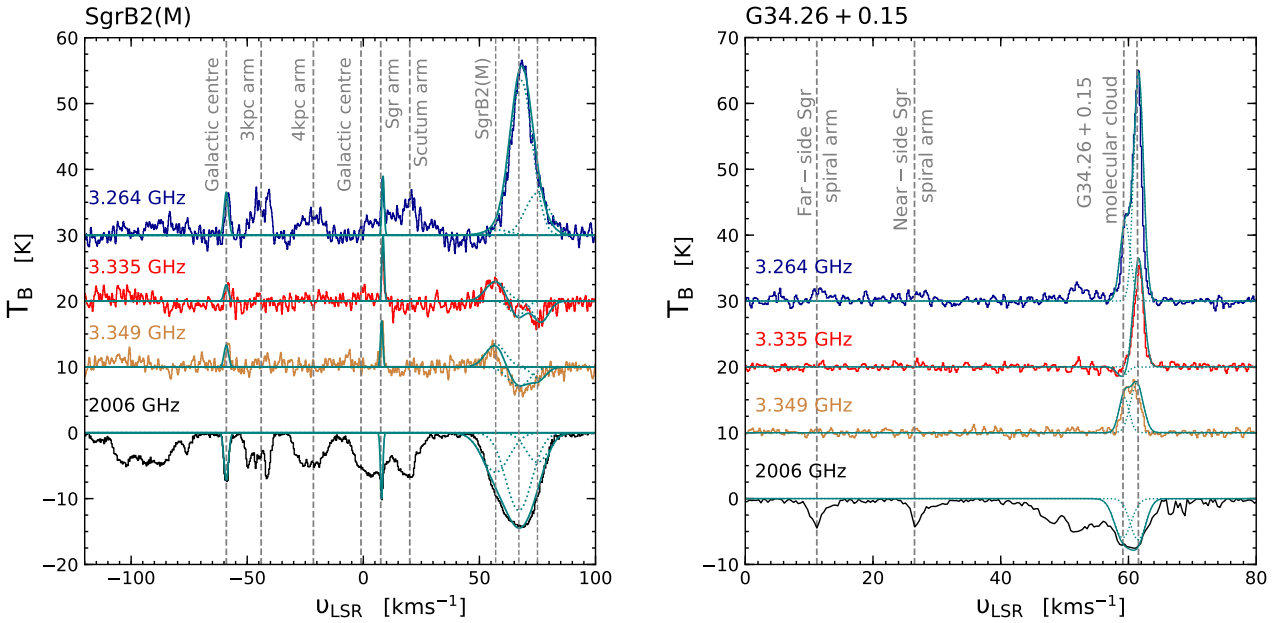

Figure 4.2: Spectra of the ground state HFS transitions of CH at 3.264 GHz (in blue), 3.335 GHz (in red), and 3.349 GHz (in dark orange) and the $N, J = 2, 3/2 \rightarrow 1, 1/2$ HFS deconvolved CH spectrum near 2006 GHz (in black) toward Sgr B2 (M) (*left*) and G34.26+0.15 (*right*). The LSR velocity scale for the 2006 GHz lines is set by the strongest HFS component. The spectra of the ground state lines are offset from the baseline by 30, 20, and 10 K. The dashed grey lines mark the main spiral- and inter-arm components crossing the LOS toward each sight line, as discussed in the text. Gaussian fits to LOS velocity features that are common to all four transitions are displayed by the solid teal curve and the dotted teal curves indicate the different components observed within the envelope of the Sgr B2 (M), and G34.26+0.15 molecular clouds, respectively.

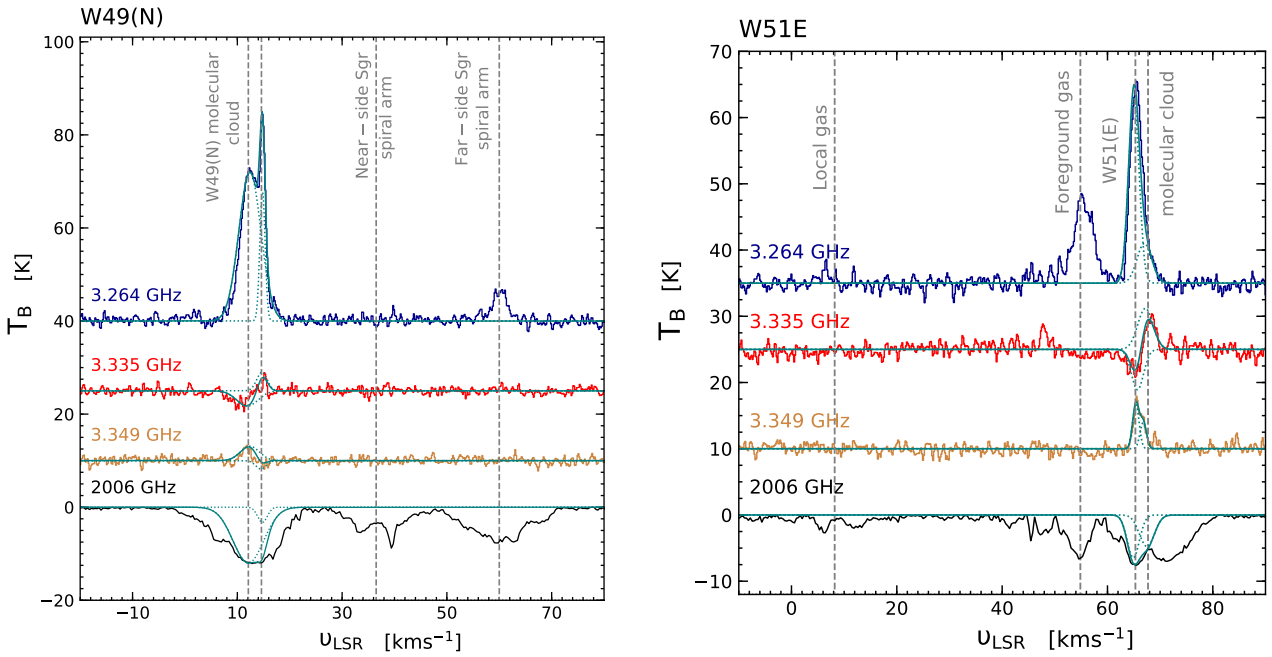

Figure 4.3: Same as Fig. 4.2 but toward W49 (N) (*left*), and W51 E (*right*). Here, the spectra of the ground state lines are offset from the baseline by (40, 35, 10, and −20 K) and (35, 25, 10, and −12 K), for W49 (N) and W51 E, respectively.

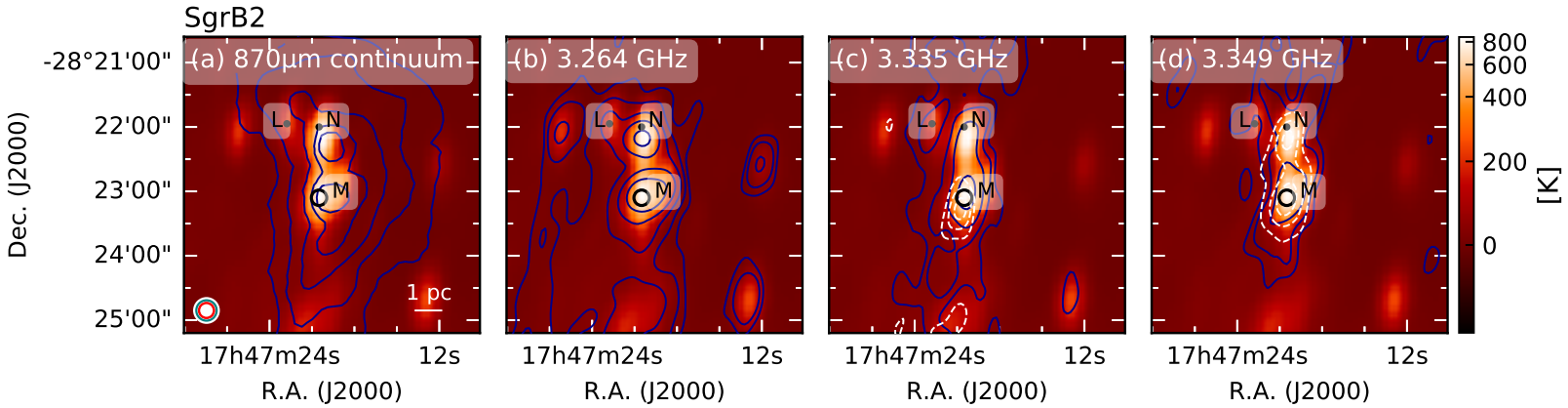

Figure 4.4: Overview of the 3.3 GHz CH line observations toward Sgr B2. Panel (a) displays the ATLASGAL 870 μm emission at contour levels starting from $5\times, 10\times, 20\times, 40\times$ and $80 \times 1\sigma$ where $1\sigma = 0.9$ Jy/beam overlaid atop the 3.3 GHz continuum emission along with the synthesised beam of the VLA observations (filled white circle) as well as the central beam of upGREAT/SOFIA (red) and the LABOCA/APEX beam (teal), for comparison. The position from which the spectra are extracted is marked by the beam in black and labelled M, we also mark the positions of Sgr B2 (N) and (L). Panels (b), (c), and (d) display the integrated intensity contours of the 3.264 GHz, 3.335 GHz, and 3.349 GHz CH lines, respectively, overlaid on top of the 3.3 GHz continuum emission. The intensities are integrated over a velocity range between 48 and 83 km s^{-1} except for that of the 3.335 GHz and 3.349 GHz CH maps, for which the emission components are integrated between 48 and 62 km s^{-1} while the absorption between between 62 and 84 km s^{-1}. The contour levels mark $5\times, 10\times, 20\times, 40\times$, and $80\times1\sigma$ where $1\sigma = 10.6, 2.65$, and 2.65 K km s^{-1} for the 3.264 GHz, 3.335 GHz, and 3.349 GHz CH emission components (solid dark blue curves) and the $3\times, 4\times$, and $5 \times 1\sigma$ levels where $1\sigma = 2.12$ K km s^{-1} for the 3.335 GHz and 3.349 GHz CH absorption components (dashed white curves).

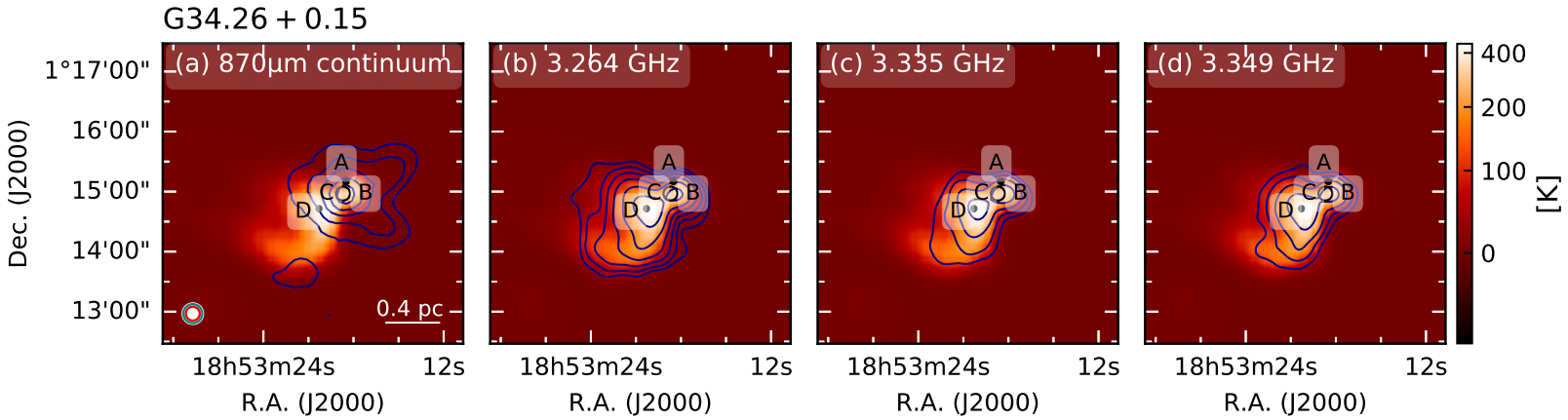

Figure 4.5: Overview of the 3.3 GHz CH line observations toward G34.26+0.15. Panel (a) displays the ATLASGAL 870 μm emission at contour levels starting from $5\times, 10\times, 20\times, 40\times$, and $80 \times 1\sigma$ where 1σ = 0.5 Jy/beam overlaid atop the 3.3 GHz continuum emission along with the synthesised beam of the VLA observations (filled white circle) as well as the central beam of upGREAT/SOFIA (red) and the LABOCA/APEX beam (teal), for comparison. The position from which the spectra are extracted is marked by the beam in black and labelled C, we also mark the positions of G34.26+0.15 A, B, and D. Panels (b), (c), and (d) display the integrated intensity contours of the 3.264 GHz, 3.335 GHz, and 3.349 GHz CH lines, respectively, overlaid on top of the 3.3 GHz continuum emission. The intensities are integrated over a velocity range between range between 57 and 64 km s^{-1}. The contour levels mark $5\times, 10\times, 20\times, 40\times, 80\times$, and $160 \times 1\sigma$ where 1σ = 2.65 K km s^{-1} for all three of the CH ground state lines (solid dark blue curves).

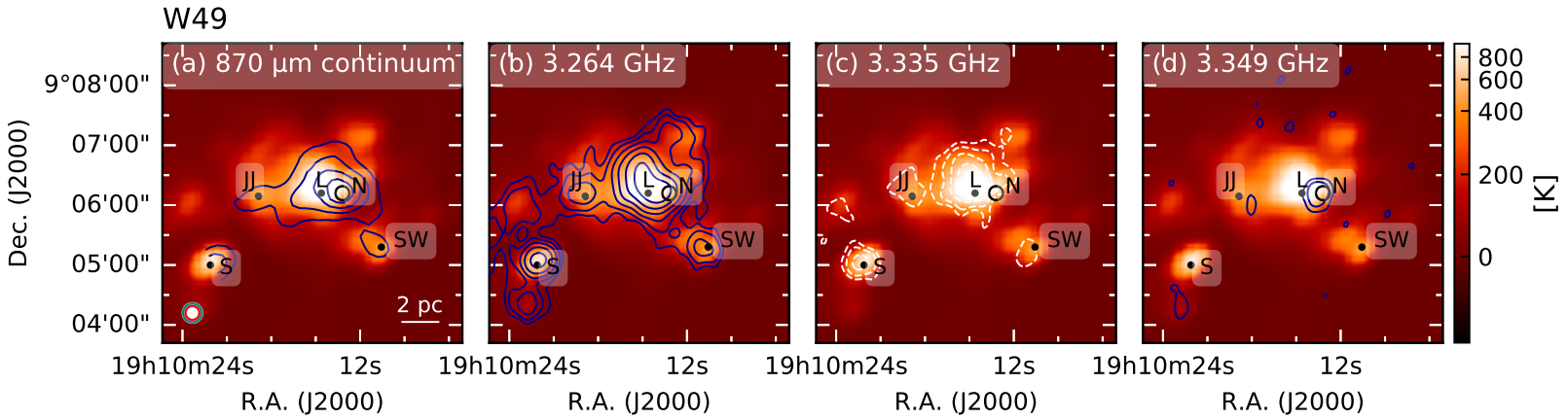

Figure 4.6: Overview of the 3.3 GHz CH line observations toward W49. Panel (a) displays the ATLASGAL 870 μm emission at contour levels starting from $5\times, 10\times, 20\times, 40\times$, and $80 \times 1\sigma$ where $1\sigma = 1$ Jy/beam overlaid atop the 3.3 GHz continuum emission along with the synthesised beam of the VLA observations (filled white circle) as well as the central beam of upGREAT/SOFIA (red) and the LABOCA/APEX beam (teal), for comparison. The position from which the spectra are extracted is marked by the beam in black and labelled N, we also mark the positions of W49 L, JJ, S, and SW as per De Pree et al. (1997). Panels (b), (c), and (d) display the integrated intensity contours of the 3.264 GHz, 3.335 GHz, and 3.349 GHz CH lines, respectively, overlaid on top of the 3.3 GHz continuum emission. The intensities are integrated over a velocity range between range between 2 and 20 km s^{-1} except in the case of the 3.349 GHz line for which the emission component was integrated between 7 and 14 km s^{-1}. The contour levels mark $5\times, 10\times, 20\times, 40\times, 80\times$, and $160 \times 1\sigma$ where $1\sigma = 6.08$, and 1.14 K km s^{-1} for the 3.264 GHz, 3.335 GHz, and 3.349 GHz CH emission (solid dark blue curves) and the $3\times, 4\times$, and $5 \times 1\sigma$ levels where $1\sigma = 2.28$ K km s^{-1} for the 3.335 GHz absorption component (dashed white curves).

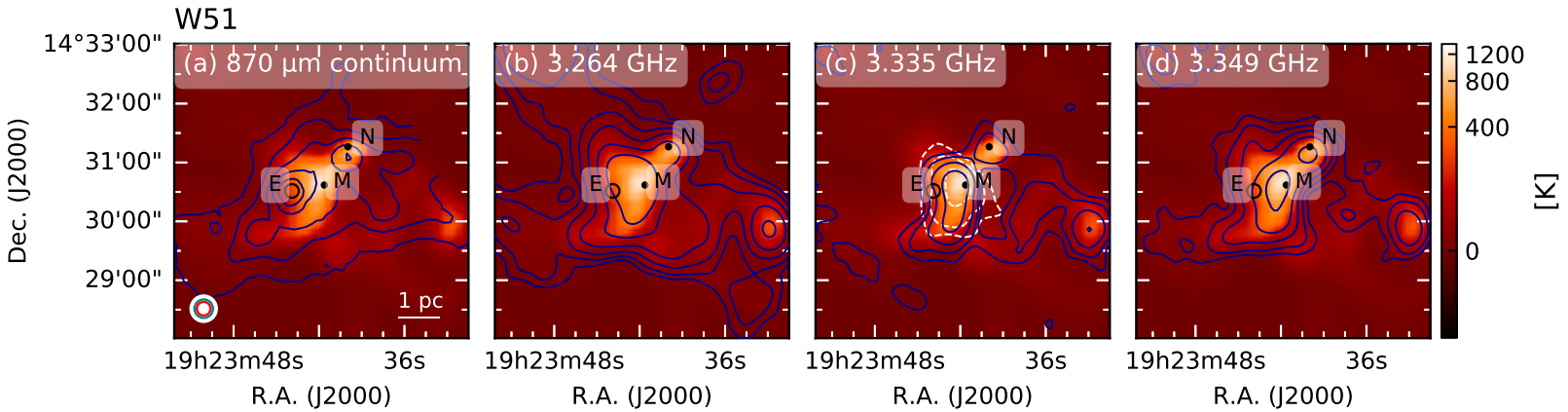

Figure 4.7: Overview of the 3.3 GHz CH line observations toward W51. Panel (a) displays the ATLASGAL 870 μm emission at contour levels starting from 5×, 10×, 20×, 40×, and 80 × 1σ where 1σ = 0.5 Jy/beam overlaid atop the 3.3 GHz continuum emission along with the synthesised beam of the VLA observations (filled white circle) as well as the central beam of upGREAT/SOFIA (red) and the LABOCA/APEX beam (teal), for comparison. The position from which the spectra are extracted is marked by the beam in black and labelled E, we also mark the positions of W49 M and N. Panels (b), (c), and (d) display the integrated intensity contours of the 3.264 GHz, 3.335 GHz, and 3.349 GHz CH lines, respectively, overlaid on top of the 3.3 GHz continuum emission. The intensities are integrated over a velocity range between range between 61 and 70 km s^{-1}, except in the case of the 3.335 GHz line whose absorption component is integrated between 60 and 66.6 km s^{-1}, while the emission between 64 and 72 km s^{-1}. The contour levels mark 5×, 10×, 20×, 40×, 80×, and 160 × 1σ where 1σ = 2.80, 0.97, and 2.80 K km s^{-1} for the 3.264 GHz, 3.335 GHz, and 3.349 GHz CH emission (solid dark blue curves) and the 3×, 4×, and 5 × 1σ levels where 1σ = 2.31 K km s^{-1} for the 3.335 GHz absorption component (dashed white curves).

The spectra of all three of the CH ground state transitions show features arising from the environment of the Sgr B2 (M) cloud near $\upsilon_{\rm lsr} = +62$ km s^{-1} and also, most distinctively, at velocities corresponding to the GC clouds and the Sagittarius spiral arm. Most remarkably the lower satellite line of CH at 3.264 GHz shows emission features across the entire LOS almost mimicking the wide band absorption seen in the HFS deconvolved spectra of CH at 2006 GHz (see left-hand panel of Fig. 4.2). This, along with the absence of clear CH features ($\geq 3\sigma$ of the noise level), at LOS velocity components (other than those discussed above), for both the main and upper satellite lines suggests that the lower satellite line is excited such that it shows enhanced emission uniformly across the different velocities covered by this sight line.

Upon comparing the spectral line profiles toward all three ground state HFS lines toward the envelope of this region, we see that there are three main components at $\upsilon_{\rm lsr} = +58, +67$, and $+75$ km s^{-1} likely tracing extended molecular gas in front of the dense molecular core. Previous investigations by Sato et al. (2000) and Neill et al. (2014) toward the Sgr B2 (M) region studied using different chemical species have already shown the envelope to comprise of different components at similar velocities. While the +67 km s^{-1} feature dominates the emission and absorption seen toward this source in the spectra of the lower ground state satellite line and the 2006 GHz FIR line, respectively, it has almost no contributions, with weak absorption if any toward the main and upper satellite lines of the CH ground state. The envelope component associated with $\upsilon_{\rm lsr} \sim +58$ km s^{-1} is seen in emission for all three of the HFS components, with the emission toward the lower satellite line being the weakest. In contrast, the +75 km s^{-1} feature shows absorption in the main and upper satellite line.

G34.26+0.15

At a distance of 1.6 kpc assuming that it belongs to the same cloud complex as G34.43+0.24 (Kurayama et al. 2011) the G34.26+0.15 SFR, has the shortest LOS in comparison to any of the sources in our current study. Lying almost tangential to the Sagittarius spiral arm, the main LOS features along this sight line correspond to those of the near-, and far-side crossings of the Sagittarius arm at +11 and +26 km s^{-1}, respectively. At radio continuum frequencies, this region displays two UCHII regions named A and B, as well as a position C which presents the prototypical example of a HII region with a cometary morphology (Reid & Ho 1985; Heaton et al. 1989, and references therein). Additionally there also exists an extended $1'$ diameter ring-like HII region referred to as component D (Reid & Ho 1985), which at $\sim$3.3 GHz shows the dominant continuum emission (see Fig. 4.5). The CH spectra are extracted from the position corresponding to component C of G34.26+0.15 but since our observations do not resolve the UCHII regions A and B from C, the beam and the subsequently extracted spectrum both contain contributions from these regions as well.

The systemic velocities associated with this region lie between $\upsilon_{\rm lsr} \sim$ +57 to +66 km s^{-1}. We recognise two main components at these velocities, one centred at the intrinsic velocity of the source near +58 km s^{-1} and one near +61.3 km s^{-1} which through studies of NH_3 has been shown to trace infalling cloud layers (Wyrowski et al. 2012). The infalling cloud component is seen in emission in the case of all three HFS transitions while the component closer to the systemic velocity shows weak absorption in the main ground state line. The spectrum of the lower satellite line further shows emission features at +11, and +51 km s^{-1} respectively, the

Table 4.3: Derived line properties. The columns are (*from left to right*): the source designation, transition frequency, LSR velocity, FWHM of the line, peak $T_{\rm B}$, the corresponding line ratio $R_i, i = 1, 2$ where $R_1 = T_{3.264\ \rm GHz}/T_{3.349\ \rm GHz}$ and $R_2 = T_{3.335\ \rm GHz}/T_{3.349\ \rm GHz}$ and the gas density, and temperature derived from the non-LTE radiative transfer modelling.

Source	Transition [GHz]	υ [km s^{-1}]	$\Delta\upsilon$ [km s^{-1}]	$T_{\rm B}$ [K]	R_i	$\log_{10}(n/{\rm cm}^{-3})$	$T_{\rm kin}$ [K]
Sgr B2 (M)	3.264	−58.4(0.1)	5.4(0.7)	6.9(1.2)	1.7	< 2.12	< 93.0
	3.335	−58.5(0.2)	5.2(0.5)	3.2(1.0)	0.8		
	3.349	−58.4(0.1)	4.6(1.0)	4.0(0.8)			
	3.264	8.2(0.0)	2.4(0.3)	6.4(1.0)	0.8	$1.97^{+0.17}_{-0.20}$	$63.8^{+8.7}_{-8.7}$
	3.335	8.3(0.0)	2.6(0.2)	9.6(1.4)	1.3		
	3.349	8.3(0.0)	2.2(0.2)	7.4(0.8)			
	3.264	58.2(0.2)	15.5(2.0)	1.2(0.9)	0.5	$3.78^{+0.24}_{-0.25}$	$124.5^{+4.5}_{-2.4}$
	3.335	57.6(0.2)	15.1(1.4)	3.7(0.6)	1.4		
	3.349	57.5(0.3)	13.5(1.6)	2.6(0.6)			
	3.264	68.6(0.1)	17.6(1.2)	24.6(2.0)	8.0	$3.03^{+0.14}_{-0.14}$	$56.3^{+4.2}_{-4.2}$
	3.335	66.8(0.2)	17.9(1.2)	-2.8(0.8)	0.9		
	3.349	66.7(0.3)	15.8(2.6)	-3.0(0.5)			
	3.264	75.6(0.5)	14.2(0.5)	6.8(0.9)	3.2	$4.43^{+0.32}_{-0.33}$	$85.4^{+4.5}_{-4.6}$
	3.335	76.4(0.2)	12.5(1.4)	-3.2(0.7)	1.5		
	3.349	75.6(0.4)	12.5(2.1)	-2.1(0.5)			
G34.26+0.15	3.264	59.6(0.1)	3.7(0.7)	13.4(1.5)	2.7	$4.44^{+0.40}_{-0.42}$	$95.5^{+9.2}_{-9.3}$
	3.335	58.5(0.5)	3.0(0.3)	-1.3(0.8)	0.3		
	3.349	59.4(0.1)	3.1(0.3)	5.0(0.8)			
	3.264	61.4(0.0)	3.5(0.4)	35.8(1.6)	4.9	$4.27^{+0.31}_{-0.32}$	$85.4^{+2.9}_{-3.0}$
	3.335	61.5(0.0)	3.8(0.2)	15.5(1.0)	2.1		
	3.349	61.0(0.0)	4.0(0.4)	7.3(0.6)			
W49 (N)	3.264	12.3(0.1)	5.4(0.2)	30.4(0.9)	7.2	$3.85^{+0.30}_{-0.32}$	$52.5^{+2.8}_{-2.9}$
	3.335	11.9(0.4)	6.1(0.9)	-3.0(0.7)	0.7		
	3.349	11.8(0.1)	5.6(0.2)	4.2(0.6)			
	3.264	15.0(0.0)	2.2(0.2)	34.7(1.1)	19.3	$3.13^{+0.14}_{-0.14}$	$82.2^{+5.6}_{-5.7}$
	3.335	15.3(0.0)	1.9(0.3)	5.4(0.8)	3.0		
	3.349	15.1(0.7)	1.7(0.6)	-1.8(0.7)			
W51 E	3.264	65.2(0.1)	5.7(0.3)	28.0(1.0)	4.0	~ 3.48	$104.3^{+3.2}_{-3.3}$
	3.335	64.5(0.5)	6.1(0.5)	-7.1(1.4)	1.0		
	3.349	65.3(0.1)	5.4(0.5)	7.3(1.2)			
	3.264	66.7(0.6)	7.7(0.8)	7.3(1.7)	2.1	< 2.64	< 98.0
	3.335	67.0(0.1)	8.0(1.6)	6.7(2.3)	1.9		
	3.349	66.7(0.1)	7.1(0.5)	3.3(1.5)			

nature (emission/absorption) of whose corresponding features in the main, and upper satellite lines are difficult to discern down to a 3σ noise level.

W49 (N)

One of the most luminous, $L \sim 10^{7.2} L_{\odot}$, (Sievers et al. 1991) SFRs in our Galaxy, W49 A, harbours several massive stellar clusters. It contains three massive SFRs the most prominent of which is W49 North (N). Also termed a mini-starburst, the W49 (N) region hosts several UC HII regions arranged in a partial ring-like structure (∼2 pc diameter) (Dreher et al. 1984; Welch et al. 1987). We label the different radio peaks following the nomenclature given by De Pree et al. (1997, 2020), who identified their positions using continuum emission maps at 7 mm, 1.3 cm and 3.6 cm. In addition to the position of W49 (N) we also mark the positions labelled L, JJ, W49 South (S) and South-West (SW) each of which represent the HII regions covered in the 3.3 GHz continuum emission maps presented in Fig. 4.6, where the continuum emission peaks at position L which lies closest to the nominal position of the W49 A GMC.

Located at a distance of 11.4 kpc (Zhang et al. 2013), the sight line toward W49 (N)intersects a large amount of foreground material. In addition to the local gas arising from the Perseus arm between −10 and +30 km s^{-1}, there are two prominent features at $\upsilon_{\rm lsr}$ = +40 km s^{-1}, and +60 km s^{-1} corresponding to the near- and far-side crossings of the Sagittarius spiral arm, respectively, as seen in the HFS deconvolved spectrum of CH at 2006 GHz displayed in the left-hand panel of Fig. 4.3. The ground state lines show two velocity components at velocities associated with the envelope of this region, redshifted from the systemic velocity of the source at +8.6 km s^{-1}, near +12 and +15 km s^{-1}, respectively. These narrow components arise from the fragmented clumps associated with dense molecular gas of the W49 (N)region as well as from neighbouring infrared star clusters as discussed in Serabyn et al. (1993) and Alves & Homeier (2003). The +12 km s^{-1} velocity component shows absorption only in the main ground state line of CH, while the nature of the +15 km s^{-1} component in the upper satellite line, seemingly showing weak absorption is difficult to discern. The lower satellite line of the CH ground state, similar to the sight lines toward Sgr B2 (M) and G34.26+0.15 shows LOS emission features toward W49 (N) as well.

W51

The W51 A GMC cloud complex, lying in the Sagittarius spiral arm at a distance of 5.4 kpc (Sato et al. 2010) has in addition to its massive protocluster, W51 Main (M) (IRS 1), two luminous condensations harboring high-mass young stellar objects present in this region, W51 North (N), also known as W51 IRS 2, and W51 East (E) which constitutes a number of compact hot molecular cores, termed e1–e8, that host hyper- or UC-HII regions (Sato et al. 2010; Ginsburg et al. 2017, and references therein). Most of the continuum emission in our 3.3 GHz VLA images is dominated by the extended emission of the W51 M region, however we focus on the widely studied W51 E region, toward a nominal position along its ridge (which in itself is not well resolved in our observations), seen as a strong dust continuum peak in Fig. 4.7.

In the spectrum of the ground state lower satellite line of CH, we see clear emission near +55 km s^{-1} that can be attributed to the compact HII region G49.4−0.3, with potentially an

absorption dip at the same velocities in the case of the main ground state line and no distinct signatures in the upper satellite line. Similar to the case for the CH observations toward W49 N, we do not see contributions of CH at velocities attributed to the molecular cloud region which for W51 E lies in a velocity interval between $\upsilon_{\rm lsr}$ = +58 km s^{-1} and +63 km s^{-1}. This is not surprising as we expect the CH abundance to peak in more diffuse cloud layers outside of the dense molecular cloud cores, sometimes offset. The most prominent features we see in our CH spectra of the ground state lines are at +65 and +67 km s^{-1}, respectively. While the former corresponds to the velocity component that is known to typically trace the extended emission along the eastern ridge of the W51 A complex where W51 E resides (see, Carpenter & Sanders 1998), the latter is associated with the +68 km s^{-1} molecular clouds that constitute a high velocity stream, first identified in early HI surveys (Burton 1970). However, it is unclear whether these two cloud components are physically related or if they represent distinct structures. For the purpose of our studies we treat them as individual components.

4.4.2 CH Column density from the 2006 GHz FIR transition

The column densities per velocity interval dυ of the 2006 GHz CH FIR lines can be computed from the deconvolved line profiles expressed in terms of optical depth (τ) versus $\upsilon_{\rm LSR}$ as follows,

$$\frac{{\rm d}N_u}{{\rm d}\upsilon} = \frac{8\pi\nu^3}{c^3 A_{\rm E}} \left[\exp\left(\frac{h\nu}{k_{\rm B}T_{\rm ex}}\right) - 1 \right]^{-1} \tau_{\rm decon}(\upsilon)\,, \tag{4.2}$$

with the appropriate spectroscopic parameters $g_{\rm u}$ (the upper level degeneracy), $E_{\rm u}$ (the upper level energy), and $A_{\rm E}$ (the Einstein A coefficient) for every given HFS transition. The upper level column density in a given velocity range is obtained by integration over υ. The total CH column density N(CH) can be calculated as

$$N({\rm CH}) = \frac{N_u}{g_u} Q \exp\left(\frac{E_{\rm u}}{T_{\rm ex}}\right)\,. \tag{4.3}$$

The partition function, Q, is itself a function of the rotation temperature, $T_{\rm rot}$, which equals the excitation temperature, $T_{\rm ex}$, under conditions of LTE. Typically, the high critical densities of the rotational transitions of many hydrides cause negligible populations of even the lowest rotationally excited levels in the rather low density regions in which these molecules are abundant. This allows their study only with absorption spectroscopy. For the case of the CH FIR lines discussed here, we compute critical densities of the order of $\sim 2 \times 10^9$ cm^{-3} using collisional rate coefficients calculated by Dagdigian (2018b) for gas temperatures between 50 and 100 K. Since, the highest gas densities we would expect along of sight lines are at most 10^5 cm^{-3} toward the envelopes (see Schmiedeke et al. 2016, for Sgr B2 (M)) of the SFRs studied in this work, the CH FIR transitions are sub-thermally excited whereby $T_{\rm ex}$ is lower than the gas kinetic temperatures. Computed for a two-level system, the value of the critical density is regarded only as an indication of the densities above which collisional processes dominate over radiative ones. In the low density limit ($\leq$ few $\times 10^2$ cm^{-3}) where the levels are in equilibrium with the cosmic microwave background (CMB) at a temperature $T_{\rm CMB}$ = 2.73 K, it is valid to assume that $T_{\rm ex} = T_{\rm CMB}$ or 3.1 K taking into account an estimated contribution from the interstellar radiation field (ISRF) (Gerin et al. 2010). In Table 4.4 we summarise

Table 4.4: Synopsis of the derived CH column densities.

Source	$\upsilon_{\rm min}$–$\upsilon_{\rm max}$ [km s^{-1}]	N(CH) [10^{14} cm^{-2}]
Sgr B2 (M)	-62– -52	0.23
	4–11	0.14
	42–90	7.28
G34.26+0.15	35–70	0.93
W49 (N)	0–25	2.21
W51 E	45–72	6.62

the values of the derived column densities computed over the velocity intervals most relevant for the following analysis. Our estimates for the values of N(CH) are in agreement with that previously determined by Wiesemeyer et al. (2018); Jacob et al. (2019). Note the caveat regarding the determination of the continuum level of the 2006 GHz line spectrum of CH toward W49 (N) as discussed in Jacob et al. (2020a).

4.4.3 Non-LTE radiative transfer analysis for the CH ground state

In an effort to characterise the physical and excitation conditions traced by the CH ground state Λ-doublet HFS transitions, we perform non-LTE radiative transfer calculations using the radiative transfer code MOLPOP-CEP (Asensio Ramos & Elitzur 2018). Based on the (coupled) escape probability formalism presented in Elitzur & Asensio Ramos (2006), this code provides solutions to the radiative transfer equation for multi-level systems, while also taking into account the effects of line overlap within a plane-parallel slab geometry. Since the code assumes the physical conditions to be uniform across the slab, namely, the gas density, $n_{\rm H}$, the gas kinetic temperature, $T_{\rm kin}$, and the molecular abundance, X, it is run in several iterations over varying physical conditions in order to sample different cloud layers. The models were computed over a density-temperature grid of size 100×100, for $n_{\rm H}$ values in the range of 25 to 10^5 cm^{-3} and gas temperatures between 50 and 175 K. Contributions from the major collision partners, that is, atomic and molecular hydrogen are weighted according to the molecular fraction, $f_{\rm H_2}$, of each modelled velocity component. We derive the column-averaged molecular hydrogen fraction using $f^N_{\rm H_2} = 2N({\rm H_2})/(N({\rm H}) + 2N({\rm H_2}))$ where the values for N(H) are taken from Winkel et al. (2017) while N(CH) values derived as discussed in Sect. 4.4.2, are used as proxies for $N({\rm H_2})$, following the relationship between the two molecules as estimated by Sheffer et al. (2008), $[{\rm CH}]/[{\rm H_2}] = 3.5^{+2.1}_{-1.4} \times 10^{-8}$. We further assume a constant ortho-to-para (OPR) ratio of 3:1 between the ortho, and para spin states of H_2, as expected for thermal equilibrium in the low-temperature limit. The radiative transfer analysis was carried out using HFS resolved rate coefficients of CH excited by collisions with atomic and molecular hydrogen computed by Dagdigian (2018b). These collisional rate coefficients are computed based on high-accuracy calculations of the potential energy surfaces (PESs) of CH–H and CH–H_2 collisions, for all transitions between the lowest 32 HFS levels for CH($X^2\Pi$) or upper level energies ≤ 300 K. They account for both direct as well as indirect collisions with H_2. More recently Marinakis et al. (2019) have calculated HFS resolved collisional rate coefficients

using the most recent ab initio PESs for collisions of CH with He. It is common practice to scale the rate coefficients for collisions with He by a factor equivalent to the reduced mass to obtain the collisional rates with para-H_2; this approximation is valid only for a limited range of gas temperatures. Here we use collisional rate coefficients for collisions with para-H_2 that are scaled from those of collisions between CH and He along with the direct collisional rate coefficients computed for collisions of CH with atomic hydrogen and ortho-H_2. We use this combination of collisional rate coefficients because when using the rates that were computed directly for the collisions with para-H_2 by Dagdigian (2018b), we find that the models are capable of producing level inversion in only the lower satellite line (see Fig. B.1). This might be a direct result of the fact that the CH rate coefficients involving collisions with para-H_2 are comparable to those for collisions with ortho-H_2. As noted by this author, this is in contrast to the trend observed for collisions of other molecules with H_2 for which the collisional cross-sections with ortho-H_2 are larger than that for para-H_2, like in related molecules, for example for OH (Schewe et al. 2015), and C_2H (Dagdigian 2018a). Therefore, we use the collisional rate coefficients for collisions of CH with para-H_2 that are scaled from the collisional rate coefficients for collisions of CH with He.

The models for each velocity component uses a fixed line width corresponding to the intrinsic values estimated from the observations of the ground state lines, as detailed in Sect. 4.4.1. External radiation from the CMB and ISRF (Mathis et al. 1983) form the main sources of heating present within these models, while internal heating by dust grains plays an important role particularly in the more diffuse environments. The dust temperature used are given by the PACS 160 μm dust continuum and taken from König et al. (2017). As discussed earlier we find that the effects of radiative excitation alone cannot create a population inversion between the two Λ-doublet levels of the ground state of CH as the excitation is followed by radiative decay. Therefore, such a simple approximation cannot create the anomalous excitation observed in CH and so we invoke the effects of FIR line overlap. Governed by a fixed set of input parameters, in each iteration the code solves the radiative transfer problem by dividing the slab into several 'zones' characterised by increasing optical depths (or column densities). The zones within each slab were constrained by the column density of the velocity component as derived using the $N, J = 2, 3/2 \rightarrow 1, 1/2$ CH lines, discussed in Sec. 4.4.2. The radiative transfer analysis is simplified by considering the distribution of the independent line ratios under the assumption that the contributions from all three of the ground state HFS transitions of CH have the same beam filling factor. In the following sections we discuss the results obtained from the non-LTE radiative transfer analysis.

4.5 Discussion

4.5.1 Physical conditions of the ground state Λ-doublet of CH

The physical conditions that prevail in the regions studied by us are constrained based on the behaviour of χ^2 across our modelled density-temperature parameter space. The χ^2 value is computed across the entire grid as follows,

$$\chi^2 = \Sigma_{i=1}^{2} \left(R_{\mathrm{i,\,obs}} - R_{\mathrm{i,mod}}\right)^2 / \sigma^2_{R_{\mathrm{i,obs}}}\,, \tag{4.4}$$

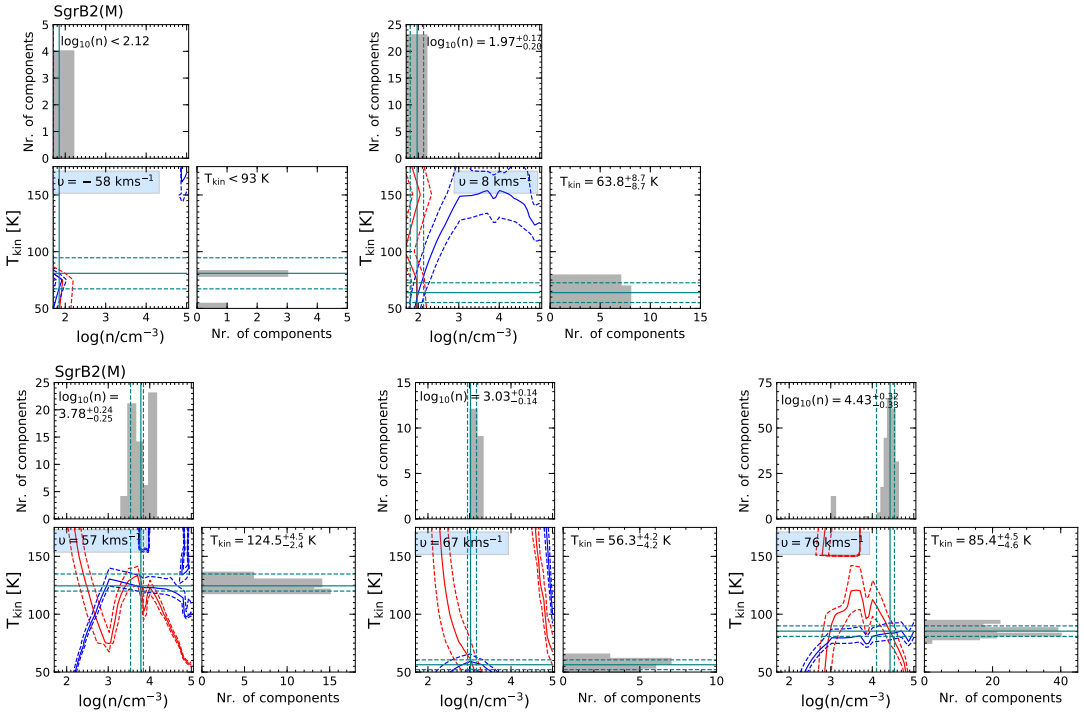

Figure 4.8: *Clockwise from the top left*: MOLPOP-CEP non-LTE radiative transfer modelling of the CH ground state transitions toward Sgr B2 (M) for LOS velocity components at -58, and +8 km s^{-1} followed by those associated with the envelope at $\upsilon_{\rm LSR}$ = +76, +67, and +57 km s^{-1}, respectively. Displayed in red and blue curves (*central plot*) are the modelled line ratios which best reproduce the observed line ratios between the 3.264 GHz, and 3.349 GHz lines and that between the 3.335 GHz, and 3.349 GHz lines and their uncertainties, respectively, as a function of n and $T_{\rm kin}$. While the corner plots display the gas density, and temperature distributions as governed by the 3 σ level of the minimum χ^2 with the median and standard deviation marked by the solid and dashed teal lines, respectively.

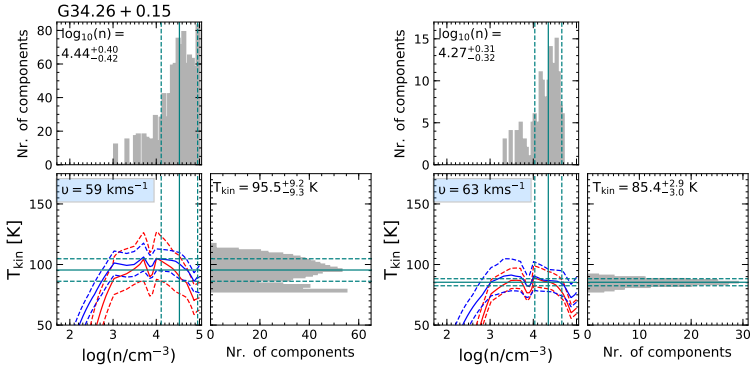

Figure 4.9: Same as Fig. 4.8 but toward the +59, and +63 km s^{-1} velocity components of G34.26+0.15.

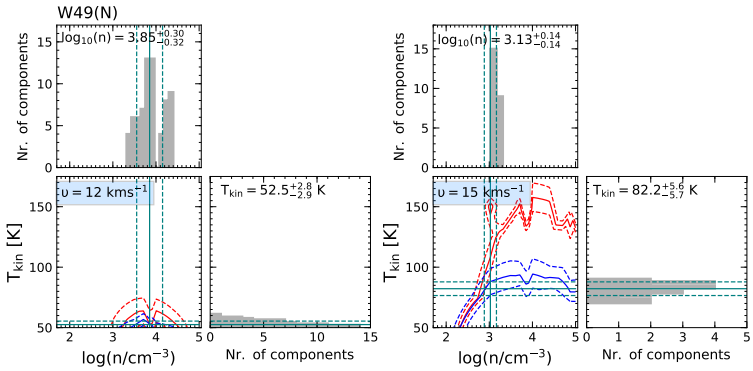

Figure 4.10: Same as Fig. 4.8 but toward the +12, and +15 km s^{-1} velocity components of W49(N).

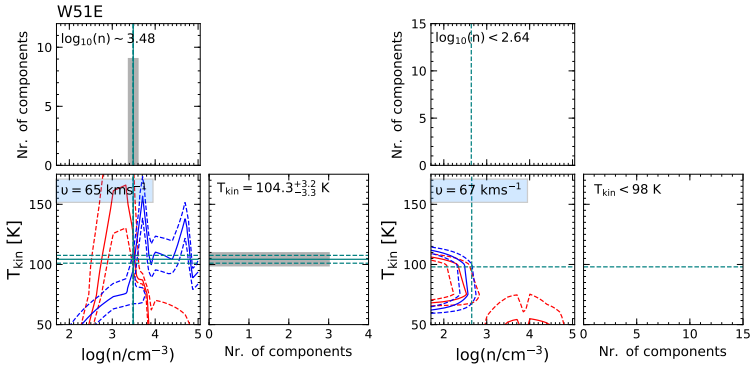

Figure 4.11: Same as Fig. 4.8 but toward the +65, and +67 km s^{-1} velocity components of W51 E. Unable to constrain the minimum χ^2 values, the parameter distributions for the velocity component at +67 km s^{-1} are not displayed here but marked are the upper limits for the gas density and temperature.

where $R_{\rm i,obs}$ and $R_{\rm i,mod}$ represent the ratio of the observed and modelled line brightness temperatures between any two of the three CH HFS lines on the $T_{\rm B}$ scale, $\sigma^2_{R_{\rm i,obs}}$ represents uncertainties in the line ratios. The independent line ratios used in our analysis are $R_1 = T_{3.264\ \rm GHz}/T_{3.349\ \rm GHz}$ and $R_2 = T_{3.335\ \rm GHz}/T_{3.349\ \rm GHz}$. The modelled solutions are constrained to the 3 σ levels of their minimum χ^2 distributions.

We summarise the resulting gas densities, and temperatures for the various velocity components observed toward each source in Table 4.3. These results are also visualised across the density-temperature plane in Figs. 4.8 to 4.11. The models describing the velocity components representing the envelopes of the different SFRs predict optically thin lines under the assumption of physical conditions consistent with what is expected for translucent clouds (see, Snow & McCall 2006). Thus our results are consistent with those of previous studies which determine the gas densities and temperatures for these warm extended envelope clouds to be $< 10^5$ cm^{-3} and < 65 K, respectively, for example toward the envelope of Sgr B2 (M) as determined by Etxaluze et al. (2013) using rotational transitions of CO. By weighting the models using a

smaller molecular fraction in comparison to that used for the envelope clouds we were able to reproduce the observed line ratios for the velocity components observed toward the LOS features. We do so, for the two LOS features consistently observed in emission in all three HFS lines toward Sgr B2 (M) at $\upsilon_{\rm LSR}$ = −58, and +8.3 km s^{-1}, respectively. In particular for the narrow LOS features, the different zones within the slab models were just able to simulate the values of the CH column density that were constrained by the 2006 GHz CH transition between $5{\times}10^{12}$ and 10^{13} cm^{-2}. The gas densities derived in this work for the LOS components of Sgr B2 (M) are similar to those derived by Thiel et al. (2019) using the absorption line studies of other simple molecules like HCO^+ whose abundance has been shown to be well correlated with that of CH in diffuse clouds (Gerin et al. 2010).

Lying just outside of the bow of a cometary-shaped UCHII region, it is widely believed that the molecular material in G34.26+0.15 is heated by the HII region (Mookerjea et al. 2007, and references therein). Therefore, from the results of our non-LTE radiative transfer modelling it is clear that the CH emission arises from warm molecular layers of moderate gas densities of 2–3×10^4 cm^{-3}. Compared to G34.26+0.15, for the envelope of W49 (N) we derive lower gas densities and temperatures. However, this is not surprising and consistent with the average physical conditions (n = 10^4 cm^{-3}, $T_{\rm kin}$ = 130 K) associated with the photo-dissociation region (PDR) of W49 (N) as derived using the [C II] 158 μm line by Vastel et al. (2001). Similarly in the W51 region we trace a warm extended gas present in the W51 A complex rather than the very compact dense e1–e8 hot molecular cores.

The large observed abundances of CH in the warm envelope layers of SFRs are conceivable because chemical models predict that the abundance of CH can be enhanced through endothermic hydrogen abstraction reactions of CH^+ ($\Delta E/k_{\rm B}$ = 4620 K; Hierl et al. (1997)), in regions with locally elevated gas temperatures as in the case of turbulent dissipation regions (TDRs; Falgarone et al. 2005; Godard et al. 2009, 2012, 2014), which is then followed by the dissociative recombination of CH_2^+ or CH_3^+ to form CH. Such a dissipation of turbulence may also be responsible for large scale velocity gradients which in turn can cause line overlap from transitions in higher rotational levels pertaining to the same sub-mm or FIR rotational transition.

Recently, a similar range of gas densities and temperatures were found to be probed by CH_2, which is also formed from the dissociative recombination of CH_3^+ (Jacob et al. 2021). Given the high energies above the ground state, 225 K, of the 68-71 GHz CH_2 lines observed in just two regions, in the past it had been believed that the CH_2 emission, unlike that of CH, was associated with the dense hot molecular cores of newly formed stars, despite the two molecules sharing the same chemical history. In contrast the recent observations of Jacob et al. (2021), which have extended the detections of this molecule, have convincingly shown that its emission arises from the warm ($T_{\rm kin}$ = 163 K) dilute (n = 3.4 × 10^3 cm^{-3}) layers of PDRs. Moreover, the $N_{K_{\rm a}K_{\rm c}} = 4_{04} - 3_{13}$ transition of CH_2 between 68 and 71 GHz observed by these authors also shows a weak masing effect in which all three of the fine-structure lines corresponding to this transition also show weak level inversion. Together, the non-LTE analysis carried out for CH_2 by Jacob et al. (2021) and CH here, support the spatial co-existence of the two molecules as well as their chemistry. For example, in the W51 region, both CH and CH_2 show stronger emission towards the extended HII region of W51 M rather than the denser and more massive

nearby regions of W51 E and W51 N. Additionally, the association of both CH and CH_2 with TDRs or warm PDR layers may open up formation and destruction routes between the two molecules that would otherwise be unlikely because of the low temperatures of the cold neutral medium (CNM).

4.5.2 CH in the cold dark cloud TMC-1 and its neighbourhood

Overall the physical conditions derived from our non-LTE analysis suggests that CH in the vicinity of the dense SFRs traces the warm translucent gas layers of their envelopes. However, in order to cross-check the validity of our results we additionally model the CH ground state lines observed toward the extensively studied dense, cold and dark Taurus Molecular Cloud-1 (TMC-1), whose kinetic temperature is well known, ≈ 10 K. As noted by Rydbeck et al. (1976) there are very few examples toward dark clouds in which the relative intensities of the CH ground state lines show departures from LTE. In TMC-1, these authors detected non-LTE behaviour only toward certain positions along the dense ridge that forms the spine of this region.

Based on their CH and OH observations, Xu & Li (2016) suggest that CH traces a C-type shock front in the boundary region between the dense gas in TMC-1 and translucent and diffuse gas. Here, the relative intensities of the CH (and the OH) radio lines indicate anomalous excitation in certain positions along its outer boundary. The observations by Goldsmith et al. (2010) of rotationally excited H_2 lines in this environment require temperatures of at least 200 K and modest H_2 column densities of 1–5 $\times 10^{18}$ cm^{-2}, which, according to these authors, 'points to an enhanced heating rate which may be the result of, e.g., dissipation of turbulence'. We suggest that this mechanism, dissipation of turbulence, which in Sect. 4.5.1 we have invoked for CH production, may likely also explain the rare instances of anomalous excitation of the CH ground state lines in such environments without strong sub-mm/FIR continuum radiation (and also co-determine their CH abundances).

Concentrating on the dense ridge of TMC-1 itself, we 'calibrate' the results with data from previous observations of the CH ground state HFS lines, carried out by Suutarinen et al. (2011) and Sakai et al. (2012). Suutarinen et al. (2011), while observing an abundance gradient in CH across the TMC-1 region, do not find significant deviations in the relative intensities of the three ground state HFS lines of CH from their expected LTE line ratio toward much of TMC-1.

Toward the cyanopolyyne peak (CP) in TMC-1, a region that shows enhanced abundances of long carbon chain molecules and other unsaturated C-bearing species (Little et al. 1979), both of the studies discussed above observe two velocity components in the CH spectra, namely, a narrow component ($\Delta\upsilon = 0.3$ km s^{-1}) and a relatively broader component ($\Delta\upsilon = 1.3$ km s^{-1}). We model the observed lines ratios of both velocity components using the same combination of collisional rate coefficients as before but reduce the number of energy levels included in the models by half. We use only the first 16 energy levels here for the case of TMC-1, in order to avoid numerical singularities that may arise when solving the equations of radiative transfer for energy levels as high as 389 K at low gas temperatures of 5 K. We run the models over a 50×50 density-temperature grid probing gas densities between 50 and 2.5×10^4 cm^{-3} and gas temperatures between 5–100 K using a slab geometry while also retaining effects of line

overlap. We also explore the parameter space for two different values of CH column densities at 5×10^{13} and 5×10^{14} cm^{-2} since the N(CH) values quoted by previous studies are determined by assuming $T_{\rm ex}$ = −60 to −20 K, a range of values that is frequently used, but it in fact holds little justification from observations. The CH ground state line ratios modelled toward TMC-1 across a sub-set of the modelled density-temperature parameter space is displayed in Fig. 4.12. Unable to converge to a single local minimum, we are only able to comment on the upper limits of the gas temperature derived toward each of the two velocity components. The upper limits for the gas temperature for the models with N(CH)=5 × 10^{13} cm^{-2} are 15 K and 18 K and 11 K and 13 K when N(CH)=5 × 10^{14} cm^{-2}, for the narrow and broad velocity components, respectively. The derived temperatures are consistent with what is expected in the TMC-1 region (see Sakai et al. 2012, and references therein) while the gas densities display only a lower limit of 130 cm^{-3}, it is also in agreement with the interpretation presented by Sakai et al. (2012), that CH and in particular the broad component traces the less dense envelope material.

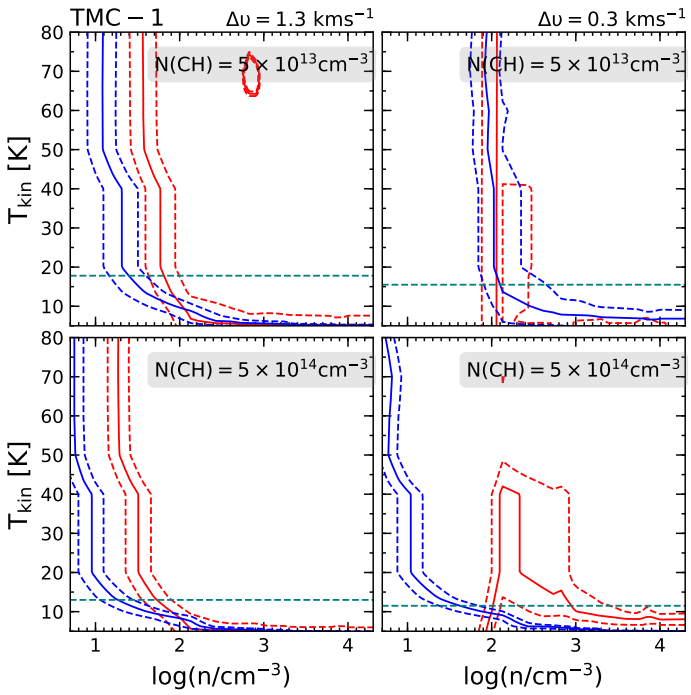

Figure 4.12: MOLPOP-CEP non-LTE radiative transfer modelling of the CH ground state transitions toward the broad (*left*) and narrow (*right*) velocity components observed toward the cyanopolyyne peak in TMC-1 for N(CH) = 5 × 10^{13} cm^{-2} (*top panel*) and 5 × 10^{14} cm^{-2} (*bottom panel*). Displayed in red and blue solid and dashed curves are the modelled line ratios which best reproduce the observed line ratios between the 3.264 GHz, and 3.349 GHz lines and the 3.335 GHz, and 3.349 GHz lines and their uncertainties, respectively, as a function of n and $T_{\rm kin}$. The dashed teal line marks the upper limit for the gas temperatures for the broad and narrow features.

4.5.3 Excitation conditions of the ground state Λ-doublet of CH

Using the physical conditions derived by the models discussed in Sect. 4.5.1, we investigate the excitation conditions of each of the ground state HFS transitions of CH. In Fig. 4.13 we display the modelled excitation temperatures of the three HFS lines of CH corresponding to the physical conditions which characterise the cloud components toward each of the sources presented in this study. The low but negative excitation temperatures inferred from the models reflect level inversion in all three of the CH ground state HFS lines. Unsurprisingly, the degree of inversion (which corresponds to the strength of the excitation temperature) is only marginally higher in the lower satellite line and is the weakest in the main line. Additionally, by comparing the LOS and envelope velocity components observed toward Sgr B2(M), we find the LOS components to show weaker excitation temperatures which in turn suggests weaker masing effects, consistent with our observations. Our results are consistent with the theoretical range of excitation temperatures determined by Bertojo et al. (1976) and Elitzur (1977), between −1.1 K and −0.5 K, which is likely fortuitous, given that these studies did not have realistic collisional rate coefficients at their disposal. They are also in the range of values derived by Magnani et al. (1992) from observational data of outflow regions and with that derived by Genzel et al. (1979) toward SFRs, within the large quoted uncertainties. Additionally across all the models discussed above, over the entire parameter space, all three HFS lines in the CH ground state are optically thin ($-0.01 < \tau < 0$) such that the total amplification of the lines is always small in comparison to that in other widely observed interstellar maser lines from, for example, the OH and H_2O molecules, whose observationally determined brightness temperatures, which are 10^{12} K or higher, require much greater 'maser gains', that is, amplification factors, $|\tau| > 20$ (see, e.g., Reid & Moran 1981; Elitzur 1982).

Moreover, the HFS lines in question have very low critical densities of $\sim$3 and 10 cm^{-3} for collisions with molecular and atomic hydrogen at $T_{\rm kin}$ = 50 K, owing to their rather low Einstein A coefficients $\sim 10^{-10}$ s^{-1}. This in turn implies that the ground state transitions of CH are easily thermalised. In Fig. 4.14, we analyse the trend between the excitation temperatures of the CH ground state HFS transitions and the gas densities for an envelope cloud model with a fixed gas temperature, CH column density and line width of 75 K, 3×10^{14} cm^{-2}, and 6 km s^{-1}, respectively. However, we find that the radio lines begin to thermalise only at gas densities greater than $n \sim 4 \times 10^6$ cm^{-3}. This density broadly corresponds to the critical density of the HFS lines of the $N, J = 1, 3/2 \rightarrow 1, 1/2$ rotational transition near 532 and 537 GHz. Therefore, at gas densities above the critical density of the 532/537 GHz transitions de-excitation by collisional processes compete with radiative ones. This decreases the amount of radiative decay in these lines and in particular that of the F'–F'' = 2^+-0^- line, which is partially responsible for the observed over population in the $F = 0^-$ level of the CH ground state and explains the flip and subsequent increase in the excitation temperatures of the CH ground state HFS lines at higher densities. This once again emphasises the role played by the FIR line overlap in the anomalous excitation of the CH ground state HFS level. It also demonstrates that using the critical density, be it in its commonly used definition or also including radiative excitation, as a criterion for the thermalisation only holds for a two level system, but not for the more involved energy levels of CH.

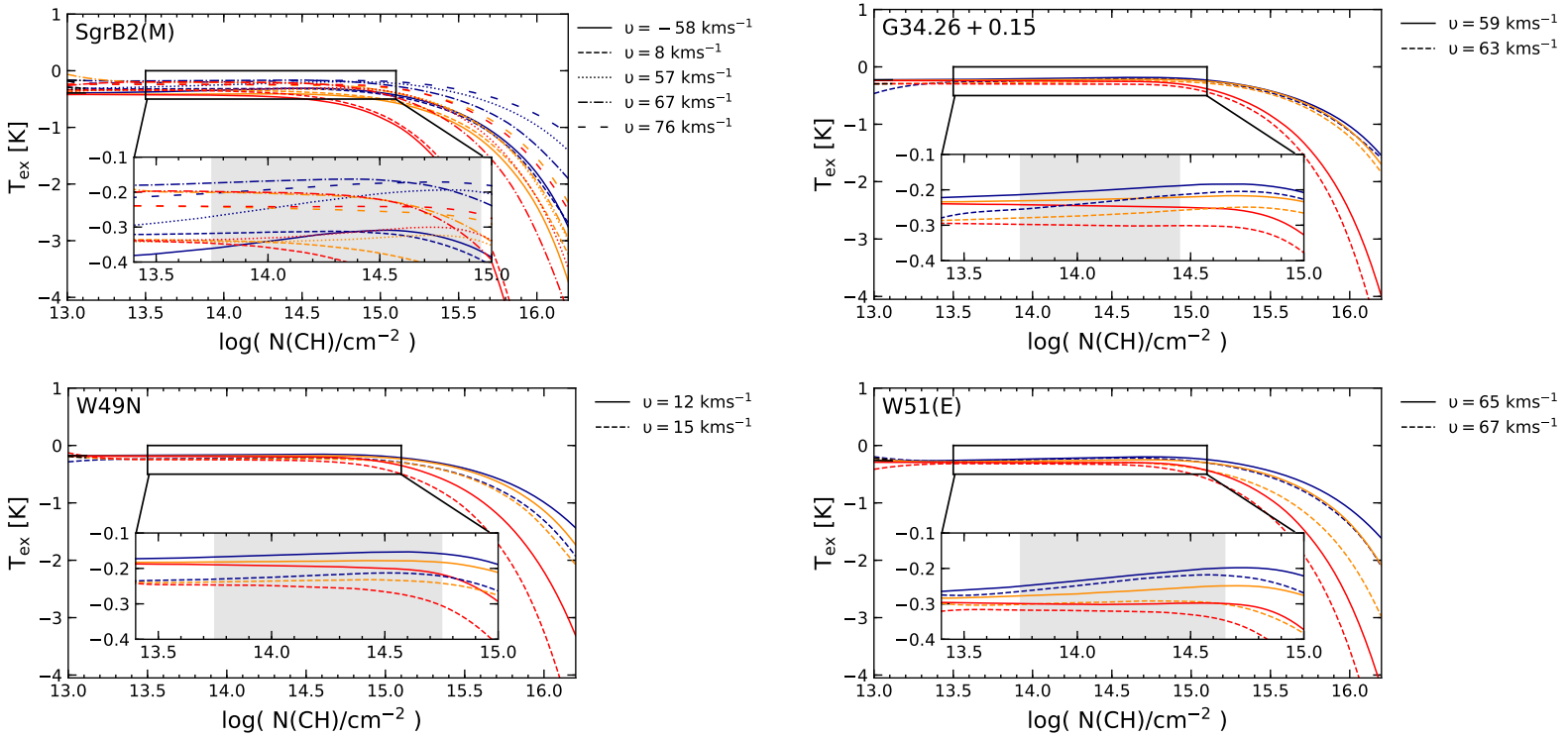

Figure 4.13: *Clockwise from top-left:* Modelled excitation temperatures of the 3.264 GHz (dark blue), 3.349 GHz (dark orange), and 3.335 GHz (red) ground state transitions of CH as a function of CH column densities for the physical conditions derived for the different velocity components toward Sgr B2 (M), G34.26+0.15, W51 E, and W49(N). The differing line styles are used to indicate results for the different velocity components as labelled. The inset panels expand on the T_{ex} values for CH column densities between 3×10^{13}–10^{15} cm^{-2} and the grey shaded regions highlight the column density intervals relevant to the velocity components in each respective source.

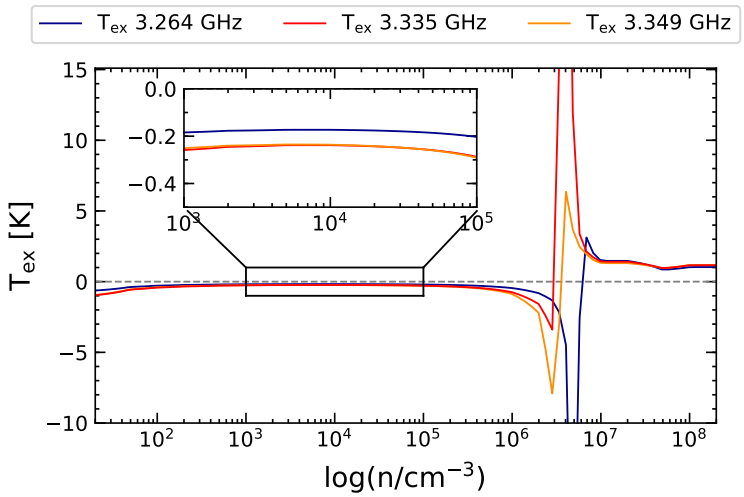

Figure 4.14: Variation in the excitation temperatures of the 3.264 GHz (dark blue), 3.349 GHz (dark orange), and 3.335 GHz (red) ground state transitions of CH as a function of gas densities at $T_{\rm kin}$ = 75 K, N(CH) = 3×10^{14} cm^{-2} and $\Delta\upsilon$ = 6 km s^{-1}. The dashed grey line marks 0 K while the inset panel expands between n=1×10^3 and 1×10^5 cm^{-3}.

4.6 Conclusions

In this study we present the first interferometric observations of the 3.3 GHz (9 cm) HFS lines of the ground state Λ-doublet of CH. Despite being widely observed since 1973, the anomalous excitation of these lines, which ubiquitously show weak maser action, has remained puzzling. While pumping cycles involving collisional excitation to the first rotational level following radiative decay back to the ground state could qualitatively explain the observed level inversions, they could not account for the relative intensities observed between the HFS lines and in particular the observed enhancement in the lower satellite line. We investigate the physical and excitation conditions of these lines using non-LTE radiative transfer analysis using recently derived collisional rate coefficients. The enhancement in the intensities of the lower satellite line are accounted for via the inclusion of pumping effects resulting from the radiative trapping caused by the overlap of FIR lines. By exploiting the synergy between the ground state and the $N, J = 2, 3/2 \rightarrow 1, 1/2$ transitions of CH at 2006 GHz (149 μm) observed using upGREAT/SOFIA, we obtain additional constraints on the column densities of the different velocity components along each sight line. Modelling only the most prominent features detected in the spectra of all three HFS lines toward each sight line, which typically corresponds to velocity components associated with the envelope of the observed SFRs, we derive gas densities characteristic of translucent clouds ($\sim 5 \times 10^2$–10^4 cm^{-3}), however we find temperatures traced by the CH ground state transitions higher than the expected range of temperatures in such regions, which are expected to be comparable to $\sim$50 K. We argue that the higher gas temperatures traced by CH likely result from this molecule's formation via non-thermal processes such as the deposition of turbulent energy into the gas. This makes CH a good tracer of the warm intermediary PDR, or TDR layers alongside CH_2, which we recently

studied (Jacob et al. 2021). The calculations presented here greatly depend upon the accuracy of the collisional rate coefficients used, while the modelling could certainly be improved by more realistic accounting for the structure of the target SFRs, like their thermal and density structure and the abundance gradient of CH in the envelopes in which it resides.

Outlook

The constraints on the excitation conditions of the ground state HFS lines of CH provided by modelling such as ours will aid to firmly establish this molecule's widely and relatively easily observable set of HFS lines at 9 cm as a powerful radio-wavelength probe of the diffuse and translucent ISM, alongside the 21 cm HI, the 18 cm OH, and the 6 cm H_2CO lines. Observing the radio lines is a much more economic means of studying this radical, as observations of its sub-mm and FIR lines, while possible with GREAT, will always be extremely expensive (in terms of observing time), with SOFIA being one of the only platforms. As to the 3.3 GHz radio lines, in addition to single dishes, for northern sources (with declination $> 40°$), the VLA is well suited for observing them interferometrically. In addition, the southern sky is becoming available with the MeerKAT array in South Africa whose 64 antennas are currently being equipped with S-band receivers that cover frequencies from 1.7 to 3.5 GHz developed and built by the MPIfR (Kramer et al. 2016).

An open question that remains is, how critical a role the sub-mm/FIR lines play in constraining the models of the 3.3 GHz ground state lines? We would argue that the value for the CH column densities they provide is essential for constraining the number of free parameters as in a radiative transfer code such as MOLPOP-CEP, which considers the source to be divided into zones of varying optical depths or column densities. For sources that lack observations of the FIR lines of CH and therefore the accurate column density measurements they deliver, one can carry out a similar analysis by invoking models which describe the abundance distribution of the studied molecule across the modelled region. The abundance is often described by using a radial power-law distribution. Several studies have previously employed such an approach when carrying out non-LTE radiative transfer calculations as presented by Wyrowski et al. (2012, 2016), who use the Monte Carlo code RATRAN to model SOFIA/GREAT observations of FIR NH_3 absorption lines to trace infall in SFRs.

Part II

Methylidyne isotopologues

Chapter 5

The first detection of ^{13}CH in the ISM

Finally I got to carbon, and as you all know, in the case of carbon the reaction works out beautifully. One goes through six reactions, and at the end one comes back to carbon. In the process one has made four hydrogen atoms into one of helium...

Hans Albrecht Bethe, Nobel Prize in Physics, 1967.

Overview

In 1939, Bethe (1939) analysed the different nuclear processes by which main-sequence stars burn hydrogen to subsequently form helium. He concluded that there were two dominant reaction pathways responsible for energy production in stars with masses comparable to that of the Sun. The first reaction, is via the proton-proton (p-p) chain which consists of the successive addition of protons to form helium. This series of reactions form the most important source of energy in low-mass main-sequence stars. As these stars evolve and exhaust the hydrogen fuel in their cores, they begin to derive energy from burning helium into carbon via the triple α reaction. This process was primarily responsible for producing ^{12}C, in early stellar populations.

The second dominant nuclear process, known as the carbon-nitrogen-oxygen (CNO) cycle (which was also being considered around the same time by von Weizsäcker (1938)), fuses hydrogen into helium using carbon, nitrogen, and oxygen as catalysts in more massive stars. This cyclic process also includes several side reactions and secondary products, and in its many iterations, leads to the formation of the CNO isotopes in addition to helium. The CNO cycle hence forms an important tool for interpreting the chemical evolution and stellar mass distribution of the Milky Way and the universe.

In this chapter, we report the discovery of the ^{13}CH isotopologue in the ISM for the first time and subsequently study the ^{12}C/^{13}C isotopic abundance ratio derived from it. This chapter is based on a paper published in *Astronomy & Astrophysics*, titled 'The first detection of ^{13}CH in the interstellar medium', Jacob et al. (2020a)[1], with minor modifications made only so as to adapt the manuscript to the layout of this thesis.

5.1 Introduction

The methylidene radical CH has received widespread attention as a general probe of diffuse and translucent interstellar clouds and in particular as a surrogate for the H_2 column density

[1]Jacob et al. A&A, 640, A125, 2020, reproduced with permission ©ESO

determinations in such environments (e.g. Federman 1982; Sheffer et al. 2008, and references therein). CH has been observed in widely different wavelength regimes, from the radio at 9 cm (Rydbeck et al. 1973) to the sub-millimetre (sub-mm) and far-infrared (FIR) ranges, at 560 μm (Gerin et al. 2010) and 150 μm (Stacey et al. 1987; Wiesemeyer et al. 2018) and the optical (4300.3 Å. e.g. Danks et al. 1984; Sheffer et al. 2008) into the far-ultraviolet (FUV) regimes (1369.13 Å, Watson 2001). The famous 4300.3 Å CH transition was one of the first three molecular lines that were detected in the interstellar medium (ISM) (Dunham 1937; Swings & Rosenfeld 1937). While an abundance of ^{12}CH data exists, very little is known about its rarer isotopologue ^{13}CH. Unlike its parent molecule, which is ubiquitously distributed in the ISM, the only known astronomical identification of ^{13}CH has been made in the solar spectrum by Richter & Tonner (1967). As for the ISM, Bottinelli et al. (2014) reported the non-detection of the $N, J = 1, 1/2 \rightarrow 1, 3/2$ and $N, J = 1, 3/2 \rightarrow 2, 5/2$ transitions of ^{13}CH towards the well-studied low-mass protostellar condensation IRAS 16293−2422.

The ^{12}C/^{13}C ratio has been widely studied towards molecular clouds in the Milky Way (e.g. Henkel et al. 1982; Steimle et al. 1986; Wilson & Rood 1994; Henkel et al. 1994) and recently, also in the nuclear regions of nearby starburst galaxies (Tang et al. 2019). It is an important diagnostic tool for probing Galactic chemical evolution or simply the nucleosynthesis history of the Galaxy. ^{12}C is synthesised as the primary product of shell and core He-burning in intermediate- and high-mass stars through the triple-α reaction, while ^{13}C is a secondary product of stellar nucleosynthesis and is produced over longer timescales. It is predominantly formed as a by-product of the carbon-nitrogen-oxygen (CNO) cycle in asymptotic giant branch (AGB) stars. Initiated by the proton capture of the ^{12}C nucleus produced from an older stellar population, the CNO-cycle forms ^{13}N, which then decays through positron emission to form the ^{13}C nucleus (^{12}C(p,γ)^{13}N(β^+)^{13}C) (Pagel 1997). The ^{13}C intermediate product is injected into the ISM by mass loss of the AGB stars, after the ashes of the helium-burning shell of these objects have intermixed with their convective envelopes in the third dredge-up (Herwig 2005). This establishes the ^{12}C/^{13}C isotopic ratio as a measure of the degree of astration present in the Galaxy. Chemical evolution models of the Galaxy (Tosi 1982; Prantzos et al. 1996) have predicted the ^{12}C/^{13}C ratio to exhibit a positive gradient, increasing with galactocentric distances and decreasing with time.

The predictions of these models have been confirmed by observational measurements of the ^{12}C/^{13}C isotopic ratio that were carried out by studying the rotational transitions of molecules such as H_2CO (Henkel et al. 1982), CO (Langer & Penzias 1990), and CN (Milam et al. 2005) and of their respective ^{13}C isotopologues at centimetre and millimetre wavelengths. At these wavelengths the lines from the isotopologues of these species are well separated, unlike in the optical regime (except for $^{12/13}CH^+$; see Ritchey et al. (2011)). While the average fit to the ^{12}C/^{13}C gradients derived independently using the three molecules mentioned above agree within the quoted error bars, their individual trends display systematic variations amongst themselves. The reasons for these variations may be related to the observations of the different tracers and/or to isotope-selective chemical processes such as gas-phase fractionation and selective photo-dissociation, which do not affect every molecule in the same way. Chemical fractionation occurs as a result of ion-molecule exchange reactions that preferentially transfer and incorporate the heavier atomic isotopes into molecules due to differences in zero-point

energies between the different isotopes (see e.g. Wilson 1999; Roueff et al. 2015). Isotopic fractionation does not affect all molecules in the same way as its degree greatly depends upon the formation pathway of the molecule and the environment in which it is formed and exists. In molecules that are susceptible to fractionation, such as CO, the chemical fractionation enriches the ^{13}C isotope and lowers the ^{12}C/^{13}C ratio, but it is increased by the selective photo-dissociation of the rarer isotopic species containing ^{13}C because its self-shielding in regions with a high UV flux is weaker (Bally & Langer 1982). In such regions, the ^{12}CO/^{13}CO ratio might therefore be higher than the underlying ^{12}C/^{13}C ratio. In denser regions where carbon exists mostly in the form of CO, ^{13}C is locked up in CO and is depleted in other carbon-bearing molecules (Roueff et al. 2015). Precise measurements of the ^{12}C/^{13}C isotopic ratio have also been made using observations of the CH$^+$ $A - X$ (0, 0) transition near 4232 Å (Ritchey et al. 2011), but their observations are limited to nearby stars (<7 kpc) that are bright (V <10 mag) in the visible wavelength range. The corresponding sub-millimetre transitions of CH$^+$ are often optically thick with saturated absorption profiles and can only yield lower limits on the carbon isotopic ratio (Falgarone et al. 2010). Hence, the high optical depths of many abundant ^{12}C -bearing molecules and effects of saturation and self-absorption pose a problem when the intensities of these lines are used, which in turn skews estimates of the ^{12}C/^{13}C ratio. In an attempt to provide additional constraints on the ^{12}C/^{13}C ratio, we here propose the use of a new tracer: CH.

CH is expected to be a good candidate for conducting isotopic ratio measures because it is an abundant species that is ubiquitously formed in the ISM, and because its spectral lines are optically thin. Quite remarkably, this is generally true for radio, sub-millimetre, FIR, and optical CH lines, except for the ground-state rotational sub-millimetre/FIR transitions near 533/536, and 2006/2010 GHz, which reach optical depths that exceed unity in absorption from the envelopes of SFRs; see for example our Fig.5.2. In particular, the hyperfine structure (HFS) components of the $N, J = 1, 1/2 \rightarrow 2, 3/2$ transitions of CH near 2 THz have recently been observed in generally unsaturated absorption, which is ideal for column density determinations (Wiesemeyer et al. 2018; Jacob et al. 2019). Models and simulations by Röllig & Ossenkopf (2013) for photo-dissociation regions (PDRs) show that the fractionation present in CH is dominated by the fractionation of its parental species. CH originates from C$^+$ and is formed through the dissociative recombination of CH_3^+,

$$C^+ \xrightarrow{H_2} CH_2^+ \xrightarrow{H_2} CH_3^+ \xrightarrow{e^-} CH \tag{5.1}$$

Hence, the degree of fractionation in CH is closely coupled with that of C$^+$. Ossenkopf et al. (2013) have studied the fractionation of C$^+$ by comparing model predictions with high-resolution observations of the fine-structure lines of [^{12}CII] and [^{13}CII] using HIFI/*Herschel*. These authors find that, at low visual extinctions, A_V, the isotopic fractionation ratio of C$^+$ is comparable to the elemental abundance ratio, but it increases with A_V at low gas temperatures by typically a factor of ∼2 at most. This is a consequence of the enrichment of ^{13}C in CO in these regions (favouring the forward reaction of the C$^+$– CO ion-molecule exchange reaction (Langer & Penzias 1990)), which results in the depletion of ^{13}C$^+$ and all subsequent species such as ^{13}CH that are formed from it. In addition, the abundance of CH is often enhanced through hydrogen abstraction reactions of CH$^+$, which is formed endothermically ($\Delta E/k_B$ =

4620 K) (Hierl et al. 1997), in shocks, or in the dissipation of turbulence (Godard et al. 2014), followed by the dissociative recombination of CH_2^+:

$$C^+ \xrightarrow[H_2,\,h\nu]{H} CH^+ \xrightarrow[H_2,\,h\nu]{H} CH_2^+ \xrightarrow{e^-} CH\,. \tag{5.2}$$

Because it is formed at high effective temperatures through non-thermal processes, CH^+ is not affected by fractionation and is believed to reflect the ambient C-isotopic ratio in the diffuse ISM. In low A_V diffuse clouds, where turbulence-driven reactions are favoured, CH, like its parent CH^+, is therefore not affected by fractionation. The abundance ratio of the CH isotopologues accordingly does not deviate from the elemental ratio of the atomic carbon isotopes.

As mentioned above, optical and UV absorption studies of CH require visually bright early-type stars as background whose light is unhampered by interstellar extinction (Federman 1982; Sheffer et al. 2008). Owing to this, they can only probe the ISM in the solar neighbourhood out to a few kiloparsec. In contrast, we observe supra-terahertz transitions of CH and ^{13}CH in absorption against the bright dust emission of far away star-forming regions (SFRs) out to the Galactic centre (GC) and beyond. Thus our absorption spectra not only probe the molecular envelopes of these sources, but also the diffuse and translucent interstellar clouds along their lines of sight over a wide range of galactocentric radii. Moreover, because of the differential rotation of the Galaxy, the absorption covers wide ranges in local standard of rest (LSR) velocity. As a caveat, we mention that because first, the expected ^{12}CH/ ^{13}CH ratios, which range from ≈20 in the GC to ≈90 at the solar circle and to even higher values beyond (Wilson & Rood 1994, and references therein), and second, because even ^{12}CH lines are predominantly optically thin, we expect a detection of ^{13}CH absorption only towards the LSR velocities of the SFRs studied because these sources have far greater column densities than the intervening diffuse clouds along their lines of sight. We present our search for ^{13}CH in the ISM along the line of sight (LOS) towards five high-mass SFRs in the Milky Way, Sgr B2(M), G34.26+0.15, W49(N), W51E, and W3(OH) and discuss its use as an unbiased tool for benchmarking the ^{12}C/^{13}C Galactic gradient.

5.2 ^{13}CH spectroscopy

Similar to CH, ^{13}CH conforms to Hund's case-b coupling, but differs in the nuclear spin, $\boldsymbol{I}$, of the carbon atom, $I(^{12}\mathrm{C})=0$ and $I(^{13}\mathrm{C})=0.5$. Because of the non-zero nuclear spin of the ^{13}C isotope, the total angular momentum $\boldsymbol{J}$ first couples with $I_1(^{13}\mathrm{C})$ to generate $\boldsymbol{F_1}$ ($\boldsymbol{= J + I_1}$), which further couples with the nuclear spin of the H atom, $I_2(\mathrm{H}) = 0.5$ to yield $\boldsymbol{F}$ ($\boldsymbol{= F_1 + I_2}$). The energy level diagram of the ^{13}CH Λ-doublet transitions that are discussed in this study are displayed in Fig. 5.1. Considerable effort has been expended in the laboratory to measure the rotational spectrum of ^{13}CH. The spectroscopic parameters of the rotational transitions of the ^{13}CH radical between the $X^2\Pi$ ground state have been measured using the technique of laser magnetic resonance (LMR) at FIR wavelengths by Davidson et al. (2004). The results of their experiments were combined with previously determined Λ-doublet intervals of the molecule by Steimle et al. (1986) to provide accurate predictions of the transition frequencies

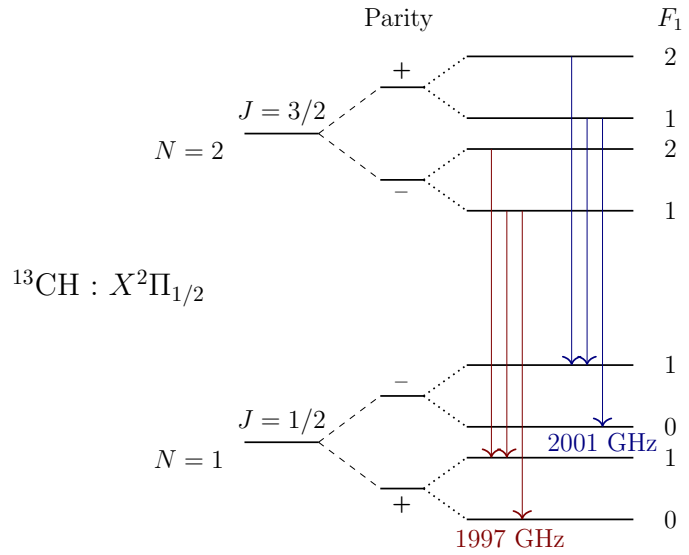

Figure 5.1: Energy-level diagram of the lower rotational levels of ^{13}CH. The hyperfine transitions of ^{13}CH that are presented in this study are highlighted using red and blue arrows. The proton hyperfine structure splittings are not included. The level separations are not to scale.

between the low-lying rotational levels and the ground state. The spectroscopic parameters of the observed $N, J = 2, 3/2 \rightarrow 1, 1/2$ transitions are tabulated in Table 5.1. The Einstein A coefficients, $A_{\mathrm{E},ij}$, were computed from the line strengths, S_{ij}, using the relation

$$A_{\mathrm{E},ij} = \left(16\pi^3 \nu_{ij}^3 / 3\varepsilon_0 hc^3\right) (2F_i + 1)^{-1} S_{ij}\, \mu^2 \tag{5.3}$$

for spontaneous emission from an energy level i to j. Here ν_{ij} is the corresponding frequency, F_i is the total hyperfine quantum number of level i, and μ represents the electric dipole moment of ^{13}CH, $\mu(^{13}\mathrm{CH})$ =1.46 Debye (Pickett et al. 1998).

Table 5.1: Spectroscopic parameters for the $N, J = 2, 3/2 \rightarrow 1, 1/2$ hyperfine structure transitions of ^{13}CH . Taken from Davidson et al. (2004).

Parity	Transition $F_1', F' \rightarrow F_1'', F''$	Frequency [GHz]	S	$A_{\mathrm{E}} \times 10^{-3}$ [s^{-1}]
$+ \rightarrow -$	$1, 3/2 \rightarrow 0, 1/2$	1997.4232	0.3331	1.1458
	$1, 3/2 \rightarrow 1, 3/2$	1997.4464	0.1666	0.5731
	$2, 5/2 \rightarrow 1, 3/2$	1997.4437	0.8327	1.9096
$- \rightarrow +$	$1, 3/2 \rightarrow 0, 1/2$	2001.5672	0.3345	1.1577
	$1, 3/2 \rightarrow 1, 3/2$	2001.2230	0.1673	0.5787
	$2, 5/2 \rightarrow 1, 3/2$	2001.3673	0.8365	1.9296

5.3 Observations

Using the upGREAT instrument[2] (Risacher et al. 2016) on board SOFIA (Young et al. 2012), we observed the $^2\Pi_{1/2}\, N, J = 2, 3/2 \rightarrow 1, 1/2$ Λ-doublet transitions of ^{13}CH over several flight series as a part of the observatory's cycle 7 campaign (under the open time project 07_0148 supplemented by guaranteed time observations). In this pilot study we carried out observations towards five well-known SFRs Sgr B2(M), G34.26+0.15, W49(N), W51E, and W3(OH). Because so far, ^{13}CH has never been detected in the ISM before, the primary source selection criterion was the existence of a strong sub-millimetre and FIR background continuum. Secondly, we selected sources that are almost evenly spaced in galactocentric distance between the GC and the solar circle in order to obtain quantitative constraints on the Galactic ^{12}C/^{13}C abundance ratio gradient. Observational properties of the different sources are summarised in Tab. 5.2. The receiver configuration comprises the (7+7) pixel low-frequency array (LFA) receiver module of upGREAT in dual polarisation. Only data from the central pixels were used because the continuum targets are unresolved in our 13.5″ full width at half maximum (FWHM) beam (scaled with frequency from the nominal 14.1″ beam width at the [CII] 158 μm line).

The spectra were taken in the double-beam switch mode, chopping at a frequency of 2.5 Hz with a chop throw between 210″ and 240″ and a chop angle of 90° (counter-clockwise against north) to account for atmospheric fluctuations and fluctuations that may arise from the instrument. The receiver was connected to an evolved version of the MPIfR fast Fourier transform spectrometer described by Klein et al. (2012). This backend provides 4 GHz bandwidth per pixel and a velocity resolution of 0.036 km s^{-1} (~244.1 kHz) over 16384 channels. In this detection experiment, the double-sideband (DSB) receiver was tuned to 1997.4437 GHz (the strongest HFS transition of the 1997 GHz Λ-doublet) in the lower sideband. Three different intermediate-frequency (IF) settings were used in our observations in order to distinguish any contamination present in the bandpass towards all sources except for W3(OH), towards which we used only a single IF setting at 1.45 GHz in our pilot search. For G34.26+0.15, W49(N), and W51E, the IF was tuned to 1.2, 1.4, and 1.6 GHz, while for Sgr B2(M), the IF was tuned to 1.4, 1.6, and 1.8 GHz. The ^{13}CH spectra obtained along the LOSs to Sgr B2(M), G34.26+0.15, W49(N), and W51E taken with each of the three IF settings are displayed in Appendix. C.1.

[2]The German REceiver for Astronomy at Terahertz frequencies (GREAT) is a development by the MPI für Radioastronomie and the KOSMA/Universität zu Köln, in cooperation with the DLR Institut für Optische Sensorsysteme.

Table 5.2: Continuum source parameters.

Source	α(J2000) [h:m:s]	δ(J2000) [° :′:″]	$\upsilon_{\rm LSR}$ [kms^{-1}]	$T_{\rm c}$ [K]	$R_{\rm GC}$ [kpc]	D [kpc]	Flight Id	$t_{\rm obs}^{(a)}$ [mins]
Sgr B2(M)	17:47:20.49	-28:23:06.00	65.2(0.6)	14.6	0.1	8.3	2019/06/10(F579)	51
							2019/06/11(F580)	101
W51E	19:23:43.90	+14:30:30.50	63.0(1.6)	9.4	6.3	5.4	2019/12/11(F646)	90
G34.26+0.15	18:53:18.49	+01:14:58.70	58.0(0.7)	8.6	7.0	1.6	2020/03/07(F669)	126
							2020/03/11(F671)	85
W49(N)	19:10:13.20	+09:06:11.88	11.8(0.4)	13.8	7.8	11.4	2020/03/05(F667)	80
							2020/03/10(F670)	55
							2020/03/12(F673)	135
							2020/03/13(F674)	57
W3(OH)	02:27:04.10	+61:52:22.00	-46.0(0.2)	5.3	10.0	2.0	2018/11/21(F529)	117
							2018/12/04(F533)	53

Notes: Columns are from left to right, the source designation, equatorial coordinates, LSR velocity, signal band continuum brightness temperature derived by means of a DSB calibration, galactocentric distance, heliocentric distance, flight id, and flight leg duration. $^{(a)}$ The observing leg time ($t_{\rm obs}$) refers to the total duration of time for which the source was observed. This includes the total (on+off) observing time as well as the overheads, which in total is typically a factor of two larger than the (on+off) time. References for the heliocentric distances: Sgr B2(M): Reid et al. (2014); W51E: Sato et al. (2010); G34.26+0.15: Zhang et al. (2009); W49(N): Zhang et al. (2013); W3(OH): Xu et al. (2006);

The spectra were further calibrated using the KALIBRATE program (Guan et al. 2012) and a forward efficiency of 0.97. Fluctuations of the continuum level can either be due to telescope-tracking problems or due to gain drifts in the mixers. From a comparison between the continuum fluxes in the high-frequency array, operated in parallel at 4.7 THz and offering a 6″ FWHM beam, we can rule out the former (which even if they occurred would not affect the line-to-continuum ratio). Gain drifts that are faster than the calibration rate, however, affect the measurement of the atmospheric total power and therefore the applied transmission correction. Because they potentially distort the line-to-continuum ratio, a new calibration strategy was applied to analyse the gain fluctuations of the GREAT receiver, thanks to the larger amount of data now available. In a first step, the most stable off-centre pixels were identified by monitoring the line areas of a simultaneously observed narrow telluric ozone line, which is largely insensitive to baseline uncertainties. Because the atmospheric emission arises in the near-field of all pixels, they must all see the same ozone line flux. From this correlation analysis, only the pixel pairs whose line flux ratios were persistently close to unity were retained to determine the atmospheric transmission correction. The quality of the correlation analysis was ensured by forming closure products of the gain ratios, including those of the central pixel used (which for our case deviates from unity by 1.6% at most). In order to eliminate spectra in the central pixel that are affected by gain drifts, only data with closure products deviating from unity by 0.4% at most were retained to determine the continuum level. The DSB-continuum level was then determined by accounting for contributions from the signal and image bands, which was added back to the spectra to obtain the correct line-to-continuum ratio. This calibration technique was applied not only to the ^{13}CH data presented in this work, but also to the previously published ^{12}CH data (Wiesemeyer et al. 2018; Jacob et al. 2019), which thus were re-calibrated for use in our analysis to avoid any inconsistencies. For the ^{12}CH spectra, we note that the continuum levels derived using the closure products are compatible with those derived using the standard calibration methods, except for W49(N). Using the closure product analysis, we derived a continuum level of 14 K for the ^{12}CH spectrum towards W49(N) that agrees with the continuum level cited by Wiesemeyer et al. (2018) within a 20% uncertainty. It is to be noted that in the analysis that follows, we adopt a value of 14 K as the continuum level of the ^{12}CH spectrum towards W49(N).

Subsequently, the fully calibrated spectra obtained from the two polarisations of the central pixel were converted into a main-beam brightness temperature scale (using a main-beam efficiency of 0.66) and analysed using the GILDAS-CLASS software[3]. The spectra were box-smoothed to ∼1.1 km s^{-1} wide velocity bins, and the spectral baselines were corrected for by removing up to a second-order polynomial. The resulting spectra obtained after carrying out a simple sideband deconvolution (discussed in Appendix C.1) are displayed in Figures 5.2 and 5.3. On average, we achieved a noise level of ∼68 mK at a velocity resolution of 1.1 km s^{-1} after the sideband deconvolution. In the following paragraphs we briefly describe the LOS properties of the observed ^{13}CH spectra and compare them with previously obtained CH spectra.

[3]Software package developed by IRAM, see `https://www.iram.fr/IRAMFR/GILDAS/` for more information regarding GILDAS packages.

Sgr B2(M): The unwavering nature of the absorption feature at υ∼64 km s^{-1} observed towards the envelope of Sgr B2(M) in each of the different IF frequency settings and the detection of its image band Λ-doublet counterpart near 2001 GHz with the absorption features displaying their expected relative intensities solidifies our detection of ^{13}CH near 1997.44 GHz at this velocity. We compare the ^{13}CH spectrum with that of CH towards Sgr B2(M) published in Jacob et al. (2019). The CH spectrum has a true continuum of 15 K and is contaminated by C_3 absorption at 2004.833 GHz arising from the image band, as indicated by the blue box in Fig. 5.2. The similarities between the CH and ^{13}CH spectra suggest the presence of weak blue-shifted sight-line absorption features in addition to the deep absorption seen near 64 km s^{-1} corresponding to the systemic LSR velocity of the molecular cloud. The shift of the atmospheric ozone feature at 2002.347 GHz in the image band towards the signal band features, by 60 km s^{-1} with each 0.2 GHz IF offset, leads to uncertainties while fitting polynomial baselines, particularly for the weaker features. The true nature of the sight-line absorption features therefore remains uncertain because of calibration and baseline uncertainties for the broad blended features. We will follow this up in future observations.

G34.26+0.15: In order to avoid the blending of the atmospheric ozone feature from the image band with the signal band features, we used an IF setting of 1.2 GHz instead of 1.8 GHz. Similar to the ^{13}CH spectrum observed towards Sgr B2(M), we see absorption at the systemic velocity of the G34.26+0.15 molecular cloud at 58 km s^{-1} in all three IF settings. However, we do not clearly detect ^{13}CH in foreground gas at velocities between 0 and 50 km s^{-1}.

W49(N): We used a setup similar to what we used for our observations towards G34.26+0.15 for those toward W49(N). In addition to ^{13}CH absorption at the velocities corresponding to the velocity of the molecular cloud, we see a weaker absorption feature close to 65 km s^{-1}, associated with the far-side crossing of the Sagittarius spiral arm. However, we do not include this feature in the analysis that follows because of its low signal-to-noise ratio.

W51E: By choosing the 1.4 GHz IF tuning as the nominal setting for carrying out the DSB deconvolution, we observe ^{13}CH absorption at the source intrinsic velocity of W51E near ∼62 km s^{-1}. When we compare this with the corresponding ^{12}CH spectrum, which closely resembles that of the $^2\Pi_{3/2}, J = 3/2 \rightarrow 5/2$ SH line at 1383.2 GHz, between 43–80 km s^{-1} (Neufeld et al. 2015b), it is not clear whether ^{13}CH shows a second absorption component at 53 km s^{-1} at the given noise level. The weaker and narrower absorption seen at 26 km s^{-1} is merely a remnant feature from the image band.

Towards W3(OH) no ^{13}CH lines are detected above the noise (77 mK at a spectral resolution of 1.1 km s^{-1}) in the spectrum at a continuum level of 5.3 K. The baseline-subtracted CH and ^{13}CH spectra towards W3(OH) are displayed in Appendix C.5. The corresponding CH spectrum is taken from Wiesemeyer et al. (2018) and has a continuum level at 5.4 K, prior to baseline removal.

Additionally, we verified whether the ^{12}C/^{13}C ratios derived by us are consistent with values derived using archival HIFI/*Herschel* data of the $N, J = 1, 3/2 \rightarrow 1, 1/2$ transitions of CH and ^{13}CH near 532 GHz. While the 532 GHz CH line displays a deep absorption feature at the systemic velocity of the Sgr B2(M) molecular cloud with a peak temperature of 1.64 K (Qin et al. 2010), the corresponding ^{13}CH transition is not detected above a 3σ noise level of 0.33 K (at a spectral resolution of 0.5 km s^{-1}) and yields a lower limit of 5 on the ^{12}C/^{13}C isotopic

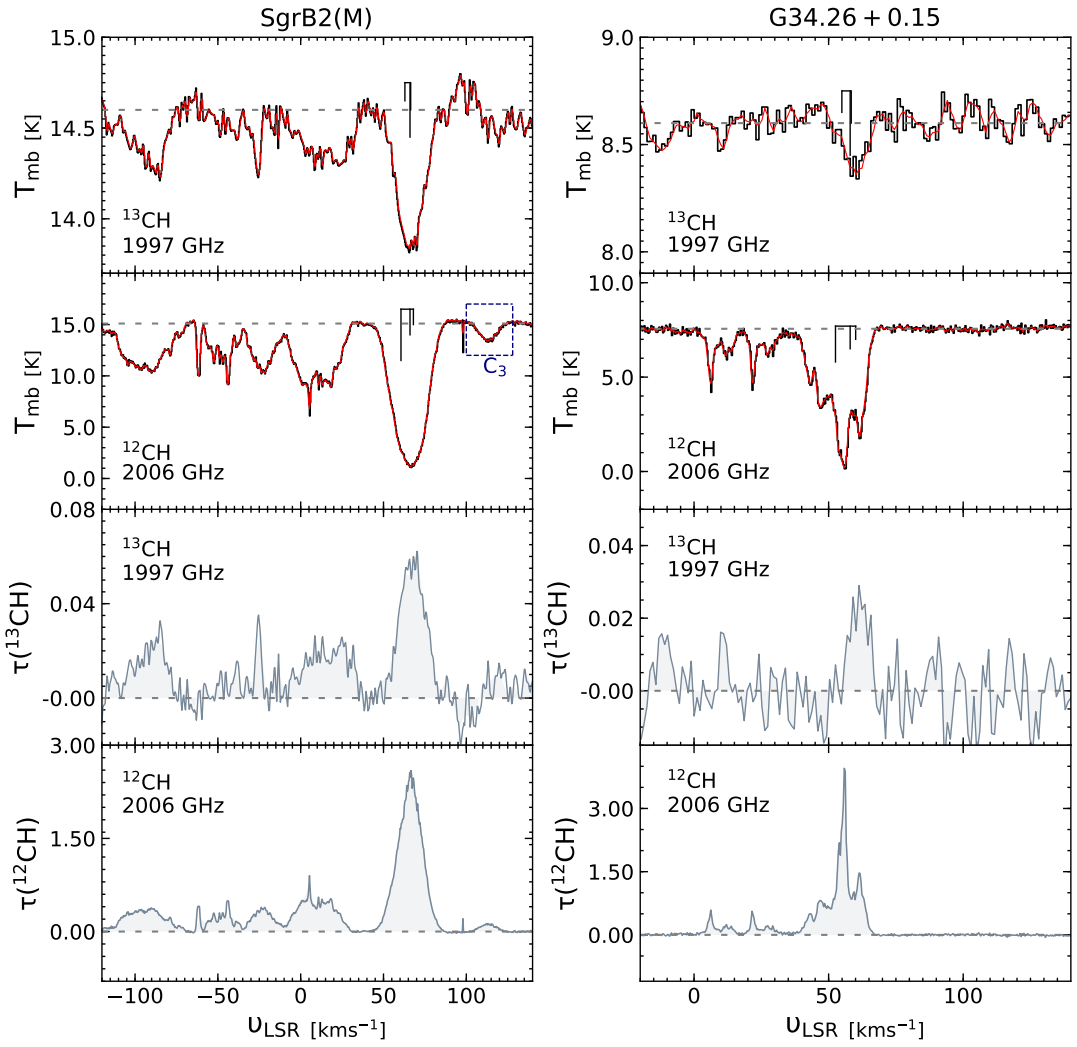

Figure 5.2: From top to bottom: $N, J = 2, 3/2 \rightarrow 1, 1/2$ transition spectra of ^{13}CH and CH near 1997 GHz and 2006 GHz, in black with their corresponding Wiener filter fits to the spectra overlaid in red towards Sgr B2(M) (*left*) and G34.26+0.15 (*right*). Followed by their Wiener filter deconvolved spectra displayed in grey in optical depth scales. The ^{12}CH spectrum towards Sgr B2(M) is contaminated by C_3 absorption at 2004.833 GHz in the image band, as indicated in blue.

ratio. Similarly, we analysed the 532 GHz CH spectra taken towards G34.26+0.15 discussed in Godard et al. (2012), W49(N) and W51E presented in Gerin et al. (2010), and W3(OH) from the *Herschel* archives[4] that also cover the corresponding ^{13}CH line frequencies. We find no signatures of ^{13}CH, and from the 3σ noise levels, we are only able to derive lower limits to the ^{12}C/^{13}C ratio of 13, 32, 17, and 68 for the above sources. We mention that in contrast to the 2 THz lines, in the 532 GHz line, the molecular cores associated with these massive SFRs

[4]See, `http://archives.esac.esa.int/hsa/whsa/`

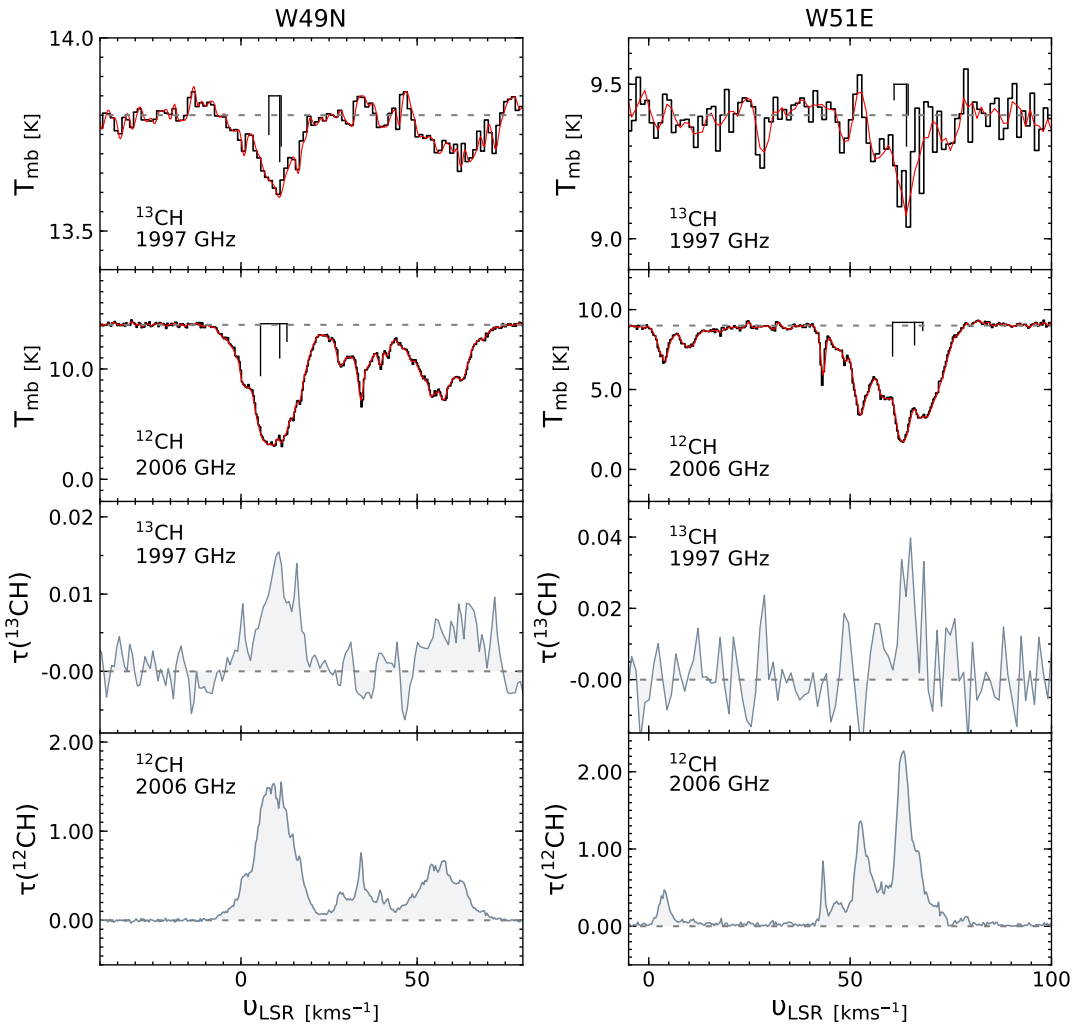

Figure 5.3: Same as Fig. 5.2, but towards W49(N) (*left*) and W51E (*right*).

show complex line profiles with both emission and absorption components. In addition, the intensities and profiles of the ^{13}CH lines are quite uncertain as their HIFI spectra are affected by a standing wave and an unknown (and not yet assessed) level of potential line contamination. Thus the formal lower limits for the ^{12}C/^{13}C ratio derived from archival HIFI/*Herschel* data quoted above should be regarded with some caution.

5.4 Analysis and discussion

High-resolution absorption line spectroscopy provides a powerful and straightforward to use tool for measuring column densities. The optical depth, τ, for a single absorption component can be calculated from the line to continuum ratio using

$$\tau = -\ln\left(T_l/T_c\right) , \tag{5.4}$$

where T_l and T_c represent the observed brightness temperatures of the line (prior to continuum subtraction) and the continuum, respectively. We determined the optical depth profile, that is, τ versus υ_LSR, using the Wiener filter fitting technique as described in Jacob et al. (2019). This fitting procedure first fits the observed spectral profile by minimising the mean square error between the model and observations and then deconvolves the hyperfine structure from the observed spectrum using the relative weights of the HFS components. Other than the observed spectrum and the spectroscopic parameters of the line to be fit, the only other input parameter required by the Wiener filter technique is the spectral noise, which is assumed to be independent of the observed signal. The resulting deconvolved optical depth signature, τ_decon, can then be converted into column density values per velocity channel, i using

$$\left(\frac{\mathrm{d}N}{\mathrm{d}\upsilon}\right)_i = \frac{8\pi\nu_i^3}{c^3}\frac{Q_\mathrm{rot}}{g_\mathrm{u}A_\mathrm{E}}\exp\left(\frac{E_\mathrm{u}}{T_\mathrm{ex}}\right)\left[\exp\left(\frac{h\nu_i}{k_\mathrm{B}T_\mathrm{ex}}\right)-1\right]^{-1}(\tau_\mathrm{decon})_i\ , \tag{5.5}$$

where the spectroscopic parameters g_u (the upper level degeneracy), E_u (the upper level energy), and A_E (the Einstein A coefficient) remain constant for a given hyperfine transition. The partition function, Q, is itself a function of the rotation temperature, T_rot, which would be equal to the excitation temperature, T_ex, under conditions of local thermodynamic equilibrium (LTE). Typically, the rotational transitions of hydrides require high critical densities to be observable in emission. Because collisional rate coefficients are currently not available for ^{13}CH, we assumed the critical density of this ^{13}CH line to be identical to the critical density of the corresponding CH transition, assuming a two-level system. Using HFS resolved collisional rate coefficients computed by Dagdigian (2018b), we find the critical densities to be $\sim 2\times10^9$ cm^{-3} at 50–100 K. Within the diffuse and translucent interstellar clouds along the LOS (n = 10 − 500 cm^{-3}) and the envelope of Sgr B2(M) (ranging from $n\sim10^3$–10^5 cm^{-3}; (Schmiedeke et al. 2016)), the gas densities are much lower than the critical density, n_crit, of these transitions, making them sub-thermally excited. Hence we can assume the excitation temperature of such sub-thermally excited lines to be low and lower than the gas kinetic temperature. In our analysis we assume T_rot to be equal to the temperature of the cosmic microwave background (CMB) radiation, T_CMB = 2.728 K (Neill et al. 2014). Because of this low rotation temperature and the inefficiency of purely collisional excitation, almost all of the CH molecules will reside in the ground-state level of the molecule. However, in the SFRs, radiative excitation by FIR dust radiation can affect the level populations (see Neufeld et al. (1997) for the case of HF). Meaningful modelling of this is beyond the scope of the present study. In any case, because the ^{12}CH and ^{13}CH lines under consideration here have moderate and low optical depths, respectively, radiative excitation is expected to affect the observed transitions from both isotopologues in a similar way, leaving the ^{12}CH/^{13}CH intensity ratio unaltered.

With the knowledge of the frequency separation of the HFS transitions of ^{13}CH, we first deconvolved the hyperfine structure from the observed spectra using the Wiener filter formalism (briefly discussed above) and then derived column densities by adopting a T_ex value equal to T_CMB and integrating over the deconvolved velocity range of the line. We derive ^{13}CH column densities between $\sim2\times10^{12}$ and 4.6×10^{13} cm^{-2} towards the different sources. Given that the optical depths are computed directly from the line-to-continuum ratio, the uncertainties in the true continuum level give rise to systemic errors in the derived column densities. We assumed a 10% error in the continuum level calibration based on the

Table 5.3: Synopsis of the derived column densities and $^{12}C/^{13}C$ isotopic ratios.

Source	$v_{min} - v_{max}$	$N(^{13}CH)$	$N(^{12}CH)$	$^{12}C/^{13}C$	
	[km s^{-1}]	[10^{13} cm^{-2}]	[10^{13} cm^{-2}]	CH	CN$^{(a)}$
Sgr B2(M)	40 – 90	$4.61^{+0.70}_{-0.71}$	$73.02^{+0.60}_{-0.68}$	$15.8^{+02.4}_{-02.4}$	>12
W51E	45 – 75	$1\ .77^{+0.20}_{-0.26}$	$66.36^{+3.30}_{-4.21}$	$37.5^{+04.6}_{-06.1}$	35±12
G34.26+0.15	35 – 70	$0.20^{+0.01}_{-0.02}$	$9.38^{+0.78}_{-0.93}$	$47.0^{+04.5}_{-06.6}$	28±4
W49(N)	-5 – 25	$0.68^{+0.11}_{-0.09}$	$22.87^{+3.56}_{-3.72}$	$33.6^{+07.5}_{-07.0}$	44±22
W3(OH)	-55 – -38	<0.11$^{(b)}$	$6.58^{+0.72}_{-1.35}$	>58	63±16

Notes: $^{(a)}$ Values taken from Milam et al. (2005) and references therein. $^{(b)}$ The column density for the non-detection was derived using the 2σ rms of level.

instrumental performance (Kester et al. 2017) and sideband dependence of the atmospheric transmission. The subsequently derived errors in the column densities (per velocity interval) were computed following the description presented in Jacob et al. (2019) and scale with the deconvolved optical depths by a constant term comprised of the spectroscopic parameters that govern the transition and the excitation temperature. We compare the ^{13}CH column densities derived here, over velocity intervals associated with the different molecular clouds, with those of their corresponding $N, J = 2, 3/2 \rightarrow 1, 1/2$ hyperfine HFS transitions of CH near 2007 GHz discussed in Wiesemeyer et al. (2018) and Jacob et al. (2019). In Tab. 5.3 we present the derived ^{12}CH and ^{13}CH column densities using the same excitation conditions by adapting Eq. 5.5, as well as the resulting $^{12}C/^{13}C$ isotopic ratio. For W3(OH), towards which the ^{13}CH line remains undetected, we derive a 2σ lower limit on the $^{12}CH/^{13}CH$ abundance ratio of > 58 over the velocity interval between (-55 – -38) km s^{-1}.

The $^{12}C/^{13}C$ isotopic abundance ratio has been determined towards the GC region using a wide variety of molecules ranging from simple species such as CO, CN, H_2CO, and HCO^+ (Henkel et al. 1982; Langer & Penzias 1990; Savage et al. 2002) to more complex ones containing more than six atoms such as CH_3CH_2CN, CH_3CCH, CH_2CHCN, and NH_2CHO (Belloche et al. 2016; Halfen et al. 2017), to name a few. The relatively lower values of the $^{12}C/^{13}C$ isotopic ratio towards the GC in comparison to the inner Galaxy, the local ISM, and the Solar System bears evidence to its advanced state of chemical evolution and reflects on its unique nucleosynthesis history. Moreover, the value of the GC strongly pivots the derived Galactic gradient. Therefore, as discussed by Halfen et al. (2017), it is essential to obtain more accurate measurements of the $^{12}C/^{13}C$ ratio towards the GC region because several of the derived molecular isotopic ratios can be hindered by effects of optical depth and saturation, chemical fractionation, and selective photo-dissociation. The limits on the $^{12}C/^{13}C$ isotopic ratio derived using CH are consistent with those derived by Savage et al. (2002) using CN for our sample of sources except for G34.26+0.15. The latter difference could be due to difficulties in deriving the ^{12}CN optical depth (i.e. an underestimation of the column density) because, as the authors of the above study state, the observed relative line intensity ratios of the HFS components does not follow LTE. The comparable isotopic compositions of the two molecular species stems from their inter-linked formation routes, as the neutral-neutral reaction between CH and N forms one of the main formation pathways for the production of CN (CH + N $\rightarrow$

CN + H) with a forward-reaction rate of $\sim 6.7 \times 10^{-11}$ cm^3 s^{-1} for a temperature of 50 K. This suggests that CH similar to CN shows negligible amounts of fractionation. Furthermore, Halfen et al. (2017) estimated ^{12}C/^{13}C isotopic ratios between 19 and 33 using several different complex organic species and an average value of $\sim 24 \pm 9$ towards the 64 km s^{-1} component of the GC source Sgr B2(N). Within the errors, the average ^{12}C/^{13}C isotopic ratio derived by these authors is also consistent with the values derived from CH and CN. This presents solid evidence that the ^{13}C isotopic enrichment in more complex molecules must arise from progenitor molecules such as CH and CN because the ^{13}C substitution of complex species by simple ion-molecule exchange reactions is not as straightforward as that of simple molecules.

In general, almost all the PDR models studied by Röllig & Ossenkopf (2013) with varying physical parameters display a ^{12}CH/^{13}CH fractionation ratio that is enhanced at higher values of $A_v (\geq 1)$. The degree of fractionation is coupled with the FUV flux present in the models; the weaker the FUV flux, the higher the fractionation ratio. The ^{12}C/^{13}C isotopic ratios we derive from CH show no indication of an enhanced value in comparison to those derived from for CN, for example, as shown in Tab. 5.3 and therefore no signature of fractionation. This is because towards the SFRs towards which we detect both ^{12}CH and ^{13}CH, the absorption from both isotopologues primarily traces the extended envelopes of these regions, which are exposed to a significant UV field and whose densities have been estimated to be about 10^3 cm^{-3} on parsec scales for Sgr B2(M) and other regions (Schmiedeke et al. 2016; Wyrowski et al. 2016). This value is typical for translucent molecular clouds. The gas-phase carbon reservoir in such regions is predominantly in either its atomic or ionised form and not locked up in CO, which means that there is enough ^{13}C and ^{13}C$^+$ present for ion-molecule exchange reactions to form ^{13}C-substituted CH.

The previously determined ^{12}C/^{13}C isotopic ratios suffer from large error bars that may either be due to opacity effects in the main isotopologue or due to other systematic effects. Therefore it is not clear whether the high dispersion in values between galactocentric radii of 4 to 8 kpc, corresponding to regions with the most molecular mass content in the Milky Way (except for the GC region), are due to actual cloud-cloud variations. If the spread is indeed due to opacity effects, then the ground-state rotational transitions of CH studied in this work, which are free from such effects, should be well suited to quantitatively constrain the ^{12}C/^{13}C ratio. By combining the ^{12}C/^{13}C ratio values derived using CH with those derived by Henkel et al. (1985), Langer & Penzias (1990), Wouterloot & Brand (1996)[5], Milam et al. (2005), Giannetti et al. (2014), Ritchey et al. (2011), Halfen et al. (2017), and Yan et al. (2019) and carrying out a weighted least-squares fit see Fig. 5.4), we derive a revised ^{12}C/^{13}C Galactic gradient of $^{12}\mathrm{C}/^{13}\mathrm{C} = 5.87(0.45)\, R_{\mathrm{GC}} + 13.25(2.94)$, where the values in parentheses represent 1σ uncertainties. The addition of our CH data points plus those from Wouterloot & Brand (1996), Ritchey et al. (2011), Giannetti et al. (2014) and Yan et al. (2019) result in values for the best-fit slope and intercept that are within the combined uncertainties consistent with the values derived by Halfen et al. (2017). The small uncertainties of the CH data result in somewhat smaller formal uncertainties of the fitted values.

[5]The authors of the cited article note that the discrepancy between the higher ratio derived form the $J = 1 - 0$ lines of ^{12}C^{18}O and ^{13}C^{18}O to the lower value from the $J = 2 - 1$ lines "is not yet explained, but may be due to the emission of the two transitions originating in different parts of the cloud with different excitation conditions."

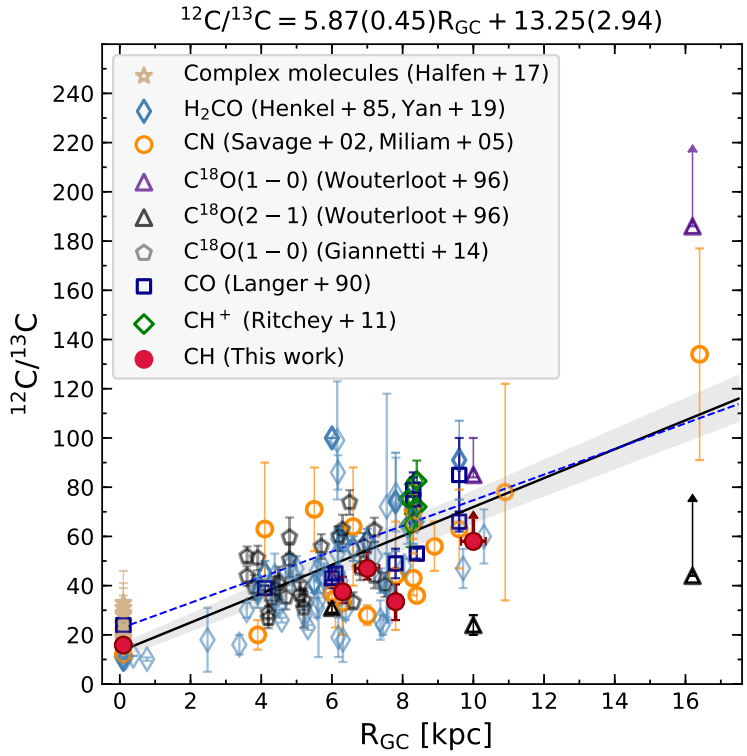

Figure 5.4: Plot of $^{12}C/^{13}C$ isotope ratios as a function of galactocentric distance, R_{GC} (kpc). The filled red circles represent the $^{12}C/^{13}C$ ratio obtained using CH (this paper), while the empty black and purple triangles, grey pentagons, yellow circles, dark blue squares, and green, light blue diamonds and tan stars are those obtained using isotopologues of $C^{18}O$ ($J = 1 - 0$ and $J = 2 - 1$ transitions) (Wouterloot & Brand 1996; Giannetti et al. 2014), CN (Savage et al. 2002; Milam et al. 2005), CO (Langer & Penzias 1990), CH^+ (Ritchey et al. 2011), H_2CO (Henkel et al. 1985; Yan et al. 2019), and complex organic molecules (Halfen et al. 2017), respectively. The black solid line represents the weighted fit to the data, and the grey shaded region demarcates the 1σ interval of this fit. For comparison, the fit obtained by Halfen et al. (2017) is displayed by the dashed blue line.

5.5 Conclusions

We reported the first detections of ^{13}CH in the ISM, namely towards the Sgr B2(M), G34.26+0.15, W49(N), and W51E massive SFRs in the Milky Way. Hyperfine structure transitions connecting sub-levels of the ^{13}CH $N, J = 2, 1/2$ and $1, 1/2$ Λ-doublet states with frequencies near 1997 GHz were observed in absorption using GREAT/SOFIA, which provides an avenue to observe frequency bands for which spectrally resolved observations were previously not possible with HIFI/*Herschel* or earlier missions. The detection of ^{13}CH along with observations of the main isotopologue CH towards the same sources opens a new, independent way for determinations of the $^{12}C/^{13}C$ isotopic abundance ratio across the Galaxy. We derive $^{12}C/^{13}C$ isotopic ratios for those of our target sources with a ^{13}CH detection and a lower limit for

W3(OH) towards which we did not detect this isotopologue. Our values agree with previous determinations made using varied chemical species and in particular CN. Our observations do not indicate a possible enhancement in the ^{12}C/^{13}C ratio derived from CH as it traces the more diffuse and translucent regions of the ISM in which CO is not the main reservoir of carbon. Furthermore, as its abundance peaks in regions of high UV radiation, CH is relatively unaffected by selective photo-dissociation and optical depth effects such as saturation. Hence, measurements of the ^{12}C/^{13}C isotopic ratio based on the fundamental rotational lines of CH potentially reflect the actual ^{12}C/^{13}C ratio in the gas.

In addition, knowledge of the ^{13}C substitution in CH will improve our understanding of interstellar chemistry because direct substitution of ^{13}C in more complex species is currently poorly understood and their observed $^{12/13}$C isotopologue ratios are speculated to originate in simpler precursors such as CH. Investigating a larger sample of SFRs at different galactocentric radii for ^{13}CH will allow for a better constraint on the average ^{12}C/^{13}C abundance ratio value in the ISM and on the Galactic ^{12}C/^{13}C gradient, facilitating accurate Galactic chemical evolution models. However, the requirement of very high signal-to-noise ratios at high spectral resolutions that are required to detect the weak ^{13}CH absorption lines greatly restricts the selection of sources to those with strong continuum backgrounds for carrying out future follow-up studies. Furthermore, we hope that our study will encourage coordinated laboratory efforts resulting in refinements of the spectroscopic parameters of ^{13}CH, for which several of the constants describing the fine structure of its transitions, for instance, are not well established yet (Halfen et al. 2008).

5.6 Prospects: The search for deuterated methylidene

Taking advantage of the new access in the sub-mm and FIR regimes provided by SOFIA, we have extended the search for CH isotopologues toward deuterated methylidene, CD, as well. Since deuterium was produced in substantial amounts only by big-bang nucleosynthesis, and its abundance since then only reduced by deuterium burning in stars, the [D]/[H] ratio is an important cosmological parameter (Planck Collaboration et al. 2020) and the primordial [D]/[H] has recently been accurately determined as $2.53 \pm 0.03 \times 10^{-5}$ (Cooke et al. 2018). Moreover, investigating the deuterium abundance our solar system, including the Ealth's oceans, can constrain its chemical history. Our search for the $N, J = 2, 3/2 \rightarrow 1, 1/2$ transition of CD at 1325 GHz towards W49 N was unsuccessful and we report an upper limit of $2.82{\times}10^{-2}$ for the resulting [CD]/[CH] column density ratio. This ratio is calculated for the known velocity of absoption for this source at a 3 σ level (1σ=105 mK). The successful discovery of CD towards W49 N would have allowed for a meaningful comparison with the OD and the [OD]/[OH] ratio.

While deuteration has been extensively observed and studied in ions and other saturated and complex molecules there is very little known about the deuterium fractionation in radicals or hydrides. Observations of the deuterium fractionation in hydrides, promise to lend useful constraints on the deuteration and formation pathways of larger species which are formed from them. Deuterium substituted hydrides similar to their hydride counterparts have fundamental

rotational transitions that lie at sub-mm and FIR wavelengths. In recent years this promise has been explored with the detection of ND (Bacmann et al. 2010), and OD (Parise et al. 2012) made using the *Herschel* Space Observatory (HSO), and the SOFIA telescope, respectively, towards the low-mass protostar IRAS 16293−2422. Both studies were aimed at understanding the formation of NH_3 and H_2O, respectively, through the deuterium fractionation present in their progenitor/chemically associated species, like, NH and OH. IRAS 16293−2422, with a rich sub-mm spectrum and notably high degree of deuterium fractionation, as established by previous observations of deuterated species like HDO (Persson et al. 2013) towards it, was previously targeted to search for CD- deuterium substituted CH by Bottinelli et al. (2014). However, their search for the $N, J = 2, 3/2 \rightarrow 1, 3/2$ and $N, J = 2, 5/2 \rightarrow 1, 3/2$ transitions of CD near 885 GHz and 916 GHz, using the HSO were unsuccessful. And so for now, CD still remains undetected in the interstellar medium.

Part III

The elusive methylene radical

Chapter 6

Hunting for the elusive methylene radical

... of course the spectrum of CH_2 has given me a great deal of pleasure ...

Gerhard Herzberg, Nobel Prize in Chemistry, 1971

Overview

Herzberg (1990) assigned the observed absorption bands near 1414.5 Å as arising due to CH_2, based on the laboratory production of the absorption spectrum of flash-photolyzed diazomethane (see Fig. 6.1). The rightful laboratory identification of CH_2 as being responsible for the 1414 Å band and not the so-called λ4050 group in cometary spectra as previously speculated (Herzberg 1942), was, as Herzberg would later recollect one of the two discoveries in his illustrious career that stands out because it gave him a good deal of satisfaction. In search of a similarly satisfying explanation for the source of its emission, in this chapter we discuss our hunt for the elusive CH_2 radical in an astronomical setting. The contents of this chapter will be published in *Astronomy & Astrophysics* as a paper titled, 'Hunting for the elusive methylene radical', Jacob et al. (2021)[1], with only minor modifications made in order to adapt it to the layout of this thesis.

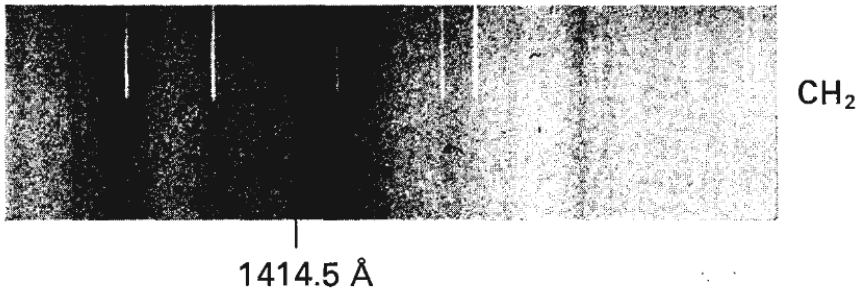

Figure 6.1: Laboratory identification of CH_2 (Herzberg 1990).

The $N_{K_aK_c} = 4_{04} - 3_{13}$ transitions of ortho-CH_2 between 68 and 71 GHz were first detected toward the Orion-KL and W51 Main star-forming regions. Given their high upper level energies (225 K) above the ground state, they were naturally thought to arise in dense, hot

[1]Jacob et al. A&A, in press, 2021, reproduced with permission ©ESO

molecular cores near newly formed stars. However, this has not been confirmed by further observations of these lines and their origin has remained unclear. Generally, there is a scarcity of observational data for CH_2 and, while it is an important compound in the astrochemical context, its actual occurrence in astronomical sources is poorly constrained. In this chapter, we aim to investigate the nature of the elusive CH_2 emission, address its association with hot cores, and examine alternative possibilities for its origin. Owing to its importance in carbon chemistry, we also extend the search for CH_2 lines by observing an assortment of regions, guided by the hypothesis that the observed CH_2 emission is likely to arise from the hot gas environment of photodissociation regions (PDRs). We carried out our observations first using the Kitt Peak 12 m telescope to verify the original detection of CH_2 toward different positions in the central region of the Orion Molecular Cloud 1. These were followed-up by deep integrations using the higher angular resolution of the Onsala 20 m telescope. We also searched for the $N_{K_aK_c} = 2_{12} - 3_{03}$ transitions of para-CH_2 between 440–445 GHz toward the Orion giant molecular cloud complex using the APEX 12 m telescope. We also obtained auxiliary data for carbon recombination lines with the Effelsberg 100 m telescope and employing archival far infrared data. The present study, along with other recent observations of the Orion region reported here, rule out the possibility of an association with gas that is both hot and dense. We find that the distribution of the CH_2 emission closely follows that of the [CII] 158 μm emission, while CH_2 is undetected toward the hot core itself. The observations suggest, rather, that its extended emission arises from hot but dilute layers of PDRs and not from the denser parts of such regions as in the case of the Orion Bar. This hypothesis was corroborated by comparisons of the observed CH_2 line profiles with those of carbon radio recombination lines (CRRLs), which are well-known PDR tracers. In addition, we report the detection of the 70 GHz fine- and hyperfine structure components of ortho-CH_2 toward the W51 E, W51 M, W51 N, W49 N, W43, W75 N, DR21, and S140 star-forming regions, and three of the $N_{K_aK_c} = 4_{04} - 3_{13}$ fine- and hyperfine structure transitions between 68-71 GHz toward W3 IRS5. While we have no information on the spatial distribution of CH_2 in these regions, aside from that in W51, we again see a correspondence between the profiles of CH_2 lines and those of CRRLs. We see a stronger CH_2 emission toward the extended HII region W51 M rather than toward the much more massive and denser W51 E and N regions, which strongly supports the origin of CH_2 in extended dilute gas. We also report the non-detection of the $2_{12} - 3_{03}$ transitions of para-CH_2 toward Orion. Furthermore, using a non-LTE radiative transfer analysis, we can constrain the gas temperatures and H_2 density to (163 ± 26) K and $(3.4 \pm 0.3) \times 10^3$ cm^{-3}, respectively, for the 68–71 GHz ortho-CH_2 transitions toward W3 IRS5, for which we have a data set of the highest quality. This analysis confirms our hypothesis that CH_2 originates in warm and dilute PDR layers. Our analysis suggests that for the excitation conditions under the physical conditions that prevail in such an environment, these lines are masering, with weak level inversion. The resulting amplification of the lines' spontaneous emission greatly aids in their detection.

6.1 Introduction

The methylene radical, CH_2, is of considerable astrophysical interest given that it is both produced and destroyed at an early stage in the sequence of ion-molecule reactions that govern interstellar chemistry (see Godard et al. 2014, and references therein). Theoretical models of the diffuse interstellar clouds in the line of sight (LOS) toward ζ Per by Black et al. (1978) and van Dishoeck & Black (1986) as well as equilibrium models of dense clouds in Orion by Prasad & Huntress (1980) have predicted CH_2 to possess abundances similar to, if not greater than, that of CH. Both species are primarily formed by the dissociative recombination of the methyl ion CH_3^+ with an electron and both are destroyed in dense clouds via reactions with atomic oxygen to form HCO and HCO^+, which are chemical species that act as building blocks for more complex interstellar molecules. Vejby-Christensen et al. (1997) computed the complete branching ratios of the different possible reaction products of the dissociative recombination reaction of CH_3^+ and found that CH_2 was the major reaction product with a branching ratio of 40%. Additionally, CH_2 has been speculated to play an important role in the photo-dissociation sequence of methane (CH_4) in cometary ice mantles (van Dishoeck et al. 1996). Despite its importance and large predicted abundances, CH_2 is yet to be detected in comets and only a handful of detections have been made in the interstellar medium (ISM), unlike the ubiquitous CH.

Even laboratory measurements of this simple radical have proven to be difficult owing to its reactive nature and to its lightness and peculiar b-type selection-rules (Michael et al. 2003; Brünken et al. 2004). The latter two characteristics result in widely spaced energy levels particularly between the energetically lowest rotational states of CH_2. With only four rotational transitions below 1000 GHz (as shown in Fig. 6.2), the rotational transitions of CH_2 are difficult to target in the laboratory, and even more so with astronomical observations, as they are either inaccessible from the ground or lie close to the edges of atmospheric windows.

CH_2 was first unambiguously detected in the ISM by Hollis et al. (1995) who identified the intrinsically strongest fine- and hyperfine-structure (HFS) transitions of the $N_{K_aK_c} = 4_{04} - 3_{13}$ multiplet of ortho-CH_2. The frequencies of the detected lines lie in the 68–71 GHz spectral range ($\approx$4.3 mm), not far from the high frequency edge of the absorption band from atmospheric O_2, which effectively demarcates the radio- from the millimetre wavelength range. Their detections became possible after accurate frequencies had been measured in the laboratory by Lovas et al. (1983). These transitions arise from levels with energies of $\sim$ 225 K above the ground state and were observed in emission toward the dense molecular 'hot cores' associated with the Kleinmann-Low Nebula in Orion Molecular Cloud 1 (Orion-KL) and W51 Main.

Following this work, several other astronomical searches for CH_2 have been published, but Lyu et al. (2001) reported the tentative detection of several of the electronic bands of CH_2 near 1410 and 1416 Å toward HD 154368 and ζ Oph in absorption. However, recently Welty et al. (2020) were only able to publish an upper limit for CH_2 absorption near 1397 Å from the relatively dense molecular core of the translucent interstellar cloud in the LOS to HD 62542. Their upper limits on the CH_2 column density are six and three times lower, respectively, than the nominal values given by Lyu et al. (2001) for HD 154368 and ζ Oph.

A breakthrough came with the detection of far-infrared (FIR) absorption lines from low-lying energy levels of both of CH_2's spin isomeric forms, the ortho- and para-CH_2, which were

discovered toward the intense dust continuum emission of the SgrB2 (M) and W49 N high-mass star-forming regions (SFRs) by Polehampton et al. (2005) from the data taken with the Long Wavelength Spectrometer (LWS, Clegg et al. 1996) aboard the Infrared Space Observatory (ISO); see also Polehampton et al. (2007). Absorption was not only found at the systemic LSR velocities of the SFRs, but also at the velocities of diffuse and translucent interstellar clouds intervening along the lines of sight. These detections were enabled by accurate frequency measurements provided by the Cologne molecular spectroscopy laboratory and astrophysics group (Brünken et al. 2004). These supra-terahertz absorption lines not only represent the first detection of CH_2 in low excitation states, but they also yield reliable total CH_2 column densities, $N(CH_2)$, of $(7.5 \pm 1.1) \times 10^{14}$ cm^{-2}, which are consistent with chemical model predictions for diffuse clouds.

In this paper, we report the detection of the $N_{K_aK_c}$ =$4_{04} - 3_{13}$ transitions of CH_2 toward nine SFRs – seven of which CH_2 is detected for the first time and attempt to address questions regarding the origin of its emission. In addition, we also report the non-detection of the para-CH_2, $N_{K_aK_c} = 3_{03} - 2_{12}$ transitions between 440–445 GHz toward the Orion molecular cloud, which were observed with the Atacama Pathfinder Experiment (APEX) 12 m sub-millimetre telescope.

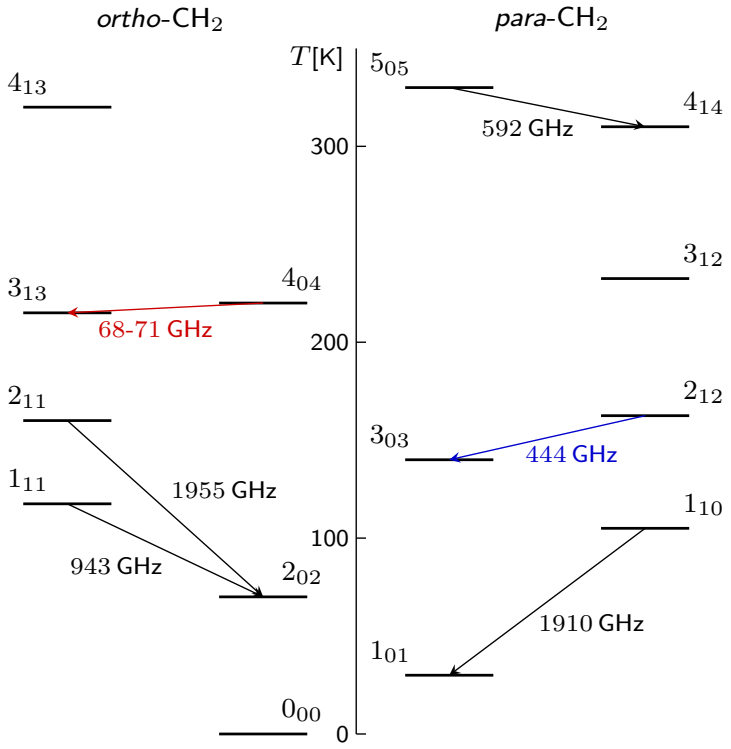

Figure 6.2: Ground state rotational energy level diagram of ortho-, and para-CH_2 up to an energy of 350 K, adapted from Brünken et al. (2004). Transitions measured in the laboratory are labelled with their respective transitions indicated by arrows. Highlighted in red and blue are the transitions that are discussed in this paper. The corresponding fine- and hyperfine structure transitions are not depicted here as they would not be visible on this scale.

6.2 CH_2 spectroscopy

For CH_2 ($^3B_1$), which has a spin angular momentum, S, of unity, a state with rigid body angular momentum quantum number, N, splits into three levels with the total angular momentum quantum numbers, J, which have values of $N + 1$, N, or $N - 1$. Each of these rotational levels ($N_{K_aK_c}$ displayed in Fig. 6.2) splits into three fine-structure levels due to spin-spin and spin-rotation interactions. Furthermore, CH_2 contains two identical protons, each with a nuclear spin, $I_H = 1/2$, and, consequently, has two nuclear-spin isomers: ortho ($I_{tot} = 1$) and para ($I_{tot} = 0$). With a total hydrogenic nuclear spin I_{tot} of unity, each of the three fine-structure levels of ortho-CH_2 further splits into three hyperfine structure (HFS) levels with total angular quantum number, F, of $J - 1$, J, and $J + 1$ for $J \neq 0$, while para-CH_2 states with $I_{tot} = 0$ do not have any HFS splitting.

6.3 Ortho-CH_2 emission at 4.3 mm – summary of previous results

The $4_{04} - 3_{13}$ rotational transitions of ortho-CH_2 lie in a rarely observed spectral window, close to the 53–66 GHz atmospheric O_2 band and comprise three main fine-structure components $J = 5 \rightarrow 4, 4 \rightarrow 3$, and $3 \rightarrow 2$ at 68.37, 70.68, and 69.01 GHz, respectively (which show additional HFS splitting). The corresponding frequencies and spectroscopic parameters of all the studied HFS transitions are summarised in Table 6.1. In addition to the HFS lines listed, with regard to the ortho-CH_2 rotational transitions, for every $J \rightarrow J-1$ fine structure transition, there is an additional pair of HFS lines with $\Delta F = 0$. The Einstein A-coefficients for these lines are smaller than those of the lines listed in Table 6.1 with $\Delta F = \Delta J = 1$ by factors between ≈ 5 and 30[2]. While these lines were covered in our band pass, none were detected; for root mean square (rms) noise levels, see Appendix D.1. Detected thus far in emission toward hot cores, the fine-structure lines of o-CH_2 and their corresponding HFS lines tabulated in Table 6.1 are naively expected to be weakly populated given the physical conditions that prevail in these regions. Intrigued by the fact that these transitions are observed in emission, Dagdigian (2018b) carried out simple non-LTE radiative transfer calculations using the one-dimensional escape probability code, RADEX (van der Tak et al. 2007). The negative excitation temperatures that they obtained suggest that the 4_{04} energy level is selectively enhanced by population inversion and that all three fine-structure transitions show weak maser emission. However, questions regarding the source of their emission or the association of these lines with the hot cores could not be definitively answered.

The Orion Kleinmann-Low (KL) nebula, one of the two regions in which Hollis et al. (1995) first detected ortho-CH_2 (hereafter o-CH_2), is the densest part of Orion Molecular Cloud 1 (OMC-1). In itself, it is a highly complex region, which encompasses: (1) the eponymous 'hot core', that is, a compact and very dense, hot >120 K) region that is surrounded by more extended dense molecular gas; (2) Orion South (here, Orion S), another hot core that, in contrast to the more famous one in KL (Zapata et al. 2011), harbours an embedded young stellar object (YSO) that was first identified as the NH_3 emission peak S6 (Batria et al. 1983) and by SiO

[2]The CDMS contains a full listing of the CH_2 transitions under: `https://cdms.astro.uni-koeln.de/cgi-bin/cdmssearch?file=c014501.cat`

Table 6.1: Spectroscopic parameters of the rotational transitions of CH_2 studied in this work.

Transition		Frequency	A_E	S_{ij}	E_u
$J' - J''$	$F' - F''$	[MHz]	1×10^{-6}[s^{-1}]		[K]
$N_{K_aK_c} = 2_{12} - 3_{03}$ (para-CH_2)					
3-4	–	444825.666	59.8	0.928	155.97
2-3	–	439960.991	64.3	1.353	156.27
1-2	–	444913.930	70.1	0.631	155.85
$N_{K_aK_c} = 4_{04} - 3_{13}$ (ortho-CH_2)					
5-4	6-5	68371.278	0.216	2.329	
	5-4	(**)68375.875	0.208	1.892	224.22
	4-3	68380.873	0.206	1.533	
4-3	3-2	70678.633	0.214	1.077	
	4-3	(**)70679.543	0.210	1.413	224.76
	5-4	70680.720	0.223	1.842	
3-2	2-1	69007.179	0.171	0.691	
	3-2	(**)69014.202	0.181	1.023	224.15
	4-3	69019.187	0.204	1.480	

Notes: The spectroscopic data - frequencies, Einstein *A*-coefficients (A_E) and line strengths (S_{ij}) were taken from Ozeki & Saito (1995) and the Cologne Database for Molecular Spectroscopy (Müller et al. 2005).**Indicates the central HFS transition, which was used to set the velocity scale in the analysis.

emission, indicating outflow activity (Ziurys & Friberg 1987), which conclusively proves the presence of an embedded YSO, probably of intermediate mass. In a complex arrangement, Orion S lies in front of an extension of the HII region and the photodissociation region (PDR) associated with the Orion Nebula (M42) (Mangum et al. 1993); (3) A high density part of this PDR presents the prominent Orion Bar (Walmsley et al. 2000). To make things complicated, the o-CH_2 spectra toward Orion-KL obtained by Hollis et al. (1995) using the NRAO[3] Kitt Peak (KP) 12 m radio telescope in Arizona, with a full width at half maximum (FWHM) beam width of 86″, covers several of these components, leaving the origin of the observed CH_2 emission unclear. Given the high energies above the ground state of these lines' (upper-level energies of ≈224 K), it was a natural conclusion to attribute the hot core to the source of their emission in Orion, whose molecular material was known to be characterised by temperatures >120 K or even higher values (see Hermsen et al. 1985, and references therein.).

In a series of attempts to elucidate the location and size of the CH_2 emission in Orion, we compared the KP 12 m telescope results with data taken with two larger telescopes, namely, the Institut de Radioastronomie Millimétrique (IRAM) 30 m and the Green Bank telescope (GBT) operated by the NRAO. We scale the emission expected to be observed with the different telescopes by the inverse of the beam filling factor, that is, $(\theta_S^2 + \theta_B^2)/\theta_S^2$. For the Orion-KL hot

[3]The National Radio Astronomy Observatory is operated by Associated Universities, Inc., under contract by the National Science Foundation.

core, we estimate a FWHM source size, θ_S, of 12″, from the Very Large Array (VLA) imaging of the NH_3 $J,K = (3,3)$ line (Pauls et al. 1983), whose energy levels are 127 K above the ground. For the FWHM beam diameters, θ_B, of the KP 12 m, and the IRAM 30 m telescopes and the 100 m GBT, we assume 86″, 35″ and 12″, respectively at ∼70 GHz. Compared to the KP 12 m telescope, this should result in 5.5 and 26 times higher main-beam brightness temperatures, T_{mb}, for the IRAM 30 m telescope and the GBT, respectively.

In 2004, we carried out observations of the 70.68 GHz fine-structure component of CH_2 using the IRAM 30 m telescope toward the Orion-KL region. Remarkably, we did not detect the o-CH_2 $J = 4 \rightarrow 3$ line toward Orion-KL down to an rms noise level of 25 mK in the T_{mb} scale, smoothed to a common velocity resolution of 0.66 km s^{-1}. If the o-CH_2 emission was indeed shown to arise from the famous hot core, then we would expect the line to have been detected with a $T_{mb} \sim 140$ mK with the IRAM 30 m telescope.

Moreover, the CH_2 transitions also remained undetected in the 67–93.6 GHz spectral line survey presented by Frayer et al. (2015) toward Orion-KL using the GBT, at an rms noise level of ∼61 mK at 68 GHz and 36 mK at 70 GHz. The 4 mm receiver on the GBT (FWHM ∼12″) was pointed directly at the position of the Orion-KL hot core. Scaling here also the KP 12 m telescope data by the beam filling factor for a compact source with a FWHM of 12″ in both the KP 12 m telescope and GBT, we expect the T_{mb} measured by the GBT to be ∼0.65 K for the $J = 5 \rightarrow 4$ transition of o-CH_2 at 68 GHz, that is, 26 times higher than that measured using the KP 12 m telescope. The non-detections of these CH_2 transitions using the IRAM 30 m telescope and the GBT suggest that o-CH_2 is simply not present within the dense Orion-KL hot core itself and that, instead, its emission arises from a more diffuse (and presumably also warm) surrounding medium. This is not surprising as chemical models (Black et al. 1978; Prasad & Huntress 1980; Lee et al. 1996) have previously predicted high abundances of o-CH_2 in both diffuse regions as well as in intermediate density gas layers at the edges of dense clouds. This motivated our search for hot o-CH_2 in Orion among regions outside of the hot core.

The remainder of this paper is structured as follows. In Sect. 6.4, we describe all our observations of CH_2, as well as those of carbon radio recombination lines (CRRLs). We present the data in Sect. 6.5. Here, we start out by quite extensively describing our attempts to clarify the origin of the 68–71 GHz $N_{K_aK_c} = 4_{04} - 3_{13}$ o-CH_2 emission lines in several diverse environments spread over ∼0.2 pc in OMC-1 and the PDR associated with the Orion Nebula.

Next, we briefly summarise our negative results for the $N_{K_aK_c} = 2_{12} - 3_{03}$ sub-millimetre wavelength transitions of para-CH_2 (hereafter p-CH_2) that have frequencies between 440 and 445 GHz. After this, we present the results of our observations of the 68–71 GHz o-CH_2 line toward other sources, which also contain PDRs, and compare them with the CRRL data. This is followed-up by our analysis of the CH_2 data in Sect. 6.6, where we describe our chemistry modelling and radiative transfer analysis. Finally, in Sect. 6.7 we discuss the main conclusions drawn from our results and provide a brief summary of the observational state of the art and future prospects of studies of interstellar CH_2 in Sect. 6.8.

6.4 Observations

Motivated by the above considerations, we searched for o-CH_2 in hot media with intermediate densities near the envelopes of hot cores, that is, PDRs, which form at the interface between HII regions and dense molecular clouds and are characterised by the density of the cloud and the strength of the far-ultraviolet (FUV) (6 eV $< h\nu <$ 13.6 eV) radiation field. In order to investigate the possible scenario in which the observed o-CH_2 emission arises from PDRs, we first re-examined the fine-structure transitions of o-CH_2 at 68 and 70 GHz and their associated HFS transitions using the KP 12 m telescope toward a number of positions in the OMC-1. Then we followed-up with observations carried out with the new receiver covering the 4 mm band of the Onsala 20 m telescope (Belitsky et al. 2015).

The majority of the additional sources toward which we carried out our search (and not located in Orion) represent well-known HII regions and giant molecular cloud (GMC) cores showing active star formation. We targeted positions corresponding to peaks identified by a previous mapping of other continuum emission and molecular lines. The observed positions coincide with bona fide HII regions and the substantial distances ($\geq$ 2 kpc) imply that their associated PDRs have little or no angular offset from the fully ionised gas and are also covered in our 52″ FWHM single-dish beam. Our study is further supplemented with observations of p-CH_2 at 444 GHz made using the APEX 12 m telescope and of CRRLs made using the Effelsberg 100 m telescope. In the following sections, we describe the technical aspects of these observations.

6.4.1 KP 12 m telescope

The observations of Orion-KL were carried out between October and November 2005 (project id: 5029) and between January and April 2006 using the 3 mm receiver of the KP 12 m telescope. The dual channel single sideband system was operated in dual polarisation mode, using the Millimetre Auto Correlator (MAC) as backend, which provided a spectral resolution of 391 kHz over 8192 channels, spanning an effective bandwidth of 300 MHz. Thus, two frequency setups were required, centred on 68.370 and 70.679 GHz to cover each of the individual 5 – 4 and 4 – 3 HFS triplets, respectively. The observed positions lie in the vicinity of the hot core region and include the hot core itself (Orion-KL in the following), as well as the Orion S[4] a position between Orion-KL and S (here referred to as KL/S), the so-called radical-ion peak (RIP) located 4′ north of Orion-KL (Ungerechts et al. 1997), and the Orion Bar, a neighbouring PDR. This Orion Bar position was neither covered by the beam of the KP 12 m, nor that of the IRAM 30 m telescopes in previous observations. Moreover, the 68-71 GHz CH_2 transitions were also not covered by the line survey carried out by Cuadrado et al. (2016) between 80–360 GHz using the IRAM 30 m telescope toward the same position. In our observations, the $\sim$ 86″ beam of the KP 12 m telescope was centred on the source coordinates tabulated in Table 6.2. The spectra were calibrated using a main beam efficiency of 0.64. The resultant spectra were then subsequently processed using the GILDAS-CLASS

[4]We pointed at a position that is at an offset of $(-5, +12)''$ relative to that used by Tahani et al. (2016) for their line survey, which is negligible given the KP 12 m's 86″ FWHM beam.

software[5] (Pety 2005) and up to a second order polynomial baseline was removed.

6.4.2 Onsala 20 m telescope

In April and May 2019, we observed the $N_{K_aK_c} = 4_{04} - 3_{13}$ transitions of o-CH_2 using the 4 mm receiver on the Onsala 20 m telescope (Walker et al. 2016) (project id: O2018b-07) and followed-up with further observations in January and February 2020. The new 4 mm receiver, equipped with a cooled dual-polarisation high electron mobility transistor (HEMT) amplifier, was tuned to a frequency of 69.52 GHz, such that all three fine-structure components (with a maximum separation of 2.3 GHz) and their respective HFS components could be observed simultaneously, while leaving enough baseline on either side of the 4 GHz IF bandpass. The FWHM beam width at this frequency (69 GHz) was measured to be 52″. The observations were carried out in dual beam switch mode with a beam throw of 10.′5. Using the 4 GHz bandwidth provided by the OSA (Onsala Spectrometer A), fast Fourier Fourier Transform spectrometer (FFTS) backend, with a spectral resolution of 76.294 kHz, we achieved a velocity resolution of 0.3 km s^{-1}. Timely pointing and focus accuracy checks were performed by observing nearby stellar SiO ($v = 1, J = 2 \rightarrow 1$) masers. The intensity calibration was done every 12 minutes using the standard chopper-wheel method, whereby the second order chopper-wheel correction term was calculated and applied following Ulich & Haas (1976). We express the intensity scale of our spectra in units of $T_{\rm mb}$, by assuming a main beam efficiency of 0.55 (on average), while the velocity scale is given with respect to the local standard of rest. Similarly to the KP 12 m data, the calibrated spectra obtained using the Onsala 20 m telescope were further analysed using the CLASS software. However, we see signatures of a regular standing-wave pattern with a frequency of $\sim$16 MHz, which are likely associated with the enclosing radome structure whose reflective properties worsen at the lower end of the 4 mm band. This is particularly so for the observations toward Orion, whose transit at the Onsala 20 m telescope is much lower in comparison to that at the KP 12 m telescope. We corrected for contributions from the standing-wave features by using a standard standing-wave removal method based on a Fast Fourier Transform analysis. The resulting spectra are then box-smoothed to velocity bins of $\sim$1 km s^{-1} and polynomial baselines up to the third order were subtracted.

[5]Software package developed by IRAM, see `https://www.iram.fr/IRAMFR/GILDAS/` for more information regarding GILDAS packages.

Table 6.2: Summary of o-CH_2 observations using the KP 12 m, and Onsala 20 m telescopes toward the Orion pointing positions and their corresponding line parameters.

Source	RA (J2000)	Dec. (J2000)	Line [MHz]	υ_{sys} [km s^{-1}]	υ_{LSR} [km s^{-1}]	$\Delta\upsilon$ [km s^{-1}]	T_{mb}^{a} [mK]	rms^{b} [mK]	S/N^{c}	$(S/N)_{tot}^{d}$
KP 12 m Telescope										
Orion-KL	05:35:14.10	-05:22:26.54	70678.633	3.0–6.0	13.4(0.6)	5.2(0.6)	12.7(3.2)	6.5	2.0	4.3
			70679.543		9.5(0.6)	5.2(0.6)	16.6(4.2)	6.5	2.5	
			70680.720		4.5(0.6)	5.2(0.6)	21.7(5.4)	6.5	3.3	
Orion S	05:35:13.10	-05:23:56.00	70678.633	6.5–8	12.4(0.4)	5.2(0.5)	20.1(3.2)	7.0	2.8	6.1
			70679.543		8.5(0.4)	5.2(0.5)	26.4(4.2)	7.0	3.8	
			70680.720		3.5(0.4)	5.2(0.5)	34.4(5.4)	7.0	4.9	
			68371.278		-13.8(0.4)	4.9(1.0)	35.2(9.6)	7.1	5.0	
			68375.875*		7.6(0.4)	5.2(0.9)	38.3(8.6)	7.0	5.4	
			68380.873		28.8(0.4)	4.8(0.8)	28.7(7.0)	7.0	4.1	
Orion-KL/S	05:35:07.60	-05:23:11.00	70678.633	6–12	16.4(0.7)	3.5(0.5)	20.1(4.6)	7.2	2.7	3.3
			70679.543		12.5(0.7)	3.5(0.5)	26.4(6.0)	7.2	3.6	
			70680.720		7.5(0.7)	3.5(0.5)	34.4(6.8)	7.2	4.7	
Orion RIP	05:35:15.80	-05:19:00.50	70678.633	8–10	12.8(0.9)	3.1(0.7)	19.9(3.6)	6.2	3.2	4.0
			70679.543		9.0(0.9)	3.1(0.7)	26.1(4.7)	6.2	4.2	
			70680.720		4.0(0.9)	3.1(0.7)	34.0(6.1)	6.2	5.5	
Orion Bar	05:35:22.80	-05:25:01.00	70678.633	9–10	15.4(0.3)	2.6(0.6)	21.1(6.0)	11.5	1.8	2.8
			70679.543		11.5(0.3)	2.6(0.6)	27.7(8.0)	11.5	2.4	
			70680.720		6.5(0.3)	2.6(0.6)	36.1(10.3)	11.5	3.1	
			68371.278		-11.4(0.3)	2.1(0.5)	33.1(11.6)	7.8	4.2	
			68375.875*		10.8(0.3)	2.2(0.5)	39.4(12.1)	7.8	5.0	
			68380.873		30.8(0.3)	2.8(0.5)	39.5(10.7)	7.8	5.0	
OSO 20 m Telescope										
Orion-KL/S (1)	05:35:16.96	-05:22:02.7	70679.633	6–12	19.4(1.8)	4.5(1.2)	23.8(7.5)	14.2	1.7	2.2
			70679.543		15.5(1.8)	4.5(1.2)	31.3(9.7)	14.2	2.2	
			70680.720		10.5(1.8)	4.5(1.2)	40.8(12.8)	14.2	2.8	
Orion-KL/S (6)	05:35:24.96	-05:22:32.7	70679.633	6–12	16.3(1.3)	4.7(0.9)	23.9(5.1)	13.8	1.7	3.1
			70679.543		12.5(1.3)	4.7(0.9)	31.4(6.6)	13.8	2.3	
			70680.720		7.5(1.3)	4.7(0.9)	40.8(8.8)	13.8	3.0	
Orion Bar (2)	05:35:22.80	-05:25:01.0	70679.633	9–10	15.4(1.0)	4.7(1.1)	28.8(14.6)	25.3	1.1	2.3
			70679.543		11.5(1.0)	4.7(1.1)	37.9(19.1)	25.3	1.5	
			70680.720		6.5(1.0)	4.7(1.1)	49.3(24.7)	25.3	1.9	
Orion Bar (5)	05:35:20.81	-05:25:17.1	70679.633	9–10	15.4(0.8)	5.0(1.0)	28.8(8.4)	15.0	1.9	3.8
			70679.543		11.5(0.8)	5.0(1.0)	37.9(11.4)	15.0	2.5	
			70680.720		6.5(0.8)	5.0(1.0)	49.3(14.5)	15.0	3.3	

Table 6.2: Continued.: Summary of o-CH_2 observations using the Onsala 20 m telescope and derived line parameters toward the other sources presented in this study.

Source	α_{J2000}	δ_{J2000}	Line [MHz]	υ_{sys} [km s^{-1}]	υ_{LSR} [km s^{-1}]	$\Delta\upsilon$ [km s^{-1}]	T_{mb}^{a} [mK]	rms^{b} [mK]	S/N^{c}	(S/N)$_{tot}^{d}$
W3 IRS5	02:25:40.5	62:05:52	70678.633	-39.0[1]	-35.1(0.5)	7.3(0.9)	22.9(6.4)	9.8	2.3	5.0
			70679.543		-39.0(0.5)	7.3(0.9)	30.0(8.4)	9.8	3.1	
			70680.720		-44.0(0.5)	7.3(0.9)	39.1(9.3)	9.8	4.0	
			68371.278		-60.4(0.3)	5.4(0.8)	21.6(4.0)	4.4	4.9	
			68375.875*		-40.1(0.3)	6.2(0.6)	25.0(3.3)	4.5	5.6	
			68380.973		-19.0(0.3)	5.5(0.5)	27.5(3.4)	4.5	6.2	
			69007.179^{e}		-59.3(0.4)	8.7(0.9)	8.2(2.7)	3.0	2.8	
			69014.202*		-39.0(0.4)	6.9(1.3)	13.3(2.8)	3.0	4.4	
			69019.187		-7.5(0.4)	9.7(2.2)	9.9(2.9)	3.0	3.3	
W51 E	19:23:44.0	14:30:30	70679.633	+57.8[2]	+60.4(0.7)	9.0(0.5)	19.9(0.6)	11.0	1.8	4.4
			70679.543		+56.5(0.7)	9.0(0.5)	26.1(0.7)	11.0	2.4	
			70680.720		+51.5(0.7)	9.0(0.5)	34.0(0.9)	11.0	3.1	
W51 M	19:23:42.0	14:30:36	70679.633	60.8[2]	+63.4(0.5)	9.2(1.1)	24.0(6.1)	9.3	2.6	4.5
			70679.543		+59.5(0.5)	9.2(1.1)	31.3(7.2)	9.3	3.4	
			70680.720		+54.5(0.5)	9.2(1.1)	40.8(9.5)	9.3	4.4	
W51 N	19:23:40.0	14:31:10	70679.633	+60.8[2]	+64.1(0.7)	9.2(0.7)	12.4(6.2)	9.2	1.3	3.4
			70679.543		+60.2(0.7)	9.2(0.7)	16.3(7.0)	9.2	1.8	
			70680.720		+55.2(0.7)	9.2(0.7)	21.2(9.0)	9.2	2.3	
W49 N	19:10:13.6	09:06:15	70679.633	+10.0[3]	+11.8(0.8)	9.2(1.0)	23.6(0.8)	11.5	2.0	4.0
			70679.543		+8.0(0.8)	9.2(1.0)	31.0(10.1)	11.5	2.7	
			70680.720		+3.0(0.8)	9.2(1.0)	40.4(13.1)	11.5	3.5	
W43	18:47:36.9	-01:55:30	70679.633	+89.4[4]	+92.8(1.1)	9.2(0.8)	11.2(4.3)	10.2	1.1	3.3
			70679.543		+88.5(1.1)	9.2(0.8)	14.7(5.4)	10.2	1.4	
			70680.720		+83.5(1.1)	9.2(0.8)	19.1(7.3)	10.2	2.0	
DR21	20:39:02.0	42:19:42	70679.633	−3.0[5]	+1.9(0.7)	9.2(0.7)	7.5(2.3)	5.4	1.4	4.1
			70679.543		-2.0(0.7)	9.2(0.7)	9.8(3.0)	5.4	1.8	
			70680.720		-7.0(0.7)	9.2(0.7)	12.8(3.8)	5.4	2.4	
W75 N	20:38:36.5	42:37:35	70679.633	+9.0[5]	+13.4(0.8)	2.4(0.1)	10.4(2.0)	5.3	2.0	3.5
			70679.543		+9.5(0.8)	2.4(0.1)	13.7(2.6)	5.3	2.6	
			70680.720		+4.5(0.8)	2.4(0.1)	17.9(3.4)	5.3	3.4	
S140	22:19:11.5	63:17:47	70679.633	−8.5[6]	-7.1(0.8)	4.7(0.6)	26.1(10.4)	16.7	1.6	3.0
			70679.543		-11.0(0.8)	4.7(0.6)	34.3(13.7)	16.7	2.1	
			70680.720		-16.0(0.8)	4.7(0.6)	44.6(17.8)	16.7	2.7	

Notes and references for Table 6.2

Notes: $^{(a)}$ Peak main-beam brightness temperature derived from the integrated intensity of the detected line features. $^{(b)}$ The rms noise level on the $T_{\rm mb}$ scale, for a spectral resolution of 0.85 km s^{-1} and 0.97 km s^{-1} for the KP 12 m, and Onsala 20 m telescopes, respectively. $^{(c)}$ The signal-to-noise (S/N) ratio with respect to the peak.$^{(d)}$ The S/N ratio of the integrated intensity calculated from the listed rms noise levels and line widths for the 70 GHz CH_2 line.$^{(e)}$ The reported intensity for this component accounts for contributions from the blended NS $J, F = 3/2, 3/2 \rightarrow 1/2, 1/2$ line at 69017.995 MHz. This line was modelled using the NS $J, F = 3/2, 5/2 \rightarrow 3/2, 1/2$ HFS line at 69002.890 MHz, which is also covered in the same bandpass.$^{(*)}$ Represents the HFS component used to determine the LSR velocity axes of the spectra shown in Figs. 6.3 and 6.9. For each HFS line the velocities of the other HFS components are listed as they appear in the spectra shown in this figure.
References: For the radial velocities toward the Orion pointing positions, see Gong et al. (2015) and references therein. For the radial velocities toward the other sources: [1] Imai et al. (2000); [2] Parsons et al. (2012); [3] Jackson & Kraemer (1994); [4] Bally et al. (2010); [5] Dickel et al. (1978); [6] Bally et al. (2002).

6.4.3 APEX 12 m telescope

The fine-structure components of the $N_{K_aK_c} = 2_{12} - 3_{03}$ transition of p-CH_2 were observed in 2013 August[6], using the high frequency channel of the sideband separating (2SB), dual frequency band First Light APEX Submillimetre Heterodyne Receiver, FLASH (hereafter FLASH-460, Heyminck et al. 2006) on the APEX 12 m sub-millimetre telescope[7] (Güsten et al. 2006). The FWHM beam size at 443 GHz is 14″. The bandpass was selected such that we covered the 444 GHz transitions in the upper sideband alongside the ^{13}CO $J = 4 \rightarrow 3$ transition at 439.088 GHz, which made for an excellent reference for monitoring the calibration during the observations. We observed the same Orion-KL, Orion S, and Orion RIP positions as discussed above, along with two positions in the Orion Bar, corresponding to the CO and HCN abundance peaks (see Nagy et al. 2015b, and references therein). The FFTS, providing a 4 GHz bandwidth in each sideband, was used as backend for these observations to achieve a spectral resolution of 76.3 kHz. The data was subsequently reduced and processed using the CLASS software with a forward efficiency of 0.95 and a main beam efficiency of 0.60. Polynomial baselines up to a second order were removed and the subsequently obtained spectrum was box-smoothed to channel widths of 1 km s^{-1}. Each pointing position was integrated on, for a total time of $\sim$ 23 mins, except for the Orion S position, toward which we carried out deeper integration[8], for a total time of 12.7 hours.

[6]Project id: M-091.F-0040-2013
[7]APEX is a collaboration between the Max-Planck-Institut fur Radioastronomie, the European Southern Observatory, and the Onsala Space Observatory.
[8]Project id: M-091.F-0045-2013

6.4.4 Effelsberg-100 m telescope

We performed CRRL measurements (project id: 08-19) toward those targets with successful detections of CH_2, in position-switching mode with the S20mm receiver of the 100-m telescope at Effelsberg, Germany[9], on 2019 5–6 July and 22–23 August. The S20mm receiver is a double-beam and dual-polarisation receiver operating in the frequency range between 12–18 GHz. This range contains $\Delta n = 1$, 'α', radio recombination lines from H, He and C with principal quantum numbers, n, between 80 and 72; see Appendix D.3. Frequencies of RRLs from all three species can be calculated following the prescriptions of Lilley & Palmer (1968), or simply retrieved from the Splatalogue database[10].

For our analysis, we only use data from the central beam of the S20 receiver. The FFTS (e.g. Klein et al. 2012) data serve as backend, each of which consists of 65536 channels. For the observations toward the different Orion positions and W3 IRS5, we used a total bandwidth of 300 MHz with a channel width of 4.6 kHz, corresponding to a velocity spacing of 0.09 km s^{-1} at 15 GHz. Our observations of the other targets utilised a total bandwidth of 5 GHz and a channel width of 38.1 kHz, corresponding to a velocity spacing of 0.76 km s^{-1} at 15 GHz. The focus was adjusted using observations of strong continuum sources at the beginning of each observing session. Pointing observations were carried out roughly every two hours toward strong continuum sources nearby. The pointing accuracy was found be less than 5″. NGC 7027 was used as the flux calibrator, and the flux calibration accuracy is estimated to be within ∼10%. The observations took about 20 hours in total. The FWHM beam width is 48″ at 15 GHz. This angular resolution allows for a meaningful comparison with the CH_2 transitions observed using the Onsala telescope at ∼69 GHz (with a FWHM of 52″). The main beam efficiency is about 0.65 and the typical system temperature is about 15 K. The data reduction was once again performed using the CLASS software.

6.5 Results

6.5.1 Line profiles

The lines of the HFS triplet of the $J = 4 \rightarrow 3$ fine structure transition of CH_2 overlap with one another because of their close frequency spacing, $\Delta\nu$, of 0.88 and 1.18 MHz, corresponding to 3.7 and 5.0 km s^{-1}, respectively. This blending of the individual components with one another broadens the observed profile. While this greatly aids in the detection of this component, it does not reveal accurate line properties, such as the intrinsic line width. On the other hand, with a frequency separation of 9.6 and 12 MHz, respectively, the individual HFS components of the $J = 5 \rightarrow 4$ and $J = 3 \rightarrow 2$ transitions of CH_2 near 68 GHz and 69 GHz, respectively, are well resolved. However, the $F = 4 \rightarrow 3$ HFS component of the latter at 69.019187 GHz is contaminated by emission from the low-lying (E_u = 3.3 K) NS $J, F = 3/2, 3/2 \rightarrow 1/2, 1/2$ line at 69.017995 GHz. Therefore, the HFS-resolved o-CH_2 line profiles are modelled by simultaneously fitting individual Gaussian profiles to the observed HFS lines using the CLASS

[9]The 100-m telescope at Effelsberg is operated by the Max-Planck-Institut für Radioastronomie (MPIFR) on behalf of the Max-Planck Gesellschaft (MPG).

[10]`https://splatalogue.online//`

software. The relative contribution of the emission from the NS transition present in the strongest HFS component of the $J = 3 \rightarrow 2$ line, is modelled by scaling its intensity with that of the $F = 5/2 \rightarrow 3/2$ transition of NS at 69.002890 GHz covered in the same bandpass, by their relative line strengths under the assumption of local thermal equilibrium (LTE).

For the blended $J = 4 \rightarrow 3$ component of o-CH_2 , we modelled the observations by using the line widths derived from the $J = 5 \rightarrow 4$ transitions near 68 GHz, which are unaffected by blending and contamination, and thereby we were able to reveal the true shape of the CH_2 emission profile. While the thus determined line width can be used to model the line profiles of the other fine structure lines, this line is unfortunately not detected toward a majority of our sources above a 3σ noise level. The rms noise levels we obtained for the different sources are listed in Appendix D.1. For those sources toward which the $J = 5 \rightarrow 4$ fine structure line is not detected, the HFS of the $J = 4 \rightarrow 3$ transition is decomposed[11] by minimising the mean square error between the modelled fit and the observations over several iterations covering a range of line widths typically between 2 and 10 km s^{-1} in steps of 0.23 km s^{-1}. This 'empirical' model simultaneously fits the three HFS lines using Gaussian profiles with: (1) positions determined by the velocity separation of the HFS lines relative to the 70.679543 GHz component; (2) one common line width; and (3) individual line intensities estimated by scaling the peak temperature by the line strength of each HFS line. Since the typical positions are well-known for a given source and the line intensities can be constrained from the observations, the line width is the only free parameter. Varying the line width in each iteration and comparing the mean square error between the observed line profile and that of the combined HFS fit, the scheme converges for the line width returning the least error. The errors in the line parameters are determined from the covariance matrix and depend on the rms noise of the system. There are additional systematic uncertainties in the line width, which are caused by the low signal-to-noise ratio (S/N) in these spectra. A summary of the derived line parameters is given in Table 6.2.

6.5.2 o-CH_2 in Orion

The spectra observed toward the different Orion positions with the KP 12 m telescope are displayed in Fig. 6.3. We detect the $J = 4 \rightarrow 3$ fine-structure component of the $4_{04} - 3_{13}$ transition of CH_2 near 70 GHz toward all the Orion pointing positions at systemic velocities between 8 and 10 km s^{-1}. A second observational setup was used toward the Orion S and Bar positions, with the band centred on the $J = 5 \rightarrow 4$ fine-structure components at 68 GHz. We were able to detect the well-separated HFS components of the 68 GHz lines toward both positions at a $\gtrsim 5\sigma$ level. In the spectrum of the 68 GHz component toward Orion S, we also detect part of the $K = 0$ to 3 ladder of the $J = 4 \rightarrow 3$ transition of methyl acetylene, that is, CH_3CCH near 68.3649 GHz.

While the measured line intensity toward Orion-KL is consistent with that of the original detection by Hollis et al. (1995), we find the line intensities derived toward the other Orion positions to be of very comparable, if not greater, strengths than the strongest emission being seen toward the Orion S position. The successful detection and higher CH_2 intensities observed toward regions outside of the hot core once again brings into question the association of the CH_2 emission with the hot core. Moreover, we detect CH_2 emission toward an intermediate

[11]This analysis was carried out using Python packages numpy and scipy (van der Walt et al. 2011).

position between Orion-KL and S, which we name Orion KL/S and toward which we would not expect any CH_2 emission if it were confined to the hot core. The detection of this high-lying CH_2 transition toward all the Orion positions with comparable line strengths, indicates an extended emission component of CH_2 arising from a rather dilute, but hot ISM component and also suggests that this molecule is simply not found within the hot core. The compatibility of the intrinsic velocity of the observed CH_2 emission toward Orion KL with that of the extended ridge component, $\upsilon_{\rm LSR}$ = 8–10 km s^{-1} (see Gong et al. 2015, and references therein), which represents the typical velocities of the ambient gas present in this region and further hints at the extended nature of the CH_2 emission. Since these observations were once again carried out using the KP 12 m telescope with a large beam size, the resulting signal may certainly contain contributions from neighbouring regions located within the beam.

In an attempt to address the question of where the CH_2 emission arises from, we studied the emission characteristics of this molecule at several positions within the Orion complex, using the Onsala 20 m telescope, which has a beam size of 54″ at 69 GHz. These results are discussed in Sect. 6.5.3. For convenience, the pointing positions chosen for our study are grouped into two, namely, the Orion KL/S and Orion Bar regions, respectively. The different positions are classified based on their proximity to either the hot core, Orion-KL, or to the PDR, the Orion Bar.

6.5.3 A closer look at the source of CH_2 emission

The Orion KL/S region

In addition to the nominal Orion-KL and Orion S positions used in our KP observations (hereafter referred to as Orion KL/S positions (2) and (5)), we also observe four positions corresponding to the massive O7V star θ^1 Ori C, position (4), which is responsible for the ionisation of the Orion Nebula, [CII] peak positions (1) and (6) selected from Pabst et al. (2019) and a position between the Orion-KL and S regions, position (3). In Fig. 6.4, we display the calibrated and baseline-subtracted spectra observed toward the different Orion KL/S positions. We detect CH_2 emission toward the two [CII] peak positions marked (1) and (6), at a $\sim 3\sigma$ level with an average rms noise of 14 mK for the two spectra. However, we see no clear signal toward the other Orion KL/S positions, above an rms noise level of 22 mK on average. For the positions toward which we do not clearly detect CH_2 , we stack and then average the spectra (taken three at a time) in order to reduce the spectral noise and investigate our suspicion that the CH_2 emission is extended. The resulting spectra are displayed in the bottom panel of Fig. 6.4. Upon scaling the fit results obtained toward positions (1) and (6), we see that all four independent combinations of the stacked and averaged profiles hint at the presence of a signal at velocities close to the systemic velocity of the source. The strongest CH_2 signals are observed in the profiles that result from the combination of positions (2, 3, 5) and (3, 4, 5). This suggests that the CH_2 emission is weakest at positions (2) and (4) which correspond to the Orion-KL hot core and the θ^1 Ori C positions, respectively. Cross-correlating the intensities integrated over a velocity range from −10 to +20 km s^{-1} (which is roughly the velocity interval over which we expect to observe CH_2 signatures) obtained toward the individual, and combined sets of pointing positions amongst each other, we find

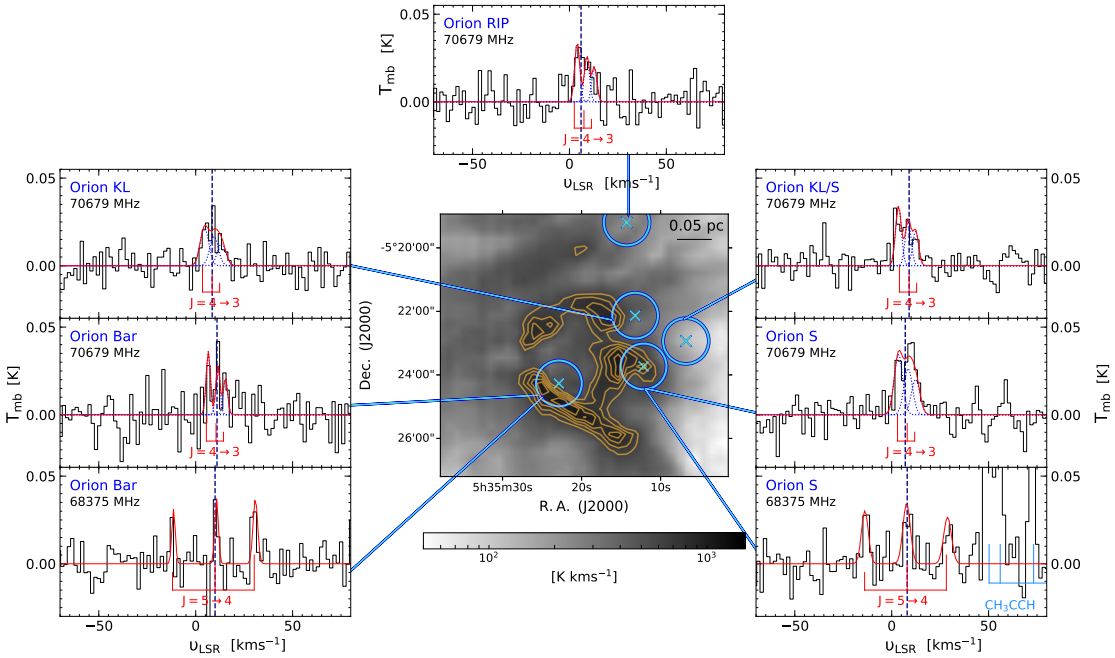

Figure 6.3: Integrated intensity map of the [CII] 158 μm emission overlaid with integrated intensity contours (orange) from 600 to 1000 K km s^{-1} in steps of 100 K km s^{-1} toward OMC-1, adapted from Pabst et al. (2019). The positions observed using the KP 12 m telescope are marked by blue crosses, while the blue circles represent the KP beam. The corresponding calibrated and baseline subtracted o-CH_2 spectra are displayed alongside the map. The individual fits to the HFS components are displayed by dotted blue curves while solid red curves displays the combined fit. The positions and relative intensities of the HFS components are marked below the spectra. The dashed blue line indicates the systemic velocities of the sources which lie between +7 and +11 km s^{-1}. In light blue we also mark the CH_3CCH lines covered in the 68375 MHz spectrum toward Orion S. The velocity scale is set by the $F' - F'' = J–J - 1$ HFS line (see Table 6.1).

that positions (2) and (4) show negative correlations toward almost all other sources. The negative and/or weak correlations (tending to zero) shown by these components (see Fig. 6.5) suggest that there is no association between them and reveal that CH_2 is likely not present within the hot core. The correlations we present were computed using the Pearson product moment correlation coefficient. This coefficient describes the strength of the linear relationship between each pair of spectra by using the standard deviation of each data set and the covariance between them. The underlying assumption made in this calculation is that the data follow a Gaussian distribution. For comparison, we also computed the correlation strengths based on non-parametric statistics by using the Spearman correlation coefficient. While the relative strengths produced by both methods are different, they both reproduce the same monotonic trends in their correlations. Since the aim of this analysis is to simply distinguish the nature of the correlation, namely positive or negative, in all subsequent analyses that make use of correlation coefficients, we use the standard Pearson coefficient.

The detection of CH_2 toward the hot core initially discussed in Hollis et al. (1995) and also in this work, can now be explained through its successful detection in the Orion KL/S (1) position. Offset from the nominal Orion KL position by (40.2″, 24.8″), a part of Orion KL/S (1) is covered by the KP 12 m beam. This resolves the observational discrepancies between the KP 12 m telescope, the GBT, and the IRAM 30 m telescope (detailed in Sect. 6.3) and indicates that the CH_2 emission is associated with gas layers similar to those traced by [CII]. Sensitivity is of course another important factor. As discussed earlier, given its extended emission, we would expect to observe CH_2 with a similar line strength using the different telescopes. The non-detections using the IRAM 30 m telescope and GBT therefore exclude the possibility that the CH_2 emission originates in compact regions like hot cores.

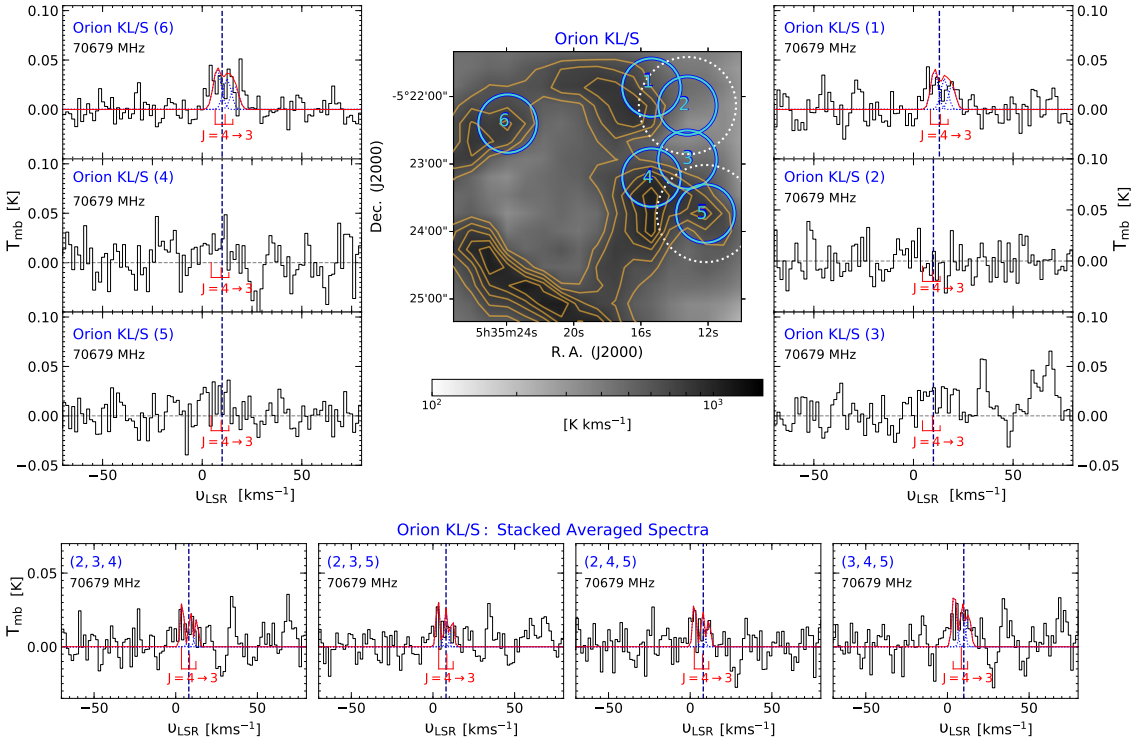

Figure 6.4: *Top*: Same as Fig. 6.3 but for o-CH_2 observations made using the Onsala 20 m telescope toward the Orion KL/S region. Blue circles represent the beam size of the Onsala 20 m telescope centred at the different pointing positions and the dotted white circle marks the KP beam at the Orion-KL and Orion S positions marked in Fig. 6.3. *Bottom*: Stacked and averaged o-CH_2 spectra obtained by combining the Orion KL/S pointing positions (2), (3), (4), and (5), taken three at a time. The line fits are scaled using the line parameters obtained toward Orion KL/S positions (1) and (6).

The Orion Bar region

In addition to the Orion Bar position previously observed using the KP 12 m telescope, which corresponds to the peak of the CO emission [hereafter known as Orion Bar position (2)], we

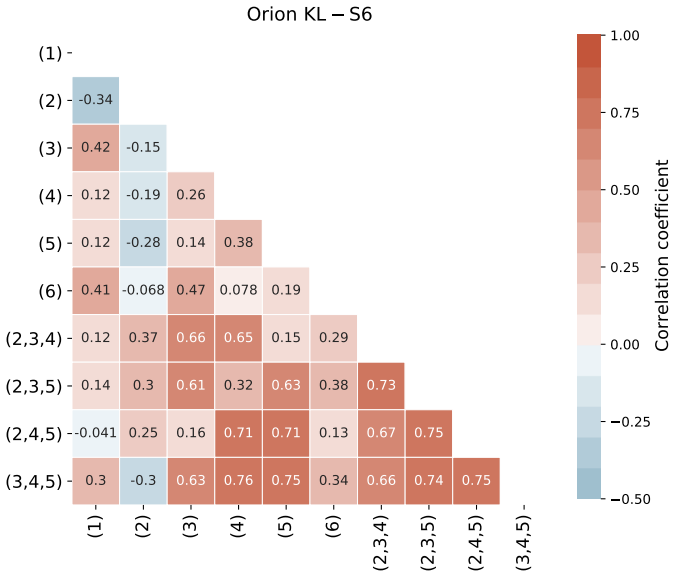

Figure 6.5: Pearson product-moment correlation coefficients between the integrated o-CH_2 intensities, observed toward the individual and combined pointing positions in the Orion KL/S region.

carried out observations toward four additional positions. They correspond to positions at or near the emission peaks of HCN, CF^+, C_2H, and CO^+ and are labelled (1), (3), (4), and (5), respectively, as displayed in Fig. 6.6. The positions were selected on the basis of previous studies by Neufeld et al. (2006), Stoerzer et al. (1995), Cuadrado et al. (2015), and Nagy et al. (2015b) and references therein. CH_2 emission is detected at a 2.3 and 4σ level toward the Orion Bar nominal position (2) and the C_2H emission peak at position (5) at an rms noise level of 25 and 15 mK, respectively. We do not detect any appreciable signal from the other Orion Bar positions, even toward positions (1) and (3) at rms noise levels down to 17 mK.

Similar to the pointing positions toward the Orion KL/S region for which we do not detect CH_2 emission, we stack and average the positions with non-detections in the Orion Bar region. The combined profiles of the independent pairs between positions (1), (3), and (4), as well as that obtained when considering all three together, are displayed in the bottom panel of Fig. 6.6. Scaling the fit parameters obtained from position (2), we find that there is a weak indication of CH_2 emission present in all the combinations. Carrying out a correlation analysis amongst the different Orion Bar positions we do not see any anti-correlations. However, from the correlation matrix presented in Fig. 6.7 we infer that position (3) has the weakest correlation coefficients particularly with that of positions (1), (4), and (5).

The observed CH_2 emission in the Orion Bar suggests that the molecule's abundance decreases as we move away from the ionisation front (near the HII region) and toward the molecular clouds deeper within the PDR. Observations of HF emission by Kavak et al. (2019) across the Orion Bar centred near the CO^+ peak reveals a similar morphology. These authors were able to show that the bulk of the HF emission peaked in a region separating the H_2 and [CII] emission from the molecular emission in the denser clumps or close to the ionisation front. A direct comparison between the CH_2 and HF emissions is difficult because both sets of observations were carried out toward different positions in the Bar. However, since emission from both species has been observed near the Orion Bar CO^+ emission peak, we can compare the CH_2 line profile with that observed for HF at this position (this corresponds to position

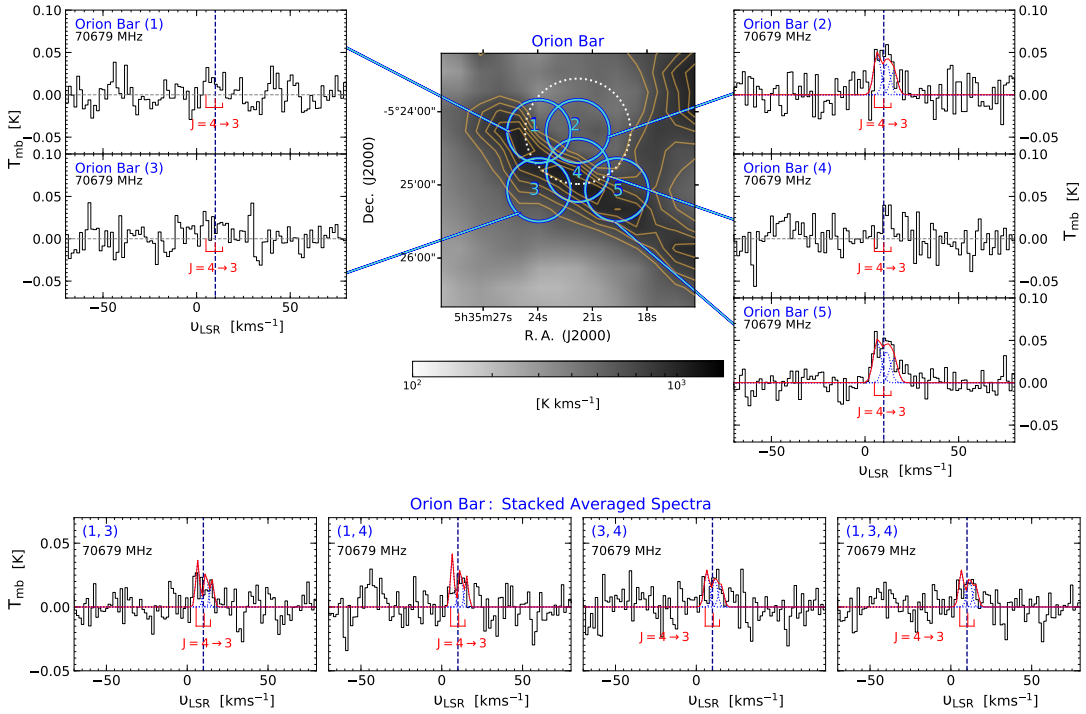

Figure 6.6: *Top*: Same as Fig. 6.4 but for o-CH_2 observations made using the Onsala 20 m telescope toward the Orion Bar region. The blue circles represent the beam size of the Onsala 20 m telescope centred at the different pointing positions and the dotted white circle marks the KP beam at the Orion Bar position marked in Fig. 6.3. *Bottom*: Stacked and averaged o-CH_2 spectra obtained by combining the Orion KL/S pointing positions (1), (3), and (4), two at a time and all together. The fits are scaled using the line parameters obtained toward Orion Bar positions (2) and (5).

(2) in Kavak et al. (2019) and position (5) in this work). Both species show peak emission at velocities and line widths that are consistent within the error bars, between 10–10.5 km s^{-1} and 4.4–5 km s^{-1}, respectively. From their line emission survey over the entire range of frequencies offered by the Herschel Heterodyne Instrument for the Far Infrared (HIFI) under the HEXOS HIFI key guaranteed time project, Nagy et al. (2015a) inferred typical line widths between 2 and 3 km s^{-1} toward the Orion Bar CO^+ peak, with the exception of a handful of species including HF. The broader line width of HF was reconciled as being due to its association with diffuse gas present in the inter-clump regions of Orion Bar. Therefore, it is conceivable that o-CH_2 is also likely to arise from a similar cloud population tracing dilute but hot (T_{kin} = 120 K) gas, unlike most of the other species studied by Nagy et al. (2015a) and others, including Cuadrado et al. (2015, 2017), which trace gas densities between 10^5 and 10^6 cm^{-3}. However, it is difficult to extend such a comparison toward the other sources in our study because HF is typically observed in absorption toward the envelope of these molecular clouds even showing several absorption components along the LOS.

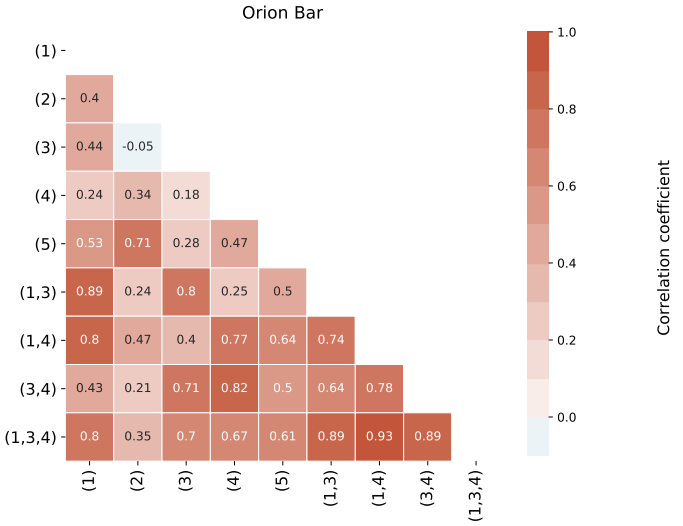

Figure 6.7: Pearson product-moment correlation coefficients between the integrated o-CH_2 intensities, observed toward the individual and combined pointing positions in the Orion Bar region.

6.5.4 p-CH_2 in Orion

The $N_{K_aK_c} = 2_{12} - 3_{03}$ transitions of p-CH_2 between 440 and 445 GHz that have upper level energies of 156 K. Lying within a sub-millimetre window, they are accessible from high-mountain sites but have gone undetected thus far. Observations of these p-CH_2 lines could potentially aid our understanding of CH_2's excitation. We do not detect any sign of the 444 GHz p-CH_2 transitions toward the different Orion positions given in Sect. 6.4.3 above an rms noise level of 77 mK on average, for a spectral resolution of 1 km s^{-1}. Moreover, even after a deeper integration toward the Orion S position, which resulted in an rms level of 8 mK, we did not detect any signatures of p-CH_2. The Einstein A-coefficients and hence, the critical densities of the 444 GHz p-CH_2 lines are two orders of magnitude larger than that of the 70 GHz o-CH_2 lines. With critical densities on the order of 2×10^7 cm^{-3} the non-detection of these lines is no surprise and consistent with our finding that CH_2 exclusively resides in hot, but low-density regions.

6.5.5 CH_2 in other sources

The results of our observations discussed thus far point to the origin of the o-CH_2 emission in regions of intermediate gas densities in the envelopes of hot cores, probing PDR layers, rather than the hot cores themselves. In order to confirm the association of the observed o-CH_2 emission with PDRs, we have also searched for o-CH_2 emission in: (1) other well-known SFRs that harbour PDRs, (2) (proto-) planetary nebulae (PNe) that are surrounded by molecule-rich envelopes that resemble the composition of PDRs and (3) supernovae remnants (SNRs). Their coordinates are listed in Tables 6.2 and D.1, alongside their assumed centroid LSR velocities and, for each line group, the rms noise levels.

We successfully detected the blended $J = 4 \rightarrow 3$ transitions of o-CH_2 in emission toward W51 M, N, and E, W49 N, W3 IRS5, W43, W75 N, DR21, and S140 at the systemic velocities of these sources. The resulting spectra are displayed in Figs. 6.8–6.10. In the following sections, we discuss the observed characteristics of this line blend for select sources in more

detail.

W51

Given that W51 Main (M) was one of the original targets toward which Hollis et al. (1995) first detected CH_2, we re-observed this position in order to first verify their detection and then carried out observations toward two luminous condensations harboring high-mass YSOs present in this region, W51 North (N), also known as W51 IRS 2, and W51(E).

The W51 cloud complex, lying in the Sagittarius spiral arm at a distance of 5.4 kpc from the Sun (Sato et al. 2010), is one of the best-studied SFRs in our Galaxy. W51 E and N are the two active and presumably youngest centres of activity, hosting the ultracompact (UC) HII regions e1–e8 and d, respectively (Ginsburg et al. 2017, and references therein), infrared and sub-millimetre continuum emission (Thronson & Harper 1979; Jaffe et al. 1984), H_2O and OH masers (Genzel et al. 1981), and knots of hot NH_3 (J, K) = (3,3) line-emitting gas (Ho et al. 1983; Goddi et al. 2015; Ginsburg et al. 2017), all of which are signposts of active star formation within cores with masses of $\gtrsim 10^4$ $M_\odot$ each. W51 N and E are separated by a projected distance of 1.′9 pc, with W51 M about halfway in between. M shows more extended FIR and radio continuum emission than E and N (Moon & Koo 1994; Thronson & Harper 1979).

We are able to unambiguously detect the $J = 4 \rightarrow 3$ fine-structure component of the $4_{04} - 3_{13}$ transition of o-CH_2 near 70 GHz toward all three positions at the source intrinsic velocities between 57 and 62 km s^{-1} (see Fig. 6.8). While the emission profiles toward each of the three positions are comparable, the strongest emission arises from the W51 M region, toward which Hollis et al. (1995) pointed the KP 12 m telescope. This is not surprising, given that the radio emission (and that from its PDR, too) has a larger angular size than that from E and N, resulting in a larger beam filling factor. Therefore, the fact that we see stronger CH_2 emission toward the extended HII region W51 M than toward the much more massive and denser W51 E and N regions, strongly supports an origin of CH_2 in extended dilute gas.

The observed line profile of the 70 GHz component toward W51 M is comparable to that reported by Hollis et al. (1995) however, we do not detect distinct emission from the HFS lines corresponding to the $J = 5 \rightarrow 4$ and $J = 3 \rightarrow 2$ fine-structure transitions near 68 GHz, and 69 GHz, toward any of the three positions above an average rms noise level of 20 mK. Therefore, in an attempt to recover an average measurement, we stacked the observed spectra toward the different W51 pointing positions by aligning their frequency scales. Due to the contamination from strong NS emission, it is difficult to disentangle the HFS features corresponding to the 69 GHz transition. However, the HFS lines of the 68 GHz component are weakly visible. In order to gauge the true nature of this emission, we further stacked each of the individual HFS lines by aligning their velocity scales. This stacking exercise revealed a 3.5 σ detection of this line with a width of 9.1 km s^{-1} and a peak line temperature of 23 mK. The line width determined from this 68 GHz component is consistent with the value of the intrinsic line width derived from the iterative HFS decomposition of the 70 GHz lines. The spectrum resulting from our stacking analysis is displayed alongside the 70 GHz lines in Fig. 6.8. This highlights the fact that the non-detection of the 68 GHz and 69 GHz transitions of CH_2 in our observations is primarily due to a sensitivity issue.

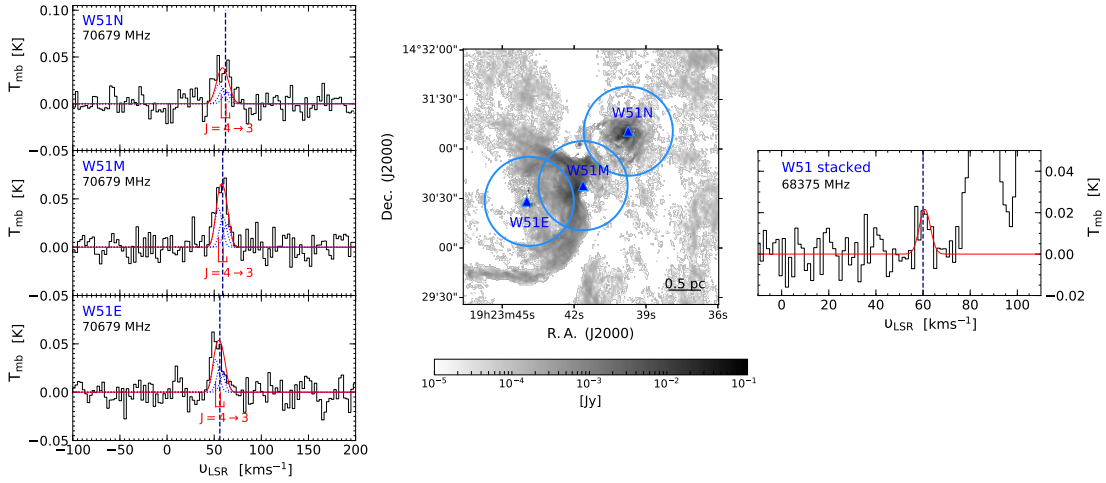

Figure 6.8: *Left*: Spectra of the o-CH_2 $J = 4 \rightarrow 3$ fine-structure level toward (*top to bottom*) W51 N, W51 M, and W51 E observed using the Onsala 20 m telescope. The individual fits to the HFS components are displayed by dotted blue curves while solid red curves display the combined fit. The positions and relative intensities of the corresponding, blended HFS components are displayed below. The dashed blue line indicates the systemic velocities of the sources which lie $\sim$+60 km s^{-1}. *Centre*: Ku-band image (14.5 GHz, tracing ionised gas) of the W51 region obtained using a combination of JVLA B and D arrays taken from Ginsburg et al. (2016), is used to indicate the different Onsala pointing positions. The distance between the different positions is greater than half the beam size of 27″ at 69 GHz. *Right*: The position- and HFS-stacked spectrum of the 68 GHz CH_2 lines. The strong emission at $v > 77$ km s^{-1} represents contamination from a CH_3CCH line (see Sect. 6.5.2).

W3 IRS5

The W3 IRS5 cluster system has a well known double IR source at the centre of an embedded cluster of a few hundred low mass stars (Megeath et al. 1996). Located in the W3-Main region at a distance of 2.1 kpc (Megeath et al. 2008; Navarete et al. 2019) and a total luminosity of 2×10^5 $L_\odot$ (Campbell et al. 1995), it is considered to be at the early stages of star formation. We detect the blended HFS transitions of o-CH_2 near 70 GHz toward this region in emission, centred around -40 km s^{-1} (with a S/N > 5), a typical velocity found for molecular lines in this region (Dickel et al. 1980) (see Fig. 6.9). Akin to the observations toward the different W51 positions, we did not achieve noise levels that are low enough to clearly detect the 68 GHz, and 69 GHz fine-structure lines. However, by stacking our data with a deep integration spectrum of a bandpass covering 67.3–69.8 GHz, obtained by one team member during the course of a different study using the OSO 20 m telescope toward this source, we were able to detect both the 68 GHz and 69 GHz transitions of o-CH_2 and their respective HFS lines as well.

We find the HFS transitions of the 68 GHz fine-structure line to be well-resolved with peak temperatures between 21 and 27 mK and line widths of 5.3–6 km s^{-1}, which are comparable with one another, as well as the HFS-stacked 68 GHz component, toward the combined W51 positions. As discussed in Sec. 6.5.1, the strongest HFS component of the 69 GHz line blends

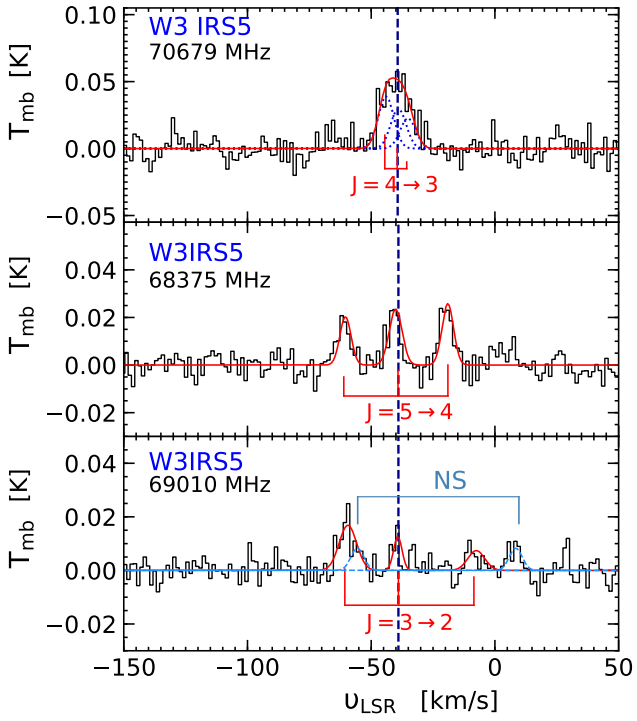

Figure 6.9: Spectra showing the HFS transitions corresponding to the $J=4 \rightarrow 3$ (*top*), $J=5 \rightarrow 4$ (*middle*) and $J=3 \rightarrow 2$ (*bottom*), fine-structure levels observed using the Onsala 20 m telescope toward W3 IRS5. The individual fits to the HFS components are displayed by red curves. The NS contamination near 69019.180 MHz that blends with the $J, F = 3,4 \rightarrow 2,3$ o-CH_2 HFS line at 69017.995 MHz is marked in light blue. The relative contribution of the NS feature is modelled using the nearby NS $F = 5/2 \rightarrow 3/2$ transition at 69002.890 MHz and is displayed in light blue. The velocity scale is set by the $F' - F'' = J–J - 1$ HFS line (see Table 6.1).

with the $F = 3/2 \rightarrow 1/2$ transition of NS. Assuming that the intensity of the blended NS line at 69.017995 GHz scales with that of the $F = 5/2 \rightarrow 3/2$ transition of NS at 69.002890 GHz by 0.36, based on their Einstein A-coefficients and upper level degeneracies, we can decompose the relative contribution of the NS line from that of o-CH_2 under the assumption that they are optically thin for conditions of LTE. The o-CH_2 spectra for both the 68 GHz, and 69 GHz transitions are displayed in Fig. 6.9 along with the modelled fit to the contamination from NS.

Other sources

In addition to the results presented in the above sections, we successfully detected o-CH_2 emission from the HFS blended $J = 4 \rightarrow 3$ transition near 70 GHz, toward W49 N, W43, W75 N, DR21, and S140 at a $\geq 3\sigma$ level. The observed spectra are displayed in Fig. 6.10 and the results are tabulated in Table 6.2.

At first glance, it appears surprising that the observed line intensities in the nearby Orion region, which is a distance of $\approx$400 pc (Menten et al. 2007; Kounkel et al. 2017), are comparable to the values we find for the other more distant regions, which are between 1.4 kpc (DR21) to 11 kpc (W49 N) away from the Earth. If all sources (including Orion) were unresolved and had an identical intrinsic size and line luminosity, then ultimately all of their emission would be detected in our beam and their measured intensities would scale with the beam-filling factor. In that case, emission from Orion would be by far the strongest. In contrast, our results indicate that the CH_2 emission from Orion is very extended and has a very low surface brightness. This means that in contrast to the other more distant sources, in the case of Orion, our beam only samples a small portion of the CH_2 emission, resulting in a low intensity in some PDR

positions, or even a non-detection in others, although CH_2 may be present over much of the volume of the PDR.

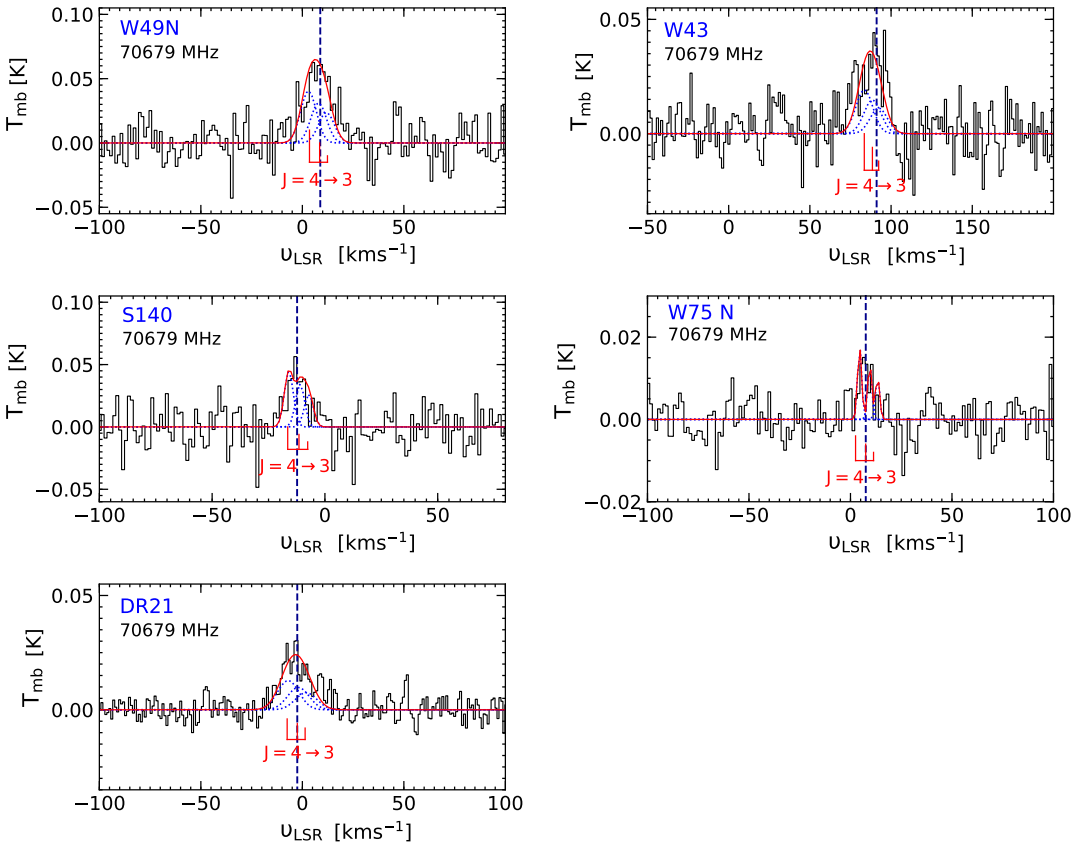

Figure 6.10: Spectra of the o-CH_2 $J = 4 \rightarrow 3$ fine-structure level toward *(clockwise from the top-left)* W49 N, W43, W75 N, DR21, and S140 observed using the Onsala 20 m telescope. The individual fits to the HFS components are displayed by dotted blue curves while solid red curves display the combined fit. The positions and relative intensities of the corresponding, blended HFS components are displayed below. The dashed blue line in each panel indicates the systemic velocities of the sources.

6.5.6 Comparison with CRRLs

The detection of o-CH_2 toward SFRs strongly suggests that CH_2 resides in all cases, as in Orion, in warm intermediate-density regions, namely PDRs, which surround the denser, fully molecular material harbouring embedded YSOs. Indeed, the HFS-decomposed line profiles of the observed CH_2 spectra show LSR velocities and line widths that are similar to those of previously observed prime PDR tracers, namely low frequency CRRLs and neutral atomic carbon lines; see, for example, Heiles et al. (1996); Wyrowski et al. (1997); Roshi et al. (2006) and Jakob et al. (2007).

Having spatial distributions, line widths, and radial velocities consistent with an origin

in the neutral gas close to the C^+/C/CO transition layer, CRRLs are particularly useful tools for probing the physical conditions and kinematics of these regions (Hoang-Binh & Walmsley 1974; Natta et al. 1994; Salas et al. 2019). Since the properties derived from the observed CRRL line profiles reflect the physical conditions of the PDR, coupling our observations of o-CH_2 with ancillary CRRL data will help us to constrain the origins of the observed o-CH_2 emission.

In the following analysis, we compare the profiles of HFS-stacked 70 GHz lines with those observed for CRRLs. Because of the small velocity (frequency) separation between the HFS lines corresponding to the 70 GHz fine-structure transitions, they appear to be blended, which makes it difficult to simply stack them. For this reason, we use the modelled results from the individual HFS fits for stacking. The expected rms noise of the stacked and averaged spectrum is then added back to the modelled HFS-stacked profile. The different steps involved in this exercise are detailed and illustrated in Appendix D.2.

In the following, as a basis for a CH_2/CRRL comparison, we use a PDR model to explore the abundance versus visual extinction (A_v) profiles of CH_2 , ionised and neutral carbon (C^+ and C^0, respectively), and other species. We then compare the model results with observational constraints derived from the line profiles.

Our models were created using a simple Python-based PDR code, PyPDR (Bruderer 2019). The code computes chemical abundances by evolving chemical rate equations iteratively, by utilising a pure gas-phase, time-dependent chemical network (except for H_2), containing 30 species, including CH_2. The input conditions used for the model are UV radiation field, G_0, in Habing units, the total gas density, $n_{\rm H}$, and the cosmic-ray ionisation rate, $\zeta_{\rm H}$. We studied two sets of models with gas densities $n_{\rm H}$ of 10^2 and 10^3 cm^{-3}, each of which was exposed to a UV radiation field of 1 and 10^4. All four models were exposed to the same cosmic-ray ionisation rates, fixed at $\zeta_{\rm H} = 2.2 \times 10^{-16}$ s^{-1}, which corresponds to the typical value expected in diffuse and translucent clouds (Indriolo et al. 2015; Neufeld & Wolfire 2016; Jacob et al. 2020b). The resulting (normalised) abundances of relevant carbon-chain species are displayed in Fig. 6.11 as a function of A_v. In both models with $G_0 = 1$, the CH_2 abundance peaks in the transition layer from C^+ to C with its distribution peaking at $A_v \lesssim 1$. The models with a higher UV radiation field show the CH_2 abundance distribution to follow more closely that of neutral atomic carbon. From both sets of modelled results, it is clear that CH_2 traces gas layers between the dissociation front (which marks the transition from H $\rightarrow$ H_2) and the molecular cloud, tracing gas layers where $C^+ \rightarrow$ C and CO is not the main reservoir of carbon. Overall, the modelled results are consistent with our premise that both CH_2 and CRRLs are probing similar cloud layers.

In Appendix D.3, we present a complete summary of the observed CRRLs; however, as an example, we display the observed recombination line spectrum toward W3 IRS5 in Fig. 6.12. Comparing the narrow line profile of the CRRL with that of the corresponding broader ($\Delta\upsilon \gtrsim 30$ km s^{-1}) H, and He RRLs, it is clear (as has been known for a long time) that the observed CRRLs do not arise from the hot ionised gas of the HII region but, rather, from the periphery of these regions, next to the neutral gas, namely, in PDRs. We separate the narrow line profiles of the CRRL transitions from those of the broader He RRLs, with which they are blended, by subtracting a Gaussian fit to He RRL from the observed spectra. The residual line profile represents the relative contribution of the CRRL which is then used in our analysis. As

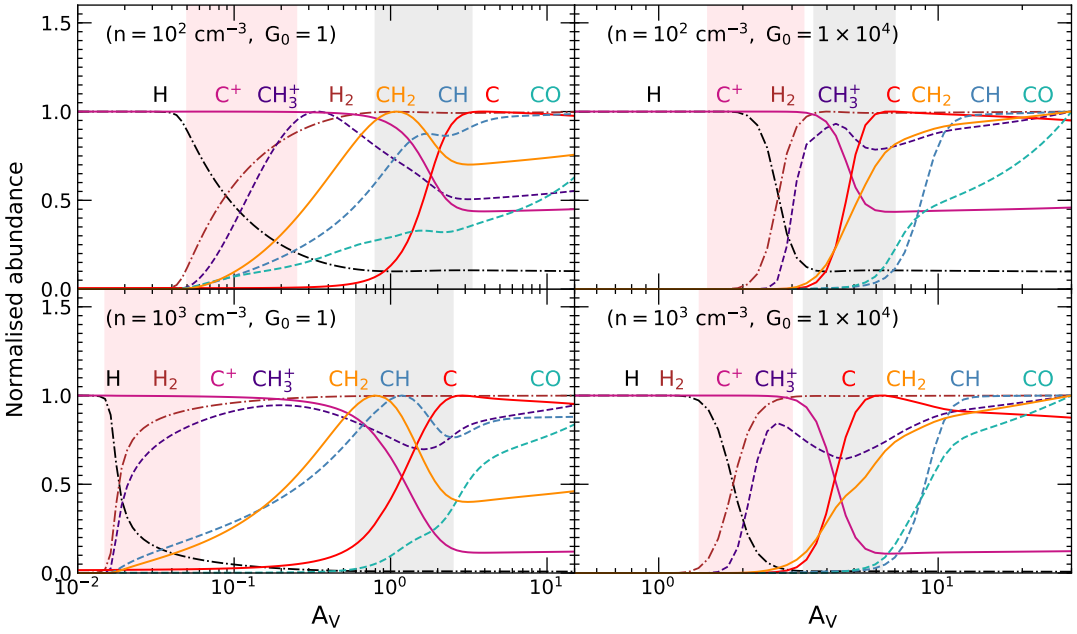

Figure 6.11: Variation of the gas-phase abundances of fundamental species in carbon chemistry, normalised by their respective peak abundances as a function of visual extinction, A_v. The cloud parameters for the different models are as follows: $n_H = 10^2$ cm^{-3}, $G_0 = 1$ (top-left), $n_H = 10^2$ cm^{-3}, $G_0 = 1 \times 10^4$, $n_H = 10^3$ cm^{-3}, $G_0 = 1$ and $n_H = 10^3$ cm^{-3}, $G_0 = 1 \times 10^4$ (bottom-right). All models presented here, use a constant cosmic-ray ionisation rate of $\zeta_H = 2.2 \times 10^{-16}$ s^{-1}. The pink and grey shaded regions in each panel, highlight the transition layer between H-H_2 and C^+-C, respectively.

mentioned in Sect. 6.4, toward some of the sources, the observational setup we used covers several RRLs with principal quantum numbers, n, ranging from 72 to 80 for $\Delta n = 1$. Since we expect the line properties of consecutive HRRLs to be similar, we can estimate calibration uncertainties by comparing the peak temperatures of the different HRRLs covered in our setups for each individual source. On average, we find the line strengths to vary by 23 % at most. Figure 6.12 shows that the centroid velocities and line widths of the CRRLs match the values of the HFS stacked CH_2 line emission. This is in agreement with the gas-phase chemistry revealed by our simple PDR models and strongly suggests that the two species trace the same gas.

It has been shown by Salgado et al. (2017), that the line widths of high frequency CRRLs (with $n < 100$) are dominated by thermal (Doppler) broadening, while Lorentzian profiles best describe low frequency CRRLs (with $n > 100$) because of collisional and/or radiation broadening. Therefore, considering the effect of line broadening as being only due to the random thermal motion of particles in the gas and non-thermal effects or turbulence, the observed line widths can be expressed as follows,

$$\Delta v = \sqrt{\Delta v_{\rm th}^2 + \Delta v_{\rm nth}^2} = \sqrt{\frac{k_B T_{\rm kin}}{m_C} + \langle \Delta v_{\rm nth} \rangle_{\rm rms}^2} \tag{6.1}$$

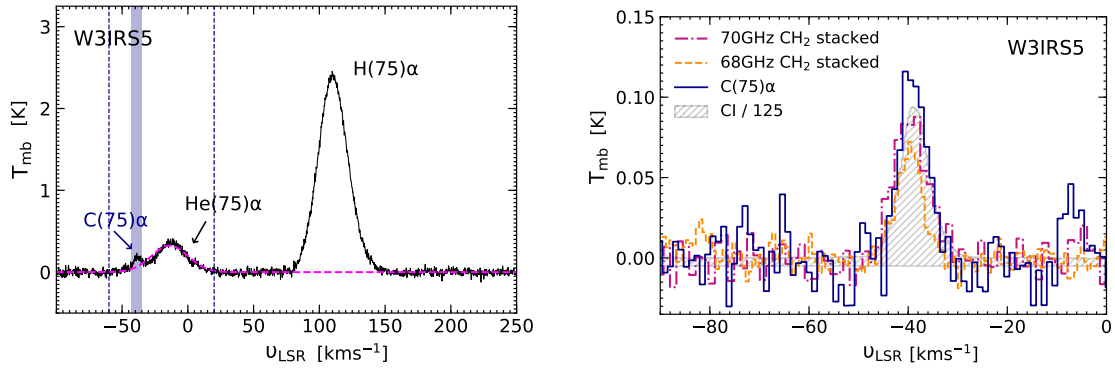

Figure 6.12: *Left*: Observed Hα, Heα, and Cα transitions for n = 75 toward W3 IRS5. The LSR velocity scale is given with respect to the Cα line at 15.82 GHz. The pink dashed curve represents the fit to the He RRL and the shaded purple region confines the CRRL. *Right*: Decomposed CRRL profile in blue alongside the 68 GHz and 70 GHz HFS-stacked CH_2 line profiles displayed by the dashed orange and dashed-dotted violet curves, respectively. The stacked profile of the 70 GHz CH_2 transition was obtained from the HFS decomposition model. The hatched grey regions display the line profile of the $^3P_1 - {}^3P_0$ transition of CI at 492.160 GHz scaled down by a factor of 125 on the $T_{\rm mb}$ scale.

where, $T_{\rm kin}$ is the gas temperature, $k_{\rm B}$ is the Boltzmann constant, $m_{\rm C}$ is the mass of the carbon atom, and $\langle \Delta\upsilon_{\rm nth} \rangle_{\rm rms}$ is the root mean-square measure of the turbulent velocities. Furthermore, based on the premise that the CRRLs and o-CH_2 lines trace the same gas layers, we assume that both species are impacted by the same turbulent flows and will hence have the same turbulent widths, $(\Delta\upsilon_{\rm nth})_{\rm CRRL} = (\Delta\upsilon_{\rm nth})_{\rm CH_2}$. Additionally, since the observed line width of the CH_2 emission is comparable to that of the CRRL (see Fig. 6.12), when re-arranging Eq. 6.1 to equate the non-thermal components, it is clear that the o-CH_2 gas temperature is simply proportional to that of the CRRL, scaled by the ratio of their masses.

From CRRL data alone, it would be difficult to accurately determine the physical conditions of the C^+ region, for example, because of uncertainties involved in their excitation or, practically speaking, simply because of the low intensities of these lines and their blending with the stronger He RRLs. These issues can be overcome by comparing the line intensities of CRRLs with those of the FIR fine-structure line of ionised carbon at 158 μm. This approach has been employed by several studies to constrain the electron density, and temperature of C^+ layers. Typically, the temperatures cover a range of values from 1000 K near the HII region to ~100 K at the outer boundaries of this C^+ layer. Modelling this layer toward the W3 region, Sorochenko & Tsivilev (2000) computed a value for the kinetic temperature, $T_{\rm kin}$, of at most 200 K and an electron density of n_e = 54 cm^{-3}. The PDR structure used in their analysis was adapted from Howe et al. (1991) and does not assume a homogeneous distribution of material but rather that it consists of dense clumps ($n_{\rm H} \sim 10^5$ cm^{-3}) embedded in a dilute medium ($n_{\rm H} \leq 300$ cm^{-3}) at $T_{\rm k} \geq 100$ K in order to be consistent with observations. Therefore, for the specific case of W3 IRS5 we can constrain the gas temperature to a value of at most 233 K using Eq. 6.1.

6.6 Discussion

6.6.1 Non-LTE radiative transfer analysis

We perform non-LTE radiative transfer calculations using the statistical equilibrium radiative transfer code RADEX (van der Tak et al. 2007), for a uniform expanding sphere geometry under the large velocity gradient (LVG) approximation. The code computes level populations, line intensities, excitation temperatures, and optical depths as a function of the physical conditions specified as input, based on the escape probability formalism. Assuming that H_2 is the primary collisional partner of CH_2 in the ISM, we carry out our non-LTE analysis by using rate coefficients recently computed by Dagdigian (2018b) for collisions between CH_2 and Helium from which we obtain o-CH_2–H_2 collisional rate coefficients by scaling the rates by factor of 1.4, for all the fine-structure transitions among the lowest 22 energy levels of o-CH_2. By adopting a background temperature of 2.73 K, with a fixed line width as estimated from the intrinsic widths of the observed Onsala spectra, we run a grid of models with varying physical conditions, with the aim to constrain the gas densities, n_{H_2}, and kinetic temperatures, T_{kin}, to values that are consistent with the observed o-CH_2 emission or its upper limits. The models were computed over a temperature-density grid of size 500×500, for T_{kin} values between 20–300 K (constrained by the collisional data) and n_{H_2} values in the range of 10–10^6 cm^{-3}. Given that we were only able to clearly detect all three sets of o-CH_2 HFS lines toward W3 IRS5, the non-LTE analysis is carried out specifically for this source. Using absorption spectroscopy, Polehampton et al. (2005) were able to (from their column density measurements) determine a [CH]/[CH_2] ratio through observations of both CH and CH_2 transitions near 150 μm and 107.7/127.6 μm, respectively, using the ISO-LWS. These authors obtained a [CH]/[CH_2] ratio of 2.7±0.5 for an ortho-to-para CH_2 ratio of 1.6, and a value closer to 3.7 for an ortho-to-para CH_2 ratio of 3 for the (systemic) +64 km/s velocity component toward Sgr B2(M), values that are consistent with results obtained by Viti et al. (2000) – whose models additionally take into account grain-surface chemistry. This corresponds to o-CH_2 abundances with respect to H_2 between 9.4×10^{-9} and 1.6×10^{-8} when scaled using the [CH]/[H_2] ratio of $3.5{\times}10^{-8}$ as determined by Sheffer et al. (2008). By using CH column densities determined toward W3 IRS5 by Wiesemeyer et al. (2018) from this radical's 150 μm ground-state transition observed using the GREAT instrument on board the Stratospheric Observatory For Infrared Astronomy (SOFIA) (Young et al. 2012) and the above [CH]/[CH_2] ratio, we can constrain the column densities of o-CH_2 to about $(4.5 \pm 1.7) \times 10^{14}$ cm^{-2} for ortho-to-para CH_2 ratios of between 1.6 and 3. We therefore ran models in the temperature-density plane for fixed values of N(o-CH_2) at 3×10^{14}, 5×10^{14} and 7×10^{14} cm^{-2}, the results of which are displayed in Fig. 6.13. The radiative transfer analysis is further simplified by assuming a beam filling factor of unity for an extended o-CH_2 cloud. From the results of each column density model, we see that the different o-CH_2 lines trace similar temperature and density conditions as indicated by their contours. We constrain these results by comparing them with the distribution of the line intensity ratio between the 70 GHz, and 68 GHz lines which are both free from contamination, in the temperature-density plane. The physical conditions that prevail in these regions are constrained based on the behaviour of χ^2_{red} across this parameter space. The χ^2_{red} value is

Table 6.3: Summary of RADEX results.

Model	N(o-CH_2) [cm^{-2}]	$\log_{10}(n_{H_2})$ [cm^{-3}]	T_{kin} [K]
I	3×10^{14}	$3.63^{+0.10}_{-0.09}$	202^{+33}_{-32}
II	5×10^{14}	$3.57^{+0.11}_{-0.10}$	163^{+27}_{-25}
II	7×10^{14}	$3.42^{+0.15}_{-0.14}$	155^{+26}_{-25}

computed across the entire grid as follows,

$$\chi^2 = \sum \left(T_{\rm r,obs} - T_{\rm r,mod}\right)^2 / \sigma^2_{T_{\rm r,obs}}, \tag{6.2}$$

$$\chi^2_{\rm red} = \chi^2/(n-1), \tag{6.3}$$

where $T_{\rm r,obs}$ and $T_{\rm r,mod}$ represent the observed and modelled line brightness temperatures on the $T_{\rm mb}$ scale, $\sigma^2_{T_{\rm r,obs}}$ represents uncertainties in the observed o-CH_2 spectra and n is the number of degrees of freedom. The $\chi^2_{\rm red}$ values were fit at a 99.9% probability for two degrees of freedom. For each column density model, we find that the $\chi^2_{\rm red}$ values show more variations with $T_{\rm kin}$ than with n_{H_2}. In Table 6.3, we summarise the estimated range of gas temperatures and densities for the different models. Across the different models we derive $T_{\rm kin}$ between (150–200) K and $n_{H_2} \sim 3 \times 10^3$ cm^{-3} consistent with not only previous chemical models (Lee et al. 1996) but also our hypothesis that o-CH_2 must arise in a hot but dilute media. The derived values of temperature are also consistent with that determined from the comparison with CRRLs, as discussed in Sect. 6.5.6. Furthermore, with critical densities of the order of 10^5 cm^{-3}, the derived densities reveal that the observed 68–71 GHz o-CH_2 emission lines arise from sub-thermally excited gas.

We expect the non-LTE analysis toward the W51 pointing positions to reproduce physical conditions similar to those derived toward W3 IRS5 since the line intensities of both the 70 GHz and 68 GHz components of CH_2, and their corresponding line ratios are comparable toward both sources. The results of this analysis confirm our suspicions and clearly addresses why CH_2 is not widely detected in the Orion Bar PDR. From the non-LTE analysis presented here, we would expect the abundance of CH_2 to peak in regions with H_2 gas densities of $\sim 3 \times 10^3$ cm^{-3} and the Orion Bar PDR, as discussed earlier, simply traces gas of higher densities ($>10^5$ cm^{-3}). The dense Orion Bar is a spatially limited region in the much larger, on average, more diffuse PDR associated with the Orion Nebula, for which a density of 10^5 cm^{-3} is a representative value (Cuadrado et al. 2015; Nagy et al. 2015a). Because of the Orion Nebula's proximity ($\approx$400 pc) this larger scale PDR is well resolved, even in our arc minute size beams. However, the other regions toward which we detect CH_2 emission are much further away and our observations sample the total extent of their large, low-density PDRs. This has already been discussed at the end of Sect. 6.5.5 and here finds support by our non-LTE calculations. Furthermore, the nominal hydrogen nucleus density we derive is a factor of $\sim$5–10 higher than the value of 500–1000 cm^{-3} estimated by Welty et al. (2020), who were only able to obtain upper limit for the CH_2 transition near 1397 Å in the translucent cloud along the LOS toward HD 62542.

As for the excitation of these lines, similar to the results obtained by Dagdigian (2018b),

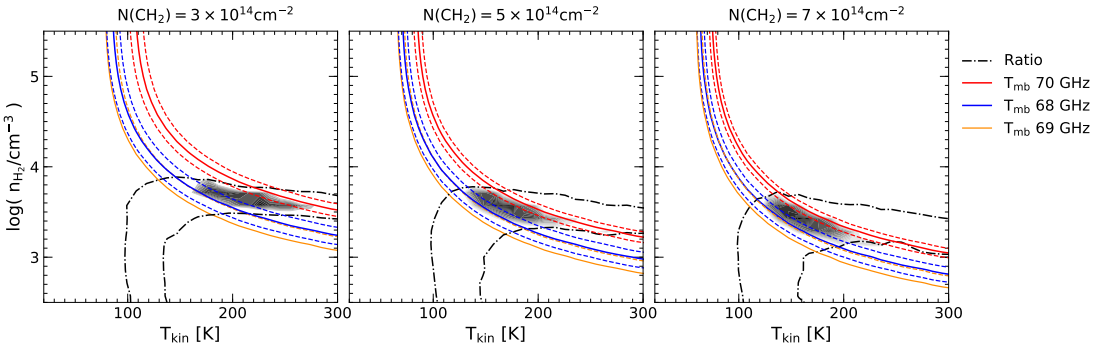

Figure 6.13: RADEX non-LTE modelling of o-CH_2 toward W3 IRS5. The solid and dashed-red, blue and orange curves represent the observed peak main-beam brightness temperatures of the 70 GHz, 68 GHz and 69 GHz, respectively, and their uncertainties. We note that for the 69 GHz o-CH_2 lines being contaminated by NS, we only represent the uncontaminated modelled intensity and an upper limit. The black dashed and dotted lines mark the limits of the brightness temperature ratio between the 70 and 68 GHz lines. The grey shaded region characterises $\chi^2_{\rm red}$ values of < 11 corresponding to a probability of 99.9 % over the temperature-density plane for models with fixed column density values of 3×10^{14} cm^{-2} (*left*), 5×10^{14} cm^{-2} (*centre*), and 7×10^{14} cm^{-2} (*right*).

we find that over the very wide range of gas densities we modelled ($n_{\rm H_2}$ = 10–10^8 cm^{-3}), our calculations produce negative opacities ($\sim -10^{-2}$) or line inversion at an excitation temperature of -0.36 K. We thus find all three of the fine-structure lines of the $4_{04} - 3_{13}$ transition of o-CH_2 seen in emission to be weak masers. From our RADEX models, we compute a $\sim$1% inversion in the population of the $4_{04} - 3_{13}$ fine structure transitions, where the percentage of population inversion for a two-level system is given by $(n_{\rm u} - n_{\rm l})/(n_{\rm u} + n_{\rm l})$ and $n_{\rm u}$, and $n_{\rm l}$ are the upper and lower energy level populations. Since the models produce masing conditions even in the absence of strong, external radiation fields and without line overlap considerations, it is clear that the observed masing effect in these high-lying lines is a robust phenomenon which preferentially populates the $N_{K_aK_c} = 4_{04}$ level over that of the $N_{K_aK_c} = 3_{13}$ level. The observed emission spectra may have contributions from the extended continuum background radiation in these regions as well as collisional pumping effects. While the weak level-inversion observed in these lines explains why they are detectable in the first place, the degree of population inversion itself is greatly dependent on the collisional rate coefficients.

We exclusively detect CH_2 within PDR cloud layers associated with HII regions and not in those associated with (P)PNe and SNRs, a few of which were also observed by us. The lack of detectable amounts of CH_2 in these types of objects can be attributed to the fact that CH_2 arises from dilute PDR layers, as implied by our non-LTE radiative transfer analysis. The PDRs surrounding (P)PNe are dense regions ($\sim 10^5 - 10^6$ cm^{-3}) as they form in the compressed inner layers of the remnant circumstellar envelopes of AGB stars (see for example Cox et al. 2002). This argument explaining the non-detection of CH_2 in (P)PNe owing to the elevated densities of their PDRs also holds true for the case of the SNRs for which upper limits are

presented in this study. Our Onsala 20 m beam was pointed toward a dense molecular clump in IC 443 residing in the interaction zone of the SNR with a molecular cloud that has gas densities as high as 10^5 cm^{-3} (Dickman et al. 1992), while for the dense molecular knots detected in high-J CO lines toward Cas A, gas densities of 10^{6-7} cm^{-3} have been determined (Wallström et al. 2013).

Using the physical conditions derived from these models and the rate coefficients calculated between p-CH_2–H_2, which are also based on calculations by Dagdigian (2018b), we predict the brightness temperatures and excitation temperature for the 444 GHz p-CH_2 transitions. The model was run for a range of gas densities $n(H_2) = 10 - 10^9$ cm^{-3} with a fixed CH_2 column density and gas temperature of N(p-CH_2) = 5×10^{14} cm^{-2} (in the limit where N(p-CH_2) = N(o-CH_2)) and T_{kin} = 163 K, respectively. The modelled results are displayed in Fig. 6.14. Up until the critical density of 2×10^7 cm^{-3} is reached, the brightness temperatures reproduced by the models are low and even slightly negative, particularly for the range of densities derived from the 70 GHz o-CH_2 lines. The excitation temperature at these frequencies is also small and close to the background radiation temperature, which, for these models, is governed by the cosmic microwave background at 2.73 K. With excitation temperatures below 10 K up to densities of 10^8 cm^{-3}, the models suggest that it is highly unlikely to observe detectable amounts of p-CH_2 at 444 GHz and in absorption, if any at all.

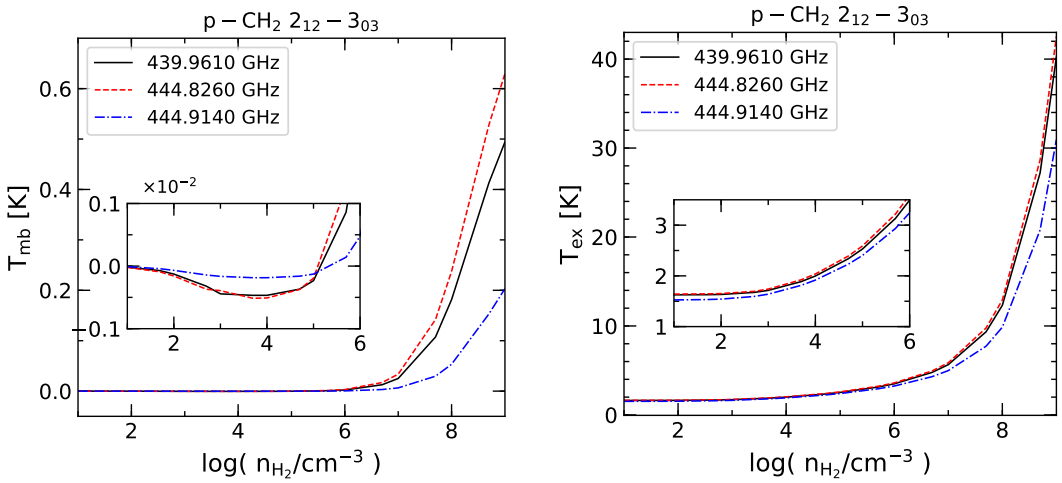

Figure 6.14: Main-beam brightness temperature (T_{mb}) and excitation temperature (T_{ex}) for the $2_{12} - 3_{03}$ fine-structure lines of p-CH_2. The inset panels expand on the (T_{mb}) and (T_{ex}) values for gas densities between 10–10^6 cm^{-3}.

6.6.2 Comparison with atomic carbon

We further compare the observed CH_2 and CRRLs with that of the neutral atomic carbon, CI, $^3P_1 - {}^3P_0$ transition at 492.160 GHz for those sources toward which this transition is available,

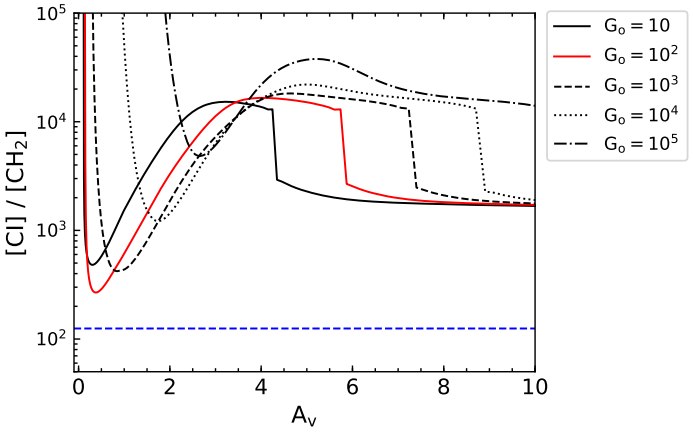

Figure 6.15: Variation in the [CI]/[CH_2] abundance ratio as a function of A_v. The different curves represent models at different values of G_o, as labelled. The dashed blue curve marks the observed [CI]/[CH_2] intensity ratio of 125.

using ancillary data from the Herschel/HIFI archive[12]. These observations, published in Gerin et al. (2015), were procured using the HIFI band 1a which provides a FWHM beam width of 43.1″ at these frequencies, which is comparable to the beam size of our CH_2 and CRRL observations. We find that the line ratio between the CI, and CH_2 70 GHz emission to be almost a constant, with a value of 125:1 toward W3 IRS5, W51 M, and W49 N, (see Fig. 6.12 and top panel of Fig. D.5). Furthermore, we see that toward W51 M and W49 N the CI emission shows two components along the LOS and, perhaps, the second component may also be present in CH_2 but has gone undetected because our observations do not attain the sensitivity necessary to detect this weaker component.

The similarity in the line intensity ratio between the emission of the CI and the 70 GHz CH_2 component toward these three sources strongly suggests that CH_2 is likely to be formed under similar physical conditions in these regions, in spite of their different levels of star-formation. Using the constraints on the physical conditions derived in Sect. 6.6.1, we revise the chemical models presented in Sect. 6.5.6. We once again ran the PyPDR code, this time for the gas density and temperature values derived from our non-LTE analysis. In order to reproduce the observed [CI]/[CH_2] line intensity ratio of 125, we carried out the analysis for different models with varied values of G_o at a fixed dust temperature of 50 K. None of the models were capable of reproducing the observed [CI]/[CH_2] line intensity ratio (see Fig. 6.15). The model that most closely matched the observations gives us a [CI]/[CH_2] ratio of 268, and was that with a $G_o = 10^2$ in Habing units for values of A_v between 0 and 1. However, overall the modelled line ratios are almost always overestimated; or rather, the CH_2 abundance is underestimated. This could either be because the underlying chemical network for CH_2 used in these models is incomplete or because the PDR model itself is too simplistic or a combination of both. Perhaps a more robust PDR model is required, namely, one which includes dust illumination by both an internal as well as an external heating source within the PDR structure.

[12]See, http://archives.esac.esa.int/hsa/whsa/

6.7 Summary and conclusions

In this work, we present observations of the $4_{04} - 3_{13}$ transitions of o-CH_2 made with both the KP 12 m and Onsala 20 m telescopes. The former observations were prompted by the non-detection of the 68–71 GHz CH_2 lines toward the Orion-KL hot core using the IRAM 30 m telescope and the GBT. Our KP observations were therefore used, firstly, to verify the original detection of CH_2 toward the Orion-KL, and secondly, to address if the CH_2 emission is extended by investigating nearby positions in OMC-1 and its related HII region/PDR. These observations confirm the detection of CH_2 toward Orion-KL and reveal higher intensities of CH_2 toward PDR positions. The interpretation of these results clearly indicates that the CH_2 emission is extended but does not constrain their source of origin. We clarify the nature of the CH_2 emission using the smaller angular beam size of the Onsala 20 m telescope. These observations show that the distribution of CH_2 toward the Orion KL-S and Orion Bar regions coincides with peaks of the [CII] emission. This is consistent with the results of simple PDR models which show that the CH_2 abundance peaks in gas layers where ionised carbon recombines to form neutral atomic carbon. As for the observations, we find that the line profiles of the CH_2 transitions are akin to those of CRRLs, which are well-known tracers of PDRs. Based on CH_2's association with PDRs, we expanded our target sample to well known HII regions, which naturally have associated PDRs, and successfully detected the 70 GHz fine-structure line and its HFS components for the first time toward W51 E, W51 N, W49 N, W43, W75 N, DR21, and S140 as well as all three of the 68–71 GHz fine- and HFS components toward W3 IRS5. Stacking each of the HFS components of the 68 GHz transition in a previously averaged spectrum of the different W51 positions revealed a 3.5σ detection of the 68 GHz CH_2 line. Carrying out a non-LTE analysis, we constrained the physical conditions of the CH_2 clouds to gas densities and temperatures of $\sim 3 \times 10^3$ cm^{-3} and 150–200 K, respectively. The physical conditions probed are consistent with those that prevail in translucent clouds and are in agreement with the results of previous theoretical models by Lee et al. (1996), who show the fractional abundances of CH_2 to peak at intermediate densities. While our non-LTE analysis was focused on W3 IRS5, the HFS-stacked and averaged pointing positions toward W51 show similar line intensities and therefore probe similar gas conditions. It is only with further, highly sensitive observations of the 68 GHz component of CH_2 can we verify if the physical properties of the gas probed by CH_2 are ubiquitous across sources. Our analysis of the excitation conditions reveal that these lines are weakly masing with low negative excitation temperatures. The weak level inversion amplifies the emission of these lines which may otherwise have remained undetectable. We also report the non-detection of the 2_{12}–3_{03} transitions of p-CH_2 toward Orion S at a 3σ upper limit of 24 mK and at 0.23 K toward the other positions in Orion.

Our results establish the $4_{04} - 3_{13}$ transition of CH_2 as tracing the hot but low density component of the ISM present in PDR layers, with its abundance peaking at the edges of dense clouds. As an essential intermediary in interstellar carbon chemistry, it is important to carry out further observations of this molecule and particularly of its energetically lower transitions. We hope that the results of our study will help guide future searches for this radical in other sources at FIR and sub-millimetre wavelengths.

6.8 Open questions and outlook

The present work provides strong observational evidence for CH_2 in PDRs of relatively low density (several times 10^3 cm^{-3}). This is supported by our radiative transfer modelling, which suggests temperatures >150 K for the CH_2-bearing material. While such densities are also found in translucent interstellar clouds, the temperatures in these clouds are thought to be much lower, 10–50(?) K (Snow & McCall 2006). Evidence for CH_2 in translucent, and maybe even diffuse interstellar clouds can also be found in the spectra of the FIR o- and p-CH_2 ground-state transitions toward Sgr B2. In these, Polehampton et al. (2005) find, absorption not only at Sgr B2's systemic velocity but also from clouds along the LOS to the Galactic centre region. Although these ISO/LWS data have a low spectral resolution, the fitted velocity components closely correspond to those of numerous mm-wavelength absorption lines that arise from such intervening clouds, whose physical conditions are still poorly constrained, but which are thought to consist of translucent or diffuse interstellar material (Thiel et al. 2019); however, for statistical reasons they are unlikely to be PDRs. This raises the question whether CH_2 can attain substantial abundance not only in PDRs, but in translucent (or even diffuse) clouds as well. The available evidence from electronic transitions discussed in Sect. 6.1 is so far inconclusive, but the procurement and analysis of further UV absorption data would be most interesting.

As for extra-galactic observations, Muller et al. (2011) do not detect o-CH_2 in the line survey they carried out with the Australian Telescope Compact Array of the 7 mm window, corresponding to rest frequencies of 57–94 GHz along two sight lines through the red-shift $z = 0.88582$ foreground galaxy that absorbs the continuum of the more distant gravitational lens-magnified blazar, PKS 1830-211. The typical densities and temperatures of the emitting gas in the foreground galaxy are a few times 10^3 cm^{-3} and 80 K, respectively, conditions that are neither dilute enough nor hot enough to excite the CH_2 lines in question. Alternatively, their survey is still too shallow to detect the CH_2 lines.

It is difficult to meaningfully constrain the CH_2 abundance just with HFS lines assigned to a single rotational level ($J = 5$) – while emission from higher frequency rotationally excited sub-millimetre CH_2 transitions will remain undetectable because of their high critical densities. To compound this difficulty, the only accessible lines that are likely to be excited; the 69–71 GHz o-CH_2 lines, extensively discussed here, are ubiquitously weak and boosted into detectability by inversion, which makes their interpretation not quite so straightforward. Moreover, the validity of the conclusions drawn from these lines is heavily dependent on the quality of the collisional rate coefficients used in the radiative transfer modelling, which are currently only available for the CH_2–He system (and were scaled by us to apply to collisions with H_2). Recently, van der Tak et al. (2020) have discussed the current status and future plans for the Leiden Atomic and Molecular Database (LAMDA). In this paper, they review, among others, the use of collisional rate coefficients for collisions of molecules with He and the usual practice of scaling to estimate H_2 rate coefficients. For the case of CH_2 they assign a low accuracy (factor of $\sim$ 3–4) for this scaling and conclude that CH_2, amongst other molecules, has 'to be the object of new scattering studies considering H_2 as a projectile'. Calculating CH_2–H_2 rate coefficients would certainly be a significant computational project. Given that in a practical sense, the complete interpretation of CH_2 emission in the ISM critically depends

on these collisional rate coefficients, it is one that should be considered.

Apart from the 68–71 GHz lines, we are only left with the UV and the FIR resonance lines. These also present a bleak picture as the former still await a convincing identification in the ISM. With regard to the FIR lines, unfortunately, neither the o- and nor the p-CH_2 ground state lines at 127.6 and 107.7 μm, respectively, were covered by the HIFI instrument on Herschel. Moreover, none of the modules of the GREAT instrument on SOFIA covers their wavelengths at present. Even if GREAT was able to do this (and it may do so in the future), detecting these lines might be difficult given their low opacities observed by ISO (with the low LWS resolution) of just 0.02 to 0.05 toward one of strongest FIR sources in the sky, Sgr B2 (whereas for the 149 μm CH ground state, lines opacities of $\sim$0.4 are determined with the same instrument). Given all these conditions, a full observational picture of CH_2 in an astrochemical context remains elusive.

Part IV

Probing the diffuse atomic ISM with a molecule

Chapter 7

Argonium as a tracer for diffuse atomic gas

It cannot, of course, be stated with absolute certainty that no elements can combine with argon; but it appears at least improbable that any compounds will be formed.

Sir William Ramsay, Nobel Prize in Chemistry, 1904.

Overview

At the end of the 19th century between 1894 and 1898, Sir William Ramsay made the spectacular discovery of five new elements- helium, neon, argon, krypton, and xenon. His discovery of the eighth column of the *Periodic Table of elements* was initially inspired by the discrepancies in the atomic weight of nitrogen, reported by Lord Rayleigh in 1892. The weight of atomic nitrogen determined from the atmosphere was found to be heavier than that determined from chemical compounds. Ramsey suspected the difference to arise from the presence of a more heavier and previously undiscovered element. In cooperation with Rayleigh, Ramsey was able to isolate this chemically inert element and thereby discover the first Noble gas element, argon (derived from the Greek word *argos* meaning *'inactive'*).

Years later, in 2010, scientists were puzzled once again by a peculiar spectrum near 617 GHz (486 μm) observed using the *Herschel* space observatory. It was speculated to be from a thus far unidentified species. The observed spectral features were first seen in absorption along the line-of-sight toward star-forming regions but was 'peculiar' because its spectrum lacked absorption signatures at velocities corresponding to that of the background molecular cloud. This hinted at the association of this *mysterious* species with primarily atomic cloud layers. While, naturally occurring Noble gas elements have not been detected on the Earth's surface or atmosphere, till date, many Noble gas containing molecules have been synthesised in the laboratory under extreme conditions. Therefore it is conceivable that molecules containing Noble gas elements may be formed in the harsh environments of space. Therefore, aided by laboratory efforts, astronomers attempted to match the unidentified spectral feature with a wide array of molecules including argonium, ArH^+. However, scientists were looking for signatures from argon-40 substituted ArH^+, as argon-40 is the most abundant isotope of argon in the Earth's atmosphere. Later through *Herschel* observations toward the Crab Nebula by Barlow et al. (2013), this unidentified feature was rightfully attributed to argon-36 substituted ArH^+,

who observed both its $J = 1 - 0$ and $J = 2 - 1$ rotational lines in emission.

Although, these detections were limited to the first quadrant of the Galaxy, the existing data suggests that ArH^+ ubiquitously and exclusively probes the diffuse atomic regions of the interstellar medium. In this study we extend the coverage of ArH^+ to other parts of the Galaxy with new observations of its $J = 1 - 0$ transition along seven Galactic sight lines toward bright sub-millimetre continuum sources, with the aim to benchmark its efficiency as a tracer of purely atomic gas. We further evaluate its correlation (or lack thereof as suggested by chemical models) with other well known atomic gas tracers like OH^+ and H_2O^+ as well as the molecular gas tracer CH, discussed in Chapter 3. This chapter is published as a paper titled 'Extending the view of ArH^+ chemistry in diffuse clouds' in *Astronomy & Astrophysics*, Jacob et al. (2020b)[1], with changes made only in order to adapt it to the layout of this thesis.

7.1 Introduction

Chemists have been fascinated by the possible existence and formation of noble gas compounds since the synthesis of the first noble gas-bearing molecule, $XePtF_6$, (Bartlett & Lohmann 1962) and the molecular ion, HeH^+, (Hogness & Lunn 1925) in the laboratory. In an astronomical setting, the helium hydride cation HeH^+ had long been predicted to be the first molecule to form in the Universe (Galli & Palla 2013) and to be detectable in planetary nebulae (PNe) (Black 1978), many years before it was actually discovered in the PN NGC 7027 (Güsten et al. 2019). A few years ago, interest in the role of noble gas-bearing molecules in astrochemistry received attention after the detection of argonium, ArH^+, the first noble gas compound detected in the interstellar medium (ISM). This serendipitous discovery was made towards the Crab Nebula supernova remnant by Barlow et al. (2013), who observed the $J = 1 - 0$ and $J = 2 - 1$ rotational transitions of ArH^+ in emission using the Fourier Transform Spectrometer (FTS) of the Herschel Spectral and Photometric Imaging REceiver (SPIRE) (Griffin et al. 2010; Swinyard et al. 2010). This led to the subsequent identification of the $J = 1 - 0$ transitions of both $^{36}ArH^+$ and $^{38}ArH^+$ in the ISM by Schilke et al. (2014), which could be attributed to spectral features that had remained unidentified for some time in spectra taken with the Heterodyne Instrument for the Far Infrared (HIFI), also on *Herschel* (de Graauw et al. 2010). These authors detected these two ArH^+ isotopologues in absorption, against the strong sub-millimetre wavelength continuum of the high-mass star-forming regions (SFRs) Sgr B2(M) and (N), G34.26+0.15, W31 C, W49(N), and W51e under the framework of the HIFI key guaranteed time programmes Herschel observations of EXtra-Ordinary Sources (HEXOS) (Bergin et al. 2010) and PRobing InterStellar Molecules with Absorption line Studies (PRISMAS) (Gerin et al. 2010). Following this, Müller et al. (2015) reported $^{36}ArH^+$ and $[]^{38}ArH^+$ absorption along two sight lines through the redshift $z = 0.8858$ foreground galaxy absorbing the continuum of the gravitational lens-magnified blazar, PKS 1830-211, using the Atacama Large Millimetre/sub-millimetre Array (ALMA, Wootten & Thompson 2009).

Quantum chemical considerations have shown that ArH^+ can form via gas phase reactions between Ar^+ and molecular hydrogen (Roach & Kuntz 1970). Additionally, Theis et al. (2015)

[1]Jacob et al. A&A, 643, A91, 2020, reproduced with permission ©ESO

have hypothesised that the formation of ArH^+ can also proceed via the dissociation of a semi-stable intermediate product, ArH_2^+:

$$\mathrm{Ar} \xrightarrow{\mathrm{CR}} \mathrm{Ar}^+ \xrightarrow{\mathrm{H_2}} \begin{cases} \mathrm{ArH}^+ + \mathrm{H} & (\Delta E = 1.436\ \mathrm{eV}) \\ \mathrm{ArH}_2^+ \rightarrow \mathrm{ArH}^+ + \mathrm{H} & (\Delta E = 1.436\ \mathrm{eV})\,. \end{cases}$$

ArH^+ is formed in diffuse interstellar clouds with predominantly atomic gas and a small molecular hydrogen content and is readily destroyed primarily via proton transfer reactions with neutral species, in particular with H_2 (Schilke et al. 2014), while photo-dissociation has been shown to be less important (Roueff et al. 2014). Chemical models by Schilke et al. (2014) and Neufeld & Wolfire (2016) suggest that ArH^+ must reside in low-density gas with very small molecular fractions, $f_{\mathrm{H_2}} = 2n(\mathrm{H_2})/[n(\mathrm{H\,I}) + 2n(\mathrm{H_2})] = 10^{-4} - 10^{-2}$, and high cosmic-ray ionisation rates, $\zeta_{\mathrm{p}}(\mathrm{H}) = 4 - 8 \times 10^{-16}\ \mathrm{s}^{-1}$, thereby establishing the unique capabilities of this cation as a tracer of purely atomic gas. Remarkably, to quote Schilke et al. (2014), 'Paradoxically, the ArH^+ molecule is a better tracer of almost purely atomic hydrogen gas than HI itself.'

The chemical significance of ArH^+ in the ISM has triggered both laboratory and theoretical studies of this molecule (Bizzocchi et al. 2016; Coxon & Hajigeorgiou 2016). Recently, Priestley et al. (2017) have discussed ArH^+ in the extreme environment of the Crab Nebula, while Bialy et al. (2019) have studied the role of super-sonic turbulence in determining the chemical abundances of diffuse gas tracers, including ArH^+.

As to observations, after the end of the *Herschel* mission in mid-2013, to observe the lines of ArH^+ and many other light hydrides in the sub-millimetre/far-infrared wavelength regime, we must rely on ground based observatories and the air-borne Stratospheric Observatory for Infrared Astronomy (SOFIA). A large part of this range cannot be accessed from the ground because of absorption in the Earth's atmosphere. Still, observations in certain wavelength intervals are possible, even from the ground, in the so-called sub-millimetre windows. The frequencies of the ArH^+ transitions, lie at the border of such a window and can be observed from high mountain sites under exceptional conditions. In this paper we present observations of the $J = 1 - 0$ transition of $^{36}ArH^+$ near 617 GHz along the line-of-sight (LOS) towards a sample of seven sub-millimetre and far-infrared bright continuum sources in the Galaxy, made with the new SEPIA660 receiver on the Atacama Pathfinder Experiment 12 m sub-millimetre telescope (APEX). The observational setup used, along with the data reduction is described in Sect. 7.2.

In addition to ArH^+, our observing setup allowed simultaneous observations of the $N_{K_aK_c} = 1_{10} - 1_{01}, J = 1/2 - 3/2$ and $J = 3/2 - 3/2$ transitions of para-H_2O^+ at 604 and 607 GHz, respectively. The H_2O^+ molecular ion plays an important role in elementary processes in the ISM and exists in two symmetric states of opposite parities, ortho- and para-H_2O^+, corresponding to the different spin configurations of the hydrogen atoms. By combining our p-H_2O^+ data with previously obtained data of o-H_2O^+, which is available for our same sample of targets, we are able to investigate the ortho-to-para ratio of H_2O^+. Studying the relative abundance of the two states can give us significant insight into the efficiency of conversion between them, the formation pathway of H_2O^+ and the thermodynamic properties of the gas

that contains it. The acquisition of the data for para-H_2O^+, as well as the retrieval of archival data is also described in Sect. 7.2. Sect. 7.3, presents the observed spectra and the derived physical parameters, which is followed by our analysis and discussion of these results in Sect. 7.4. Finally, our conclusions are given in Sect. 7.5.

7.2 Observations

The $J = 1-0$ transition of $^{36}ArH^+$ (hereafter ArH^+) was observed in 2019 July–August (Project Id: M-0103.F-9519C-2019) using the Swedish-ESO PI (SEPIA660) receiver (Belitsky et al. 2018; Hesper et al. 2018) on the APEX 12 m sub-millimetre telescope. It is a sideband separating (2SB), dual polarisation receiver, covering a bandwidth of 8 GHz, per sideband, with a sideband rejection level >15 dB. The observations were carried out in wobbler switching mode, using a throw of the wobbling secondary of 120″ in azimuth at a rate of 1.5 Hz, fast enough to reliably recover the continuum emission of the background sources which represent sub-millimetre bright massive clumps within SFRs in the first and fourth quadrants of the Galaxy, selected from the APEX Telescope Large Area Survey of the GALaxy at 870 μm (ATLASGAL) (Schuller et al. 2009; Csengeri et al. 2014). Information on our source sample is given in Table 7.1. The receiver was tuned so that the lower sideband (LSB) was centred at a frequency of 606.5 GHz, covering both the $N_{K_aK_c} = 1_{10} - 1_{01}, J = 3/2 - 1/2$ and $J = 3/2 - 3/2$ fine-structure transitions of p-H_2O^+ at 604.678 and 607.227 GHz, respectively, while the upper sideband (USB) was centred at a frequency of 618.5 GHz that covers the ArH^+ $J = 1 - 0$ transition at 617.525 GHz (and also includes an atmospheric absorption feature at 620.7 GHz). The spectroscopic parameters of the different transitions that are studied in this work are discussed in Table. 7.2.

Our observations were carried out under excellent weather conditions, with precipitable water vapour (PWV) levels between 0.25 and 0.41 mm, corresponding to an atmospheric transmission at the zenith better than or comparable to 0.5 in both sidebands and a mean system temperature of 880 K, at 617 GHz. In Fig. 7.1 we display the corresponding atmospheric zenith transmission from the APEX site and, for comparison, we also present the atmospheric transmission for PWV = 1.08 mm, which corresponds to the 50% percentile[2] of the PWV values measured over a span of more than 12.8 years on the Llano de Chajnantor (Otarola et al. 2019). The atmospheric transmission curves presented in Fig. 7.1 are computed based on the *am* transmission model[3] developed by the Smithsonian Receiver Lab at the Smithsonian Astrophysical Observatory. On average we spent a total (on+off) observing time of 2.3 hr towards each Galactic source. The half power beam-width (HPBW) is 10.″3 at 617 GHz. The spectra were converted into main-beam brightness temperature units using a forward efficiency of 0.95 and a main-beam efficiency of ∼0.39 (determined by observing Mars). The calibrated spectra were subsequently processed using the GILDAS/CLASS software[4]. The spectra obtained towards the different sources were smoothed to velocity bins of ∼1.1 km s^{-1} and a first

[2]Meaning that the PWV content was 1.08 mm or lower for half of the covered time period.

[3]See `https://www.cfa.harvard.edu/~spaine/am/` for more information on the *am* atmospheric model.

[4]Software package developed by IRAM, see `https://www.iram.fr/IRAMFR/GILDAS/` for more information regarding GILDAS packages.

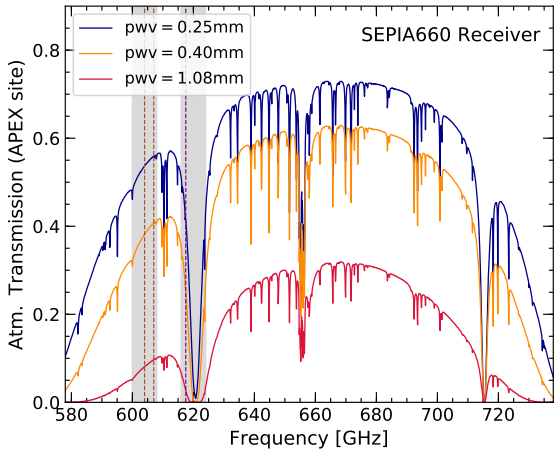

Figure 7.1: Calculated atmospheric zenith transmission of the entire 450 μm submillimeter window for the site of the APEX telescope for three values of the precipitable water vapour column: 0.25 mm (dark blue), 0.40 mm (orange), and 1.08 mm (red). The grey shaded regions mark the 8 GHz frequency windows covered by each of the two sidebands (separated by 8 GHz) of the SEPIA660 receiver. The dashed brown and pink lines mark frequencies of the p-H_2O^+ and ArH^+ lines discussed in this work, respectively.

order polynomial baseline was removed.

In addition to the results of the ArH^+ and p-H_2O^+ observations described above, we use complementary APEX data of OH^+, some of which has already been published by Wiesemeyer et al. (2016). The ancillary o-H_2O^+ data used here, was procured as a part of the Water in Star-forming regions with Herschel (WISH) survey (van Dishoeck et al. 2011) using the HIFI instrument on the Herschel Space Observatory and retrieved using the Herschel Science Archive[5]. The spectroscopic parameters of these lines are also summarised in Table. 7.2.

Furthermore, to be able to constrain the theoretical predictions of ArH^+ abundances, we obtained archival data of the HI 21 cm line. We use archival data of HI absorption and emission from the THOR survey[6] for AGAL019.609−00.234, data presented in Winkel et al. (2017) for AGAL031.412+0.31 and data from the SGPS database (McClure-Griffiths et al. 2005)[7] for the remaining sources. By combining the absorption profiles with emission line data, we were able to determine HI column densities as described in Winkel et al. (2017). The results of the HI analysis, namely the optical depth, spin temperatures, and HI column densities along with the corresponding HI emission and absorption spectra are given in Appendix E.1. We also compare the ArH^+ line profiles with those of molecular hydrogen derived from its diffuse gas proxy, CH, using data presented in Jacob et al. (2019) for AG330.954−00.182, AG332.836−00.549 and AG351.581−00.352. We also present CH 2 THz data that was previously not published, towards AG10.472+00.027 observed using the upGREAT receiver on board SOFIA. The observational setup used, is akin to that detailed in Jacob et al. (2019), for the other sources.

[5]http://archives.esac.esa.int/hsa/whsa/

[6]THOR is The HI/OH/Recombination line survey of the inner Milky Way observed using the Very Large Array (VLA) in C-configuration (Beuther et al. 2016).

[7]SGPS is the Southern Galactic Plane Survey, which combines data from the Australia Telescope Compact Array and the Parkes Radio Telescope.

Table 7.1: Properties of the sources analysed in this work.

Source	Coordinates (J2000)				$d^{(a)}$	Ref	$\upsilon_{\rm LSR}$	$T_{\rm c}^{(b)}$
ATLASGAL Name	α [hh:mm:ss]	δ [dd:mm:ss]	l[°]	b[°]	[kpc]		[km s^{-1}]	[K]
AG10.472+00.027	18:08:38.20	−19:51:49.60	10.472	+0.028	8.6	[1]	+67.6	3.50
AG19.609−00.234	18:27:37.98	−11:56:36.60	19.608	−0.233	12.7	[2]	+40.8	1.85
AG31.412+00.307	18:47:34.30	−01:12:46.00	31.411	+0.308	5.3	[3]	+98.2	1.62
AG330.954−00.182	16:09:53.01	−51:54:54.80	330.952	−0.181	5.7	[4]	−91.2	4.54
AG332.826−00.549	16:20:10.65	−50:53:17.60	332.824	−0.549	3.6	[3]	−57.1	2.55
AG337.704−00.054	16:38:29.42	−47:00:38.80	337.704	−0.053	12.3	[5]	−47.4	1.30
AG351.581−00.352	17:25:25.03	−36:12:45.30	351.581	−0.352	6.8	[5]	−95.9	2.51

Notes: $^{(a)}$Heliocentric distance to the source. $^{(b)}$Main-beam brightness temperature of the continuum at 617 GHz.
References: For the heliocentric distances: [1] Sanna et al. (2014); [2] Urquhart et al. (2014); [3] Moisés et al. (2011); [4] Wienen et al. (2015); [5] Green & McClure-Griffiths (2011);

Table 7.2: Spectroscopic properties of the studied species and transitions.

Species	Transition		Frequency	$A_{\rm E}$	$E_{\rm u}$	Receiver/Telescope
	$J' - J''$	$F' - F''$	[GHz]	[s^{-1}]	[K]	
ArH^+	$1 - 0$	—	617.5252(2)	0.0045	29.63	SEPIA660/APEX
p-H_2O^+	$3/2 - 1/2$	—	604.6841(8)	0.0013	59.20	SEPIA660/APEX
$N_{K_a,K_c} = 1_{1,0} - 1_{0,1}$	$3/2 - 3/2$	—	607.2258(2)	0.0062	59.20	SEPIA660/APEX
OH^+	$1 - 1$	$1/2 - 1/2$	1032.9985(7)	0.0141	49.58	1.05THz Rx./APEX
$N = 1 - 0$		$3/2 - 1/2$	1033.0040(10)	0.0035		
		$1/2 - 3/2$	1033.1129(7)	0.0070		
		$3/2 - 3/2$	1033.1186(10)*	0.0176		
o-H_2O^+	$3/2 - 1/2$	$3/2 - 1/2$	1115.1560(8)	0.0171	53.52	HIFI/*Herschel*
$N_{K_a,K_c} = 1_{1,1} - 0_{0,0}$		$1/2 - 1/2$	1115.1914(7)	0.0274		
		$5/2 - 3/2$	1115.2093(7)*	0.0309		
		$3/2 - 3/2$	1115.2681(7)	0.0138		
		$1/2 - 3/2$	1115.3035(8)	0.0034		
CH	$3/2 - 1/2$	$1 - 1$	2006.74886(6)	0.0111	96.31	upGREAT/SOFIA
$^2\Pi_{3/2}, N = 2 - 1$		$1 - 0$	2006.76258(6)	0.0223		
		$2 - 1$	2006.79906(6)*	0.0335		

Notes: The spectroscopic data are taken from the Cologne Database for Molecular Spectroscopy (CDMS, Müller et al. 2005). The H_2O^+ frequencies were actually refined considering astronomical observations (see Appendix A of Muller et al. 2016). For the rest frequencies, the numbers in parentheses give the uncertainty in the last listed digit. $^{(*)}$Indicates the strongest hyperfine structure transition, which was used to set the velocity scale in the analysis.

It is essential to account for calibration uncertainties in the absolute continuum level as the line-to-continuum ratio forms the crux of the analysis that we present in the following sections. In order to attest for the reliability of the quoted continuum brightness temperatures, we measured the fluctuations in the continuum level across scans and also compared the ArH^+ continuum fluxes with ancillary continuum data at 870 μm observed using the LABOCA bolometer at the APEX telescope as part of the ATLASGAL survey. The scatter in the continuum levels across scans is < 12%, on average and the ArH^+ continuum fluxes, correlate well with that of the 870 μm continuum emission, with a relative scatter of 5%. We present a more detailed discussion on the same, in Appendix E.2.

7.3 Results

Figs. 7.2-7.5 present the calibrated and baseline subtracted spectra of all the transitions discussed in this work for all the sources observed. In general, spectra observed along the LOS towards hot-cores often show emission from a plethora of molecules, including complex organic species, to the extent that they can form a low level background, 'weeds', of emission lines, many of which remain unidentified (see, e.g. Belloche et al. 2013). Features from these species 'contaminate' the absorption profiles and make it difficult to gauge the true depth of the absorption features, potentially leading to gross underestimates of the subsequently derived column density values. In the following paragraphs we briefly discuss the main weeds that contaminate those parts of the spectra that are relevant for our absorption studies.

Towards all the Galactic sources in our sample, except for AG31.412+00.307, the LOS ArH^+ absorption is blended with emission from the high-lying (E_u = 473 K) HNCO, v = 0, ($28_{1,27} - 27_{1,26}$) transition at 617.345 GHz (Hocking et al. 1975) that originates in the hot molecular cores associated with the SFR that provides the continuum background radiation. Additionally, the HNCO emission line contaminant at 617.345 GHz lies very close to the H_2CS ($18_{2,17} - 17_{2,16}$) transition at 617.342 GHz (Johnson et al. 1972). To infer the extent of the contribution from H_2CS we compared it to another H_2CS transition covered in the same sideband. We do not detect the H_2CS ($18_{2,16} - 17_{2,15}$) transition at 620.165 GHz which has a comparable upper level-energy, and -degeneracy, and Einstein A coefficient as that of the H_2CS ($18_{2,17} - 17_{2,16}$) line, above a noise level of ~83 mK at a spectral resolution of 1.1 km s^{-1}. This leads us to conclude that the H_2CS transition at 617.342 GHz may not significantly contaminate our spectra.

In the p-H_2O^+ absorption spectra at 607 GHz, we see blended emission features particularly at the systemic velocity of the SFRs in this study, from $H^{13}CO^+$ ($J = 7 - 6$) and CH_3OH $J_k = 12_2 - 11_1$ E transitions at 607.1747 (Lattanzi et al. 2007) and 607.2159 GHz (Belov et al. 1995), respectively. The LOS is also contaminated by the D_2O ($J_{K_a,K_c} = 1_{1,1} - 0_{0,0}$) transition at 607.349 GHz (Matsushima et al. 2001). Detected thus far only towards the solar type protostar IRAS16293-2422 (Butner et al. 2007; Vastel et al. 2010), it is unlikely that there is significant contamination from D_2O absorption in our spectra. Observations of the o-H_2O^+ spectra which were performed in double sideband mode, covered the ^{13}CO (10 – 9)

transition at 1101.3 GHz (Zink et al. 1990) in the LSB, alongside the o-H_2O^+ line in the USB. This ^{13}CO emission feature blends with the LOS absorption profile of o-H_2O^+ towards AG10.472+00.027 and to a lesser extent with that of AG19.609−00.234 and AG31.412+00.307.

While, it is imperative to accurately model the degree of contamination in order to determine physical quantities within the velocity intervals concerned, there are several uncertainties in the 'residual' absorption obtained from fitting the observed emission features. Therefore, we do not model contributions from the different contaminants present along the different sight lines but rather exclude the corresponding velocity intervals from our modelled fits and analysis. However, by doing so, it is possible that we ignore impeding emission features and emission line-wings, which remain undetected because they are absorbed away below the continuum. This can lead to potential uncertainties in the derived optical depths particularly in the velocity intervals neighbouring the emission. In the following sections, we carry out a qualitative and quantitative comparison between the (uncontaminated) absorption features, for the different species and for each individual source.

7.3.1 Line-of-sight properties

The Galactic sources we have selected in this work, which predominantly provide the background radiation for our absorption studies, are luminous ($L > 10^4 L_\odot$) as they are dusty envelopes around young stellar objects with typical signposts of massive star-formation such as class II methanol masers and/or ultracompact (UC) HII regions. Much of this work addresses the investigation of trends of various quantities with Galactocentric distance. To allow this, the spectrum towards each sight line is divided into local standard of rest (LSR) velocity intervals that correspond to absorption features arising from different spiral-arm and inter-arm crossings. The velocities of these LOS absorption components are then mapped on a model of Galactic rotation to relate them to the Galactocentric distance, $R_{\rm GAL}$. The values for $R_{\rm GAL}$ were computed by assuming a flat rotation curve, with the distance between the Sun and the Galactic centre (GC), R_0, and the Sun's orbital velocity, Θ_0, assumed to be 8.15 kpc and 247 km s^{-1}, respectively, as determined by Reid et al. (2019). We have also compared our distance solutions with those reported in Urquhart et al. (2018), who have analysed the kinematic properties of dense clumps present in the ATLASGAL survey, which covers our sources. Furthermore, it is to be noted that our assumption of a flat rotation curve is only valid for $R_{\rm GAL} \gtrsim 4$ kpc as shown in Fig. 11 of Reid et al. (2019). For smaller values of $R_{\rm GAL}$ and for a general check on all distances, we employed the parallax-based distance calculator accessible from the website of the Bar and Spiral Structure Legacy survey (BeSSeL)[8].

In general, over velocity intervals that correspond to the envelopes of the individual molecular cloud cores, the 'systemic' velocities, ArH^+ shows very weak to almost no absorption unlike the other molecules. The absence of ArH^+ at these velocities is in line with chemical models that predict ArH^+ to exist exclusively in low-density atomic gas, $f_{\rm H_2} = 10^{-4}$–10^{-2} (Schilke et al. 2014; Neufeld & Wolfire 2016). As discussed in Sect. 7.2, the LSB of the SEPIA660 receiver was tuned to cover the p-H_2O^+ transitions near 604 and 607 GHz. Invariably across

[8]See, http://www.vlbi-astrometry.org/BeSSeL/node/378)

our entire sample of sources, we do not detect any clear absorption features from the p-H_2O^+ line at 604 GHz at an average noise level of 23 mK (at a spectral resolution of 1.1 km s^{-1}), owing to its weaker line strength in comparison to the p-H_2O^+ line at 607 GHz. Hence, we do not discuss the former p-H_2O^+ transition in the remainder of our study.

AG10.472+00.027

The sight line towards AG10.472+0.027, which is at a distance of 8.55 kpc (Sanna et al. 2014), crosses several spiral arms in the inner Galaxy. This results in a broad absorption spectrum covering an LSR velocity range from −35 to 180 km s^{-1}. All the molecules show absorption at $\upsilon_{\rm LSR}$ between −35 and 48 km s^{-1}, which arises partly from inter-arm gas and partly from the near-side crossing of the Sagittarius arm and Scutum-Centaurus arm. Within this velocity range, the absorption profiles form a nearly continuous blend except for p-H_2O^+, which has an unidentified emission feature at ∼3 km s^{-1} and generally narrower features. In contrast, the OH^+ absorption covers a larger velocity range than the other molecules and almost saturates within 0 and 45 km s^{-1}. The features at $\upsilon_{\rm LSR} > 80$ km s^{-1} are associated with the 3 kpc arm and the Galactic bar. Both p-H_2O^+ and o-H_2O^+ only weakly absorb at $\upsilon_{\rm LSR} > 130$ km s^{-1}; the former is also affected by some unknown emission features. However, ArH^+ shows absorption features similar to OH^+ with strong absorption dips at 80 and 127 km s^{-1}. The high-velocity component likely traces gas that lies beyond the GC belonging to the 135 km s^{-1} arm (Sormani & Magorrian 2015). CH has a narrow absorption dip at ∼150 km s^{-1} unlike the other atomic gas tracers, while ArH^+ and OH^+ have prominent absorption at 170 km s^{-1}. The corresponding HI spectrum with very little continuum, has a poor signal-to-noise ratio, which results in negative values in regions with large noise levels. However, the Bayesian analysis of the HI spectrum described in Winkel et al. (2017), which is used to derive the column density and spin temperature, correctly accounts for these noise effects amongst other spatial variations along the LOS.

AG19.609-00.234

AG19.609−00.234 is a massive star-forming clump at a heliocentric distance of 12.7 kpc (Urquhart et al. 2014) with an absorption spectrum extending from −10 to 150 km s^{-1}. The absorption at $\upsilon_{\rm LSR}$ between −10 and 20 km s^{-1} primarily traces inter-arm gas between the Perseus and outer arms and parts of the Aquila Rift, followed by weak absorption near 27 km s^{-1} from the envelope of the molecular cloud. While the absorption dips between 35 and 74 km s^{-1} (seen most clearly in the o-H_2O^+ spectrum), arising from the near and far side crossings of the Sagittarius spiral-arm. Unsurprisingly, there is no ArH^+ absorption at 40 km s^{-1} but ArH^+ shows red-shifted absorption tracing layers of infalling material associated with the molecular cloud. Infalling signatures towards this hot molecular cloud have previously been studied by Furuya et al. (2011), whose observations of the $J = 3 \rightarrow 2$ transitions of ^{13}CO and ^{18}CO show inverse P-Cygni profiles or red-shifted absorption alongside a blue-shifted emission component. The ArH^+ spectrum also shows a narrow absorption feature at 80 km s^{-1} possibly from the edge of the spiral arm. The strongest absorption feature seen in the ArH^+ spectrum lies close to 113 km s^{-1} from the Scutum-Centaurius arm, which is notably a weaker

component in the o-H_2O^+ and HI spectra.

AG31.412+00.307

Located on the Scutum-Centaurus arm at a distance of 5.55 kpc (Moisés et al. 2011), the line of sight towards this young-stellar object, AG31.412+00.307, crosses the Sagittarius arm at velocities roughly between 30 and 55 km s^{-1} and the Perseus arm at velocities <20 km s^{-1}. The ArH^+ absorption profile mimics that of HI with only minor offsets in the peak velocities ($<$ 1 km s^{-1}) of the absorption components. Moreover, the ArH^+ absorption seen close to the source's intrinsic velocity at 98 km s^{-1} traces infalling material. Unfortunately, because of the poor signal-to-noise ratio of the OH^+ spectrum it is very difficult to make an accurate component-wise comparison.

AG330.954-00.182

Located at a distance of 5.3 kpc (Wienen et al. 2015), AG330.954−00.182 lies in the Norma spiral arm and is a bright ATLASGAL 870 μm source in the fourth quadrant. It has an absorption profile that extends from −130 to 20 km s^{-1}. The gas between −60 and 20 km s^{-1} traces the near and far-side crossings of both the Scutum-Centaurius as well as the Sagittarius spiral-arms. The ArH^+ spectrum shows absorption at −115 km s^{-1}, a feature which is not present in the other species. There is weak ArH^+ absorption close to 90 km s^{-1}, which maybe associated with the molecular cloud itself. The line profile resembles a single absorption component as seen in the HI spectrum and not two components of comparable depths as seen in the OH^+ and o-H_2O^+ spectra.

AG332.826-00.549

The sight line towards AG332.826−00.549, which has a near kinematic distance of 3.6 kpc (Moisés et al. 2011), primarily traces the Scutum-Centaurius and Sagittarius spiral-arms. Overall, the observed profiles of the different species in terms of their shape, are in concordance with each other. Akin to the ArH^+ spectrum, the spectra of the other ionised species in our study, p-, and o-H_2O^+, and OH^+, all show their strongest absorption features near −40 km s^{-1} and red-shifted absorption tracing infalling material similar to G19.609−00.234. This feature whilst present in the HI spectrum is much weaker in comparison to the absorption at velocities corresponding to the molecular cloud which is expected, but is weaker, also in comparison to other LOS features and is not prominent in the CH spectrum.

AG337.704-00.054

At a distance of ∼12.3 kpc (Green & McClure-Griffiths 2011), AG337.704−00.054 is one of the most distant Galactic sources in our sample. Absorption features cover a range of velocities from -135 to ∼ +20 km s^{-1}. The LOS absorption at negative velocities between -140 and -60 km s^{-1} arise from the 3 kpc and the Norma spiral arms. The ArH^+ spectrum shows contiguous absorption over the entire velocity range cited, unlike the spectra of the other molecular ions and even HI.

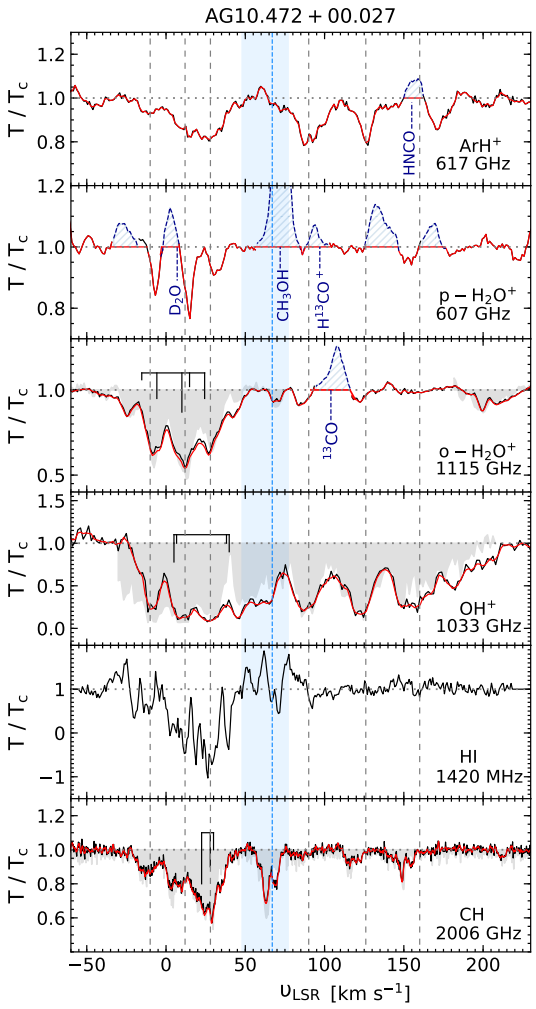

Figure 7.2: From top to bottom: Normalised spectra showing transitions of ArH^+, p-H_2O^+, o-H_2O^+, OH^+, HI, and CH, towards AG10.472+00.027, in black. The vertical dashed blue line and blue shaded regions mark the systemic velocity and the typical velocity dispersion of the source. The vertical dashed grey lines indicate the main absorption dips. Red curves display the Wiener filter fit to the observed spectra except for the HI spectra. The relative intensities of the hyperfine structure (HFS) components of the o-H_2O^+ and the OH^+ and CH transitions are shown in black above their respective spectra and the grey shaded regions display their HFS deconvolved spectra. Contaminating emission features are marked by the blue hatched lines and are excluded from the modelled fit and analysis.

AG351.581-00.352

AG351.581−00.352 is a bright and compact HII region at a distance of 6.8 kpc (Green & McClure-Griffiths 2011) that is located between the 3 kpc arm and the beginning of the Norma arm. Notably, ArH^+ has its strongest absorption peak at -27 km s^{-1}, arising from the Scutum arm while OH^+ and o-H_2O^+ both peak close to 50 km s^{-1}, tracing gas from the Norma arm. At the current rms noise level of the ArH^+ spectrum, it is difficult to ascertain the presence of absorption components at positive velocities that are clearly observed in the spectra of the other molecular ions, HI and CH.

7.3.2 Spectral fitting

The optical depth, τ is determined from the radiative transfer equation for the specific case of absorption spectroscopy ($T_l = T_c e^{-\tau}$), given knowledge of the continuum background temperature, T_c. The optical depth profile is then analysed using the Wiener filter fitting technique as described in Jacob et al. (2019). This two step fitting procedure first fits the

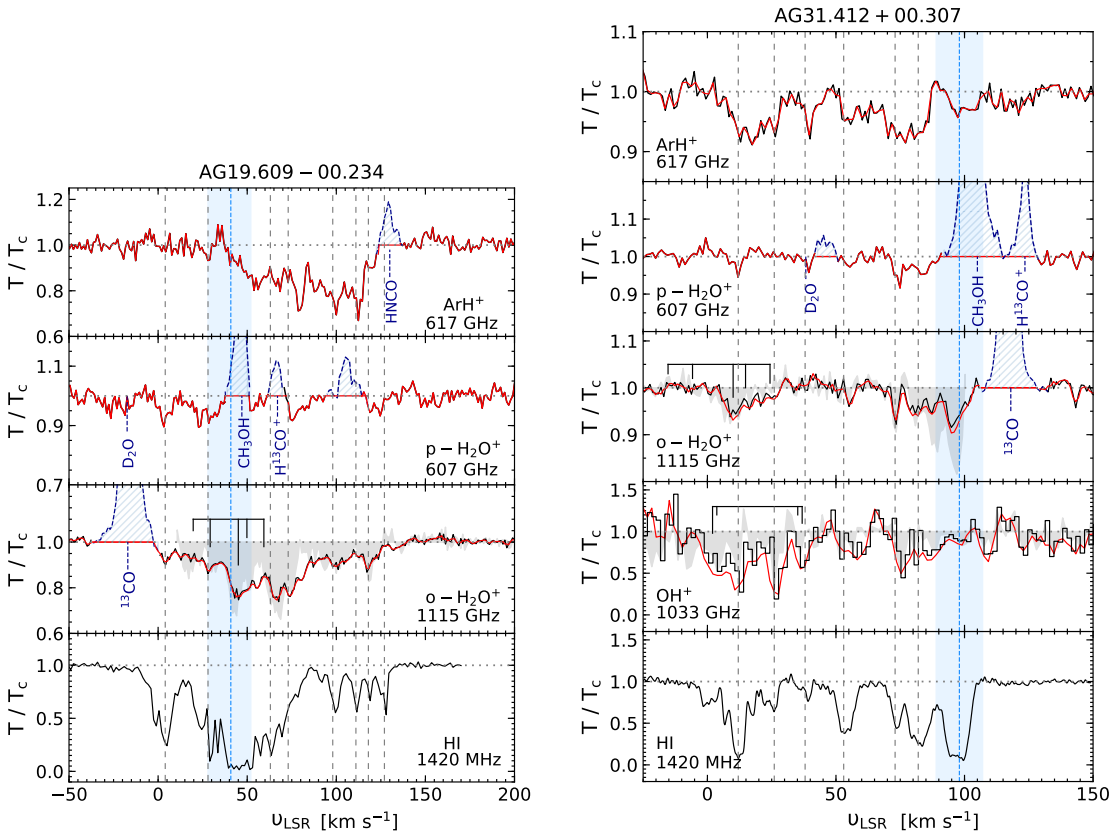

Figure 7.3: Same as Figure. 7.2 but toward AG19.609−00.234 (*left*) and AG31.412+00.307 (*right*). There is no OH^+, and CH spectra of the transitions studied here, available for AG19.609−00.234, while only the corresponding CH spectrum is not available for AG31.412+00.307.

spectrum based on the Wiener filter, which minimises the mean square error between the model and observations and then deconvolves the HFS from the observed spectrum, if any. When fitting lines that do not exhibit HFS, the procedure simply assumes that there is only a single HFS component whose frequency corresponds to that of the fine-structure transition itself. In addition to the observed spectrum and the spectroscopic parameters of the line to be fit, the only other input parameter required by the Wiener filter technique is the spectral noise, which is assumed to be independent of the signal. Furthermore, the technique also assumes that the lines are optically thin and under conditions of local thermodynamic equilibrium (LTE).

7.3.3 Column density

From the resultant optical depth profile, we determine the column densities per velocity interval, $\mathrm{d}N/\mathrm{d}\upsilon$, using

$$\left(\frac{\mathrm{d}N}{\mathrm{d}\upsilon}\right)_i = \frac{8\pi\nu_i^3}{c^3}\frac{Q(T_{\rm ex})}{g_{\rm u}A_{\rm E}}\mathrm{e}^{E_{\rm u}/T_{\rm ex}}\left[\exp\left(\frac{h\nu_i}{k_{\rm B}T_{\rm ex}}\right)-1\right]^{-1}(\tau_i) \tag{7.1}$$

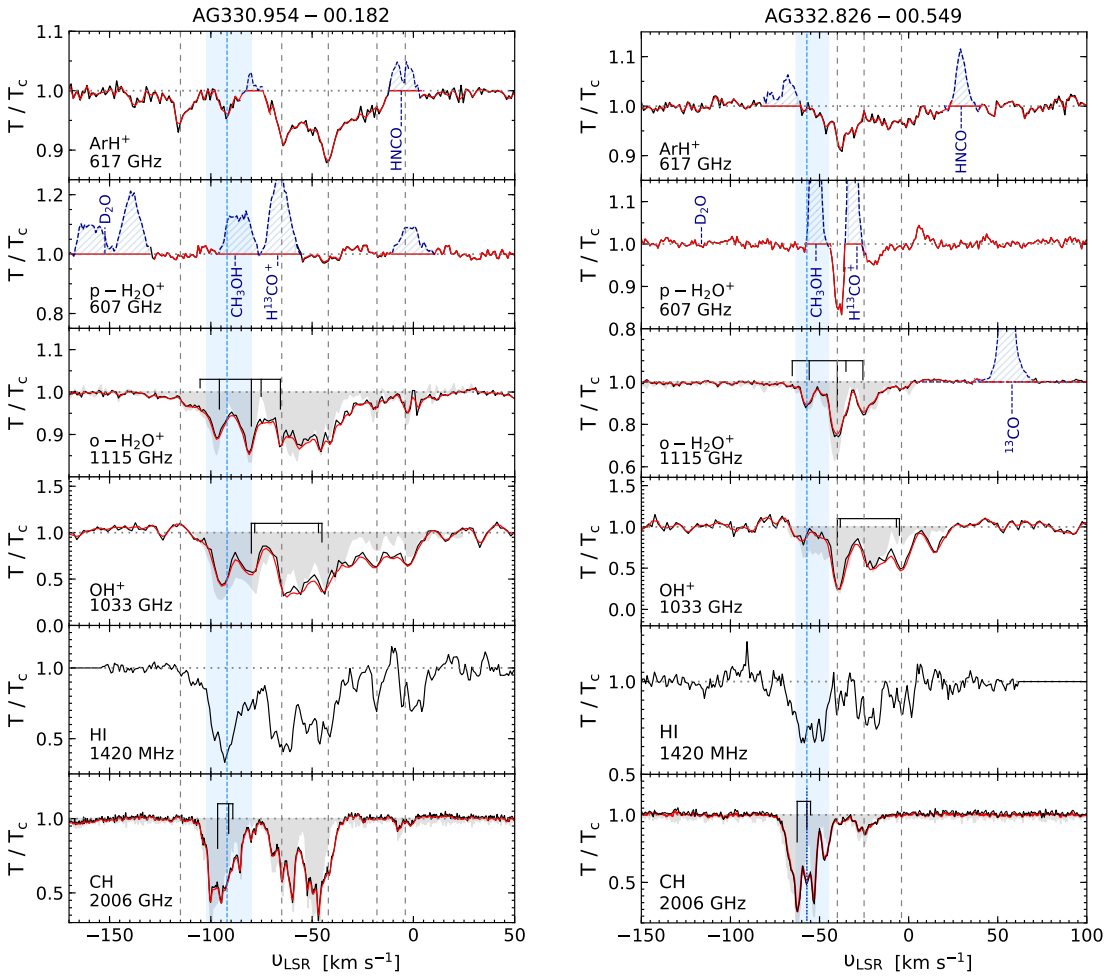

Figure 7.4: Same as Figure. 7.2 but toward AG330.954−00.182 (*left*) and AG332.826−00.549 (*right*).

for each velocity channel, i. For a given HFS transition, all of the above spectroscopic terms remain constant, except for the partition function, Q, which itself is a function of the rotation temperature, $T_{\rm rot}$. Under conditions of LTE $T_{\rm rot}$ is equal to the excitation temperature, $T_{\rm ex}$. We further assume that almost all the molecules occupy the ground rotational state where the excitation temperature, $T_{\rm ex}$, is determined by the cosmic microwave background radiation, $T_{\rm CMB}$, of 2.73 K. This is a valid assumption for the conditions that prevail in diffuse regions where the gas densities, (n(H) $\leq$ 100 cm^{-3}), are sufficiently low enough that collisional excitation becomes unimportant. However, this assumption may no longer be valid for those features that arise from the dense envelopes of the molecular clouds in which collisions can dominate, resulting in higher excitation temperatures. Therefore, the column densities derived by integrating Eq. 7.1 over velocity intervals associated with the molecular cloud components, only represent lower limits to the column density values. Combining all our sources, we are broadly able to identify a total of 38 distinct absorption features; however, we could only assign

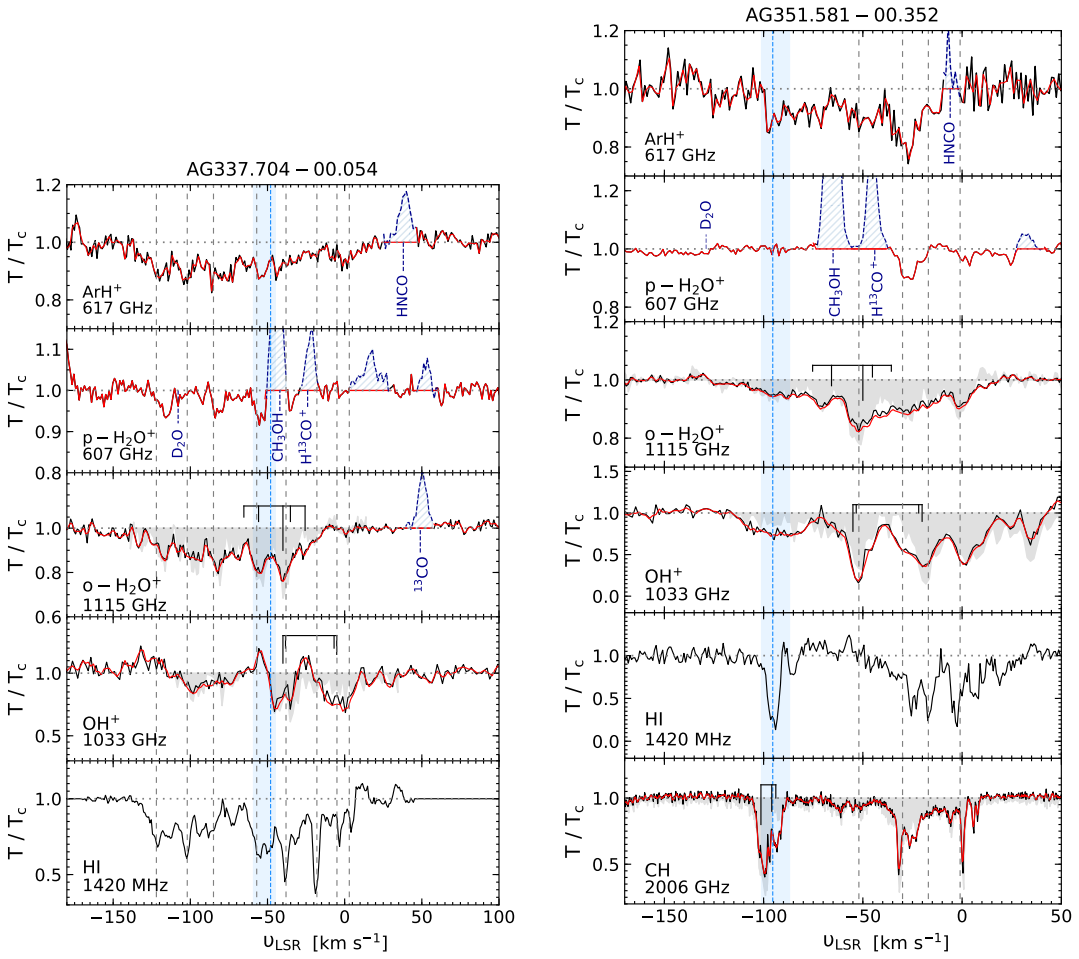

Figure 7.5: Same as Figure. 7.2 but toward AG337.704−00.054 (*left*) and AG351.581−00.352 (*right*). There is no CH spectrum of the transitions studied here, available for AG337.704−00.054.

33, 15, and 35 of these features to ArH^+, p-, and o-H_2O^+ absorption, respectively, due to the blending of different species present along the different LOS. The column densities that we have derived for each species and towards each sight line are summarised in Table 7.3. The ArH^+ column densities are found to vary between $\sim 6 \times 10^{11}$ and 10^{13} cm^{-2} across inter-arm and spiral-arm clouds along the different sight lines. The derived p-H_2O^+ column density values also show a similar variation, towards our sample of sources.

The accuracy of the reported column density values is mainly limited by uncertainties present in the continuum level and not the absolute temperature calibration. The errors in the WF analysis are computed using Bayesian methods to sample a posterior distribution of the optical depths. In this approach, we sampled 5000 artificial spectra each generated by iteratively adding a pseudo-random noise contribution to the absorption spectra, of each of the different species prior to applying the WF deconvolution. The standard deviation in the additive noise is fixed to be the same as that of the line free part of the spectrum. The deconvolved

optical depths and the subsequently derived column densities per velocity interval, sample a point in the channel-wise distribution of the column densities, across all the spectra. Since, the posterior of the optical depths is not normally distributed, we describe the profiles of the distributions by using the median and the inter-quartile range. This removes any bias introduced on the mean by the asymmetric nature of the distributions. We then determined the sample mean and standard deviation following Ivezić et al. (2019). The deviations from the newly derived mean are then used to determine the errors.

7.3.4 Cosmic-ray ionisation rate

Ionisation by cosmic-rays is the primary ionisation mechanism that drives ion-molecular reactions, within diffuse atomic clouds. As discussed in Sect. 7.1, the formation of ArH^+ is initiated by the ionisation of argon atoms by cosmic-rays. Therefore, knowledge of the primary ionisation rate per hydrogen atom, $\zeta_p(H)$, is vital for our understanding of the ensuing chemistry. In this section, we investigate the cosmic-ray ionisation rates towards our sample of sources, which can be determined by analysing the steady-state ion-molecular chemistry of OH^+ and o-H_2O^+ .

In the diffuse ISM, both OH^+ and o-H_2O^+ are mainly destroyed either via reactions with H_2 or recombination with an e^-. The relevant reactions are summarised below, alongside their reaction rates which are taken from Tran et al. (2018), Mitchell (1990), and the KIDA database[9] (Wakelam et al. 2012):

$$\begin{aligned}
OH^+ + H_2 &\rightarrow H_2O^+ + H; && k_1 = 1.0 \times 10^{-9}\ \mathrm{cm^3 s^{-1}} \\
OH^+ + e^- &\rightarrow H + O; && k_2 = 6.6 \times 10^{-8}\ \mathrm{cm^3 s^{-1}} \\
H_2O^+ + H_2 &\rightarrow H_3O^+ + H; && k_3 = 9.7 \times 10^{-10}\ \mathrm{cm^3 s^{-1}} \\
H_2O^+ + e^- &\rightarrow \left.\begin{aligned} &O + H_2; \\ &H + OH; \\ &H + O + H; \end{aligned}\right\} && k_4 = 7.4 \times 10^{-7}\ \mathrm{cm^3 s^{-1}}\ .
\end{aligned}$$

Since our analysis does not require the exact branching information between the products formed from the recombination of H_2O^+ with an e^-, k_4 cites the total reaction rate. The rates for reactions with H_2 are independent of the gas temperature, T, while, the recombination reactions have a weak dependence on it with $k \propto T^{-0.49}$. The reaction rates for the latter were computed at a temperature of 100 K corresponding to the typical HI spin temperature along the LOS towards the sources in our sample. Moreover, the transitions that we study mainly probe warm diffuse gas with typical values of T between 30 and 100 K (Snow & McCall 2006). Decreasing the temperature from 100 K to 30 K would result in an 80% increase in the reaction rates.

Following the steady-state analysis presented in Indriolo et al. (2012), the cosmic-ray ionisation rate may be written as

$$\varepsilon\zeta_p(H) = \frac{N(OH^+)}{N(H)} n_H \left[\frac{f_{H_2}}{2} k_1 + x_e k_2\right], \tag{7.2}$$

[9] http://kida.obs.u-bordeaux1.fr

Table 7.3: Synopsis of derived quantities.

Source	$v_{\rm LSR}$ Range [km s^{-1}]	$R_{\rm GAL}^{(a)}$ [kpc]	N(ArH$^+$) [10^{12} cm^{-2}]	N(OH$^+$) [10^{14} cm^{-2}]	N(p-H$_2$O$^+$) [10^{13} cm^{-2}]	N(o-H$_2$O$^+$) [10^{13} cm^{-2}]
AG10.472	(−35, 0)	10.82	$1.94^{+0.04}_{-0.06}$	$2.12^{+0.11}_{-0.16}$	—	$1.71^{+0.22}_{-0.34}$
+00.027	(0, 48)	5.56	$10.27^{+0.17}_{-0.21}$	$3.60^{+0.28}_{-0.33}$	> 1.05	$3.42^{+0.49}_{-0.62}$
	(48, 77)$^{(b)}$	3.50	$1.51^{+0.04}_{-0.05}$	$1.07^{+0.09}_{-0.12}$	—	$0.22^{+0.03}_{-0.05}$
	(77, 105)	3.12	$6.48^{+0.19}_{-0.23}$	$1.23^{+0.15}_{-0.19}$	—	—
	(105, 138)	2.38	$4.46^{+0.10}_{-0.14}$	$1.62^{+0.14}_{-0.18}$	—	—
	(138, 190)	1.48	—	$1.46^{+0.10}_{-0.13}$	—	$0.34^{+0.03}_{-0.04}$
AG19.609	(−12, 16)	8.04	$1.19^{+0.03}_{-0.04}$	—	$0.31^{+0.01}_{-0.02}$	—
−00.234	(16, 35)	6.75	$0.91^{+0.03}_{-0.05}$	—	$0.38^{+0.07}_{-0.08}$	$0.42^{+0.10}_{-0.11}$
	(35, 60)$^{(b)}$	4.50	$4.44^{+0.14}_{-0.18}$	—	—	$1.12^{+0.22}_{-0.22}$
	(60, 87)	4.34	$7.82^{+0.24}_{-0.28}$	—	—	$1.23^{+0.19}_{-0.17}$
	(87, 105)	3.32	$6.95^{+0.33}_{-0.36}$	—	—	$0.38^{+0.07}_{-0.09}$
	(105, 115)	3.01	$4.43^{+0.36}_{-0.42}$	—	—	$0.13^{+0.08}_{-0.09}$
	(115, 135)	2.73	—	—	$0.18^{+0.01}_{-0.01}$	$0.29^{+0.07}_{-0.10}$
AG31.412	(−8, 31)$^{(*)}$	7.05	$2.41^{+0.05}_{-0.06}$	$0.60^{+0.05}_{-0.07}$	$0.16^{+0.01}_{-0.02}$	$0.21^{+0.04}_{-0.04}$
+00.307	(31, 46)$^{(*)}$	6.39	$0.68^{+0.03}_{-0.05}$	$0.12^{+0.03}_{-0.05}$	—	< 0.05
	(46, 65)$^{(*)}$	5.49	$0.86^{+0.03}_{-0.05}$	$0.10^{+0.04}_{-0.06}$	> 0.08	$0.09^{+0.02}_{-0.03}$
	(65, 88)$^{(*)}$	4.71	$2.27^{+0.07}_{-0.09}$	$0.19^{+0.01}_{-0.03}$	$0.24^{+0.02}_{-0.02}$	$0.25^{+0.04}_{-0.06}$
	(88, 108)$^{(b,*)}$	4.64	$0.68^{+0.02}_{-0.03}$	$0.09^{+0.01}_{-0.02}$	—	$0.63^{+0.13}_{-0.18}$
AG330.954	(−130, −74)$^{(b)}$	4.43	> 1.24	$1.20^{+0.05}_{-0.07}$	—	$0.73^{+0.06}_{-0.09}$
−00.182	(−74, −57)	4.92	$1.44^{+0.06}_{-0.08}$	$0.42^{+0.09}_{-0.13}$	—	$0.45^{+0.12}_{-0.16}$
	(−57, −32)	5.78	$2.85^{+0.09}_{-0.11}$	$0.70^{+0.10}_{-0.13}$	$0.16^{+0.00}_{-0.01}$	$0.51^{+0.07}_{-0.08}$
	(−32, −10)	7.03	$1.13^{+0.04}_{-0.05}$	$0.05^{+0.01}_{-0.02}$	$0.06^{+0.01}_{-0.01}$	$0.10^{+0.02}_{-0.03}$
	(−10, 20)	8.54	—	$0.06^{+0.01}_{-0.02}$	—	$0.13^{+0.02}_{-0.03}$
AG332.826	(−85, −33)$^{(b)}$	5.30	—	$1.18^{+0.04}_{-0.07}$	—	$1.21^{+0.09}_{-0.16}$
−00.549	(−33, −12)	7.02	$1.10^{+0.04}_{-0.05}$	$0.42^{+0.07}_{-0.09}$	—	$0.41^{+0.10}_{-0.15}$
	(−12, 20)	8.67	$1.26^{+0.03}_{-0.04}$	$0.15^{+0.01}_{-0.02}$	$0.13^{+0.00}_{-0.01}$	$0.25^{+0.05}_{-0.06}$
AG337.704	(−145, −110)	3.12	$3.53^{+0.08}_{-0.11}$	$0.10^{+0.01}_{-0.01}$	$0.25^{+0.09}_{-0.10}$	$0.60^{+0.08}_{-0.11}$
−00.054	(−110, −97)	3.25	$2.19^{+0.15}_{-0.18}$	$0.07^{+0.01}_{-0.03}$	—	$0.32^{+0.13}_{-0.19}$
	(−97, −80)	3.73	$2.78^{+0.13}_{-0.16}$	$0.07^{+0.02}_{-0.02}$	$0.14^{+0.01}_{-0.01}$	$0.63^{+0.21}_{-0.22}$
	(−80, −65)	4.43	$2.60^{+0.13}_{-0.17}$	$0.08^{+0.01}_{-0.02}$	$0.11^{+0.01}_{-0.01}$	$0.33^{+0.13}_{-0.14}$
	(−65, −45)$^{(b)}$	5.17	$3.03^{+0.12}_{-0.14}$	$0.18^{+0.02}_{-0.03}$	—	$0.79^{+0.15}_{-0.16}$
	(−45, −25)	5.29	$2.31^{+0.09}_{-0.11}$	$0.16^{+0.02}_{-0.04}$	—	$0.70^{+0.16}_{-0.18}$
	(−25, −13)	6.91	$0.71^{+0.04}_{-0.06}$	$0.06^{+0.01}_{-0.02}$	—	$0.10^{+0.05}_{-0.08}$
	(−13, 7)	8.62	$1.56^{+0.06}_{-0.08}$	$0.12^{+0.03}_{-0.04}$	—	$0.12^{+0.02}_{-0.04}$
AG351.581	(−120, −70)$^{(b)}$	1.66	$5.56^{+0.08}_{-0.11}$	$0.80^{+0.03}_{-0.04}$	—	$0.46^{+0.05}_{-0.06}$
−00.352	(−70, −39)	3.18	$4.26^{+0.11}_{-0.13}$	$0.92^{+0.08}_{-0.13}$	—	$0.87^{+0.15}_{-0.20}$
	(−39, −7)	4.50	$6.40^{+0.15}_{-0.20}$	$0.80^{+0.08}_{-0.09}$	$0.43^{+0.10}_{-0.15}$	$0.61^{+0.11}_{-0.14}$
	(−7, 25)	9.74	—	$0.44^{+0.04}_{-0.07}$	$0.24^{+0.05}_{-0.09}$	$0.36^{+0.05}_{-0.08}$

Notes: $^{(a)}$The galactocentric distance for each velocity interval is computed using, $R_{\rm GAL} = R_0 \frac{\Theta(R_{\rm GAL})\sin(l)\cos(b)}{v_{\rm lsr}+\Theta_0\sin(l)\cos(b)}$, with R_0 = 8.15 kpc, Θ_0 = 247 km s^{-1} (Reid et al. 2019) and assuming a flat Galactic rotation curve, i.e, $\Theta(R_{\rm GAL}) = \Theta_0$ for $R_{\rm GAL} > 5$ kpc. We used the BeSSeL distance calculator, to both cross-check and determine lower $R_{\rm GAL}$ values. The distances are computed at the mean velocity within each velocity interval. $^{(b)}$Indicates the velocity intervals corresponding to the molecular cloud.

Table 7.3: Continued.

Source	v_{LSR} Range [km s^{-1}]	H_2O^+ OPR	N(HI) [10^{21} cm^{-2}]	f_{H_2} $OH^{+(c)}$	f_{H_2} $CH^{(d)}$	ζ_p(H) [10^{-16} s^{-1}]
AG10.472	(−35, 0)	—	$4.62^{+1.34}_{-1.96}$	< 0.019	$0.77^{+0.04}_{-0.04}$	< 4.52
+00.027	(0, 48)	< 3.26	$8.60^{+2.09}_{-3.66}$	> 0.031	$0.87^{+0.04}_{-0.05}$	> 4.52
	(48, 77)$^{(b)}$	—	$2.64^{+0.84}_{-1.11}$	> 0.005	$0.88^{+0.02}_{-0.03}$	> 2.48
	(77, 105)	—	$0.80^{+0.26}_{-0.33}$	—	$0.89^{+0.06}_{-0.06}$	—
	(105, 138)	—	$0.64^{+0.22}_{-0.27}$	—	$0.92^{+0.05}_{-0.06}$	—
	(138, 190)	—	$0.76^{+0.32}_{-0.27}$	$0.005^{+0.001}_{-0.001}$	$0.94^{+0.06}_{-0.06}$	$12.03^{+1.30}_{-1.33}$
AG19.609	(−12, 16)	—	$5.38^{+0.46}_{-0.68}$	—	—	—
−00.234	(16, 35)	$1.10^{+0.33}_{-0.37}$	$5.51^{+0.37}_{-0.76}$	—	—	—
	(35, 60)$^{(b)}$	—	$16.99^{+27.4}_{-6.38}$	—	—	—
	(60, 87)	—	$4.09^{+0.34}_{-0.52}$	—	—	—
	(87, 105)	—	$1.36^{+0.13}_{-0.16}$	—	—	—
	(105, 115)	—	$0.82^{+0.08}_{-0.09}$	—	—	—
	(115, 135)	$1.61^{+0.40}_{-0.56}$	$1.33^{+0.13}_{-0.15}$	—	—	—
AG31.412	(−8, 31)$^{(*)}$	$1.31^{+0.26}_{-0.30}$	$11.98^{+3.23}_{-6.83}$	$0.013^{+0.003}_{-0.003}$	—	$0.37^{+0.00}_{-0.03}$
+00.307	(31, 46)$^{(*)}$	—	$2.71^{+0.93}_{-1.30}$	$0.031^{+0.026}_{-0.030}$	—	$0.18^{+0.07}_{-0.06}$
	(46, 65)$^{(*)}$	< 1.13	$2.78^{+0.92}_{-1.35}$	$0.100^{+0.010}_{-0.008}$	—	$0.29^{+0.08}_{-0.07}$
	(65, 88)$^{(*)}$	$1.04^{+0.17}_{-0.26}$	$8.11^{+1.01}_{-4.26}$	$0.108^{+0.020}_{-0.015}$	—	$0.29^{+0.03}_{-0.02}$
	(88, 108)$^{(b,*)}$	—	$14.69^{+11.7}_{-9.96}$	> 0.776	—	> 1.08
AG330.954	(−130, −74)$^{(b)}$	—	$7.75^{+1.71}_{-3.48}$	$0.014^{+0.004}_{-0.004}$	$0.30^{+0.08}_{-0.06}$	$1.34^{+0.01}_{-0.02}$
−00.182	(−74, −57)	—	$3.01^{+0.52}_{-1.33}$	> 0.026	$0.43^{+0.03}_{-0.03}$	> 1.62
	(−57, −32)	$3.18^{+0.44}_{-0.54}$	$3.66^{+1.02}_{-1.57}$	$0.023^{+0.004}_{-0.004}$	$0.34^{+0.02}_{-0.02}$	$1.78^{+0.84}_{-1.01}$
	(−32, −10)	$1.67^{+0.43}_{-0.57}$	$2.43^{+0.91}_{-1.02}$	$0.103^{+0.004}_{-0.004}$	$0.04^{+0.01}_{-0.01}$	$0.39^{+0.03}_{-0.02}$
	(−10, 20)	—	$2.63^{+0.95}_{-1.11}$	> 0.058	$0.14^{+0.06}_{-0.04}$	$0.45^{+0.11}_{-0.04}$
AG332.826	(−85, −33)$^{(b)}$	—	$9.19^{+3.80}_{-5.06}$	$0.025^{+0.006}_{-0.007}$	$0.35^{+0.07}_{-0.05}$	$1.45^{+0.10}_{-0.07}$
−00.549	(−33, −12)	—	$2.26^{+0.30}_{-0.79}$	> 0.24	$0.16^{+0.04}_{-0.03}$	> 2.04
	(−12, 20)	$1.92^{+0.38}_{-0.48}$	$2.81^{+0.15}_{-0.52}$	$0.073^{+0.014}_{-0.010}$	$0.10^{+0.01}_{-0.01}$	$0.88^{+0.07}_{-0.07}$
AG337.704	(−145, −110)	$2.41^{+0.92}_{-1.06}$	$2.43^{+0.87}_{-2.13}$	$1.080^{+0.070}_{-0.064}$	—	$4.06^{+0.41}_{-0.22}$
−00.054	(−110, −97)	—	$1.34^{+0.47}_{-0.12}$	$0.190^{+0.030}_{-0.031}$	—	$2.67^{+0.42}_{-0.28}$
	(−97, −80)	$4.50^{+1.53}_{-1.60}$	$1.89^{+0.00}_{-0.69}$	—$^{(e)}$	—	—
	(−80, −65)	$3.00^{+1.21}_{-1.30}$	$2.42^{+0.55}_{-0.85}$	$0.255^{+0.030}_{-0.030}$	—	$1.56^{+0.21}_{-0.15}$
	(−65, −45)$^{(b)}$	—	$3.88^{+1.31}_{-2.00}$	$0.162^{+0.030}_{-0.040}$	—	$2.18^{+0.15}_{-0.41}$
	(−45, −25)	—	$3.12^{+1.04}_{-1.57}$	$0.089^{+0.032}_{-0.029}$	—	$2.14^{+0.38}_{-0.32}$
	(−25, −13)	—	$2.01^{+0.56}_{-1.20}$	> 0.048	—	$0.50^{+0.08}_{-0.11}$
	(−13, 7)	—	$2.44^{+0.91}_{-1.11}$	> 0.026	—	$0.57^{+0.02}_{-0.01}$
AG351.581	(−120, −70)$^{(b)}$	—	$2.20^{+0.20}_{-0.98}$	$0.087^{+0.003}_{-0.004}$	$0.57^{+0.04}_{-0.04}$	$1.98^{+0.04}_{-0.06}$
−00.352	(−70, −39)	—	$1.34^{+0.52}_{-0.56}$	> 0.554	$0.47^{+0.05}_{-0.03}$	$12.85^{+1.44}_{-1.12}$
	(−39, −7)	$1.41^{+0.41}_{-0.60}$	$4.85^{+1.87}_{-2.03}$	$0.314^{+0.005}_{-0.008}$	$0.45^{+0.05}_{-0.04}$	$1.23^{+0.22}_{-0.25}$
	(−7, 25)	$1.50^{+0.37}_{-0.61}$	$4.78^{+1.84}_{-2.00}$	$0.027^{+0.010}_{-0.004}$	$0.28^{+0.03}_{-0.03}$	$1.02^{+0.12}_{-0.13}$

Notes: $^{(c),(d)}$Represent f_{H_2} values derived using Eq. 7.4 and 7.3, respectively. Where H_2 column densities for the latter are determined from those of CH (Jacob et al. 2019) using [CH]/[H_2] = $3.5^{+2.1}_{-1.4} \times 10^{-8}$ (Sheffer et al. 2008). $^{(e)}$Faces a singularity as the denominator approaches 0.$^{(*)}$Represents velocity intervals with low signal-to-noise ratios, for which molecular hydrogen fractions are calculated using the upper limits of the derived $N(OH^+)$ values.

where, k_1 and k_2 are the rates of the reactions between OH^+ and H_2, and OH^+ and a free electron. As introduced in Neufeld et al. (2010), ε is an efficiency factor that represents the efficiency with which ionised H forms OH^+. The efficiency parameter was predicted by chemical models (Hollenbach et al. 2012) to vary between 5% and 20% as it is dependent on the physical properties of the cloud. Observationally, this efficiency has been determined only towards the W51 region by Indriolo et al. (2012) to be 7 ± 4%, using the spectroscopy of OH^+, H_2O^+ and H_3^+. For our calculations we use a value of $\varepsilon = 7$%.

While, $N(OH^+)$ and $N(H)$ are determined from observations, n_H refers to the gas density, for which we adopt a value of $n_H \approx 35$ cm^{-3}. This value corresponds to the mean density of the cold neutral medium at the solar circle, $R_{GAL} \approx 8.3$ kpc (Indriolo et al. 2012, 2015). The electron abundance, x_e in diffuse clouds is often considered to be equal to the fractional abundance of ionised carbon, $x_e = 1.5 \times 10^{-4}$ (Sofia et al. 2004). Under the conditions that prevail over the diffuse regions of the ISM, this is a valid assumption because C^+ is responsible for most of the free electrons and therefore the electron abundance, with negligible contributions from other ionised species. This assumption however, breaks down in regions of high $\zeta_p(H)/n(H)$ where ionisation by H becomes significant, like in the Galactic centre (Le Petit et al. 2016).

The molecular fraction, f_{H_2} is typically defined as,

$$f_{H_2} = \frac{2n(H_2)}{n(H) + 2n(H_2)}, \tag{7.3}$$

and can be re-written in terms of the $N(OH^+)/N(H_2O^+)$ ratio by

$$f_{H_2} = \frac{2x_e k_4/k_1}{N(OH^+)/N(H_2O^+) - k_3/k_1}, \tag{7.4}$$

where, $N(H_2O^+)$ is the total column density of H_2O^+, $N(H_2O^+) = N(\text{p-}H_2O^+) + N(\text{o-}H_2O^+)$. For those velocity intervals for which absorption is detected only in one of either the o- or p-H_2O^+ lines we present a lower limit on the molecular fraction. The molecular hydrogen fractions hence derived using Eq. 7.4 has a median value of $f_{H_2} = (5.8 \pm 3.0) \times 10^{-2}$. Alternatively, we can also compute the column-averaged molecular hydrogen fraction $f_{H_2}^N = 2N(H_2)/(N(H) + 2N(H_2))$ by using $N(CH)$ as a tracer for $N(H_2)$, following the relationship between the two molecules estimated by Sheffer et al. (2008), $[CH]/[H_2] = 3.5^{+2.1}_{-1.4} \times 10^{-8}$. However, the column-averaged molecular fractions derived towards the different velocity intervals using CH column densities are higher (by almost an order of magnitude) than those derived using Eq. 7.4. This difference arises from the fact that CH resides in, and therefore traces molecular gas unlike both OH^+ and H_2O^+.

The cosmic-ray ionisation rates we infer from the steady-state chemistry of OH^+ (and H_2O^+) using Eq. 7.2 lie between 1.8×10^{-17} and 1.3×10^{-15} s^{-1}. Resulting in an average value of $\zeta_p(H) = (2.28 \pm 0.34) \times 10^{-16}$ s^{-1} towards the sight lines studied here. The uncertainties in $\zeta_p(H)$ quoted in this work reflect the uncertainties in the derived column density values. The impact of the uncertainties associated with the assumptions made in this analysis, on the derived cosmic-ray ionisation rates are discussed in more detail in Schilke et al. (2014) and Indriolo et al. (2015). Within the statistical errors, this result is consistent with the cosmic-ray

ionisation rates that were previously determined using H_3^+ by Indriolo & McCall (2012) and OH^+ and H_2O^+ by Indriolo et al. (2015); Neufeld & Wolfire (2017).

The derived values for the cosmic-ray ionisation rate are summarised in Table. 7.3 and in Fig. 7.6 we display their variation with galactocentric distance. The cosmic-ray ionisation rates in the extreme environment of the GC, are generally found to be higher than in the general Galactic environment and cover a range of values over two orders of magnitude between $\sim 10^{-16}$ and 1.83×10^{-14} s^{-1} as discussed in Indriolo et al. (2015) and references therein. At galactocentric distances <5 kpc the ionisation rates that we derive in this study are comparable to those derived by Indriolo et al. (2015) at larger distances. This might hint to the fact that the gradient seen by these authors at $3 < R_{\rm GAL} < 5$ kpc from the LOS components towards the GC sources (like M-0.13-0.08, M-0.02-0.07, Sgr B2(M) and Sgr B2(N)) are higher than the average cosmic-ray ionisation rate present in these spiral arms because these velocity components may contain contributions from the GC. At $R_{\rm GAL} > 5$ kpc, the cosmic-ray ionisation rates derived in this work are systematically lower than those derived in Indriolo et al. (2015) however, several of the ionisation rates derived by these authors, that lie below $\sim 5 \times 10^{-17}$ s^{-1} only represent upper limits to the cosmic-ray ionisation rates.

We derive a slope, m, of -0.012 from $\zeta_{\rm p}$(H) versus $R_{\rm GAL}$, for galactocentric distances that lie within $4 < R_{\rm GAL} < 8.5$ kpc. Our analysis thus far assumes a constant value for n(H) equal to the mean gas density of cold gas near the solar circle, which itself varies with galactocentric distances as discussed in Wolfire et al. (2003). Neufeld & Wolfire (2017) took this, as well as variations in the UV radiation field ($\chi_{\rm UV}$) over Galactic scales into account and described the galactocentric gradient in the cosmic-ray ionisation rate as follows,

$$\frac{d\log_{10}\zeta_{\rm p}({\rm H})}{dR_{\rm GAL}} = m + 1.7\frac{d\log_{10}n({\rm H})}{dR_{\rm GAL}} - 0.7\frac{d\log_{10}\chi_{\rm UV}}{dR_{\rm GAL}}, \tag{7.5}$$

where, $\zeta_{\rm p}({\rm H})/n({\rm H}) \propto [\chi_{\rm UV}/n({\rm H})]^{-0.7}$. From the models presented in Wolfire et al. (2003), which characterise the nature of neutral gas present within the Galactic disk, $d\log_{10}n({\rm H})/dR_{\rm GAL}$ and $d\log_{10}\chi_{\rm UV}/dR_{\rm GAL}$ have values of -0.110 kpc^{-1} and -0.106 kpc^{-1}, respectively. Using, the scale length, $\left[{\rm dln}\zeta_{\rm p}({\rm H})/{\rm d}R_{\rm GAL}\right]^{-1}$, hence derived and the mean value of the cosmic-ray ionisation rate of their data-set, these authors derive the Galactic gradient to be $\zeta_{\rm p}({\rm H}) = (2.2 \pm 0.3)\exp\left[(R_{\rm o} - R_{\rm GAL}\right]/4.7$ kpc$) \times 10^{-16}$ s^{-1}, where $R_{\rm o} = 8.5$ kpc and $R_{\rm GAL}$ between 3-8.5 kpc. Following the analysis presented by Neufeld & Wolfire (2017), briefly discussed above, we derive a revised cosmic-ray ionisation rate gradient as,

$$\zeta_{\rm p}({\rm H}) = (1.80 \pm 0.70)\exp\left[(R_{\rm o} - R_{\rm GAL})/3.46\ {\rm kpc}\right] \times 10^{-16}\ {\rm s}^{-1}$$

using a scale length of 3.46 kpc and a mean cosmic-ray ionisation rate of $(1.80\pm0.70)\times10^{-16}$ s^{-1} (where the value in parenthesis is the standard error), across the combined sample of sight lines studied in Indriolo et al. (2015) and this work for galactocentric distances that lie within $4 < R_{\rm GAL} < 8.5$ kpc and a gas density of 35 cm^{-3}. We have excluded the $\zeta_{\rm p}$(H) values derived for the Galactic centre sources.

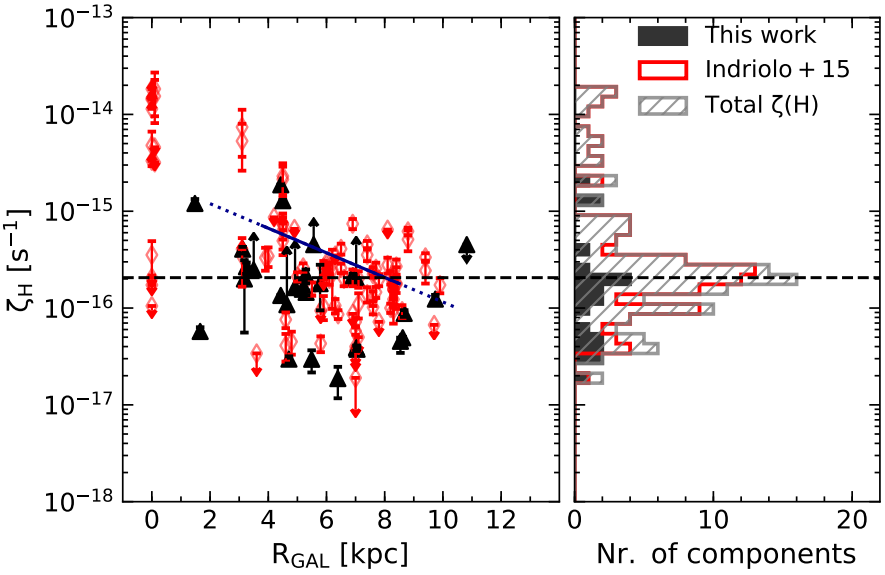

Figure 7.6: *Left*: Cosmic-ray ionisation rates derived from OH^+ vs. galactocentric distance. The filled black triangles and unfilled red diamonds represent $\zeta_p(H)$ values derived from the LOS absorption features observed in this study and in Indriolo et al. (2015), respectively. The dashed black line marks the median value of the total $\zeta_p(H)$ distributions. The solid-dotted line represents the derived cosmic-ray ionisation rate gradient. *Right*: Histogram distributions of $\zeta_p(H)$ derived in this work displayed in black, that from Indriolo et al. (2012) in red, and the combined distribution by the hatched grey region.

7.3.5 H_2O^+ analysis

For H_2O^+, the lower energy spin variant is o-H_2O^+ owing to its C_{2v} symmetry and $^2B_1$ ground state, unlike the case of H_2O, for which the lowest energy level is the 0_{00} level of the p-H_2O spin isomer. The lowest ortho- and para-rotational levels of H_2O^+ have an energy difference of ≈30.1 K and the fine structure levels of the ortho ground state ($I = 1$) further undergo HFS splitting, while those of the para ($I = 0$) state do not. Under the typical conditions present in the diffuse ISM, the rotational temperature (as discussed in Sect. 7.3.3) is close to T_{CMB}, which makes it valid to assume that most of the molecules will exist in the lowest ortho and para rotational states.

The conversion between the ortho- and para-states of a species, typically occurs via proton exchange reactions with either atomic H or H_2. Since, atomic H is the most abundant species along our diffuse LOS, we expect the proton exchange in H_2O^+ to primarily take place via gas phase reactions with H. Moreover, in the presence of H_2, H_2O^+ ions may energetically react to form H_3O^+ and a hydrogen atom:

$$\text{p-}H_2O^+ + H \rightleftharpoons \text{o-}H_2O^+ + H\,.$$

Since, the two spin states can be moderately coupled via collisions, the OPR is given by

$$\text{OPR} = \frac{Q_{\text{ortho}}}{Q_{\text{para}}} \exp\left(\Delta E / T_{\text{ns}}\right)\,, \tag{7.6}$$

where $Q_{\rm ortho}$ and $Q_{\rm para}$ represent the partition functions of the respective states, ΔE is the energy difference between the two states, $\Delta E = -30.1$ K (it is negative because the lowest ortho state lies at a lower energy level than the lowest para state, unlike in H_2O) and $T_{\rm ns}$ is the nuclear spin temperature. At low temperatures, the partition function of the para- and ortho-states are governed by the degeneracy of their lowest fine-structure and HFS levels, respectively. Both states have the same quantum numbers and degeneracy, which implies that, as the rotational temperature approaches 0 K, the ratio of the partition functions approaches unity (see, Appendix A of Schilke et al. 2010). Therefore, in the analysis that follows we assume that, $Q_{\rm ortho} = Q_{\rm para}$. Since, the largest uncertainty in our derived OPR arises from the uncertainties in the absorption features of the p-H_2O^+ profile, we only carry out this analysis in those velocity intervals that are the least contaminated. From our column density calculations, we derive OPR values between $\sim 1:1$ and 4.5:1, which is compatible with the equilibrium value of three, within the error bars. We find a mean OPR for H_2O^+ of 2.1:1 which corresponds to a mean nuclear spin temperature of 41 K.

7.4 Discussion

7.4.1 Properties of ArH^+ as a tracer of atomic gas

We derive ArH^+ abundances relative to atomic H column densities, $X(ArH^+) = N(ArH^+)/N(HI)$, that span over roughly two orders of magnitude varying between 4.6×10^{-11} and 1.6×10^{-8}, with an average value of $(1.6 \pm 1.3) \times 10^{-9}$. In Fig. 7.7, by combining our ArH^+ data points with values from the sight lines studied in Schilke et al. (2014), we compare the derived column densities and abundances of ArH^+ with atomic hydrogen column densities. Over the entire range, the ArH^+ column densities cluster at $N(H) = (2.7 \pm 1.6) \times 10^{21}$ cm^{-2}. We observe a large spread in the ArH^+ abundances derived, even for the molecular cloud (MC) components. This is mainly because of the high optical depths of the HI data and to a lesser extent because, towards some of the sources in our sample, we see that ArH^+ traces layers of infalling material associated with the molecular cloud. Figure 7.7 does not reveal a strong correlation between ArH^+ and HI, as we had expected because HI traces different phases of the ISM with varying degrees of molecular fraction. Moreover, the HI emission at certain velocity intervals may be a superposition of both the near- and far-side components of the Milky Way, often leading to blending effects which can potentially bias the inferred spin temperatures and column densities.

We subjected the entire ArH^+/HI data-set to a regression analysis and find $\log(X(ArH^+)) = (-0.80 \pm 0.20) \log(N(H)) + (7.84 \pm 4.28)$ with a correlation coefficient of 38% at a 99.99% confidence level. This translates to a power-law relation between ArH^+ and HI column densities of $N(ArH^+) \propto N(H)^{0.2}$. This can be viewed as a global relation as the behaviour of the power-law index (or slope in logarithmic-scales) does not appreciably vary between the diffuse LOS and dense molecular cloud components and there is no clear power-law break. Observations in the past have shown that considerable amounts of HI gas exist within molecular clouds, whose population is maintained via the destruction of H_2 by cosmic-rays (e.g. Wannier et al. 1991; Kuchar & Bania 1993). Hence, the HI gas along any given LOS in our study, also contains gas that resides inside molecular clouds with a fractional abundance, [H]/[H_2], ~ 0.1%. From Fig. 7.7, we find that as N(HI) increases, $X(ArH^+)$ decreases due to the increasing amounts

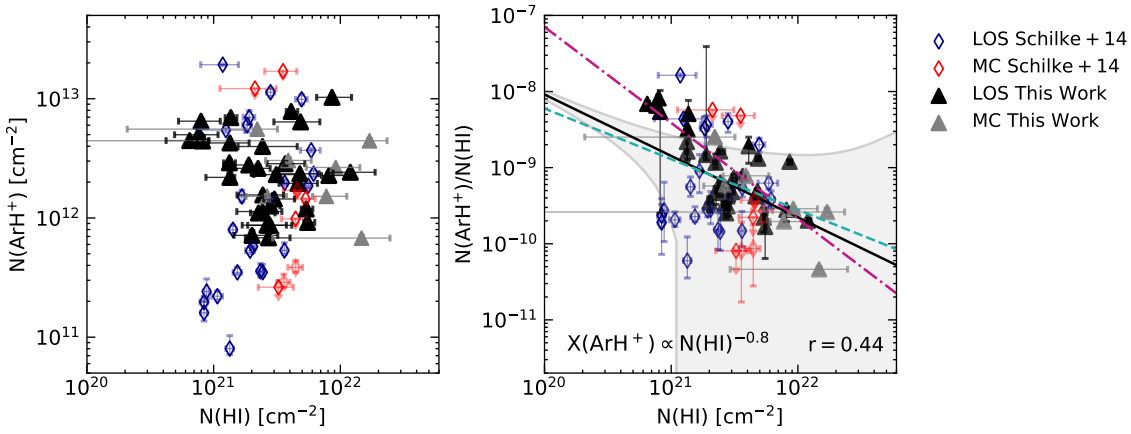

Figure 7.7: *Left*: $N(\mathrm{ArH^+})$ vs. $N(\mathrm{H})$. *Right*: $X(\mathrm{ArH^+}) = N(\mathrm{ArH^+})/N(\mathrm{HI})$ vs. $N(\mathrm{H})$. The data points include column density values derived towards the MC and LOS features from our sample of sources indicated by filled grey and black triangles, as well as those from Schilke et al. (2014) marked by unfilled red and blue diamonds, respectively. The solid black line displays the power-law relation to the combined data-set, $X(\mathrm{ArH^+}) \propto N(\mathrm{HI})^{-0.78}$, with the grey shaded region representing the 1σ-level of the weighted fit. The dashed cyan and dashed-dotted pink curves represent the fits to only the LOS and only the MC components, respectively.

of dense gas traced by HI gas. It is therefore clear that only a small fraction of the HI gas traces the same cloud population as that traced by $\mathrm{ArH^+}$. Based on the astrochemical models presented by Schilke et al. (2014), if we assume the abundance of $\mathrm{ArH^+}$ to be a constant ($X(\mathrm{ArH^+}) = 2\times10^{-10}$) for cloud depths ≤ 0.01 mag which corresponds to an average molecular fraction of 10^{-3}, then we find that only 17.3% of the LOS HI gas traces these conditions.

As detailed in Schilke et al. (2014), $\mathrm{ArH^+}$ is destroyed primarily via proton transfer reactions with $\mathrm{H_2}$ or atomic oxygen, and photodissociation.

$$\mathrm{ArH^+ + H_2 \rightarrow Ar + H_3^+\,;} \qquad k_5 = 8\times10^{-10}\ \mathrm{cm^3 s^{-1}}$$
$$\mathrm{ArH^+ + O \rightarrow Ar + OH^+\,;} \qquad k_6 = 8\times10^{-10}\ \mathrm{cm^3 s^{-1}}$$
$$\mathrm{ArH^+ + h\nu \rightarrow Ar^+ + H\,;} \qquad k_7 = 1.0\times10^{-11}\chi_{\mathrm{UV}} f_{\mathrm{A}}\ \mathrm{s^{-1}}$$

The photodissociation rate of $\mathrm{ArH^+}$ was estimated by Alekseyev et al. (2007), to be $\sim 1.0\times10^{-11} f_{\mathrm{A}}\ \mathrm{s^{-1}}$ for an unshielded cloud model uniformly surrounded by the standard Draine UV interstellar radiation field. However, for the particular environment of the Crab nebula the photodissociation rate has been calculated to be much higher at $1.9\times10^{-9}\ \mathrm{s^{-1}}$ (Roueff et al. 2014). The attenuation factor, f_{A}, is given by an exponential integral and is a function of visual extinction, A_{v}. Schilke et al. (2014) derive values of f_{A} between 0.30 and 0.56, increasing as you move outward from the centre of the cloud, for a cloud model with $A_{\mathrm{v}} = 0.3$. In our analysis we use a value of 0.43 for f_{A}, mid-way through the computed range of values. We further assume a gas density $n(\mathrm{H}) = 35\ \mathrm{cm^{-3}}$, an atomic oxygen abundance (relative to H nuclei) of

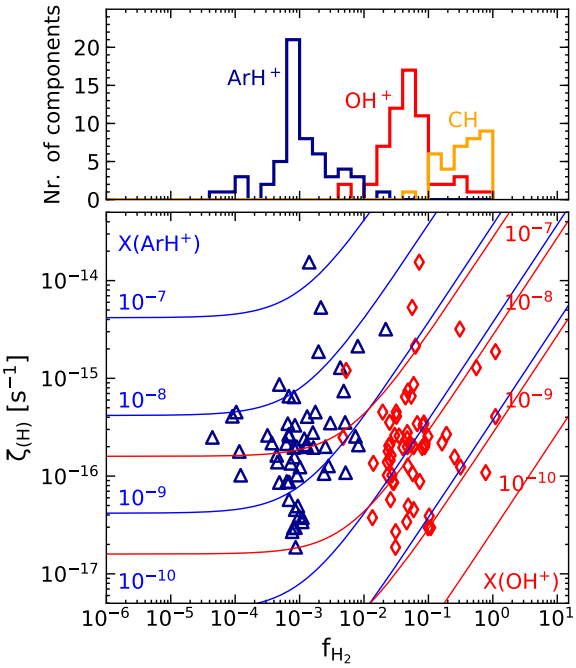

Figure 7.8: *Top*: Distribution of molecular gas fraction (f_{H_2}) traced by ArH^+ (blue), OH^+ (red) and CH (orange). *Bottom*: Contours of $X(ArH^+)$ (blue) and $X(OH^+)$ (red) abundances with respect to $N(H)$ in the f_{H_2}–$\zeta_p(H)$ plane. Blue triangles and red diamonds represent the corresponding values derived from the LOS observations presented in Schilke et al. (2014) and this work.

3.9×10^{-4} and an argon abundance close to its solar abundance of 3.2×10^{-6} (Lodders 2008). Using these values the cosmic-ray ionisation rate is approximated as follows,

$$\zeta_p(H) = \frac{N(ArH^+)}{N(H)} \left(\frac{k_5 n(H_2) + k_6 n(O) + k_7}{11.42} \right), \tag{7.7}$$

$$= \frac{N(ArH^+)}{N(H)} \left(\frac{0.5005 + 448\, f_{H_2}}{1.2 \times 10^6} \right). \tag{7.8}$$

Re-arranging Eq. 7.8, we express it in terms of f_{H_2}, as follows:

$$f_{H_2} = 2.68 \times 10^3 \left[\frac{\zeta_p(H)}{X(ArH^+)} - 4.17 \times 10^{-7} \right] \tag{7.9}$$

Substituting the ArH^+ abundances derived from observations into Eq. 7.9 and by assuming that the ArH^+ ions are exposed to the same cosmic-ray flux as OH^+ and H_2O^+, we derive the molecular fraction of the gas probed by ArH^+. Of course, there is the caveat that ArH^+ does not necessarily trace the same gas as that traced by both OH^+, and H_2O^+ and therefore, need not be exposed to the same cosmic-ray ionisation flux. Our results find ArH^+ to probe a range of molecular fractions, with a median value of $8.8{\times}10^{-4}$. This is in agreement with the results obtained from chemical models presented in Neufeld & Wolfire (2017), which suggest that the observed ArH^+ abundance resides in regions with molecular fractions that are at most 10^{-2}. The molecular fraction analysis displayed in Fig. 7.8, derived from the observed abundances of ArH^+, OH^+, and CH using Eqs. 7.9, 7.4, and 7.3, respectively, clearly shows the transition between different phases of the ISM, from the diffuse atomic to the diffuse/translucent molecular gas.

We further compare the Galactic radial distribution of the azimuthally averaged ArH^+, OH^+ and o-H_2O^+ column densities with those of HI toward a combined sample set that contains

sight lines presented in both Schilke et al. (2014) and this work. The probability distributions of the different column densities were computed using the kernel density estimation method, for a Gaussian kernel. This analysis was carried out for galactocentric distances between 4 and 9 kpc, since we have only a limited number of data points at $R_{\rm GAL}$<4 kpc and $R_{\rm GAL}$>9 kpc making it difficult to comment on the nature of the distribution at these distances. Although we only cover a small number of background continuum sources in the Galaxy (but sample many LOS), the distribution of N(HI) vs. galactocentric radii presented in Fig. 7.9, for the common $R_{\rm GAL}$ coverage, resembles that of the HI emissivity presented by Pineda et al. (2013) for 500 LOS across the Galaxy. The HI column densities we derived peak at $R_{\rm GAL}$ = 5.1 kpc corresponding to the intersection of the Perseus and Norma spiral-arms with a possible narrower peak between 7.5 and 8 kpc arising from the Scutum-Crux arm.

Atomic gas predominantly exists in thermal equilibrium between two phases of the ISM namely, the cold neutral medium (CNM) and the warm neutral medium (WNM). Pineda et al. (2013) used the HI emission line to trace the total gas column but were able to separate the relative contributions from gas in the CNM, and WNM by using constraints from HI absorption studies. Their analysis revealed that the CNM is the dominant component within the inner Galaxy peaking close to the 5 kpc arm while it is the WNM that contributes toward the peak in the outer Galaxy at 8 kpc. The radial distribution of the ArH^+ column densities peaks between 4–4.5 kpc slightly offset from the HI peak with almost an anti-correlation at 4.7 kpc. At $R_{\rm GAL}$>5 kpc, the $N(ArH^+)$ profile decreases mimicking the radial trend followed by the CNM component. However, there maybe a potential increase in the column densities near 8 kpc but we cannot as yet confirm the presence of this peak as we require more sightline information toward the outer Galaxy ($R_{\rm GAL}$ > 8 kpc). If ArH^+ does have a WNM component our results are in agreement with the idea that ArH^+ is formed in the outermost layers of the cloud. The column density distributions of OH^+ and o-H_2O^+ on the other hand, peak behind the 5 kpc ring, with a significant contribution at 4–4.5 kpc similar to the ArH^+, which we do not see in the HI data. Since, the column densities at 7 and 7.5 kpc are much greater than that at 8 kpc for OH^+ and o-H_2O^+ distributions, the presence of a secondary peak in the outer Galaxy, seems unlikely.

7.4.2 Comparison of ArH^+ with other atomic gas tracers

In this section, we investigate the correlation between the column density of ArH^+ with that of other tracers of atomic gas such as OH^+ and o-H_2O^+ and with molecular gas traced by CH. Combining our sample with data taken by Schilke et al. (2014); Indriolo et al. (2015); Wiesemeyer et al. (2016, 2018) and Jacob et al. (2019), in Fig. 7.10 we show the correlation between the 62, 57, and 40 sight lines toward which both ArH^+ and o-H_2O^+ (left), OH^+ (centre), and CH (right), respectively, have been detected. The distribution of the OH^+, and o-H_2O^+ column density components associated with the molecular cloud environment of these star-forming regions displays a large dispersion in comparison to the LOS components with no clear correlations over the range of ArH^+ column densities probed, reflected by weakly negative correlation coefficients of −0.02 and −0.08, respectively. In addition, as expected the ArH^+ and CH column densities derived over molecular cloud velocities are anti-correlated with a correlation coefficient of −0.30. This emphasises that ArH^+ probes cloud layers with

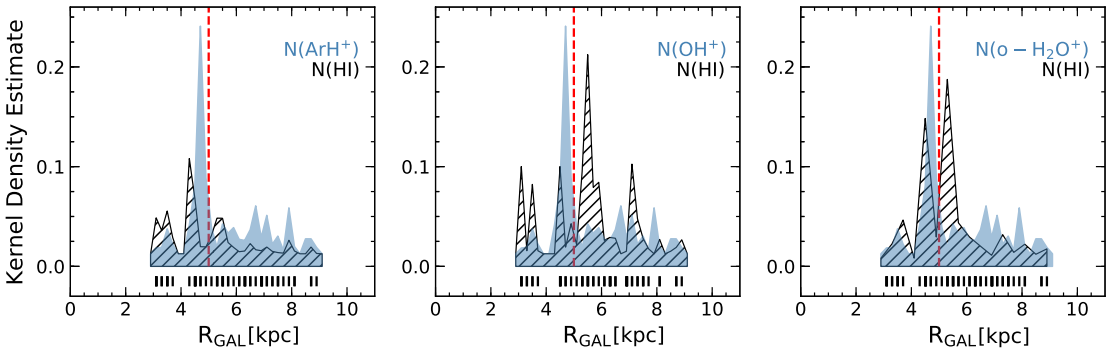

Figure 7.9: Kernel density distributions of ArH^+ (*top*), OH^+ (*centre*) and o-H_2O^+ (*bottom*) column densities as a function of galactocentric distances (black hatched regions). The sampling of the distribution is displayed as a rug plot and is indicated by the solid black lines below the density curves. The dashed red line marks the 5 kpc ring.

slightly different properties from those traced by not only CH but also o-H_2O^+ and OH^+.

The global correlation of the LOS components are described using a power-law of the form $N_Y = cN_X^p$, where c is the scaling factor and p is the power-law index, and N_X, N_Y represent the column densities of the different species. The fit parameters and correlation coefficients (at a 99.99% confidence interval), corresponding to the derived correlations, amongst the different species across all the data points (both LOS and MC) are summarised in Tab. 7.4. We chose to describe the correlation using a power-law trend after comparing the residuals and correlation coefficients obtained from this fit with those obtained from fitting a linear regression of the form, $N_Y = mN_X + c$. Moreover, a positive y-axis intercept would suggest the presence of either o-H_2O^+, OH^+ or H_2 in the absence of ArH^+ or vice-versa for a negative intercept and interpreting this would require the aid of additional chemical models.

As discussed earlier, the different species may not be spatially co-existent and the observed correlations may result from the fact that an increase in the total column density of each sightline subsequently, increases the column density of each phase. Therefore, one would expect there to be a weak correlation between the column densities in each phase, along any given LOS. We investigate this by comparing the abundances of these species as a function of the molecular fraction of the gas they trace. From Fig. 7.11 it is clear that ArH^+ and OH^+ and H_2O^+ all trace the same cloud layers only in a small range of molecular gas fractions between 1.5×10^{-3}–3×10^{-2}, while CH traces the more dense molecular gas. We further notice that the distribution of CH abundances shows a positive correlation with f_{H_2} while, that of OH^+ is anti-correlated and both, ArH^+, and H_2O^+ remain almost constant at $X(ArH^+) = (4.7\pm0.2)\times10^{-10}$ and $X(H_2O^+) = (1.3\pm1.0)\times10^{-9}$.

7.4.3 H_2O^+ ortho-to-para ratio

Of the 14 absorption components for which we were able to compute the OPR of H_2O^+, 9 show values significantly lower than the value of 3:1 with 6 of the derived OPRs lying close to unity. Such low values of the OPR are conceivable as the corresponding spin temperatures (derived in the absence of a rotational excitation term as in Eq. 7.6) reflect the typical kinetic

Table 7.4: Summary of correlation power-law fit parameters as a function of $N(ArH^+)$ (N_X).

N_Y	Power-law index (p)	Coefficient (c)	Pearson's r-value
$N(o\text{-}H_2O^+)$	0.51 ± 0.11	$(2.77 \pm 0.60) \times 10^6$	0.50
$N(OH^+)$	0.37 ± 0.13	$(1.02 \pm 0.18) \times 10^9$	0.35
$N(CH)$	0.42 ± 0.18	$(3.65 \pm 0.91) \times 10^8$	0.36
$N(H_2)^{(a)}$	0.42 ± 0.18	$(1.04^{+0.67}_{-0.50}) \times 10^{15}$	0.36

Notes: $^{(a)}$ $N(H_2)$ values were derived using $N(CH)$ following the relationship determined by Sheffer et al. (2008), $[CH]/[H_2] = 3.5^{+2.1}_{-1.4} \times 10^{-8}$.

temperatures of the diffuse clouds. However, amongst some sightline components the OPR is as high as $4.50^{+1.53}_{-1.60}$ which point to cold environments with spin temperatures as low as 20 K. Perhaps similar to studies of the OPR of H_2 by Flower et al. (2006), the OPR of H_2O^+ at these low temperatures maybe governed by the kinematic rates of its formation and destruction processes.

Moreover, the OPR of H_2 greatly impacts the observed OPR of H_2O^+ because the latter is synthesised in diffuse clouds via an exothermic reaction between OH^+ and H_2. To assess this, requires the determination of the fraction of ortho- and para-H_2O^+ formed from the reacting fractions of both ortho- and para-H_2 states whilst abiding by the spin selection rules. After estimating the fractions of ortho- and para-H_2O^+, Herbst (2015) derived an OPR for H_2O^+ of 2:1 and concludes that this approach fails as it requires all the reacting, parent H_2 molecules to exist in the ortho-state in order to reproduce the higher observed OPR values.

In Fig. 7.12, we investigate the impact of cosmic-ray ionisation rates on the OPR ratio of H_2O^+. In the discussion that follows we do not include those data points corresponding to GC sources studied in Indriolo et al. (2015), as the unique nature of this region results in very high cosmic-ray ionisation rates ($\zeta_p(H) > 10^{-15}$ s^{-1}). As can be seen, the OPR of H_2O^+ thermalises to a value of three when increasing $\zeta_p(H)$ from $\sim 2.8 \times 10^{-17}$ up to $\sim 4.5 \times 10^{-16}$ s^{-1}. This is because an increase in the cosmic-ray flux results in an increase in the abundance of atomic H, thus efficiently driving the (H_2O^+ + H) proton-exchange reaction. Within the cited error bars the OPR saturates to a value of three at a median $\zeta_p(H) = (1.8 \pm 0.2) \times 10^{-16}$ s^{-1}. The lack of a correlation beyond this value may suggest that the destruction of H_2O^+ via reactions with H_2 and free electrons dominates over the proton exchange reaction. If this is true, then the increase in the OPR is controlled by the kinematics of the destruction pathways. Such variations in the destruction reactions of both the ortho and the para forms have been experimentally detected for the dissociative recombination reaction of the H_3^+ ion by Glosík et al. (2010). Such a preferential recombination of the para-state of H_2O^+ over that of its ortho-state might explain the higher observed values of the OPR. However, laboratory measurements of the recombination cross-sections of rotational excitation of the ortho- and para-states of H_2O^+ are required to confirm whether the lowest para state undergoes recombination reactions faster than its ortho counterpart. Alternatively, in regions with high values of $\zeta_p(H)$ where

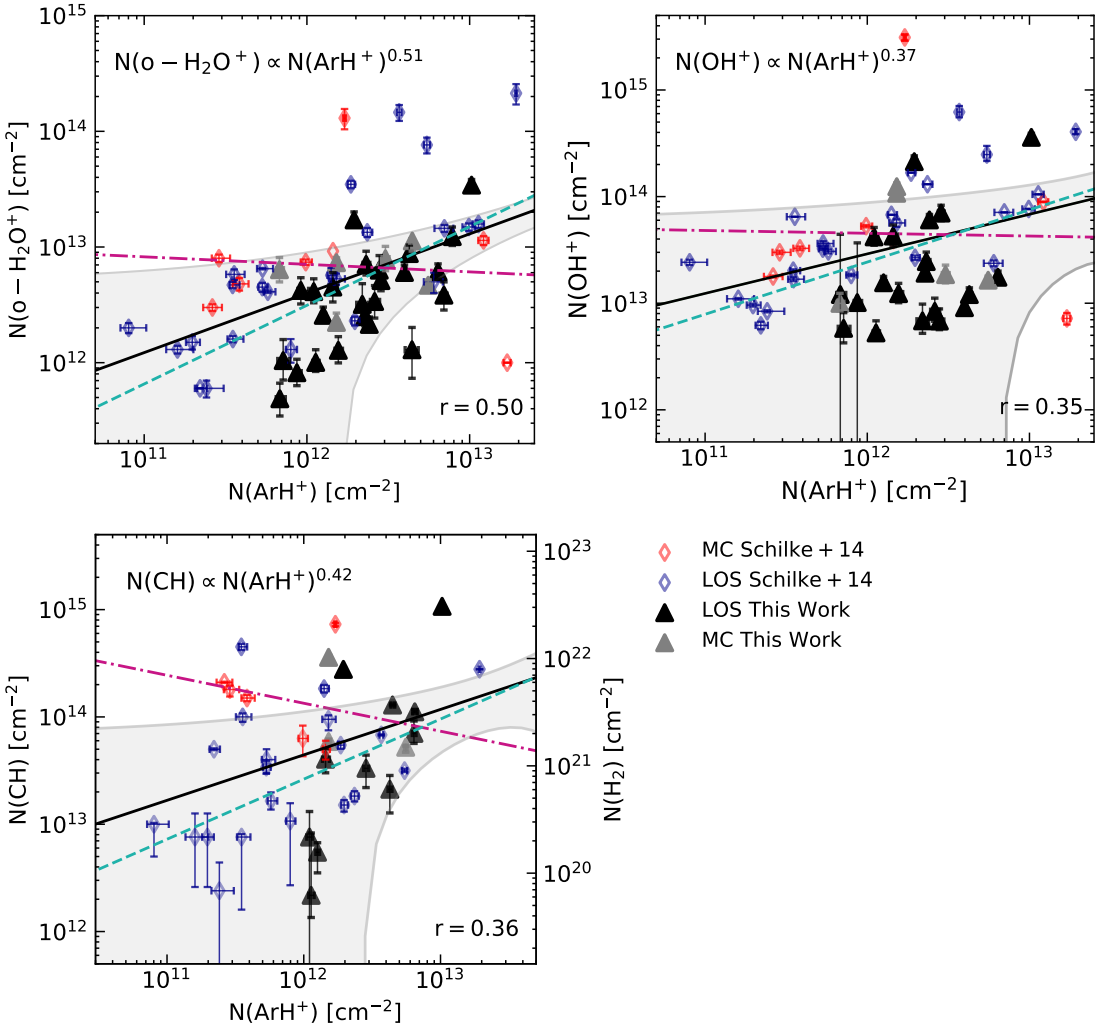

Figure 7.10: Comparison of the ArH^+ column density to that of o-H_2O^+ (*left*), OH^+ (*centre*) and CH (*right*). Black, and grey filled triangles indicate the column density values derived within velocity intervals corresponding to LOS absorption and molecular cloud (MC) toward the Galactic sources presented in this study. Additionally, the blue and red unfilled diamonds mark the LOS and MC column densities derived toward the sources discussed in Schilke et al. (2014). The solid black curve represents the best fit to the combined data set including both the LOS and MC components with the grey shaded region displaying the 1 σ interval of the weighted regression. The dashed cyan and dashed-dotted pink curves represent the fits to only the LOS and only the MC components, respectively.

protons are largely abundant, reactions between H_2O and protons can be a competing formation pathway for the production of H_2O^+ ions ($k \sim 1 - 4 \times 10^{-8}$ cm^{3}s^{-1} for T = 10–100 K). This further complicates the analysis as we now have to take into account the OPR of the reacting H_2O molecules and its corresponding efficiency in producing either ortho- or para-H_2O^+ states. However, this requires detailed modelling of the dust-grain and gas-phase processes that govern

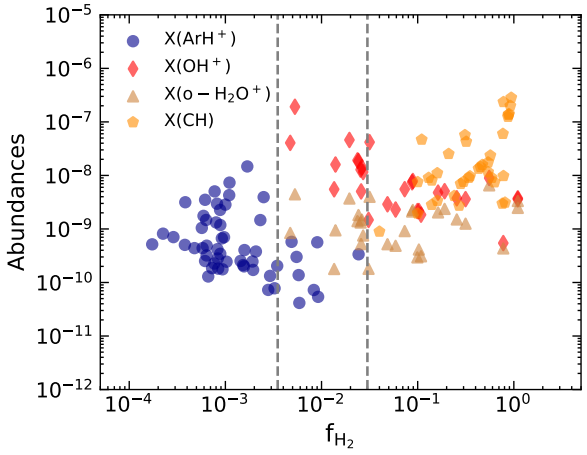

Figure 7.11: Molecular abundances with respect to atomic hydrogen as a function of molecular gas fraction (f_{H_2}). The blue circles, red diamonds, tan triangles, and yellow pentagons represent the abundances of ArH^+, OH^+, H_2O^+ and CH, respectively. The dashed grey lines enclose within them the cloud layers traced by ArH^+, OH^+ and H_2O^+.

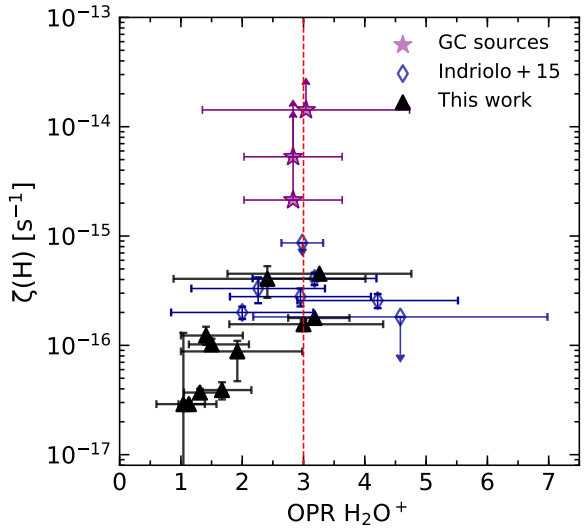

Figure 7.12: Observed OPR of H_2O^+ vs. the cosmic-ray ionisation rates derived using the steady state analysis of the OH^+ and H_2O^+. The results from this work are marked by black triangles while those from Indriolo et al. (2015) are displayed by blue diamonds. For comparison we display the OPR of H_2O^+ derived by these authors toward GC sight lines using purple stars. The dashed red line marks the equilibrium OPR value of three.

the OPR of H_2O, which is beyond the scope of this paper. The main source of uncertainty in this analysis is in the column density estimates of p-H_2O^+ which may be under-estimated in velocity intervals that are affected by contamination from emission lines or over-estimated in regions with D_2O absorption.

7.5 Conclusions

In this paper we present our observations searching for ArH^+ absorption along the LOS toward seven star-forming regions in the Galaxy. Our successful search toward all our targets has doubled the sample of known ArH^+ detections, which allows us to constrain the physical properties of the absorbing medium. We determined ArH^+ column densities over 33 distinct velocity intervals corresponding to spiral-arm and inter-arm crossings and find a mean ArH^+ abundance, $X(ArH^+) = N(ArH^+)/N(H)$ of $1.5 \pm 0.9 \times 10^{-9}$ with a power-law relationship between ArH^+ and atomic hydrogen of $N(ArH^+) \propto N(H)^{0.2}$. We do not detect any ArH^+

absorption at the systemic velocities of these sources except for signatures that trace infalling material.

By analysing the steady state chemistry of OH^+, and o-H_2O^+ along with the abundances determined from observations, we derived molecular hydrogen fractions, f_{H_2}, of the order of 10^{-2}, consistent with previous determinations of f_{H_2} by Neufeld & Wolfire (2016). We subsequently derived cosmic-ray ionisation rates with a mean $\zeta_p(H)$ value of $(2.28\pm0.34)\times10^{-16}$ s^{-1}. Assuming that the observed population of ArH^+ ions are also exposed to the same amount of cosmic-ray irradiation, we derived the molecular fraction of gas traced by ArH^+ to be on average 8.8×10^{-4}. Moreover, the distribution of the column densities of ArH^+–OH^+, ArH^+–o-H_2O^+ and ArH^+–CH, while being moderately correlated for material along the LOS, shows almost no correlation or even a negative one for the material associated with the molecular cloud environments. These results observationally highlight that ArH^+ traces a different cloud population than its diffuse atomic gas counterparts OH^+, and o-H_2O^+ and the diffuse molecular gas tracer CH. Additionally, the Galactic distribution profile of the ArH^+ column densities resembles that of HI within the inner Galaxy ($R_{GAL} \lesssim 7$ kpc). A pronounced peak at 5 kpc is dominated by contributions from the CNM component of atomic gas (Pineda et al. 2013), while the WNM component primarily contributes in the outer Galaxy. While we find a larger dispersion of $N(ArH^+)$ values at $R_{GAL} > 7$ kpc, our analysis does not clearly find evidence for a secondary peak at 8 kpc as it is limited by the number of sight lines. Proving or disproving the presence of this feature, to ultimately distinguish between the different components of the neutral gas probed by the ArH+, would require further observations covering sight lines present in the outer Galaxy. While our results confirm the value of ArH^+ as a tracer of purely atomic gas, there are several sources of uncertainties that can bias them. These include the validity of the assumptions we made in computing the molecular fraction and the systematic effects that the blending of the HI emission particularly at and close to the sources' systemic velocities has on the derived column densities.

Through our H_2O^+ analysis, we have derived OPRs that are both above and below the expected equilibrium value of three with a mean value of 2.10 ± 1.0. This corresponds to a nuclear spin temperature of 41 K which is within the typical range of gas temperatures observed for diffuse clouds. However, a majority of the velocity components show OPRs close to unity, increasing steeply to the standard value of three with increasing cosmic-ray ionisation rates up to $\zeta_p(H) = (1.8 \pm 0.2) \times 10^{-16}$ s^{-1}. Beyond this value, the OPR shows no correlation with $\zeta_p(H)$, indicating that from that point on reactions with H_2 take over as the dominant destruction pathway in its chemistry. The general deviations of the OPR of H_2O^+ may also be inherited from the OPR of its parent species, namely H_2 or H_2O and the efficiency in converting between the two spin states.

Chapter 8

Extragalactic argonium

The great spirals... apparently lie outside our stellar system.

Edwin Powell Hubble, 1917.

Overview

It was while hunting for faint nebula at the Mount Wilson Observatory, that Hubble observed Cepheids in Andromeda (M31). Estimating its distance to be several times that of the outer limits of the Milky Way, Hubble concluded that the great spirals lay outside of the Milky Way. This discovery by Hubble has shaped our understanding of the Universe as being composed of innumerable galaxies that extend across the Universe, thereby pioneering the fields of extragalactic astronomy and observational cosmology.

The detections of argonium, ArH^+, along several sight lines within the Milky Way that cross various spiral arms have shown that this ion is an ubiquitous component of diffuse interstellar clouds (see Chapter 7). So far, the only extragalactic detection of ArH^+ has been made in absorption toward the redshift $z = 0.89$ galaxy that acts as a gravitation lens on the much farther away blazar PKS 1830−211. Being formed in predominantly atomic gas by reactions between Ar^+, initially ionised by cosmic-rays and atomic and molecular hydrogen, ArH^+ has been shown to be an excellent tracer of atomic gas as well as the impeding cosmic-ray ionisation rates. In this work, we extend the observations of ArH^+ in extragalactic sources to examine its use as a tracer of the atomic ISM in the nearby active galaxies, NGC 253 and NGC 4945 as well as a lower limit toward Arp 220 observed using the SEPIA660 receiver on the APEX 12 m telescope. The two sidebands of this receiver allowed us to observe the $N_{K_aK_c} = 1_{1,0} - 1_{0,1}$ transitions of para-H_2O^+ at 607.227 GHz simultaneously with the ArH^+ line. We model the optically thin spectra of ArH^+ and p-H_2O^+ and compare their observed line profiles with that of other well-known atomic gas tracers such as OH^+ and o-H_2O^+ and the molecular gas tracer HF. From the steady-state analysis of the OH^+–H_2O^+ chemistry we derive the molecular fraction traced by ArH^+ bearing clouds to be $\sim 10^{-3}$. We further study the ortho-to-para ratio of H_2O^+ and find that the derived ratios do not significantly deviate from the equilibrium value of three.

8.1 Introduction

Over the duration of its operation, from 2009–2013, the Herschel Space Observatory (HSO) allowed high spectral resolution observations of a variety of molecular hydrides and hydride

ions, several of them newly discovered. Many of their rotational transitions cannot be observed from the ground at all because these high frequency lines lie in parts of the sub-millimetre (sub-mm)/far-infrared (FIR) wavelength range that are blocked by absorption in the Earth's atmosphere. One of the many highlights of the Herschel mission, and a real surprise, has been the fortuitous detection of the $J = 1 - 0$ and $J = 2 - 1$ transitions of argonium, ArH^+ in emission toward the Crab Nebula by Barlow et al. (2013). Following it, Schilke et al. (2014) were able to successfully assign, previously unidentified absorption features near 617 GHz to ArH^+, along the lines-of-sight (LOS) toward five star-forming regions. It turned out that, fortunately, the $J = 1 - 0$ transition of ArH^+ lies at a wavelength that is accessible with ground based telescopes at high mountain sites under exceptional weather conditions, and Jacob et al. (2020b) were recently able to detect ArH^+ toward seven more sightlines in the inner Galaxy using the Atacama Pathfinder Experiment (APEX) 12 m sub-mm telescope. Combined, these observations reveal that the ArH^+ molecular ion exclusively probes diffuse atomic material and is ubiquitously present in the Milky Way. This raises questions on the existence and nature of ArH^+ in extragalactic sources.

Limited by the instrumental resolution, spectrally diluting potential narrow absorption features, previous observations toward extragalactic sources, using the Herschel Spectral and Photometric Imaging REceiver (SPIRE) (Griffin et al. 2010; Swinyard et al. 2010) on board the HSO did not detect the ArH^+ $J = 1 - 0$ and $J = 2 - 1$ lines. Therefore, very little is known about the nature and abundance of ArH^+ outside of the Milky Way. Till date there exists only a single detection of ArH^+ in extragalactic space, carried out by Müller et al. (2015). These authors were able to detect the $J = 1 - 0$ transitions of $^{36}ArH^+$ and $^{38}ArH^+$ through the intermediate redshift $z = 0.8858$ foreground galaxy absorbing the continuum of the gravitational lens-magnified blazar, PKS 1830−211 along two different sightlines using the Atacama Large Millimetre/sub-millimetre Array (ALMA) (Wootten & Thompson 2009).

Primarily residing in atomic gas with molecular hydrogen fractions, f_{H_2} between 10^{-2}–10^{-4} (Schilke et al. 2014; Neufeld & Wolfire 2016; Jacob et al. 2020b), the abundance of ArH^+ is sensitive to the X-ray and cosmic-ray fluxes that permeate the surrounding media as its formation is initiated by the reaction between H_2 and atomic argon ionised by either X-rays and/or cosmic-ray particles. Therefore, observations of the ground state transitions of ArH^+ provide a unique tool for probing atomic gas and estimating ionisation rates. Regions permeated by a high flux of cosmic-rays can be heated by them to high gas temperatures, which in turn strongly influences the initial conditions of star-formation and the initial mass function (IMF) (Papadopoulos et al. 2011).

In this paper we present our search for ArH^+ toward three luminous galaxies, Arp 220, NGC 253 and NGC 4945, using the SEPIA660 receiver on the APEX 12 m telescope. All three systems have been extensively studied over a wide range of wavelengths. In particular, a plethora of molecules have been observed toward these sources, including common hydrides and their cations, e.g., OH, OH^+, H_2O, H_2O^+. Arp 220 is the archetypical ultra-luminous infrared galaxy (ULIRG). A merging system, it hosts two compact nuclei (Baan & Haschick 1995; Rodríguez-Rico et al. 2005) that are surrounded by an immense amount of gas and dust (Scoville et al. 1997; Engel et al. 2011) with dust temperatures between 90 and 160 K (Sakamoto et al. 2008) and a luminosity of 0.2–1 $\times 10^{12}\, L_\odot$. Notably, the intense starburst activity within the dense interstellar medium (ISM) of its nuclear regions causes stars to form

Table 8.1: Properties of studied sources.

Source	Coordinates (J2000)		D	$v_{\rm helio}$	$T_{\rm c}^{a}$
	α [hh:mm:ss]	δ [dd:mm:ss]	[Mpc]	[km s^{-1}]	[K]
Arp 220	15:34:57.20	+23:30:11.00	72.0	5434.0	0.05
NGC 253	00:47:32.98	−25:17:15.90	3.0	240.0	0.21
NGC 4945	13:05:27.48	−49:28:05.60	3.8	585.0	0.54

Notes: [(a)]Main-beam brightness temperature of the continuum at 617 GHz.
References: Distances are taken from the NASA Extragalactic Database (NED) at `https://ned.ipac.caltech.edu`.

at a rate of up to 50–100 $M_\odot$ yr^{-1} (Smith et al. 1998), which is >50 times that in the disk of the Milky Way galaxy today (Robitaille & Whitney 2010) and ∼1000 times that in its central molecular zone (Immer et al. 2012). NGC 253 is a barred prototypical starburst galaxy part of the Sculptor group, with an infrared luminosity of $1.7 \times 10^{10}\,L_\odot$ (Radovich et al. 2001). Its strong nuclear starburst, drives a ∼100 pc-scale molecular gas outflow/wind seen, e.g., by CO observations (Bolatto et al. 2013a). It has been suggested that at the centre of this barred spiral a weak AGN coexists with the strong starburst, an issue that is still under debate (e.g., Müller-Sánchez et al. 2010; Gutiérrez et al. 2020). NGC 4945 is an infrared-bright galaxy with a Seyfert nucleus, signifying an accreting supermassive black hole, in the Centaurus group with a luminosity of $2.4 \times 10^{10}\,L_\odot$ (Brock et al. 1988). It is the brightest Seyfert 2 Galaxy and hosts a deeply enshrouded AGN at its centre which is revealed by X-ray emission in the 100-keV sky (Iwasawa et al. 1993). The AGN is surrounded by a strongly absorbing, inclined circumnuclear starburst ring with a radius of ∼50 pc (Chou et al. 2007).

Taken together, the small sample of sources selected for this study cover a wide range of nuclear environments. The observations are described in Sect. 8.2, followed by a qualitative and quantitative analysis of the data and a discussion of the results in Sect. 8.3. Finally, in Sect. 8.4 we discuss our main findings and summarise our results.

8.2 Observations

Using the Swedish-ESO PI (SEPIA660) receiver (Belitsky et al. 2018; Hesper et al. 2018) of the APEX 12 m sub-mm telescope, we were able to carry out observations of the $J = 1 - 0$ transition of ^{36}ArH$^+$ (hereafter ArH$^+$) between 2019 July and August (Project Id: M9519C_103). The SEPIA660 receiver is a two sideband (2SB), dual polarisation receiver that covers a bandwidth of 8 GHz, per sideband, with a sideband rejection level >15 dB. The observations were carried out in wobbler switching mode, using a secondary wobbler throw of 180″ in azimuth at a rate of 1.5 Hz. Combined with the atmospheric stability at the high APEX site, this observing method allows reliable recovery of the sources' continuum levels.Properties of our source sample are summarised in Table 8.1.

We tuned the upper sideband (USB) to a frequency of 618.5 GHz to cover the ArH$^+$ $J = 1 - 0$ transition at 617.525 GHz. This allowed us to simultaneously observe the $N_{K_a K_c}$ =

$1_{10}-1_{01}, J = 3/2-1/2$, and $J = 3/2-3/2$ transitions of p-H_2O^+ at 604.678 and 607.227 GHz in the lower sideband (LSB), centred at a frequency of 606.5 GHz. The USB also covers an atmospheric absorption feature close to 620 GHz. Our observations were carried out under excellent weather conditions, with precipitable water vapour (PWV) levels between 0.25 and 0.41 mm, corresponding to an atmospheric transmission better than or comparable to 0.5 in both sidebands and a mean system temperature of 1874 K, at 617 GHz. On average we spent a total (on+off) observing time of 6.5 hours toward each source. The typical half power beam-width (HPBW) is 10.″3 at 617 GHz. The HPBW at this frequency corresponds to 3.5 kpc at the distance toward Arp 220 and 0.15 kpc and 0.19 kpc for NGC 253 and NGC 4945, respectively. Therefore, while the beam covers the majority of the Arp 220 system, it only probes the nucleus and foreground disk gas of the latter two galaxies. We converted the spectra into main-beam brightness temperature scales by using an antenna forward efficiency, $F_{\rm eff}$, of 0.95 and a main-beam efficiency, $B_{\rm eff}$, of 0.41 (determined from observations of Mars). The calibrated spectra were subsequently processed using the GILDAS/CLASS software[1]. The spectra obtained toward the different sources were box-smoothed to velocity bins of $\sim$4.5 km s^{-1} and a first order polynomial baseline was removed. Our search for ArH^+ toward Arp 220 was unsuccessful and we do not detect any lines in the sideband down to a noise level of 2 mK at a spectral resolution of 4.5 km s^{-1}. Therefore, we do not include Arp 220 in our analysis but quote a 3σ upper limit of 6 mK for the ArH^+ $J = 1-0$ transition in this source.

In addition to the results of the ArH^+ and p-H_2O^+ observations newly presented in this work, we use complementary archival HIFI/*Herschel* data of other well known tracers of atomic gas, namely, OH^+ and o-H_2O^+ , which were acquired as a part of the Herschel EXtraGALactic (HEXGAL) guaranteed time key project (PI: Güsten), published by van der Tak et al. (2016) and also of the diffuse molecular gas tracer HF observed by Monje et al. (2014). The HIFI HPBWs at the frequencies of the OH^+, o-H_2O^+, and HF transitions studied in the above work are comparable to one another at 22″, 20″, and 17″ respectively. We also compare the profiles of the ArH^+ line with those of the HI 21 cm line and subsequently determine the ArH^+ abundances. For this we use archival interferometric data of HI absorption and emission for NGC 253 and NGC 4945, observed using the Australia Telescope Compact Array (ATCA) with beam sizes of 4.″9 × 10.″3 and 7.″9 × 9.″4, respectively. The HI column densities were determined as described in Winkel et al. (2017), by combining the absorption profiles with emission line data. The results of this HI analysis, resulting in determinations of the optical depth, spin temperatures, and HI column densities along with the corresponding HI emission and absorption spectra is given in Appendix F.1. The spectroscopic parameters of all the lines described above are summarised in Table 8.2.

We analysed the stability of the quoted continuum levels at 617 GHz across scans (or time) and found the measured fluctuations to lie within 14%. This is illustrated in Fig F.2 and is not surprising as the observations were carried out using a wobbling secondary with a fast switching rate which guaranteed the removal of any drifts that may arise due to atmospheric instabilities. Furthermore, we find the 617 GHz continuum flux to be well correlated with the continuum flux at 870 μm observed using the Large APEX Bolometer Camera (LABOCA)

[1]Software package developed by IRAM, see `https://www.iram.fr/IRAMFR/GILDAS/` for more information regarding GILDAS packages.

at the APEX telescope presented in Weiß et al. (2008). This leads us to conclude that the continuum levels used are fairly reliable.

8.3 Results and discussion

8.3.1 Spectral line properties

The calibrated and baseline-subtracted spectra toward NGC 253 and NGC 4945 are presented in Figure 8.1. In the following paragraphs we qualitatively discuss the observed ArH^+ and p-H_2O^+ features and compare them to spectra of OH^+, o-H_2O^+, HF, and HI. As mentioned above, our tuning setup simultaneously covers both the $J = 3/2 - 1/2$ as well as the $J = 3/2 - 3/2$ fine structure transitions from the $(1_{1,0} - 1_{0,1})$ level of p-H_2O^+ at 604.678 and 607.227 GHz. However, toward both NGC 253 and NGC 4945, we do not detect the $J = 3/2 - 1/2$ fine structure transition near 604 GHz above a noise level of ∼3 and 7 mK at a spectral resolution of 4.5 km s^{-1}, respectively and is therefore, not discussed further in the text. For both NGC 253 and NGC 4945, we assume source sizes of ∼20″, which were previously determined by Wang et al. (2004); Aladro et al. (2015); Pérez-Beaupuits et al. (2018) and references therein, using molecular emission maps of abundant species like CO. The beam sizes of all the species studied here (see Table 8.2) are either smaller than or comparable to this source size.

NGC 253

The ArH^+ line profile toward NGC 253 displays a P-Cygni profile with blueshifted absorption, covering a velocity range from ∼90 to 270 km s^{-1} and weak redshifted emission at higher velocities. The absorption feature is centred at a velocity of 210 (±3.7) km s^{-1}, which is lower than the systemic velocity of the source (∼240 km s^{-1}). In comparison, other species like OH^+ (although saturated between 185 and 235 km s^{-1}), o-H_2O^+ and HF all show spectra with similar P-Cygni profiles with comparable velocity shifts from the systemic value of the source. The corresponding HI profile shows an asymmetric absorption component, centred at a blueshifted velocity of ∼218 km s^{-1} with the deeper component at ∼200 km s^{-1}. The velocity shift observed in the HI spectrum has been interpreted as evidence for a rotating nuclear disk of cold gas in this Galaxy (Koribalski et al. 1995). Additionally, the observed P-Cygni profiles characterise the radial motion of gas, which is indicative of outflows from the central region.

NGC 4945

Toward NGC 4945, the ArH^+ line displays an asymmetric absorption profile between 455–715 km s^{-1}, similar to what is observed in the spectra of OH^+, o-H_2O^+ and HF lines. As discussed in Monje et al. (2014), van der Tak et al. (2016) and references therein, there are at least two velocity components, however unlike the other molecules and molecular ions, the broader component in ArH^+ is centred at 510 km s^{-1} and the narrower one at 605 km s^{-1} while for the other species the broader component is the redshifted absorption feature.

Table 8.2: Spectroscopic properties of the studied species and transitions.

Species	Transition		Frequency	A_E	E_u	Receiver/Telescope	θ_{FWHM}
	$J' - J''$	$F' - F''$	[GHz]	[s^{-1}]	[K]		[″]
ArH^+	1 – 0	—	617.525	0.0045	29.63	SEPIA660/APEX	10
p-H_2O^+	3/2 – 1/2	—	604.678	0.0013	59.20	SEPIA660/APEX	10
($1_{1,0} - 1_{0,1}$)	3/2 – 3/2	—	607.227	0.0062	59.20	SEPIA660/APEX	
OH^+	2 – 1	5/2 – 3/2	971.803*	0.0182	46.64	HIFI/Herschel	22
(1–0)		3/2 – 1/2	971.805	0.0152			
		3/2 – 3/2	971.919	0.0030			
o-H_2O^+	3/2 – 1/2	3/2 – 1/2	1115.150	0.0171	53.52	HIFI/Herschel	20
($1_{1,1} - 0_{0,0}$)		1/2 – 1/2	1115.186	0.0274			
		5/2 – 3/2	1115.204*	0.0309			
		3/2 – 3/2	1115.262	0.0138			
		1/2 – 3/2	1115.298	0.0034			
HF	1 – 0	—	1232.476	0.0242	59.14	HIFI/Herschel	17

Notes: The spectroscopic data are taken from the Cologne Database for Molecular Spectroscopy (CDMS, Müller et al. 2005). The H_2O^+ frequencies were actually refined considering astronomical observations (see Appendix A of Muller et al. 2016).(*)Indicates the strongest HFS transition, which was used to set the velocity scale in the analysis.

Table 8.3: Synopsis of the derived column densities.

Source	v_{min}–v_{max}	$N(ArH^+)$	N(p-H_2O^+)	N(o-H_2O^+)	$N(OH^+)$	N(HF)	N(HI)
	[km s^{-1}]	10^{13}[cm^{-2}]	10^{13}[cm^{-2}]	10^{14}[cm^{-2}]	10^{14}[cm^{-2}]	10^{14}[cm^{-2}]	10^{20}[cm^{-2}]
NGC 253	55–295	2.12 ± 0.16	5.53 ± 0.22	2.51 ± 0.36	>6.31	1.40 ± 0.60	2.90 ± 2.30
NGC 4945	445–725	2.16 ± 0.10	11.07 ± 0.14	6.15 ± 0.16	>4.40	1.61 ± 0.68	2.36 ± 0.97

In the p-H_2O^+, o-H_2O^+, OH^+[2], and HF spectra, the two absorption components are observed to be almost symmetric about the Galaxy's systemic velocity at 585 km s^{-1} (Chou et al. 2007). This may indicate that the observed absorption arises from non-circular motions associated with the Galaxy's bar. A similar absorption dip is seen in the emission line profiles of lines from higher density gas tracers like HCN, HCO^+, CN (Henkel et al. 1990) and also from CO (Whiteoak et al. 1990) near 640 km s^{-1}. It likely traces foreground molecular gas that is moving toward the nucleus. The HI absorption spectrum against the nuclear continuum of the source, also displays a similar profile with two absorption components with dips at ~540 and ~620 km s^{-1}. The observed shift in the centres of both the ArH^+ absorption components in comparison to that of the other molecules, suggests that ArH^+ does not trace the same layers of infalling molecular gas as the other molecules and molecular ions but rather traces mostly or exclusively atomic gas layers, as expected.

8.3.2 Column densities

The line profiles can be expressed in terms of the optical depth, τ, using the radiative transfer equation, which for the particular case of absorption spectroscopy is given by $T_\mathrm{b} = T_\mathrm{c} e^{-\tau}$, where T_b and T_c are the line, and the background continuum brightness temperatures, respectively. For NGC 253, we compute optical depths for the absorption profile obtained after subtracted the emission component. The emission component is modelled by fitting a Gaussian profile centred at the systemic velocity of the source. We fit the optical depth profile on heliocentric velocity scales, i.e., τ vs. υ_helio, using the Wiener filter fitting technique as described in Jacob et al. (2019) by minimising the mean square error between the model and observations. For species like OH^+ and o-H_2O^+, whose rotational transitions further undergo hyperfine-structure (HFS) splitting, this algorithm additionally deconvolves the HFS from the observed spectrum using the relative spectroscopic weights of the different HFS components. Other than the observed spectrum and the spectroscopic parameters of the line to be fit, the only other input parameter required by the Wiener filter technique is the spectral noise, which is assumed to be independent of the observed signal. However, the Wiener filter faces singularities in portions of the spectrum in which the observed line profiles saturate or the line-to-continuum ratio tends to zero. This is the case for the OH^+ spectrum towards NGC 253, which shows saturated absorption at blueshifted velocities between 185 and 235 km s^{-1} (see Fig. 8.1). We model this line by scaling, on the main-beam temperature scale, the model of the o-H_2O^+ line profile by the ratio of their column densities as determined by van der Tak et al. (2016). The OH^+ HFS deconvolution is then performed on this scaled model. The physical quantities that are directly derived from this model strictly represent lower limits.

The resulting optical depth profiles are used to derive column densities as follows, assuming that the foreground absorption covers the background continuum source entirely:

$$N_\mathrm{tot} = \frac{8\pi\nu^3}{b_\mathrm{ff} c^3} \frac{Q(T_\mathrm{ex})}{g_\mathrm{u} A_\mathrm{E}} \mathrm{e}^{E_\mathrm{u}/T_\mathrm{ex}} \left[\exp\left(\frac{h\nu}{k_\mathrm{B} T_\mathrm{ex}}\right) - 1\right]^{-1} \int \tau \mathrm{d}\upsilon \,. \tag{8.1}$$

For a given species, all the spectroscopic terms in Eq. 8.1 namely, the upper level energy,

[2]The OH^+ spectrum contains a second absorption feature, which is the result of image band contamination from the CH_3OH $J_k = 9_4 - 8_3$ E2 line near 959.8 GHz (Xu & Lovas 1997).

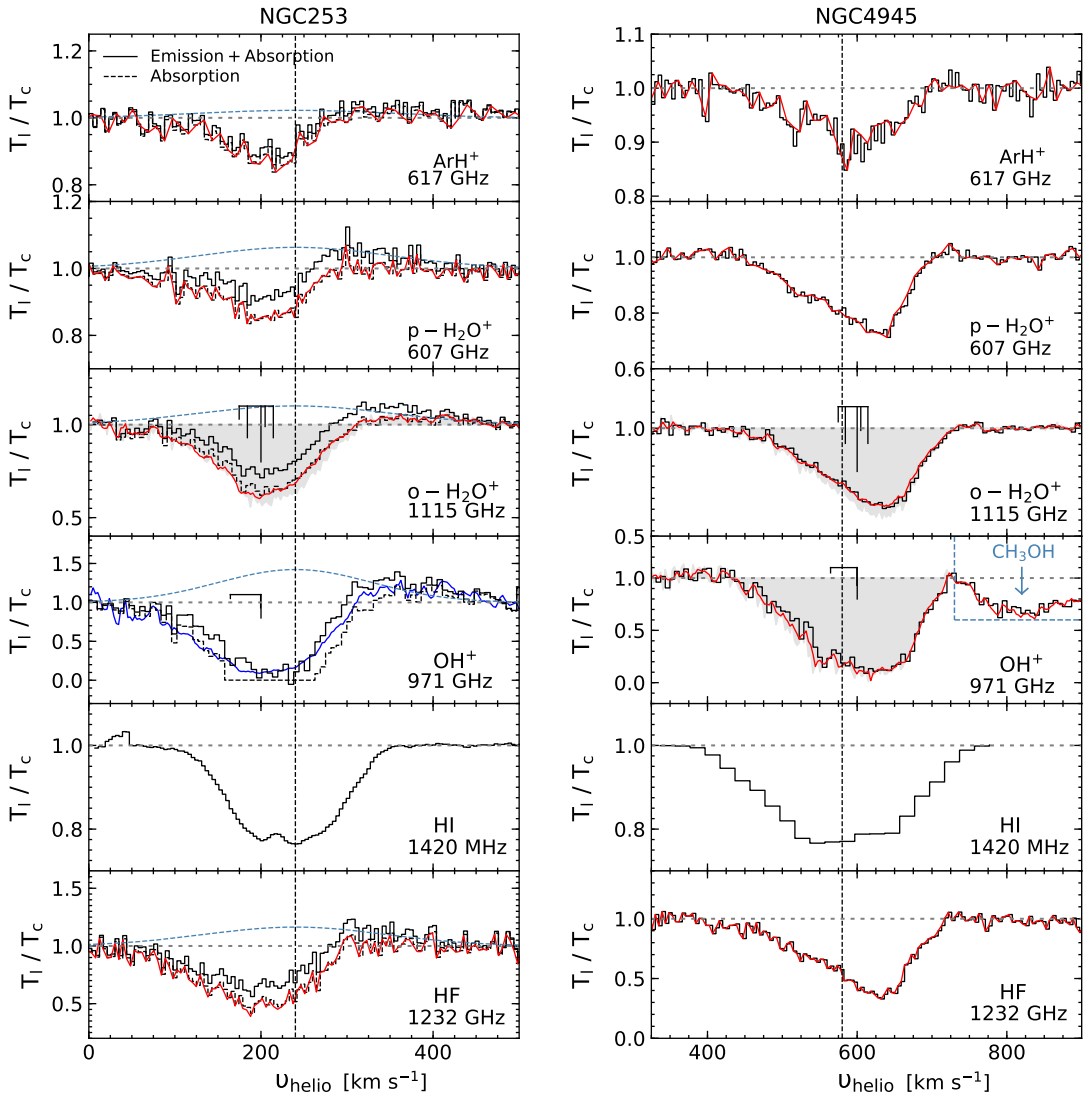

Figure 8.1: *From top to bottom*: Normalised spectra of ArH^+, p-H_2O^+, o-H_2O^+, OH^+, HI and HF toward NGC 253 (*left*) and NGC 4945 (*right*), respectively. In the spectra for NGC 253, the dotted blue lines display the Gaussian fit to the emission component. The dashed black line represents the individual absorption profiles after subtracting the Gaussian fit with their Wiener filter fits overlaid in red for all species except HI. The relative intensities of the HFS components of the o-H_2O^+ and OH^+ transitions are shown in black above their respective spectra and the grey shaded regions display their HFS deconvolved spectra. The vertical dashed black lines mark the systemic velocity of NGC 253 and NGC 4945 at 240 km s^{-1} and 563 km s^{-1}, respectively. Note, that the OH^+ line profile toward NGC 253 is saturated at blueshifted velocities and is fit by scaling the o-H_2O^+ profile as detailed in the text (dark blue curve) while that toward NGC 4945 is contaminated by CH_3OH $J_k = 9_4 - 8_3$ E line near 959.8 GHz originating from the image sideband (marked in blue).

E_u, the upper level degeneracy, g_u, and the Einstein A coefficient, A_E, all remain constant, except for the partition function, Q, which itself is a function of the rotation temperature, T_{rot}. Under conditions of local thermodynamic equilibrium (LTE), T_{rot} is equal to the excitation temperature, T_{ex}. The excitation of the molecules is straightforward as most of the particles are expected to occupy the ground state level, owing to the large Einstein A coefficients of all the lines involved, resulting in high critical densities of the order of a few $10^7\,cm^{-3}$ (see Table 8.2 for the Einstein A coefficients). Assuming a complete ground state occupation, we can approximate the excitation temperature to be less than the energy of the upper level above the ground and equal to the radiation temperature of the cosmic microwave background ($T_{CMB} = 2.73\,K$). Similar assumptions for the excitation temperatures have been made by van der Tak et al. (2016) in their analysis. Since, $T_{CMB} < T_{ex} < E_u/k_B$, the column densities derived for the different species studied here only represent lower limits. Further, the derived column densities are corrected to a first order for beam dilution effects, using the beam filling factor, b_{ff}, following $b_{ff} = \left[\left(\theta_s^2 + \theta_b^2\right)/\theta_s^2\right]$ where, θ_s, and θ_b represent the molecular source size and the beam size, respectively. The column densities hence derived over the velocity interval between 55–295 km s^{-1} for NGC 253, and 445–725 km s^{-1} for NGC 4945, are summarised in Table 8.3.

8.3.3 Gas properties

Cosmic-rays are an important source of heating and ionisation in interstellar and intergalactic media, driving ion-molecular reactions, including those responsible for the formation of ArH^+ (Roach & Kuntz 1970; Theis et al. 2015).

$$\mathrm{Ar} \xrightarrow{\mathrm{CR}} \mathrm{Ar}^+ \xrightarrow{\mathrm{H_2}} \begin{cases} \mathrm{ArH}^+ + \mathrm{H} & (\Delta E = 1.838\,\mathrm{eV}) \\ \mathrm{ArH_2} & (\Delta E = 1.930\,\mathrm{eV}) \\ \mathrm{ArH_2^+} \rightarrow \mathrm{ArH}^+ + \mathrm{H} & (\Delta E = 0.493\,\mathrm{eV}) \end{cases}$$

Hence, as a key ingredient in the ensuing chemistry, the abundance of ArH^+ is sensitive to the cosmic-ray ionisation rate, $\zeta_p(H)$ and to the molecular fraction, $f(H_2)$ of the gas probed. The cosmic-ray ionisation rates in both NGC 253 and NGC 4945 have previously been determined by analysing the steady-state chemistry of O-bearing ions like OH^+ and H_2O^+ by van der Tak et al. (2016). These authors derived $\zeta_p(H)$ values between 6×10^{-17} and $8\times10^{-16}\,s^{-1}$. Following the steady-state analyses presented by these authors and Indriolo & McCall (2012), we derive revised cosmic-ray ionisation rates by including contributions from para-H_2O^+ in the analysis. The value of $N(H)$ used in our calculations is given by $N(HI) + 2\times N(H_2)$, where $N(H_2)$ is obtained by using $N(HF)$ as a surrogate for molecular hydrogen, where the abundance of HF is assumed to be 5×10^{-10} (Emprechtinger et al. 2012). Including contributions from para-H_2O^+ has changed the cosmic-ray ionisation rates only slightly to 6.2×10^{-17} and $1.6\times10^{-15}\,s^{-1}$ toward NGC 253 and NGC 4945, respectively. The higher values of $\zeta_p(H)$ derived toward NGC 4945 reflect the larger columns of p-H_2O^+ probed. The derived values are in agreement with the range of values covered by $\zeta_p(H)$ in the Milky Way (Indriolo & McCall 2012; Indriolo et al. 2015; Jacob et al. 2020b). However, values for the cosmic-ray ionisation rate estimated toward the nuclei of ULIRGs like Arp 220, NGC 4418 and Mrk 231, are almost three orders

of magnitude higher with a lower-limit of $\zeta_{\rm p}({\rm H}) > 10^{-13}\,{\rm s}^{-1}$ (González-Alfonso et al. 2013, 2018), similar to those derived in the Galactic centre (GC). These variations in the ionisation rates reflect the higher levels of energetic phenomena present in the centres of these Galaxies in comparison to their disks.

Under the assumption that the cloud layers containing ArH^+ are exposed to the same cosmic-ray ionisation flux as those traced by both OH^+, and H_2O^+, we can derive the molecular fraction, $f_{\rm H_2}$, of the gas probed by ArH^+, using the ArH^+ abundances (with respect to HI) derived from observations as a constraint. We first present the relation between $\zeta_{\rm p}({\rm H})$, $X({\rm ArH^+})$ and $f({\rm H_2})$ by analysing the steady-state ion-molecular chemistry of ArH^+ as presented by Schilke et al. (2014). ArH^+ is destroyed primarily via proton transfer reactions with H_2 or atomic oxygen, and photodissociation:

$$\begin{aligned}
&{\rm ArH^+ + H_2 \rightarrow Ar + H_3^+\,;} && k_5 = 8\times10^{-10}\ {\rm cm^3 s^{-1}}\\
&{\rm ArH^+ + O \rightarrow Ar + OH^+\,;} && k_6 = 8\times10^{-10}\ {\rm cm^3 s^{-1}}\\
&{\rm ArH^+ + h\nu \rightarrow Ar^+ + H\,;} && k_7 = 1.0\times10^{-11}\,\chi_{\rm UV} f_{\rm A}\ {\rm s^{-1}}\,.
\end{aligned}$$

The photodissociation rate of ArH^+ was estimated by Alekseyev et al. (2007) to be $\sim 1.0\times 10^{-11} f_{\rm A}\ {\rm s^{-1}}$ for an unshielded cloud model that is uniformly surrounded by the standard Draine UV interstellar radiation field. Recently, Roueff et al. (2014) calculated photodissociation rates of ArH^+ that were much higher, at $1.9\times10^{-9}\,{\rm s^{-1}}$, but for the specific environment of the Crab nebula. The attenuation factor, $f_{\rm A}$, is given by an exponential integral and is a function of visual extinction, $A_{\rm v}$. For a cloud model with $A_{\rm v} = 0.3$, Schilke et al. (2014) derived values for $f_{\rm A}$ between 0.30 and 0.56 that increase as you move outwards from the centre of the cloud. For our analysis, we use a value for $f_{\rm A}$ which lies mid-way through the computed range of values, at 0.43. We further assume an atomic oxygen abundance (relative to H nuclei) of 3.9×10^{-4} and an argon abundance close to its solar abundance of 3.2×10^{-6} (Lodders 2008). van der Tak et al. (2016) suggest that the dense and diffuse gas phases are well mixed toward these galaxies, owing to the similarities between the observed line profiles of OH^+ and H_2O^+ to that of H_2O and HI. Therefore, one can imagine the gas to be distributed such that there exists pockets of diffuse gas in a bed of dense material. Akin to these authors, who derived the cosmic-ray ionisation rates for NGC 253 and NGC 4945 by analysing the steady-state chemistry of OH^+ and H_2O^+, we assume a gas density, n(H), of $35\,{\rm cm^{-3}}$ (Indriolo et al. 2015) for the OH^+–H_2O^+ absorbing clouds in our analysis. Using these values, the cosmic-ray ionisation rate can be approximated as

$$\zeta_{\rm p}({\rm H}) = \frac{N({\rm ArH^+})}{N({\rm H})}\left(\frac{k_5 n({\rm H_2}) + k_6 n({\rm O}) + k_7}{11.42}\right), \tag{8.2}$$

$$= \frac{N({\rm ArH^+})}{N({\rm H})}\left(\frac{0.5005 + 448 f_{\rm H_2}}{1.2\times10^6}\right). \tag{8.3}$$

Eq. 8.3 is re-arranged and expressed in terms of $f_{\rm H_2}$, as

$$f_{\rm H_2} = 2.68\times10^3\left[\frac{\zeta_{\rm p}({\rm H})}{X({\rm ArH^+})} - 4.17\times10^{-7}\right]. \tag{8.4}$$

Using Eq. 8.4, the molecular fractions of the gas probed by ArH^+ are found to be $\sim 2 \times 10^{-3}$ and 10.7×10^{-2} for NGC 253 and NGC 4945, respectively. In comparison HF traces gas that is almost completely molecular.

The abundances of ArH^+ and cosmic-ray ionisation rates in both the starburst galaxies NGC 253 and NGC 4945 are comparable with marginally higher rates observed in NGC 4945. This may reflect its weak AGN activity, however, it is uncertain whether the non-detection of ArH^+ toward Arp 220 is because this system's X-ray emission is not capable of ionising Ar or whether it is a combined effect of sensitivity and the low continuum level. By combining previous estimates of the cosmic-ray ionisation rates derived for Arp 220, of $\zeta_p(H)>10^{-13}$ s^{-1} (González-Alfonso et al. 2013; van der Tak et al. 2016), with our upper limit for the ArH^+ abundance of 2.5×10^{-11} (determined by integrating the 3σ detection limit quoted in Sect. 8.2 over a line width of 743 km s^{-1} (Mirabel 1982) and $N(H_2)=1 \times 10^{24}$ cm^{-2} (Downes & Eckart 2007)), we are unable to derive reasonable values for the molecular fraction traced by ArH^+. This could likely be because our beam covers the entire galaxy and we only use a single value for the cosmic-ray ionisation rate rather than a gradient that decreases away from the centre of the galaxy as demonstrated within the Milky Way by Indriolo et al. (2015); Jacob et al. (2020b). Moreover, while ionisation by cosmic-rays plays an important role in heating the gas in the nuclear environment of galaxies (Bradford et al. 2003), heating by X-rays (Usero et al. 2004) and by stellar UV radiation (in widespread photodissociation regions, PDRs) (Hollenbach & Tielens 1997), dynamical shock heating (García-Burillo et al. 2001) to a name a few, can all be prominent sources of heating in these regions and it is not possible to discriminate between their contributions merely an analysis such as ours.

8.3.4 H_2O^+ ortho-to-para ratio

The H_2O^+ molecular ion exists in two symmetric states, ortho- and para-H_2O^+ that have opposing parities due to the interaction between the magnetic moment of the unpaired electron and protons. Studying the ratio of molecules in these two states can provide insight into the formation pathway and thermodynamic properties of the gas. In the following paragraphs we determine the ortho-to-para ratio (OPR) of H_2O^+ and derive the nuclear spin temperature.

Unlike H_2O, the lowest ground state of its molecular ion, H_2O^+ corresponds to its ortho state as a result of its C_{2v} symmetry and $^2B_1$ ground state configuration. The fine structure level of the ortho-H_2O^+ spin state, with a nuclear spin, I, of 1 further undergoes HFS splitting while, para-H_2O^+ with $I = 0$, does not. The lowest rotational levels of each spin state, $N_{K_aK_c} = 1_{1,1} - 0_{0,0}$ ortho-H_2O^+ and $N_{K_aK_c} = 1_{1,0} - 1_{0,1}$ para-H_2O^+, respectively, have a an energy difference of 30.1 K. With the assumption that the rotational temperature is close to $T_{CMB} = 2.73$ K, one would expect most of the ions to occupy either of its ground state levels. Similar to H_2 and H_2O, H_2O^+ is expected to exhibit an OPR of at least 3:1 (Townes & Schawlow 1975). Typically the conversion between the ortho and para states of H_2O^+ occurs via gas phase reactions with atomic hydrogen as follows,

$$\text{p-}H_2O^+ + H \rightleftharpoons \text{o-}H_2O^+ + H$$

while H_2O^+ energetically reacts with molecular hydrogen to yield H_3O^+. Moderately coupled

via collisions, the OPR between the two spin states of H_2O^+ is given by,

$$\mathrm{OPR} = \frac{Q_{\mathrm{ortho}}}{Q_{\mathrm{para}}} \exp\left(-\Delta E / T_{\mathrm{ns}}\right) , \tag{8.5}$$

where Q_{ortho} and Q_{para} represent the partition functions of the respective states, ΔE is the energy difference between them, $\Delta E = -30.1$ K and T_{ns} is the nuclear spin temperature. The value of ΔE is expressed as a negative quantity because the lowest ortho state has a lower energy than the lowest para state (unlike in H_2O). As discussed in Schilke et al. (2010) (see Appendix A), at low temperatures, the partition functions of the two states are governed by the degeneracy of their lowest fine-structure and HFS levels. Having the same quantum numbers and upper level degeneracies, the ratio of the partition functions approach unity as the rotational temperature tends to 0 K. The OPR determined toward NGC 253 is quite large with a median value of roughly 4.5±3.0 derived from the column density per velocity interval, whereas, that derived toward NGC 4945 is 3.5±1.2 both of which are consistent with the equilibrium value of three within the quoted error bars. Subsequently, these ratios correspond to nuclear spin temperatures between 15 and 24 K, which suggests the association of H_2O^+ with the cold molecular gas surrounding the warm nuclear disk, rather than the disk itself. These results are visualised in Figs. 8.2 and 8.3, where we display the distribution of the derived column densities per velocity intervals (corresponding to the spacing of the velocity channel bins) for ortho-, and para-H_2O^+, the OPR and the nuclear spin temperature, over the relevant velocity intervals.

Theoretical studies carried out by Tanaka et al. (2013) on the ortho to para exchange reactions of H_2O^+ reveal quite low reaction rates, which implies that the OPR of H_2O^+ does not significantly deviate from the equilibrium value of three, particularly at low temperatures. However, observed values of the OPR of H_2O^+ are greater than 3. In diffuse regions irradiated by X-rays and/or cosmic-rays, the chemistry of H_2O^+ is initiated by the charge transfer between ionised hydrogen and oxygen atoms to form O^+, which is subsequently followed by reactions with H_2 to first form OH^+ and then H_2O^+. Alternatively, in regions with higher molecular fractions, both OH^+ as well as H_2O^+ can be formed via reactions between H_3^+ and oxygen atoms (Hollenbach et al. 2012, and references therein). Lastly, H_3O^+ can also be formed from the ionization and charge exchange reactions of H_2O in denser environments. The derived OPR of H_2O^+ are >3 and point to cold environments with spin temperatures ∼20 K.

Since the diffuse and dense gas volumes along the sight lines toward these galaxies are well mixed, the OPR of parent species such as H_3^+, H_2, and H_2O, from which H_2O^+ originates, may impact the observed OPR of H_2O^+ (see for example the studies on the OPR of H_2 presented by Flower et al. 2006). Destruction reactions of both the ortho- and para- forms of H_3^+ via dissociative recombination have been experimentally investigated by Glosík et al. (2010), who observe that the preferential recombination of the para-state over that of its ortho-state which can also lead to OPRs >3. However, a better understanding of the OPR of H_2O^+ requires a detailed understanding (not only) of what fraction of the observed H_2O^+ is formed along each of the different chemical pathways toward its formation, but also the efficiency with which either H_2O^+ state (ortho or para) is formed in both quiescent and turbulence or shock dissipated regions.

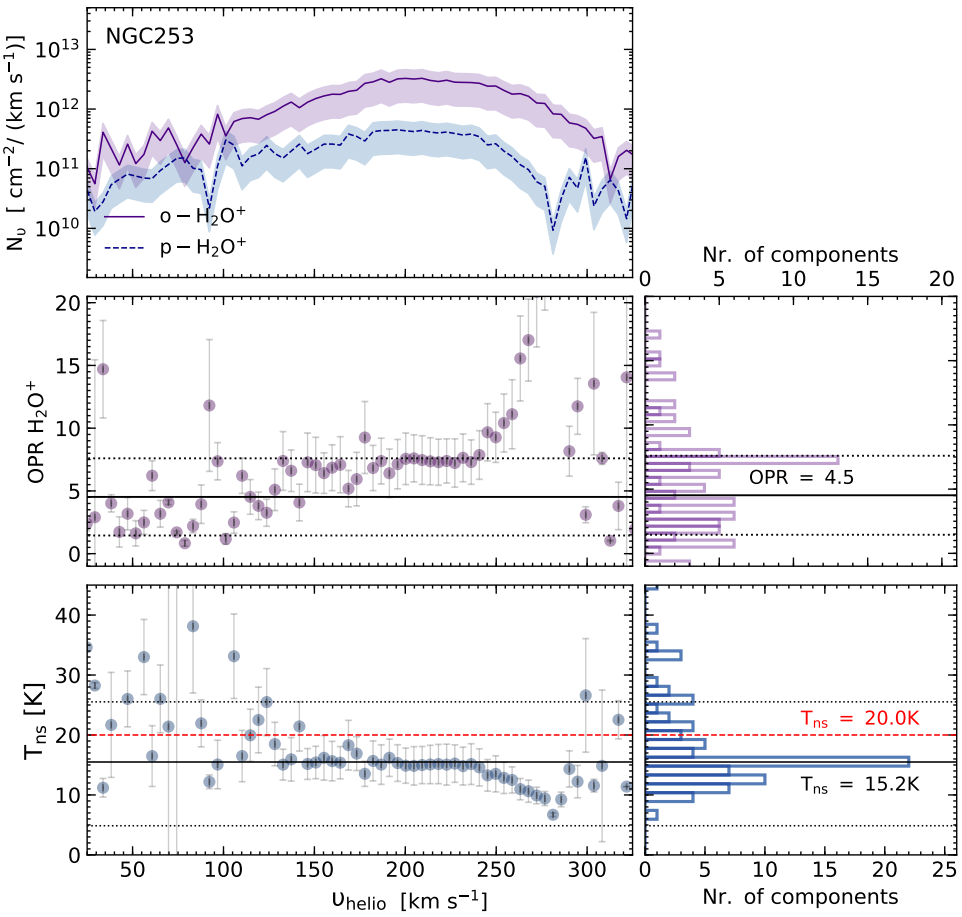

Figure 8.2: *Top panel:* Column density per velocity interval distribution of o-H_2O^+ (solid purple) and p-H_2O^+ (dashed blue) over the entire velocity interval covering absorption towards NGC 253. Middle panel: OPR H_2O^+ distribution *(left)* and corresponding histogram *(right)*. *Bottom panel:* Nuclear spin temperature distribution *(left)* and histogram *(right)*. The dashed red line represents the value of the spin temperature derived from the median value of the H_2O^+ OPR. The median and 1 σ levels of the OPR and nuclear spin temperature are marked by solid and dashed black lines, respectively.

Furthermore, investigating the influence of cosmic-ray ionisation on the OPR of H_2O^+ for star-forming regions within the Milky Way, Jacob et al. (2020b) find that the OPR of H_2O^+ thermalises to the equilibrium value of three with increasing rates of cosmic-ray ionisation up to a value of $\sim 2 \times 10^{-16}$ s^{-1}, beyond which there exists no credible correlation. The correlation between cosmic-ray ionisation rates and OPRs suggests that the higher abundances of atomic hydrogen present in regions exposed to higher cosmic-ray fluxes is able to efficiently drive the proton-exchange reaction causing a change in the OPR. Placing the current results into context, we find that the data points for both lie in the thermalised region of Fig 8.4, with OPRs near three within the uncertainties. We see that NGC 4945 approaches the trend shown by the GC sight lines studied by Indriolo & McCall (2012) in the Milky Way. This, as discussed above,

likely results from the weak AGN activity in NGC 4945 which is absent in NGC 253.

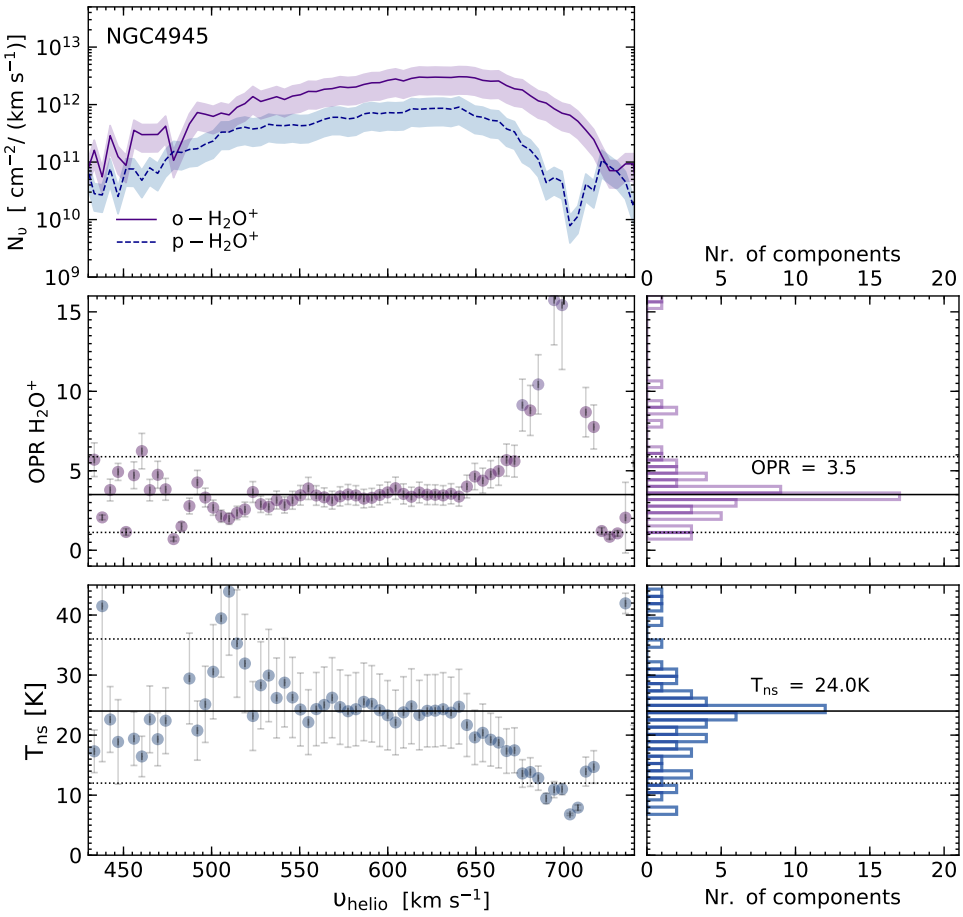

Figure 8.3: Same as Fig. 8.2 but towards NGC 4945. The median value for T_{ns} derived from the distribution is the same as that obtained from deriving T_{ns} using the median OPR for H_2O^+.

8.4 Conclusions

Well established as a tracer for purely atomic gas, outside of the Milky Way the noble gas species ArH^+ had only been detected toward the intermediate redshift $z = 0.89$ gravitational lens system PKS 1830−211. In this work we extend the notion that ArH^+ is a ubiquitous tracer of diffuse atomic gas toward external galaxies by presenting observations of its $J = 1 - 0$ transition.

We present the detection of ArH^+ in absorption toward two nearby galaxies, NGC 253 and NGC 4945 and also report the non-detection of ArH^+ toward Arp 220. In addition to ArH^+ we also report the detection of the $J = 3/2 - 1/2$ transition of p-H_2O^+ at 607 GHz toward the former. We compare the observed profiles of ArH^+ and p-H_2O^+ lines with those of the HI 21 cm line and lines from the well known atomic gas tracers OH^+ and o-H_2O^+ and the molecular gas tracer, HF. Using the cosmic-ray ionisation rates derived by analysing the steady-state

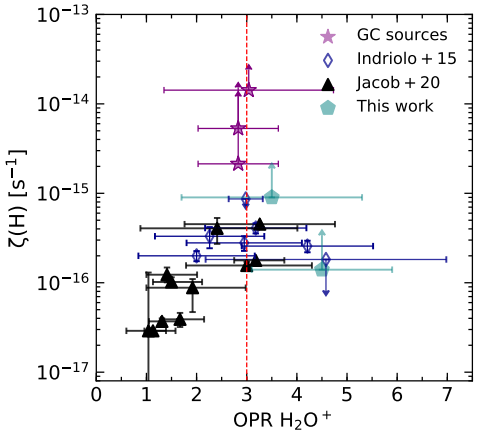

Figure 8.4: Observed OPR of H_2O^+ versus the cosmic-ray ionisation rates derived using the steady-state analysis of the OH^+ and H_2O^+. The results from this work are marked by teal pentagons while the blue diamonds and black triangles display the results for sight lines studied in the Milky Way by Indriolo et al. (2015) and Jacob et al. (2020b). For comparison we display the OPR of H_2O^+ also derived by Indriolo & McCall (2012) towards GC sight lines using purple stars. The dashed red line marks the equilibrium OPR value of three.

chemistry of OH^+ and H_2O^+ and by assuming that the cloud populations bearing ArH^+ are exposed to the same cosmic-ray ionisation rates, we derive the molecular fraction of the gas traced by ArH^+ toward both galaxies to be between 10^{-3} and $\sim 10^{-2}$. This is consistent with estimates made within the Milky Way by Schilke et al. (2014); Neufeld & Wolfire (2016); Jacob et al. (2020b). From the detection of p-H_2O^+ we estimate the H_2O^+ OPR of 4.5 and 3.5 toward NGC 253 and NGC 4945, and subsequently derive values for the nuclear-spin temperature of 15 and 24 K, respectively. The variation in the H_2O^+ OPR with cosmic-ray ionisation rates follows the trend displayed by sight line components toward star-forming regions within the Milky Way other than those toward the GC.

In order to comment on the ubiquity and chemistry of ArH^+ and its possible role in probing the energetics of extragalactic sources, the searches for ArH^+ need to be extended to a wider source sample. Since its chemistry and properties are widely studied, alongside with OH^+ and o-H_2O^+, it may be promising to search for ArH^+ toward a range of extragalactic sources hosting various levels of nuclear activity, which was a selection criterion for the Herschel EXtraGALactic (HEXGAL) survey which was aimed at studying the physical and chemical composition of the ISM in galactic nuclei using HIFI spectroscopy.

Chapter 9

Summary and outlook

Everything is both simpler than we can imagine, and more complicated than we can conceive.

Johann Wolfgang von Goethe, poet, playwright, naturalist and statesman

9.1 Summary

This thesis presents results on the physical nature and chemistry of diffuse and translucent molecular clouds that comprise a large part of the interstellar medium (ISM). It contains a detailed analysis of new high spectral resolution observations of the methylidyne radical, CH, as well as that of the related molecules ^{13}CH and CH_2 and thus addresses the fundamentals of interstellar carbon chemistry. In addition, it significantly extends our knowledge of argonium, ArH^+, a new unique molecular tracer of atomic diffuse interstellar clouds. The observations of these and various related hydride species were carried out with a wide variety of sub-mm and radio telescopes.

In the following, we discuss the main results, part by part and review the status of the questions we set out to address in Chapter 1.

Part I: Probing the diffuse and translucent molecular ISM

- In Chapter 3 we derived CH column densities using the $N, J = 1, 1/2 \rightarrow 2, 3/2$ transitions of CH near 2 THz and subsequently studied the azimuthally averaged radial distribution of N(CH) over the Milky Way. We found that the radial profile shows a dual peak between 5 and 7 kpc (see Fig. 9.1). This is not surprising since most of the Galactic material by mass is concentrated within the spiral arms at these distances. Moreover, we find that the N(CH) distribution scaled to $N(H_2)$ (using $[CH]/[H_2] = 3.5\times10^{-8}$; Sheffer et al. (2008)) is similar to that obtained by Pineda et al. (2013), who used the [CII] 158 μm emission to trace the CO-dark gas under the framework of the Galactic Observations of Terahertz C+ (GOT C+ Pineda et al. 2013) survey. While the overall resemblance between the H_2 column density profiles derived using CH with those from CII lends credence to its use as a tracer for H_2, at larger galactocentric distances (>8 kpc), the derived column densities of H_2 obtained using CH are lower than those traced by CII. Owing to the reduced rates of star formation and lower elemental abundances present in the outer Galaxy (Gerin et al. 2015), it is conceivable that CH is not sufficiently formed at these distances. However, an accurate interpretation requires a larger sample of sight lines covering sources in the outer Galaxy as well, observations of which are likely to be

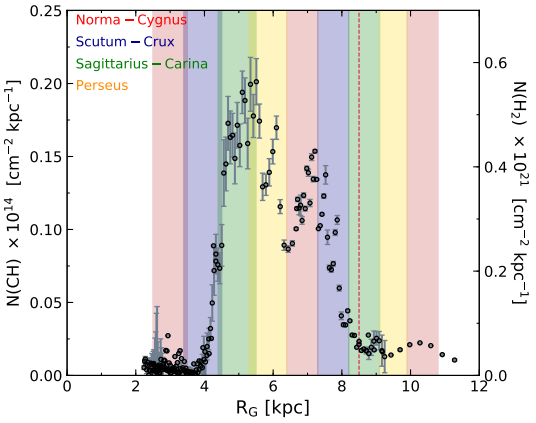

Figure 9.1: Radial distribution of CH column densities toward lines of sight probed in this study except Sgr B2 (M). The column density values for each distance interval are averages over the underlying distribution. The secondary y-axis display $N(H_2)$ values computed using the Sheffer et al. (2008) relation. The dashed red vertical line indicates the galactocentric distance to the Sun. The spiral arm locations typical for a fourth quadrant source, are plotted with spiral arm widths of 0.85 kpc. Same as Fig. 3.9.

carried out using upGREAT/SOFIA in the future. Furthermore, using CH as a surrogate for H_2, we also determined the abundance of the OH molecule (another tracer of the DMG) in the diffuse regions of the ISM to be $X(\mathrm{OH}) = 1.09 \times 10^{-7}$ with respect to H_2.

- While the $N, J = 2, 3/2 \rightarrow 1, 1/2$ transition of CH at 2 THz studied in Chapter 3 is a robust tool for determining reliable CH column densities, they can currently only be observed with SOFIA, which can only provide a limited amount of observing time. In contrast (as discussed in Chapter 1) the radio transitions of CH at 3.3 GHz have been widely observed with relative ease. However, the HFS components of this ubiquitously observed transition display line intensities that are inconsistent with the assumptions of local thermodynamic equilibrium (LTE). While population inversion within these levels have long been studied, the excitation of these transitions are not well understood as models have been unable to reproduce the observed relative intensities between the different lines, particularly those involving its lower satellite line ($F = 0^- \rightarrow 1^+$).

  In Chapter 4, we investigated the nature of the (generally) weak CH ground state maser by exploring synergies between the CH radio ground state and the FIR rotational levels (studied in Chapter 3), through statistical equilibrium calculations aided by recent measurements of the relevant collisional rate coefficients. We modelled the physical and excitation conditions traced by CH using the non-LTE radiative transfer code MOLPOP-CEP (Asensio Ramos & Elitzur 2018) by invoking the effects of FIR line overlap and constraining the modelled output by using CH column densities derived from its FIR transitions. The physical conditions reveal that CH resides within warm PDR layers tracing gas temperatures between 50 and 125 K. This hints at the likely formation of CH mainly via the dissipation by turbulence, which would also explain the observed departures in the CH line intensities from that at LTE, near dark clouds or regions lacking FIR continuum emission. We are able to reproduce the observed level inversion in all three of the ground state HFS lines of CH and derive excitation temperatures of −0.3 K consistent with previous theoretical predictions. These constraints on the excitation conditions of the ground state HFS lines of CH will help establish the 3.3 GHz transitions of CH as powerful probes of the diffuse and translucent ISM at radio-wavelengths, which can be studied at high resolutions using interferometers such as the VLA and the MeerKAT

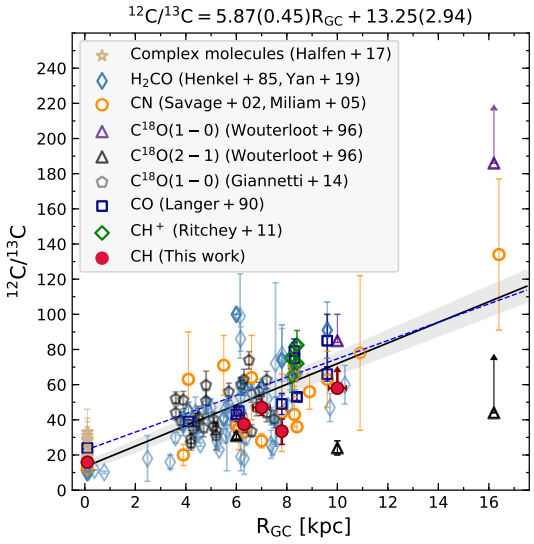

Figure 9.2: Plot of $^{12}C/^{13}C$ isotope ratios as a function of galactocentric distance, R_{GC} (kpc). The filled red circles represent the $^{12}C/^{13}C$ ratio obtained using CH. The black solid line represents the weighted fit to the data, and the grey shaded region demarcates the 1σ interval of this fit. For comparison, the fit obtained by Halfen et al. (2017) is displayed by the dashed blue line. Same as Fig 5.4.

array.

Part II: Methylidene isotopologues

- The ubiquity of molecules containing carbon in the ISM has turned the determination of the ratio between the abundances of carbon's two stable isotopes, $^{12}C/^{13}C$, into a keystone for Galactic chemical evolution studies. Whilst displaying a rising gradient with galactocentric distance, this ratio, when measured using observations of different molecules (CO, H_2CO, and others) shows systematic variations depending on the tracer used. These observed inconsistencies often arise from either optical depth effects, chemical fractionation or isotope-selective photo-dissociation. In Chapter 1 we had proposed the use of CH, formed from C^+ mainly via turbulence-driven chemistry or via UV-driven chemistry, CH reflects the fractionation of C^+, and does not show any significant fractionation effects unlike other molecules previously used to determine the $^{12}C/^{13}C$ isotopic ratio which makes it an ideal tracer for the $^{12}C/^{13}C$ ratio throughout the Galaxy.

  In Chapter 5 we report the first detection of ^{13}CH in the ISM toward the four star-forming regions, Sgr B2 (M), G34.26+0.15, W49 N and W51 E. By comparing the derived column densities of ^{13}CH with previously obtained SOFIA data of the corresponding transitions of the main isotopologue ^{12}CH (as determined in Chapter 3), we derive the $^{12}C/^{13}C$ isotopic ratio toward our sample of sources and by adding our values to previous calculations of the $^{12}C/^{13}C$ Galactic isotopic gradient we derive a revised Galactic gradient, such that $^{12}C/^{13}C$ = 5.85(0.50) R_{GC} + 15.03(3.40) (see Fig 9.2). Potentially reflecting the actual $^{12}C/^{13}C$ ratio, CH will not only provide constraints on future Galactic chemical evolution models but being a progenitor to the formation of more complex species the ^{13}C substitution in CH will aid in our understanding of the degree of fractionation present in these species.

Part III: The elusive methylene radical

- The high upper level energies (225 K) of the $N_{K_aK_c} = 4_{04} - 3_{13}$ transitions of ortho-CH_2 between 68 and 71 GHz, together with their (low angular resolution) detection toward hot cores led astronomers to associate the observed CH_2 emission as arising in dense, hot molecular cores. This is ruled out by our observations made using the Kitt Peak 12 m and Onsala 20 m telescopes as well as that of others as detailed in Chapter 6, we investigate alternative explanations for the origin of CH_2. Toward the central region of the Orion Molecular Cloud 1, we find that the distribution of the CH_2 emission closely follows that of the [CII] 158 μm emission, while CH_2 is undetected toward the hot core itself. The observations show extended emission which likely arises from hot but dilute layers of PDRs and not from the denser parts of such regions as in the case of the Orion Bar. We confirmed this hypothesis by comparing the observed CH_2 line profiles with those of carbon radio recombination lines (CRRLs), which are well-known tracers of PDRs.

  In Chapter 6 we also report the detection of the 70 GHz fine- and hyperfine structure components of ortho-CH_2 toward the W51 E, W51 M, W51 N, W49 N, W43, W75 N, DR21, and S140 star-forming regions, and three of the $N_{K_aK_c} = 4_{04} - 3_{13}$ fine- and hyperfine structure transitions between 68 and 71 GHz toward W3 IRS5. Despite lacking information on the spatial distribution of CH_2 in these regions, aside from that in W51, we once again see a correspondence between the profiles of CH_2 lines and those of CRRLs. We also observe stronger CH_2 emission toward the extended HII region W51 M rather than toward the much more massive and denser W51 E and N regions, which strongly supports the origin of CH_2 in extended dilute gas. We verify this by carrying out a non-LTE radiative transfer analysis using the code RADEX, and constrain the gas temperatures and H_2 density to (163 ± 26) K and $(3.4 \pm 0.3)\times10^3$ cm^{-3}, respectively, for the 68–71 GHz ortho-CH_2 transitions toward W3 IRS5, for which we have a data set of the highest quality.

  This analysis confirms our hypothesis that CH_2 originates in warm and dilute PDR layers, much like its chemical counterpart, CH (discussed in Chapter 4). Furthermore, under the physical conditions that prevail in these warm PDRs, our analysis of the excitation conditions of these CH_2 lines suggests that they are masering, with weak level inversion. In an astronomical setting, with widely spaced energy levels the rotational transitions of CH_2 are either inaccessible from the ground or lie close to the edges of atmospheric windows, deeming a *full* observational picture of CH_2, still elusive!

Part IV: Probing the diffuse atomic ISM with a molecule

- In Chapters 7 and 8, we modelled the optically thin absorption spectra of ArH^+, OH^+, ortho-H_2O^+ and either CH (discussed in Chapter 3) or HF. Comparing their derived

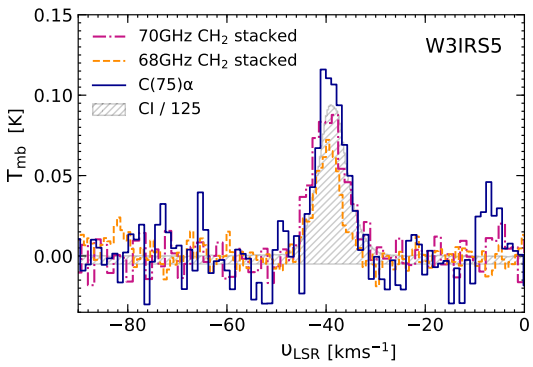

Figure 9.3: Decomposed CRRL profile in blue alongside the 68 GHz and 70 GHz HFS-stacked CH_2 line profiles displayed by the dashed orange and dashed-dotted violet curves, respectively. The stacked profile of the 70 GHz CH_2 transition was obtained from the HFS decomposition model. The hatched grey regions display the line profile of the $^3P_1 - {}^3P_0$ transition of CI at 492.160 GHz scaled down by a factor of 125 on the $T_{\rm mb}$ scale. Same as right-hand panel of Fig. 6.12.

column densities, we find the different molecules to only be weakly correlated with one another. By analysing the steady-state chemistry of OH^+ and o-H_2O^+, we derive on average a cosmic-ray ionisation rate, $\zeta_{\rm p}$(H), of $(2.3 \pm 0.3)\times10^{-16}$ s^{-1} towards the sight lines studied in this work and derive the cosmic-ray ionisation rate gradient across galactocentric distances, such that $\zeta_{\rm p}({\rm H}) = (1.80 \pm 0.70)\exp\left[(R_{\rm o} - R_{\rm GAL})/3.46\ {\rm kpc}\right] \times 10^{-16}$ s^{-1} for galactocentric distances that lie within $4 < R_{\rm GAL} < 8.5$ kpc.

Furthermore, by using the derived values of $\zeta_{\rm p}$(H) and the observed abundances of ArH^+ we constrain the molecular fraction of the gas traced by ArH^+ to lie below 2×10^{-2} with a median value of 8.8×10^{-4}. Carrying out a similar analysis for the other species we find that the ArH^+, OH^+ and H_2O^+ all trace the same cloud layers only in a small range of molecular fractions between 1.5×10^{-3}–3×10^{-2}, while CH (and HF) traces denser molecular gas layers (see Fig 9.4). This analysis clearly shows the transitions between different phases of the ISM from diffuse atomic to the diffuse and translucent molecular gas.

Over Galactic scales, we see that the distribution of $N(ArH^+)$ is associated with that of N(H), particularly in the inner Galaxy (within 7 kpc of the Galactic centre) with potentially even contributions from the warm neutral medium (WNM) phase of atomic gas at larger galactocentric distances. In the future, by extending the chemistry of ArH^+ to even more sight lines and upon comparing the HI profile derived using ArH^+ with the radial distribution of HI contributed by the WNM and the CNM estimated by Pineda et al. (2013), we will be able to address questions regarding the nature of the ArH^+ gas; whether it is formed in the CNM or WNM?

9.2 Ongoing and future work

9.2.1 A search for rotationally excited CH

Revisiting the energy level diagram of CH, displayed here in Fig. 9.5, the work carried out in this thesis has concentrated on the study of the radio ground state (see Chapter 4), and

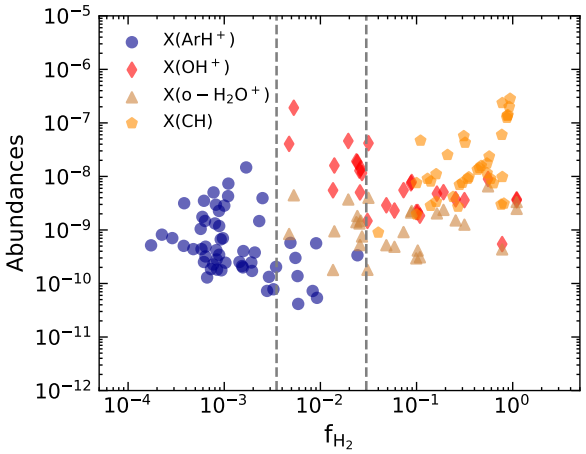

Figure 9.4: Molecular abundances with respect to atomic hydrogen as a function of molecular gas fraction (f_{H_2}). The blue circles, red diamonds, tan triangles, and yellow pentagons represent the abundances of ArH^+, OH^+, H_2O^+ and CH, respectively. The dashed grey lines enclose within them the cloud layers traced by ArH^+, OH^+ and H_2O^+. Same as Fig. 7.11.

FIR (and sub-mm) fundamental rotational (see Chapter 3) transitions of CH by exploring the possible synergies between these levels. Fraught with anomalous excitation effects, the interpretation of the observed gross features of the CH ground state lines is not straightforward, as discussed in Chapter 4. However, the detection and behaviour of the Λ-doublet transitions of CH corresponding to the $N, J = 1, 3/2$ level will greatly complement and aid in constraining the physical and excitation conditions of these models. Therefore as a pilot study we have proposed to investigate the $N, J = 1, 3/2$ level Λ-doublet transitions of CH at 700 MHz (see Table 9.1 for the line frequencies). Corresponding to the first rotationally excited level of CH, these lines are of particular interest because they are energetically close to the ground state, at 25.6 K while all higher energy transitions lie at energies greater than 96 K (see Fig 9.5).

Unfortunately, observing the 700 MHz lines of CH has not been an easy task, primarily because this low frequency radio band is hindered by man-made radio interferences, commonly referred to as radio frequency interference (RFI). Often far stronger than the celestial signals, the RFI that troubles radio observatories not only hails from external sources but arises internally as well, with its strongest contributions caused by the scientific instruments in use at the observatories themselves. As a consequence, only a single study reports detections of these lines: Ziurys & Turner (1985). These authors reported the detection of (only) the two main hyperfine lines, i.e., $F = 2^- \rightarrow 2^+$ and $F = 1^- \rightarrow 1^+$ towards W51 A in absorption made with the Arecibo 300 m telescope (see left panel in Fig. 9.6). The observed line profiles of the 700 MHz spectra of CH have comparable line widths to those of ground state transitions at the velocity of the molecular cloud near 60 km s^{-1} (see right panel in Fig. 9.6), which strongly suggests that both sets of lines arise from the same region, a prerequisite for their use in constraining the governing excitation conditions. In addition, Rydbeck et al. (1973) proposed that this Λ-doublet in the $N, J = 1, 3/2$ level is responsible for the observed enhancement of the lower satellite line of the ground state, as its energy is low enough for it to selectively affect the population of the ground state transition's energy levels. In addition to helping our understanding of the maser action of the ground state, the detection of the 700 MHz transitions of CH will make for potentially highly interesting new magnetic field probes as they showcase Zeeman splitting (Truppe et al. 2014). The Zeeman effect (splitting of spectral lines in the

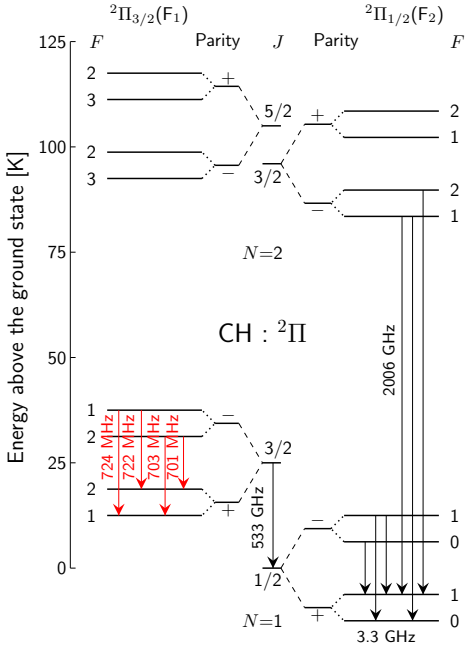

Figure 9.5: Energy level diagram of the electronic ground state of CH. The different transitions studied in this thesis are marked by black arrows while the Λ-doublet transitions of the first excited state of CH are highlighted in red.

presence of a magnetic field) is the only tool to directly measure magnetic, B, field strength in the ISM. Moreover, CH, whose abundance peaks at diffuse and translucent cloud densities ($n_{\rm H}$ = 10^2–10^3 cm^{-3}) will be able to probe the lower end of the absolute magnetic field flux density–gas density relation, $|B| \propto n^k$, where the power-law index, k, has a value of 0.65 (Crutcher et al. 2010). Since CH is also present in PDRs, it has the potential to probe the B-fields in such regions as well. It is complementary to OH, the only other molecular B-field tracer for both environments. The initial detection by Ziurys & Turner (1985) was followed up by further observations toward the W51 also using the Arecibo 300 m telescope which aided Turner (1988) in detecting all four hyperfine transitions within the $N, J = 1, 3/2$ level (see Fig. 9.6).

Table 9.1: Spectroscopic parameters of the N, J = 1, 3/2 rotational transitions of CH measure with high precision by Truppe et al. (2014).

Transition $F' \rightarrow F''$	Frequency [MHz]	$A_{\rm E}$ [$10^{-12}\times$s^{-1}]
$2^- \rightarrow 2^+$	701.6770	2.0672
$2^- \rightarrow 1^+$	703.9783	0.2318
$1^- \rightarrow 2^+$	722.4876	0.4177
$1^- \rightarrow 1^+$	724.7883	2.1096

In our pilot study, we are using the capabilities of band 4 of the upgraded Giant Metrewave Radio Telescope (uGMRT) to concentrate on successfully detecting the 700 MHz lines of CH toward a select number of PDRs as we expect the lines to probe such regions surrounding the edges of dense gas, which have densities $\sim 10^5$ cm^{-3}.

Our data will also allow us to assess the feasibility of using the uGMRT for carrying out

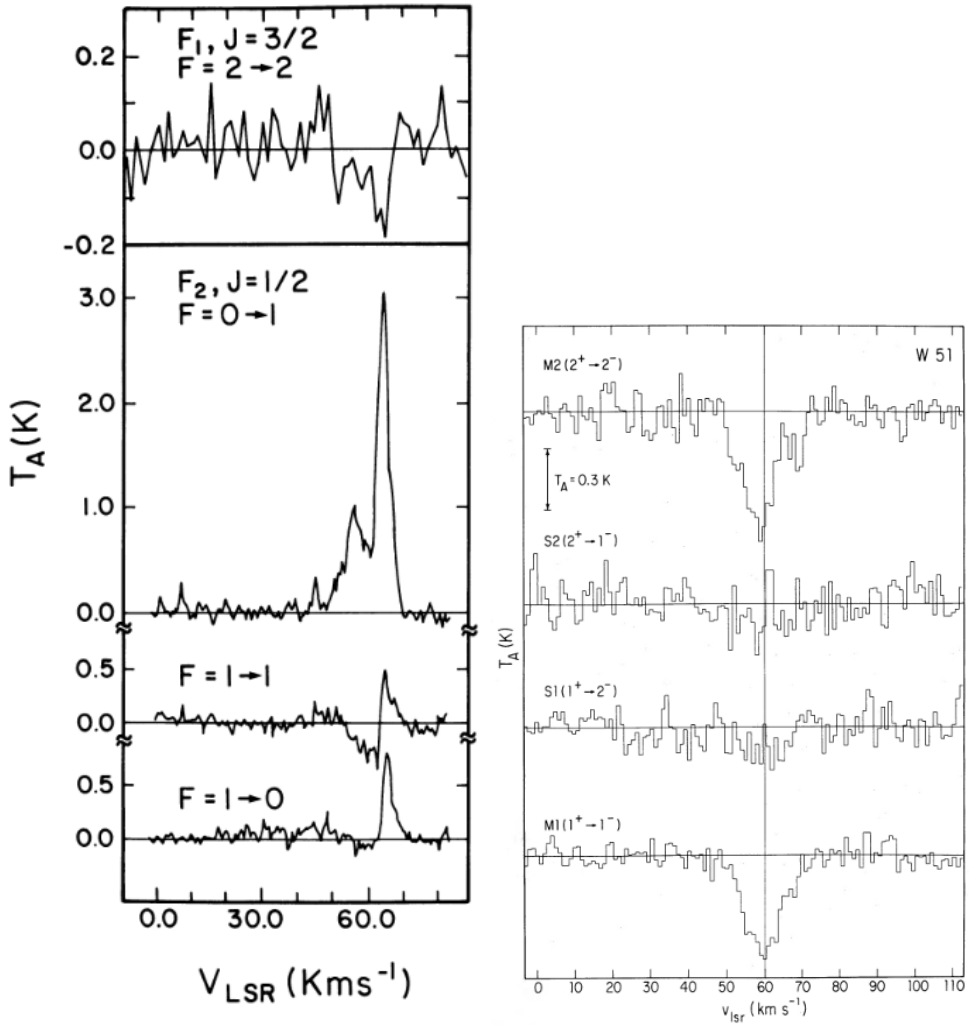

Figure 9.6: *Left:* The spectra of the main hyperfine transitions of the CH Λ-doublet near 700 MHz towards W51 A detected by Ziurys & Turner (1985) compared to the weakly masing ground state lines observed by Genzel et al. (1979). *Right*: The spectra of all four HFS lines of CH near 700 and 720 GHz detected toward W51 A by Turner (1988).

such observations in the future. We have also covered within the large bandwidth provided by the uGMRT a number of α H-, He- and C-RRLs with principal quantum numbers, n, ranging from 208 to 211, which form ideal tracers of PDRs (as discussed in Chapter 6). In addition to W51, our sample consists of the well-known star-forming regions W43 (one of the regions toward which Ziurys & Turner (1985) also report detections of the 700 MHz CH line, but give no details) and Sgr B2 as well as that of other famous PDRs M8, M17, and DR21. We note that OH Zeeman observations of DR21 have recently accomplished the first $B-$ field measurement in a PDR, see (Koley et al. 2021) (of which I am a co-author).

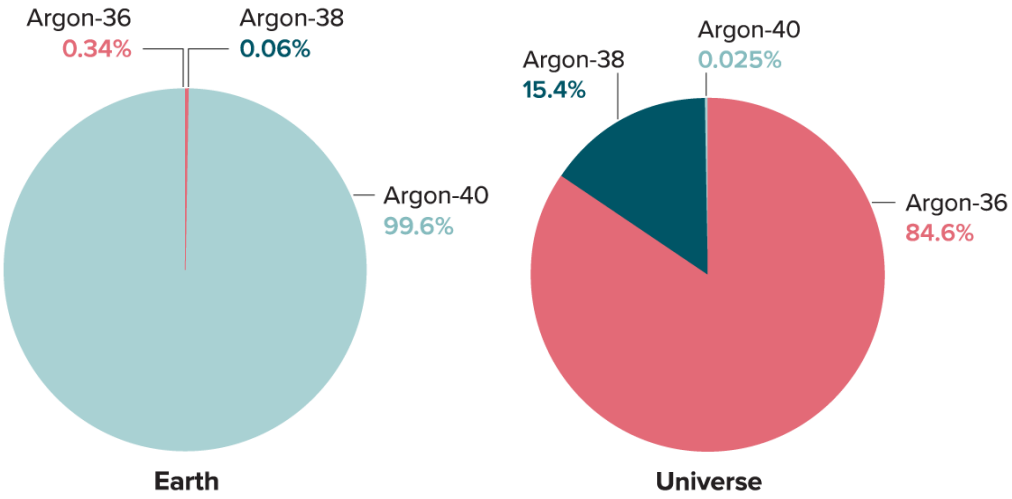

Figure 9.7: Argon isotope abundance on Earth (*left*) and in space (*right*). Source: Knowable magazine.

9.2.2 Argonium isotopes in the diffuse ISM

The argonium ion, ArH^+, was the first astrophysical molecule containing a noble gas element to be detected in the ISM, thanks to the new avenue provided by the *Herschel* mission. As discussed in Chapters 7 and 8, the observations we carried out using the APEX 12 m telescope were able to extend the detection of ArH^+ not just within the Milky Way galaxy but also toward two luminous nearby galaxies. These observations allowed us to compare the observed ArH^+ line profiles with those of other tracers of atomic gas (like OH^+ and o-H_2O^+) and investigate their radial distribution. However, very little is known about its isotopologues $^{38}ArH^+$ and $^{40}ArH^+$. Given that on Earth, 99.6% of all Argon is contained in the ^{40}Ar isotope and the ^{36}Ar/^{38}Ar ratio is 5.6, the $^{36}ArH^+/^{38}ArH^+$ ratio observed in the ISM came as a big surprise. The relative abundances of the argon isotopes on Earth and in space, is visualised through pie charts as shown in Fig. 9.7. However, Schilke et al. (2014), only report the detection of $^{38}ArH^+$ toward a single source Sgr B2 (M) using HIFI/*Herschel*. Solar and interstellar Argon is estimated to comprise of 15.4% ^{38}Ar which, similar to ^{36}Ar is primarily produced via oxygen burning in explosive nucleosynthesis (Woosley et al. 2002).

We have proposed, to detect ^{38}Ar substituted ArH^+ toward the same seven sources we detected $^{36}ArH^+$ toward, once again using the APEX 12 m telescope (see Chapter 7), to study variations (or lack there of) in the $^{36}ArH^+/^{38}ArH^+$ isotopic ratio. In addition, we will be able to simultaneously observe the $H^{35}Cl$ and $H^{37}Cl$ lines near 625 GHz in the other sideband and subsequently compare its chemistry with that of its isoelectronic counterpart ArH^+. Chemical models by Kobayashi et al. (2011), predict that the $^{35}Cl/^{37}Cl$ isotopic ratios close to the solar system value of 3.13 (Lodders et al. 2009) are nucleosynthesis products of massive stars and core-collapse supernovae while values close to 2 are nucleosynthesis products of low-metallicity AGB stars or higher-metallicity Type II supernovae. Therefore variations in the chlorine isotopic ratio via nucleosynthesis enrichment will also offer insight into the evolutionary history of molecular material and its composition.

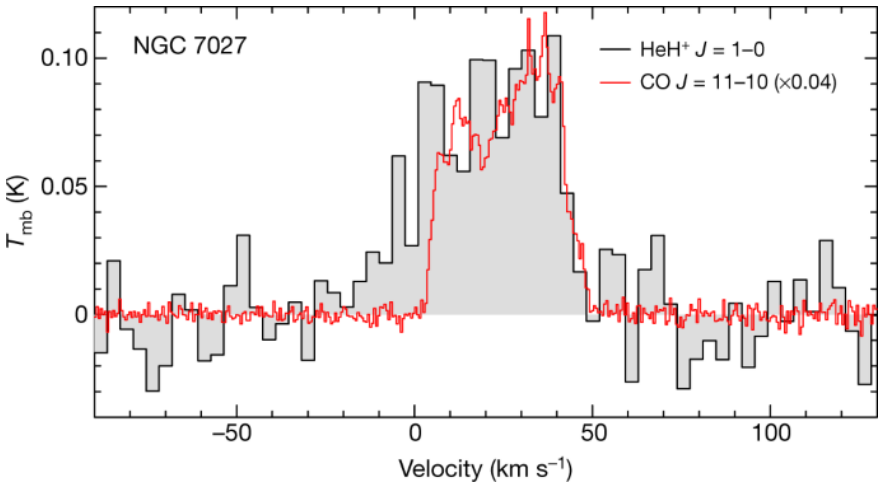

Figure 9.8: Spectrum of the HeH^+ $J = 1 - 0$ ground-state rotational transition, observed with upGREAT onboard SOFIA pointed towards NGC 7027 and the CO J= 11 − 10 line for comparison (red). Figure taken from Güsten et al. (2019).

Our proposal has been accepted and is scheduled to be observed in the near future.

9.2.3 A search for HeH^+ in the He enriched compact HII region W3A

The main product of helium chemistry, the helium hydride ion (HeH^+) is formed in the Early Universe, well before the cosmic recombination era was completed (Galli & Palla 2013). It was identified in the laboratory almost 100 years ago, by means of mass spectroscopy (Hogness & Lunn 1925) and its presence in space was hypothesised by Black (1978); Dabrowski & Herzberg (1980); Roberge & Dalgarno (1982) to be detectable in planetary nebulae (PNe) or over-pressurised HII regions. In small amounts, it has also been predicted to occur behind dissociative shocks (Neufeld & Dalgarno 1989), and in Jupiter's ionosphere (e.g. Barrow & Matcheva 2011; Egert et al. 2017). The search for HeH^+, ensued since the 1970s but it was first successfully detected only very recently toward the planetary nebula NGC 7027 by Güsten et al. (2019) (see Fig. 9.8), using the upGREAT instrument on board SOFIA. This recent detection has renewed interest in the role of HeH^+ in astrochemistry.

Owing to its astronomical importance, it is therefore crucial to expand searches for this molecular ion in space. Planning searches toward other planetary nebulae and compact and ultra-compact HII regions in environments forming massive stars, we had written an observing time request as a part of the SOFIA cycle 9 call for proposals, which has recently been accepted. In particular, we proposed to search for HeH^+ emission from the HII region W3 A. This nearby high-mass star-forming region stands out from other HII regions owing to its unusual helium enrichment. A helium abundance well in excess of the primordial abundance was reported by Roelfsema & Goss (1991); Roelfsema et al. (1992); Adler et al. (1996) toward W3 A based on observations of helium radio recombination lines. The highly in-homogeneous distribution of ionised helium mapped by these authors across the W3 A region increases in abundance as one moves away from the centre of the source toward the periphery.

At the time this thesis is submitted, the scheduling of these observations is in the early planning stages. Either way, the detection or non-detection of HeH^+ toward W3 A will have important ramifications on helium chemistry, prove or disprove the uniqueness of this ion toward NGC 7027 and ultimately, guide future searches for it toward other sources.

Appendix A

Appendix to Chapter 3

A.1 Convolution model

Figure A.1 presents an example that showcases the effects of HFS splitting on astrophysical spectra. The deviations between the observed spectrum and noise-degraded spectrum (resulting from the convolution model) computed using residuals, vary on average between −0.03 and +0.02.

A.2 Assessment of the WF fit

In this appendix, we discuss the quality of the WF fit prior to deconvolution. This analysis aims to curb the propagation of biases introduced from an inadequate fit into any derived quantities. For this reason, we carry out a residual analysis to test the validity of the WF fitting model and its underlying assumptions. The 'residuals' of a fit may be viewed as deviations in the values predicted by the model from what is observed. Given that the Wiener filter itself is derived by minimising the mean square error (MSE) between the data and the model (Sect. 3.2.1), one would not expect large discrepancies. Figure A.2 displays the combined results of the residuals obtained for each source.

The left panel shows no clear pattern or structure, with the residuals randomly scattered around zero. The lack of any uniform structure reveals that our assumptions of a linear system with an independent noise signal is maintained. From the right panel, we see that the residuals are normally distributed for each source, with a mean of 0.001, and standard deviation of 0.024. Only 2.4 and 3.7 % of all the residual points lie outside the 99 and 95 % confidence intervals. These outliers can be attributed to small variations in the power spectrum of the additive noise that lead to an over-(positive-valued residual) or under-(negative-valued residual) estimation of the true noise level. Such inaccuracies in the estimated noise are more pronounced at the spectral peaks, and correspond to the outliers seen in Fig. A.2. Overall, the residuals validate our fit and confirm our assumptions by reproducing independent errors that are not serially-correlated with a near constant variance and normal distribution.

A.3 Computational efficiency of the WF algorithm

From the mathematical formulation presented in Sect. 3.2.1, the WF can be interpreted as a kernel acting on the inverse filter. If the signal happens to be much stronger than the noise, then $(\mathrm{S/N})^{-1} \approx 0$, in which case the WF kernel reduces to $H^{-1}(\tilde{\nu})$ or the inverse filter. Alternatively, if the signal is weak in comparison to the noise, then $(\mathrm{S/N})^{-1} \to \infty$ and $W(\tilde{\nu}) \to 0$ and the WF attenuates contributions from higher noise levels which characterises it as a bandpass filter.

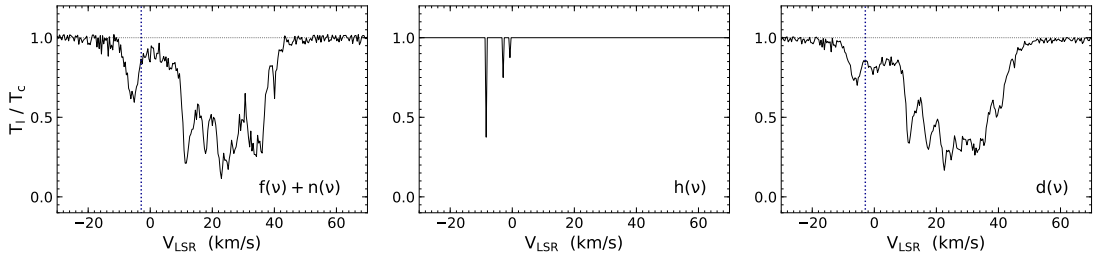

Figure A.1: Convolution model illustrated for LOS toward AGAL010.624−00.384. The input signal with additive noise or the original (deconvolved) spectrum (*left*) is convolved with the normalised HFS weights (*centre*) to produce the resulting convolved spectrum or the observed noise-degraded spectrum (*right*).

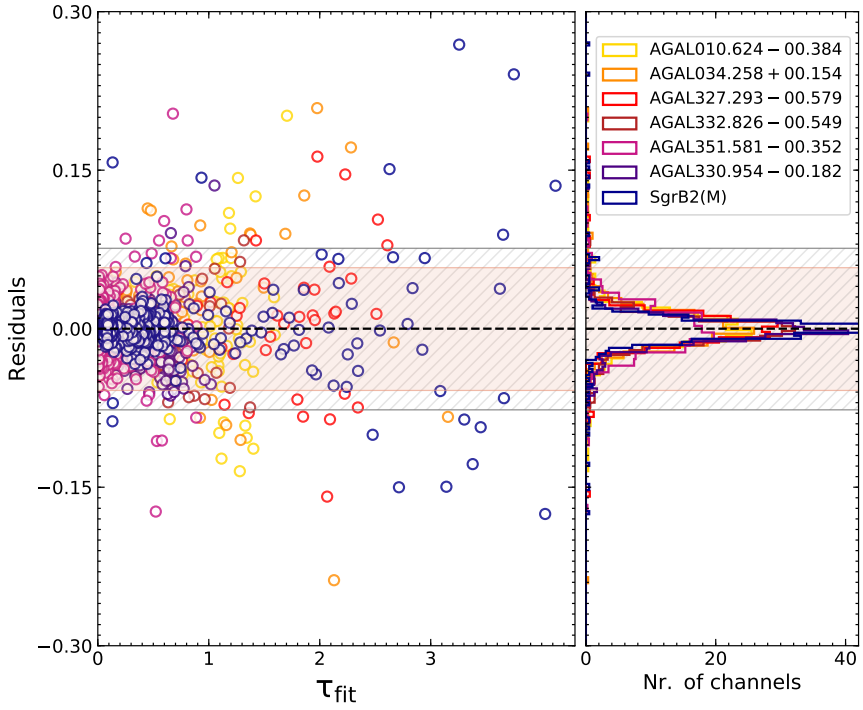

Figure A.2: *Left panel*: optical depth residuals versus WF fit. The different coloured markers correspond to residuals computed from the WF fits to the different sources. *Right panel*: distribution of residuals corresponding to different sources. They follow approximate normal distributions centred slightly off-zero around +0.001 for all seven sources. The grey (hatched) and pink regions bound the 99 % and 95 % confidence intervals, respectively.

WF deconvolution, while efficient in its performance, is still an approximate method, in the sense that its main drawbacks arise from the MSE constraint, which is also, ironically, what sets it apart form other filters. The process of aptly minimising the overall MSE carries out inverse filtering by accounting for additive noise. However, since the human eye is willing to accept more noise than allowed for by the filter (provided that it is spatially associated with the spectral

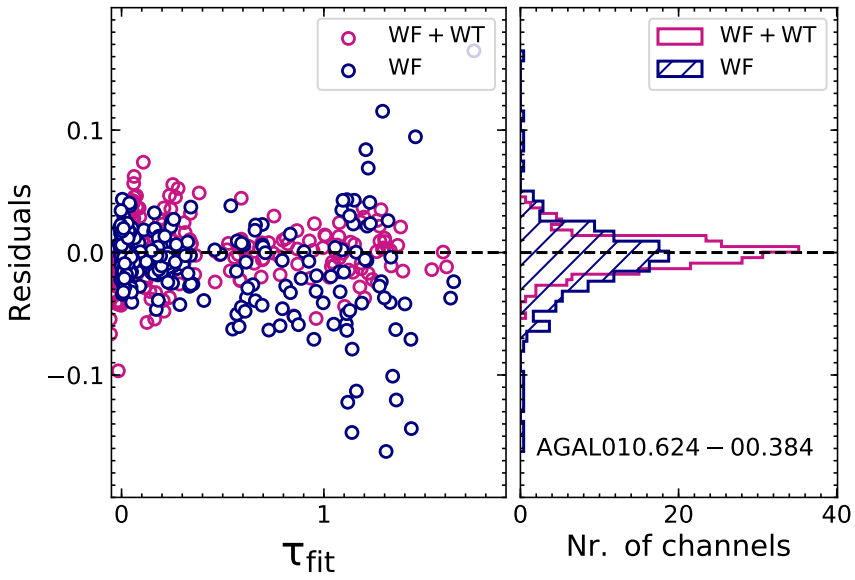

Figure A.3: *Left*: scatter plots of residuals obtained from the WF fit and WF + WT (ForWARD) algorithm against their fits in dark blue and magenta, respectively. *Right*: weighted distributions of residuals from the WF fit alone (blue hatched region) and the WF + WT (magenta).

profile), the restored spectra might seem unpleasantly smooth. This is because the trade-off between filtering and noise smoothing holds true only up to a second order in precision, meaning the required levels of degradation are not always achieved when characterising the signal. This leads to deviations between the obtained results and the true optimum. Hence the main performance limitation arises form the finite variance in the noise at any given channel and its treatment. These effects are seen in the form of small fluctuations in the WF fit (as discussed in Appendix A.2), particularly in regions of the spectra where the S/N is very large. One could then turn toward using this response as a respectable initial guess, and repeating the same filtering process over multiple iterations in order to improve the restored spectrum. This iterative line of thought is futile, because the scheme converges as $\mathrm{H}(\tilde{\nu}) \rightarrow 0$. The non-iterative nature of the WF is in fact one of its biggest advantages, as it is less time-consuming, and, additionally, aids in any subsequent Monte Carlo-based error estimates.

The wavelet transform (WT) is another method used to quantify the degree of noise attenuation. Based on the quantisation of a signal in the form of wavelets, the WT has the advantage that it characterises the local behaviour of a signal while maintaining all temporal information, unlike the FT. The Fourier-wavelet regularisation deconvolution (ForWARD) algorithm developed by Neelamani et al. (2004) is one such technique that combines deconvolution in the Fourier domain with noise suppression in the wavelet domain. In this approach, the WF deconvolution product is first decomposed in the wavelet domain into a scaling function, which acts as a low-pass filter and a wavelet function or a band-pass filter, which in turn constitutes each wavelet level. A second step of wavelet de-noising was added to our existing WF algorithm, in order to improve the robustness and efficiency of this method. Once again, we visualise the fit through its residuals as shown in Fig. A.3 toward a single source AGAL010.624−00.384.

In general, both sets of residuals are scattered randomly and centred around zero. The outliers in the WF fit are curbed when it is followed by the use of the WT, giving rise to a less variant or narrower distribution. However, the wavelet domain analysis is more suited to transient or time-varying signals, whereas our spectra are time independent. A subtle problem that this creates in a time-invariant system is that the wavelet domain is sparse (reduced number of data points) because of the wavelet decomposition of the spectral signal, and remains sparse over consecutive iterations. This makes it difficult to conclude whether the WT actually takes into account the outliers, or whether their effects are averaged out in the process of forming wavelets. While the addition of the WT to the WF deconvolution makes it more robust and rigorous, it has a longer computational time, and application to time-invariant systems makes it non-ideal.

A.4 Impact of using a single excitation temperature on derived column densities

The column densities presented in Table. 3.3 are derived using the WF deconvolution by assuming a single excitation temperature of 3.1 K for all components. Since the critical densities, $n_{\rm crit}$[1] of the CH transitions presented in this work ($\sim 2.4 \times 10^9$ cm^{-3}, assuming a gas temperature value of 50 K) are several orders of magnitude higher than the typical conditions that prevail over the foreground LOS clouds, almost all the CH molecules are expected to be in the ground state. Furthermore, the large values of $n_{\rm crit}$ imply that population of any rotational level above the ground state of CH must arise from radiative excitation processes rather than collisional excitation, as shown by Black (1994). As mentioned in Sect. 3.4.1, radiative excitation is unlikely for CH molecules residing in locations that correspond to velocity intervals associated with the diffuse and the translucent regions. Using higher values for the excitation temperature, we model the absorption features associated with the molecular environment of the bright FIR continuum sources (Fig. A.4). Changes in the excitation temperature between 3.1 and 10 K result in uncertainties in the calculated column densities that are less than 15%, while this margin increases to nearly 50% as $T_{\rm ex} \rightarrow 30$ K. While a proper estimation of the excitation temperature requires a thorough radiative transfer description across the envelope of the continuum source, here, we merely illustrate how the calculated column densities are affected by the assumption of a single excitation temperature.

A.5 Additional tables

A.6 Correlation plots for individual sources

This Appendix showcases the N(OH)-N(CH) correlations toward the individual sources.

[1]The critical densities for CH are computed using rate coefficients calculated by Dagdigian (2018b) and Einstein A coefficients as given in Table. 3.2.

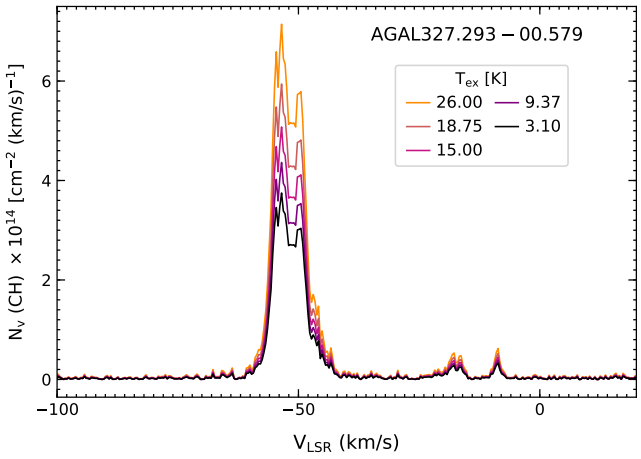

Figure A.4: Variation in WF deconvolved column density profile toward AGAL327.293−00.579 at varying values of excitation temperature between 3.1 and 26 K.

Table A.1: Spectroscopic parameters of other studied transitions.

Species	Transition		Frequency	A_E	E_u
	J	$Parity, F$	[GHz]	[s^{-1}]	[K]
CH	3/2 → 1/2	$^-1 \rightarrow 1^+$	532.7216	0.020	25.76
		$^-1 \rightarrow 0^+$	532.7239	0.062	
		$^-2 \rightarrow 1^+$	532.7933	0.041	
OH	5/2 → 3/2	$^+2 \rightarrow 2^-$	2514.2987	1.367	120.75
		$^+2 \rightarrow 3^-$	2514.3167	13.678	
		$^+1 \rightarrow 2^-$	2514.3532	12.310	

Notes: The spectroscopic data for other studied CH and OH transitions - quantum numbers, frequencies, Einstein A coefficients and upper level energies were taken from the Cologne Database for Molecular Spectroscopy (Müller et al. 2001).

Table A.2: Synopsis of N(OH)/N(CH) regression toward individual sources, except AGAL351.581−00.352.

Source	N(OH)/N(CH)	Pearson's r-value	N(OH)/N(H_2) ($\times 10^{-7}$)
AGAL010.624−00.384	5.66 ± 0.06	0.75	1.98
AGAL034.258+00.154	2.48 ± 0.17	0.67	0.87
AGAL327.293−00.579	4.13 ± 0.11	0.46	1.44
AGAL330.954−00.182	2.78 ± 0.07	0.68	0.97
AGAL332.826−00.549	9.70 ± 0.48	0.32	3.40

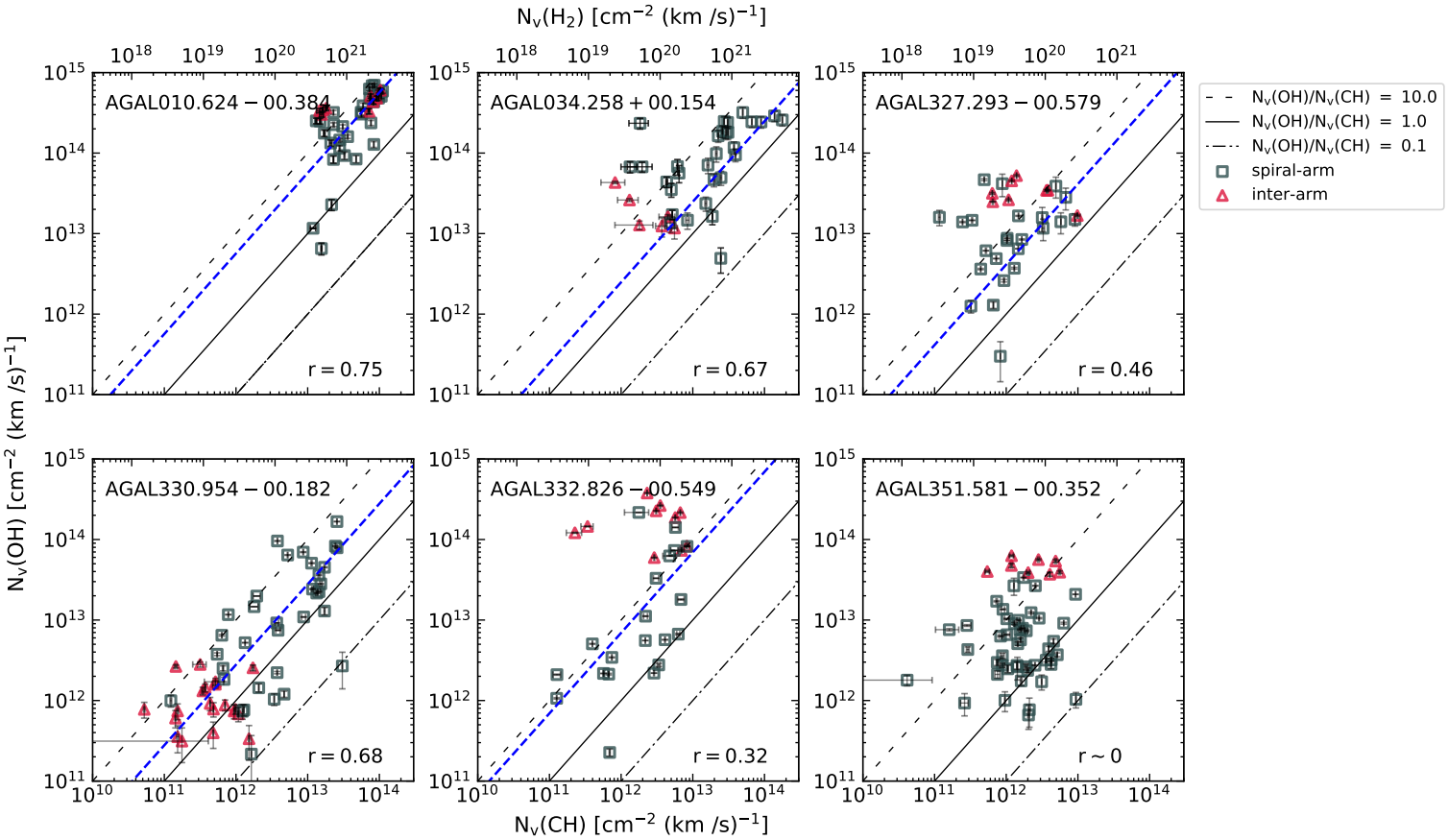

Figure A.5: Correlation between CH and OH column densities derived using the WF deconvolution algorithm toward (*clockwise*) AGAL010.624−00.384, AGAL034.258+00.154, AGAL327.293−00.579, AGAL330.954−00.182, AGAL332.826−00.549 and AGAL351.58−00.352. The different markers indicate contributions from spiral-arm (in blue), and inter-arm gas (in red). The linear regression is shown by the blue dashed line along with N(OH)/N(CH) ratios of 0.1, 1 and 10. Secondary x-axis represents H_2 column densities obtained using the CH/H_2 abundance ratio given by Sheffer et al. (2008). The corresponding Pearson's correlation coefficients are given in the lower-right corners.

Appendix B

Appendix to Chapter 4

B.1 Impact of using different collisional rate coefficients

In this appendix we illustrate the results obtained when using collisional rate coefficients computed directly for collisions of CH with para-H_2. The excitation temperatures are computed over a range of CH column densities but for a fixed gas temperature and line width of 75 K and 6 km s^{-1} for two sets of gas densities at 5×10^2 and 5×10^3 cm^{-3}. We see that for both cases the MOLPOP-CEP models reproduce positive values for the excitation temperatures of all three of the CH ground state HFS lines until CH column densities of $\sim10^{14}$ cm^{-2}. Beyond this value the lower satellite shows a rapid increase in the excitation temperature following which it decreases to negative values thereby displaying level inversion in this line.

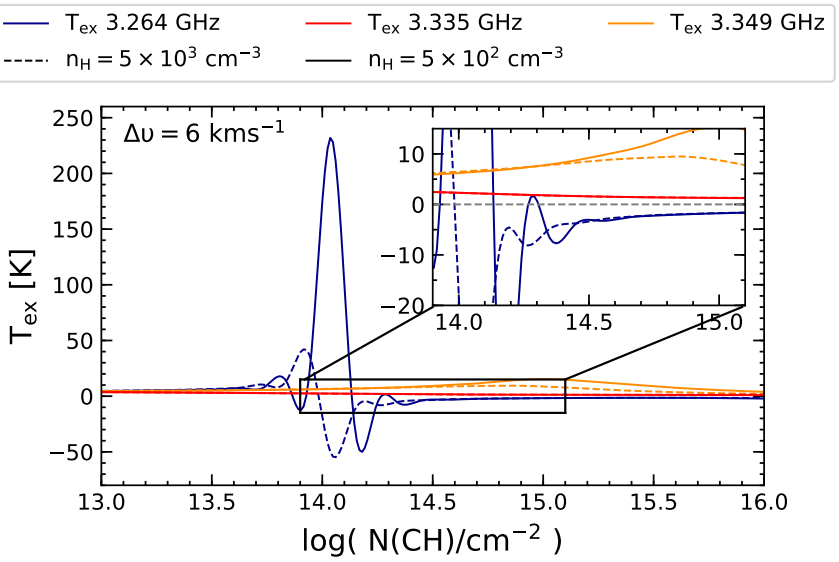

Figure B.1: MOLPOP-CEP non-LTE radiative transfer model of the ground state HFS lines of CH using a combination of collisional rate coefficients for collisions of CH with ortho-H_2, para-H_2, and atomic hydrogen all computed by Dagdigian (2018b). The solid and dashed blue, red and dark orange curves represent the excitation temperatures of the 3.264 GHz, 3.335 GHz and 3.349 GHz CH lines, as a function of N(CH) for $n = 5\times10^2$, and 5×10^3 cm^{-3}, respectively for models with $T_{\rm kin} = 75$ K and $\Delta\upsilon = 6$ km s^{-1}. The inset panel expands on the $T_{\rm ex}$ values for CH column densities between 10^{14}–10^{15} cm^{-2}.

Appendix C

Appendix to Chapter 5

C.1 Sideband deconvolution

In Fig. C.1 we display the ^{13}CH spectra towards Sgr B2 (M) obtained from the different IF settings at 1.4, 1.6, and 1.8 GHz, respectively. The secondary x-axis displayed in each panel shows the velocity scale in the image band LSR. Each IF offset of 0.2 GHz corresponds to a shift of the image band features by 60 km s^{-1}. When an IF setting of 1.4 GHz is used, both sets of Λ-doublet features are well separated, with the hyperfine components corresponding to the 1997 GHz doublet originating from the signal band, while those corresponding to the 2001 GHz doublet arise from the image band. The ^{13}CH (signal band) Λ-doublet is seen in absorption, with a deeper absorption feature seen at 1996.589 GHz that possibly arises from the $J_{K^-,K^+} = 4_{3,2} \rightarrow 3_{2,1}$ transitions of H_2S. Several transitions of H_2S have previously been detected towards the Sgr B2 (M) (Tieftrunk et al. 1994) and Sgr B2 (N) (Neill et al. 2014) SFRs, with the higher frequency transitions typically seen in absorption towards the envelope of these hot cores. This transition lying close to 1996 GHz has previously not been detected using HIFI/*Herschel* because it lies outside the tuning range of HIFI Band 7. However, the $J_{K^-,K^+} = 6_{1,6} \rightarrow 5_{0,5}$ high-energy transition of H_2S at 1846.76 GHz with a lower level energy ∼239 K was observed using HIFI/*Herschel* towards Sgr B2 (M) as a part of the HIFI/*Herschel* observations of EXtra-Ordinary Sources (HEXOS) (Bergin et al. 2010) guaranteed time key programme, which was aimed at investigating the chemical composition of several sources in the Orion and Sgr B2 SFRs. The spectrum of H_2S near at 1846.76 GHz observed towards Sgr B2 (M) using HIFI (observation id 1342206640) shows an absorption profile which is similar to that of the signal-band feature we observed, with comparable line widths and peak temperatures, which further validates our assumption that this line arises from H_2S.

Despite pushing the 2001 GHz Λ-doublet transitions into the atmospheric ozone feature at 2002.347 GHz, the additional observing setup with an IF of 1.6 GHz was used to confirm the origin of the deeper absorption feature in the signal band. When we use this setup, it is clear that the deeper H_2S absorption feature must arise from the signal band while further confirming our detection of ^{13}CH absorption towards the envelope of the SFR. However, we require a third IF setting in order to confirm the presence of weak sight-line absorption features. When the IF offset is increased to 1.8 GHz, the ^{13}CH features arising from the image band approach the ^{13}CH features arising from the signal band. We compare the average of the residuals between two independent IF settings with the average of the IF co-added spectrum. Whilst affirming the presence of weaker LOS absorption features by suppressing the image-band contributions, this does not present a complete DSB deconvolution. This can be mathematically formulated as described below.

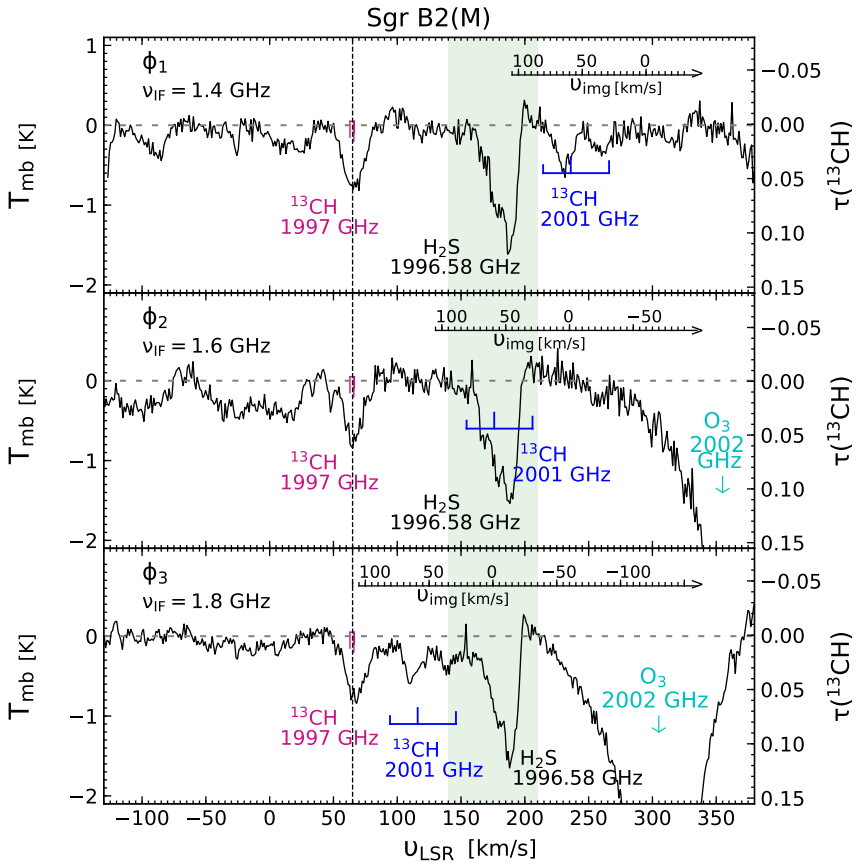

Figure C.1: Calibrated and baseline-subtracted observed ^{13}CH spectra at an IF setting of 1.4 GHz (*top panel*), 1.6 GHz (*central panel*), and 1.8 GHz (*bottom panel*) towards Sgr B2 (M). The secondary y-axis in each panel presents the optical depth scale. Signal bandpass contamination, possibly from the $J_{K^-,K^+} = 4_{3,2} \rightarrow 3_{2,1}$ transitions of H_2S at 1996.589 GHz, is displayed by the green shaded region. The hyperfine transitions corresponding to the 1997 GHz Λ-doublet arising from the signal band are displayed in pink, while that of the 2001 GHz Λ-doublet arising from the image band is displayed in blue. The change in IF pushes both the second Λ-doublet and the atmospheric ozone feature at 2002.347 GHz (telluric rest frame, marked in cyan) towards the signal band features. The secondary x-axis in each panel represents the image band LSR velocity scale.

We represent the DSB ^{13}CH spectrum obtained from each IF setting as a function of velocity as

$$\phi(\upsilon)_i = \phi_{\rm sig}(\upsilon) + \phi_{\rm img}(\upsilon_i - \upsilon), \tag{C.1}$$

where $i = 1, 2, 3$ correspond to the different IF settings at 1.4, 1.6, and 1.8 GHz, respectively, υ_i is the signal-band velocity at which the image-band velocity is equal to zero and $\phi_{\rm sig}$, and $\phi_{\rm img}$ represent the signal and image-band contributions. According to Eq. C.1, the average of

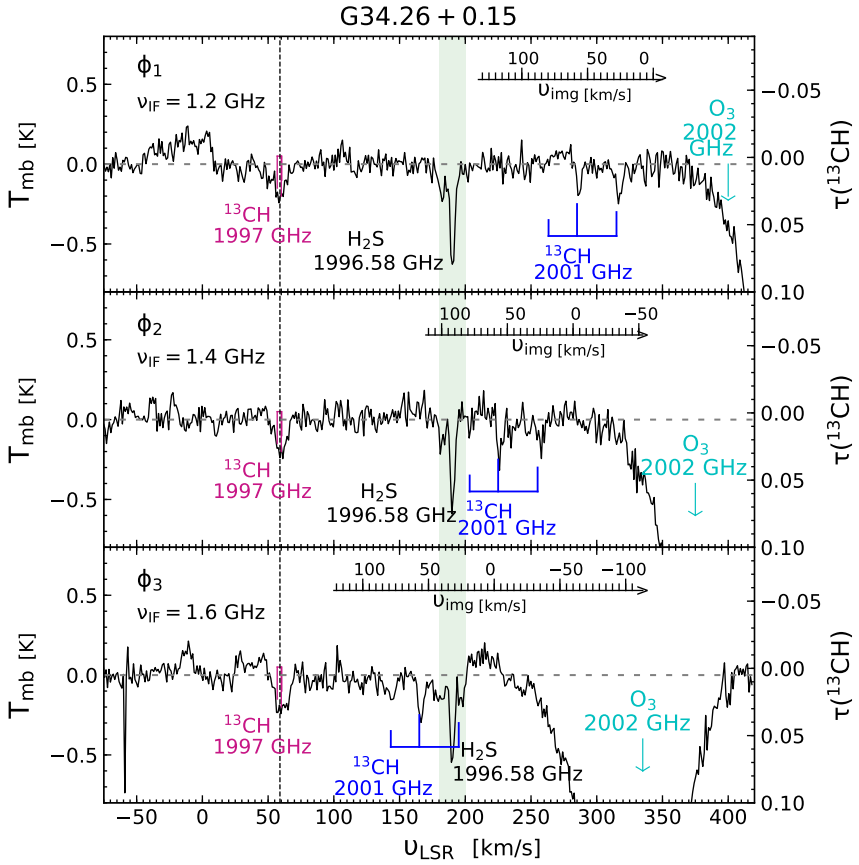

Figure C.2: Same as Fig. C.1, but towards G34.26+0.15 for IF settings of 1.2, 1.4, and 1.6 GHz (*from top to bottom*).

the IF co-added spectrum is

$$\phi(\upsilon)_{\rm avg} = \phi_{\rm sig}(\upsilon) + \frac{1}{3}\left(\phi_{\rm img}(\upsilon_1 - \upsilon) + \phi_{\rm img}(\upsilon_2 - \upsilon) + \phi_{\rm img}(\upsilon_3 - \upsilon)\right) . \tag{C.2}$$

The set of independent residuals between the different IF settings using the spectrum with an IF = 1.4 GHz as reference is

$$\phi(\upsilon)_{1\text{-}2} = \phi(\upsilon)_1 - \phi(\upsilon)_2 , \tag{C.3}$$

$$\phi(\upsilon)_{1\text{-}3} = \phi(\upsilon)_1 - \phi(\upsilon)_3 . \tag{C.4}$$

The average of these residuals will reduce the image-band features from the spectra with IF settings 1.6 and 1.8 GHz by half,

$$\phi_{\rm residual\text{-}avg} = \left(\phi(\upsilon)_{1\text{-}2} + \phi(\upsilon)_{1\text{-}3}\right)/2 \tag{C.5}$$

$$= \left(2\phi_{\rm img}(\upsilon_1 - \upsilon) - \phi_{\rm img}(\upsilon_2 - \upsilon) - \phi_{\rm img}(\upsilon_3 - \upsilon)\right)/2. \tag{C.6}$$

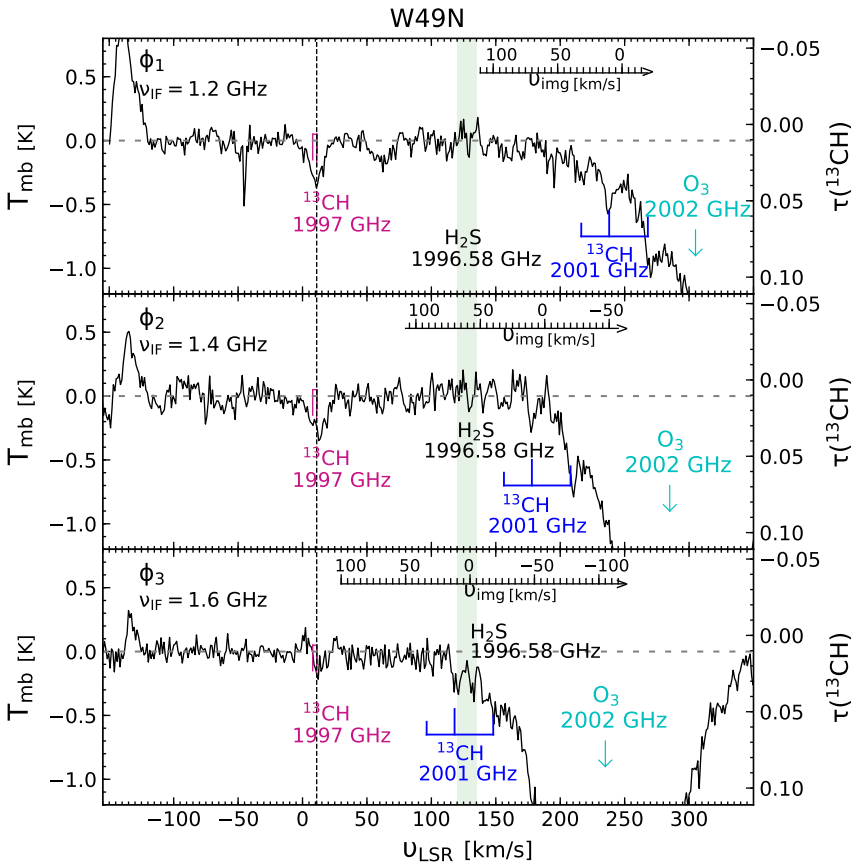

Figure C.3: Same as Fig. C.1, but towards W49(N) for IF settings of 1.2, 1.4, and 1.6 GHz (*from top to bottom*) .

Subtracting Eq. C.6 from Eq. C.2 yields

$$\phi_{\text{resultant}} = \phi_{\text{avg}} - \phi_{\text{residual-avg}} \tag{C.7}$$

$$= \phi_{\text{sig}}(\upsilon) - \frac{2}{3}\phi_{\text{img}}(\upsilon_1 - \upsilon) + \frac{5}{6}\phi_{\text{img}}(\upsilon_2 - \upsilon) + \frac{5}{6}\phi_{\text{img}}(\upsilon_3 - \upsilon). \tag{C.8}$$

While this exercise models the contribution of the 2001 GHz transitions of ^{13}CH , it does not confirm the profiles of the LOS features. Additionally, discrepancies in the noise level between the three spectral tunings arising from different integration times between them may lead to errors in the sideband reconstruction. However, the detection of ^{13}CH at the systemic velocity of the Sgr B2 (M) molecular cloud remains undisputed.

A similar DSB deconvolution was carried out for G34.26+0.15, W49(N), and W51E using a nominal IF setting of 1.2, 1.2, and 1.4 GHz as reference, respectively. The spectra observed using each of the three different IF tunings towards each of these sources are displayed in Figures C.2, C.3, and C.4. We clearly detect the ^{13}CH 1997 GHz Λ-doublet component at the respective systemic velocities of G34.26+015, W49(N), and W51E in all three IF settings at 1.2, 1.4, and 1.6 GHz, but the hyperfine lines of the 2001 GHz Λ-doublet component either lie at the

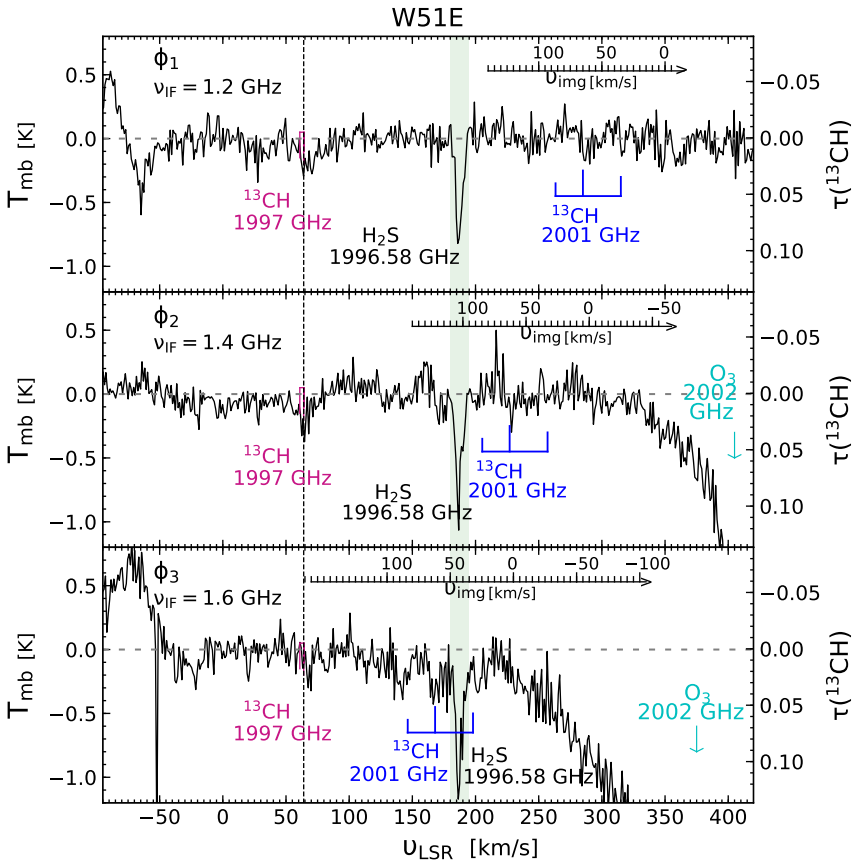

Figure C.4: Same as Fig. C.1, but towards W51E for IF settings of 1.2, 1.4, and 1.6 GHz (*from top to bottom*).

edge of the ozone feature for an IF setting of 1.2 GHz or move into the H_2S absorption feature for the higher IF tuning at 1.6 GHz. Although the detection of ^{13}CH towards the systemic velocities of these sources is confirmed, it is once again difficult to establish the presence of any LOS features after the sideband deconvolution.

C.2 ^{13}CH spectrum towards W3(OH)

In this appendix we display the ^{13}CH spectrum towards W3(OH).

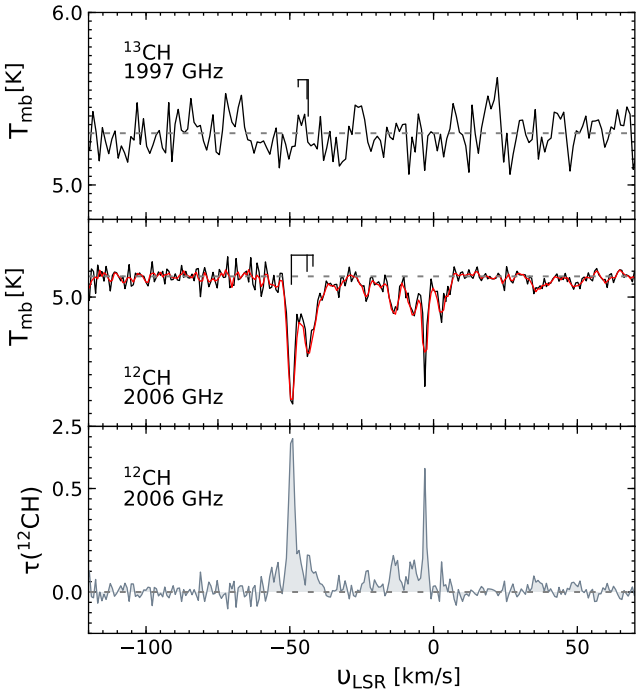

Figure C.5: Spectra of the $N, J = 2, 3/2 \rightarrow 1, 1/2$ transitions of ^{13}CH near 1997 GHz (*top*) and CH near 2006 GHz (*middle*) observed towards W3(OH) in black. The Wiener filter model of the observed CH spectrum is overlaid in red. The bottom panel presents the Wiener filter deconvolved CH spectrum in optical depth scales.

Appendix D

Appendix to Chapter 6

D.1 CH_2 non-detections

In this appendix we list the rms noise levels for the sources toward which we do not detect any o-CH_2.

D.2 CH_2 70 GHz HFS stacking

As mentioned in Sec. 6.5.5 and 6.5.6, we stack the HFS-decomposed model fits of each of the individual HFS components of the 70 GHz transition of CH_2 , prior to comparing its line profile with the observed line profiles of the CRRLs. Furthermore, in order to carry out a more objective comparison we incorporated the expected noise of the (stacked and averaged) 70 GHz spectra by including an additive Gaussian noise term. As an example, the different steps that are a part of this exercise are illustrated for the 70 GHz spectrum observed toward W3 IRS5 in Fig. D.1.

D.3 Observed recombination lines

In this appendix we present the observed spectra of the different RRLs. As mentioned in Sect. 6.4, there are two observing setups used for these observations. The first setting observed only the H-, He-, and CRRLs for a principal quantum number of 75, near 15 GHz. This setup was used to carry out observations toward the different Orion positions and W3 IRS5 (displayed in Fig. 6.12). The second setup was used for the remainder of the sources toward which o-CH_2 was observed, utilising a 5 GHz bandwidth from 12.5-17.5 GHz, which covered RRLs with principal quantum numbers between 80 and 72. Subsequently, for these sources, the RRL profiles for the different quantum numbers are stacked and averaged; based on these profiles, the contributions of the He RRL (modelled using a Gaussian fit) is subtracted to yield the CRRL profile used in the analysis.

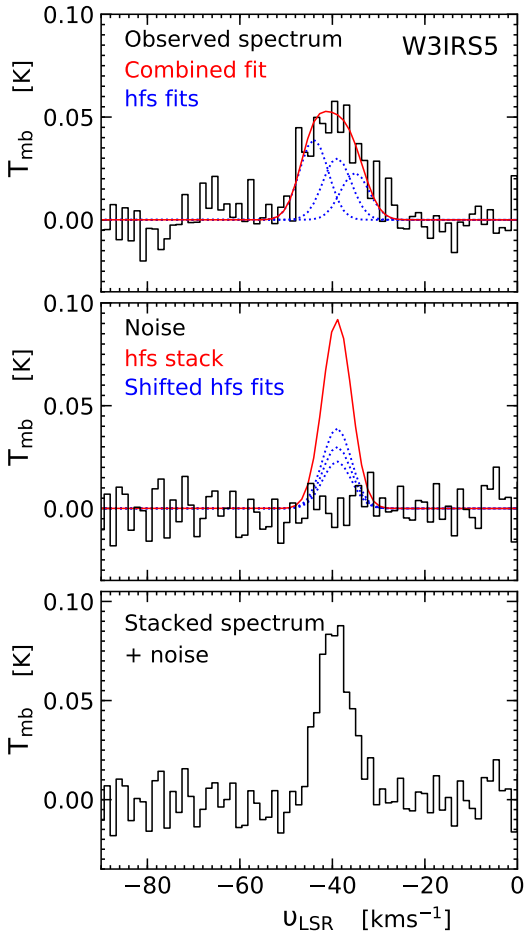

Figure D.1: *Top*: The observed o-CH_2 70 GHz spectrum towards W3 IRS5 (black) alongside the HFS decomposed fits (dotted blue) and the combined fit (red). *Middle*: The HFS stacked profile (red) with the fit to each HFS component shifted to the systemic velocity of the source (dotted blue) and the Gaussian noise profile (black). *Bottom*: The resultant stacked spectrum with the addition of noise (black).

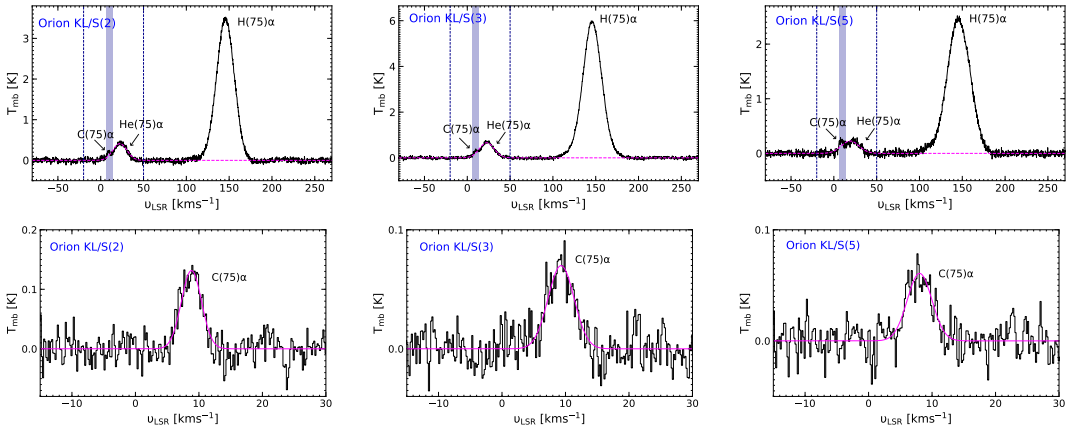

Figure D.2: *Top*: H-, He-, and CRRLs toward different Orion KL/S OSO pointing positions, with the Gaussian fit to the He-RRL displayed by the dashed magenta curve. *Bottom*: The resulting CRRL with the Gaussian fit to the profile displayed in magenta. The velocity scale is given with respect to the CRRL.

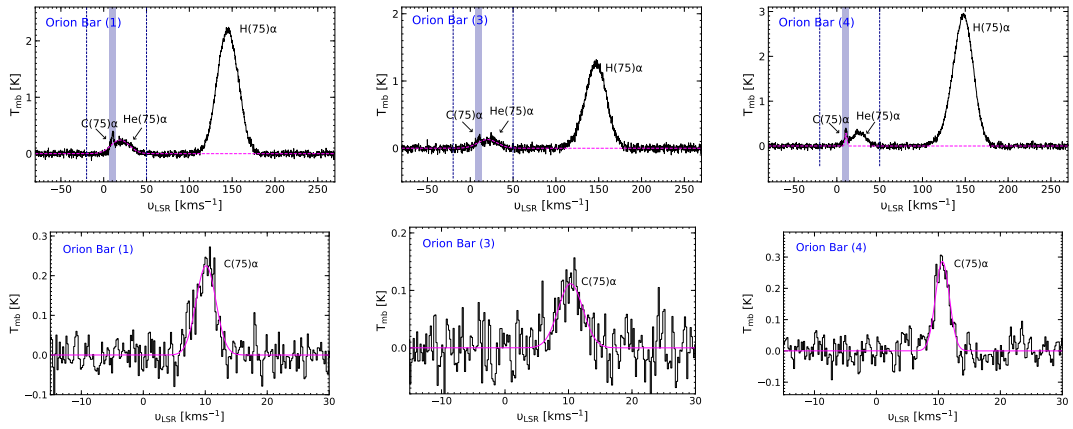

Figure D.3: Same as Fig. D.2, but toward the Orion Bar OSO pointing positions.

Table D.1: Onsala 20 m telescope non-detections.

Source	RA (J2000)	Dec. (J2000)	υ_{LSR} [kms^{-1}]	Line [GHz]	rms* [mK]
Orion	05:35:16.96	-05:22:02.7	+9.7	68	40
KL/S (1)				69	33
Orion	05:35:14.28	-05:22:27.5	+9.0	70	24
KL/S (2)				68	53
				69	48
Orion	05:35:14.28	-05:23:16.5	+9.0	70	23
KL/S (3)				68	55
				69	43
Orion	05:35:16.46	-05:23:22.7	+9.0	70	27
KL/S (4)				68	61
				69	37
Orion	05:35:13.10	-05:23:56.0	+9.0	70	17
KL/S (5)				68	40
				69	30
Orion	05:35:24.96	-05:22:32.7	+9.0	68	30
KL/S (6)				69	25
Orion	05:35:25.30	-05:24:34.0	+11.0	70	17
Bar (1)				68	34
				69	25
Orion	05:35:22.80	-05:25:01.0	+11.0	68	55
Bar (2)				69	38
Orion	05:35:25.40	-05:25:25.0	+11.0	70	18
Bar (3)				68	41
				69	30
Orion	05:35:23.10	-05:24:35.0	+11.0	70	23
Bar (4)				68	47
				69	41
Orion	05:35:20.81	-05:25:17.1	+11.0	68	38
Bar (5)				69	28
W51 E	19:23:44.00	14:30:30.00	+55.3	68	21.
				69	18
W51 M	19:23:42.00	14:30:36.00	+58.4	68	24
				69	21
W51 N	19:23:40.00	14:31:10.00	+60.0	68	15
				69	12
W49 N	19:10:13.55	09:06:14.70	+8.8	68	26
				69	21
W43	18:47:36.89	-01:55:30.20	+91.1	68	26
				69	19
DR21	20:39:02.00	42:19:42.00	-2.5	68	11
				69	7
W75 N	20:38:36.45	42:37:35.10	+7.5	68	9
				69	8
S140	22:19:11.53	63:17:46.90	-12.3	68	34
				69	25

Table D.1: Continued.

Source	RA (J2000)	Dec. (J2000)	$\upsilon_{\rm LSR}$ [kms^{-1}]	Line [GHz]	rms* [mK]
W3(OH)	02:27:04.10	61:52:22.00	-46.0	70	7
				68	13
				69	8
S233	05:35:51.19	35:44:12.90	-17.5	70	10
				68	17
				69	15
S235	05:40:53.30	35:41:49.00	-57.0	70	19
				68	37
				69	30
CRL618	04:42:53.62	36:06:53.30	-26.0	70	60
				68	100
				69	80
CRL2688	21:02:18.27	36:41:37.00	-32.0	70	12
				68	20
				69	18
NGC7023	21:01:36.90	68:09:48.00	2.5	70	12
				68	24
				69	22
NGC7027	21:07:01.75	42:14:10.00	8.9	70	6
				68	11
				69	9
NGC7538	23:13:37.20	61:30:00.00	-64.9	70	19
				68	38
				69	28
Cas A	23:23:24.90	58:50:03.30	-46.0	70	8
				68	15
				69	12
IC443	06:18:02.70	22:39:03.00	-4.4	70	10
				68	16
				69	14

Notes: Columns are, left to right, source name, J2000 coordinates of observed position, assumed LSR velocity, line ID and 1σ rms noise level. $^{(*)}$ On the $T_{\rm mb}$ scale the rms noise is quoted for a spectral resolution of 0.97 km s^{-1}. All the sources are SFRs, except for NGC7027 which is a planetary nebula, CRL618 and CRL2688, which are protoplanetary nebulae and Cas A and IC443, which are supernova remnants. NGC7023 is a reflection nebula with a PDR.

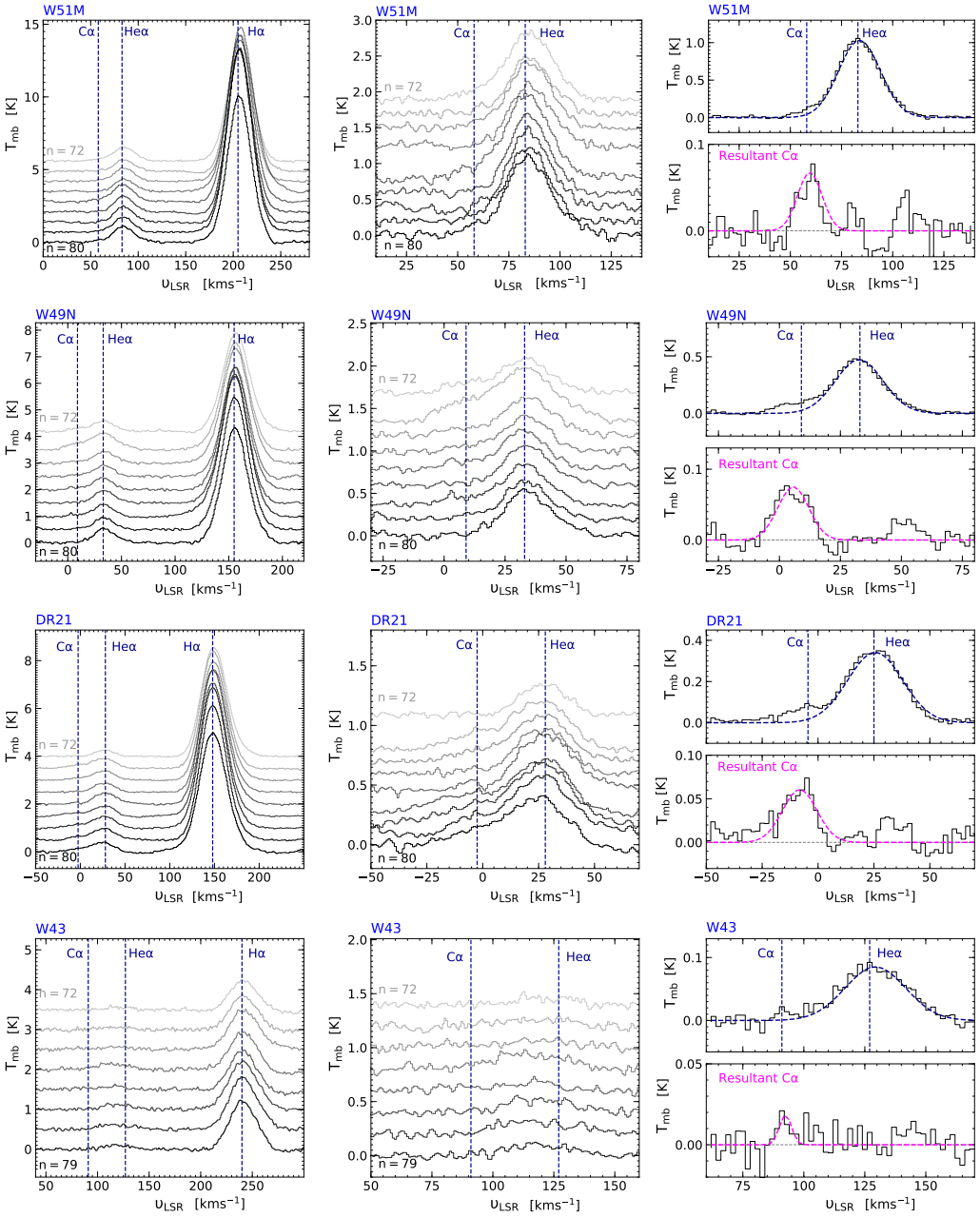

Figure D.4: *Left:* H-, He-, and CRRLs observed with the Effelsberg 100 m telescope for α lines with principal quantum number, n, from 72 (*top*) to 80 (*bottom*) (except toward W43) in steps of $\Delta n = 1$. The position of the different lines are marked by dashed dark blue lines. The spectra are uniformly offset by 0.5 K on the $T_{\rm mb}$ scale. *Centre*: Zoomed in view of the He-, and C-RRL. The offsets are not uniform but varied for the ease of viewing with a typical offset of 0.2 K on the $T_{\rm mb}$ scale. *Right*: The average He-, and C-RRL profile (*top*) with the Gaussian fit to the He RRL presented by the dashed dark blue curve. The resulting CRRL profile is displayed below with its fits given by the dashed magenta Gaussian. The velocity scale is given with respect to the CRRL. The different panels from top to bottom represent spectra that are obtained toward W51 M, W49 N, DR21, and W43, respectively.

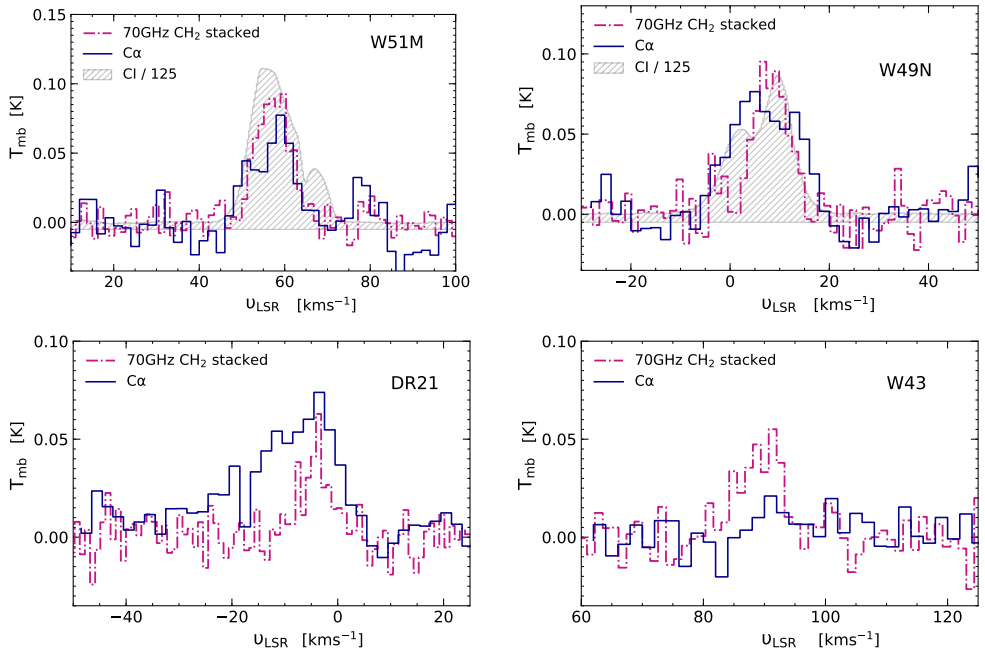

Figure D.5: Decomposed CRRL profile in blue alongside the 70 GHz HFS stacked CH_2 line profile displayed by the dashed-dotted violet curve toward (*clockwise from top*) W51 M, W49 N, DR21, and W43, respectively. The stacked profile of the 70 GHz CH_2 transition was obtained from the HFS decomposition model. The hatched grey regions in the W51 M and W49 N spectra display the line profiles of the $^3P_1 - ^3P_0$ transition of CI at 492.160 GHz scaled down by a factor of 125 on the T_{mb} scale.

Table D.2: Best fit Gaussian parameters for the CRRLs.

Source	υ [km s^{-1}]	$\Delta\upsilon$ [km s^{-1}]	T_{mb} [mK]
Orion KL/S (2)	8.8(0.1)	3.7(0.2)	140.0(5.4)
Orion KL/S (3)	9.3(0.1)	4.8(0.3)	74.4(3.3)
Orion KL/S (5)	8.1(0.1)	4.6(0.3)	64.7(3.3)
Orion Bar (1)	10.1(0.1)	3.7(0.2)	239.4(8.5)
Orion Bar (3)	10.3(0.2)	4.6(0.5)	118.8(9.1)
Orion Bar (4)	10.6(0.1)	2.6(0.1)	304.6(11.1)
W3 IRS5	-38.4(0.1)	6.8(0.4)	131.4(6.6)
W51 M	59.8(1.0)	6.1(1.8)	69.0(3.7)
W49N	5.6(0.6)	6.7(1.5)	79.0(3.7)
DR21	-8.2(2.6)	7.7(1.5)	60.5(6.1)
W43	92.4(0.6)	2.4(1.0)	18.6(3.6)

Appendix E

Appendix to Chapter 7

E.1 HI analysis

In this appendix we present the HI absorption ($T_{\rm on}$) and emission spectra ($T_{\rm off}$), along with derived quantities such as the optical depth, spin temperature and column density. The solid black curve in the continuum normalised on-source spectrum, $T^{\rm on,obs}/T^{\rm sou,obs}_{\rm cont}$ (top panel) represents the absorption profile smoothed to the resolution of the emission data. Classically the off-source spectrum is taken from a position next to the source of interest (well outside of the beam width). However, in the Milky Way disk, HI is subject to strong spatial fluctuations and using a single off position would be error prone. Therefore, in Winkel et al. (2017) a spatial filtering technique using a ring (or doughnut-shaped) kernel was applied to obtain an interpolated brightness temperature, shown in the second panel (black curve). For comparison, in the panel displaying spin temperatures, we also plot the brightness temperature in blue and lastly, the column density panel also displays the uncorrected column density profile, $N^{*}_{\rm HI}$. The blue and grey shaded regions indicate the 1σ (68% percentile) and 3σ (99.7% percentile) confidence intervals, respectively. Additionally in each panel, we mark the systemic velocity and velocity dispersion of each source by the dashed pink line and shaded pink regions, respectively. A detailed description is presented in Winkel et al. (2017).

E.2 Continuum level uncertainties

In this Appendix we briefly discuss the reliability of the absolute calibration of the continuum brightness temperatures used in our analysis. As a first check, we binned our observations across scans (time), toward each individual source over velocity intervals/channels previously used to estimate the continuum and baseline. Assessing the relative fluctuations in the continuum level will reveal the stability of its measurement. From Fig. E.4, it can be seen that the scatter in the continuum level, over different scans, is less than 10% for all the sources in our study except AG330.954−00.182 and AG332.826−00.549 which shows a slightly large scatter of 18%. Not showing any major variations, leads us to conclude that the continuum levels are fairly reliable. It is important to note here that the observations were carried out using the wobbling secondary with a fast switching rate which was essential in removing any drifts due to atmospheric instabilities.

As discussed earlier in the text, we have also carried out a comparison between the continuum flux levels of our ArH^{+} observations with the peak fluxes obtained from the 870 μm continuum data from the ATLASGAL survey (Fig. E.5). We see that our data is well correlated with the 870 μm continuum emission with a relative scatter $< 5\%$.

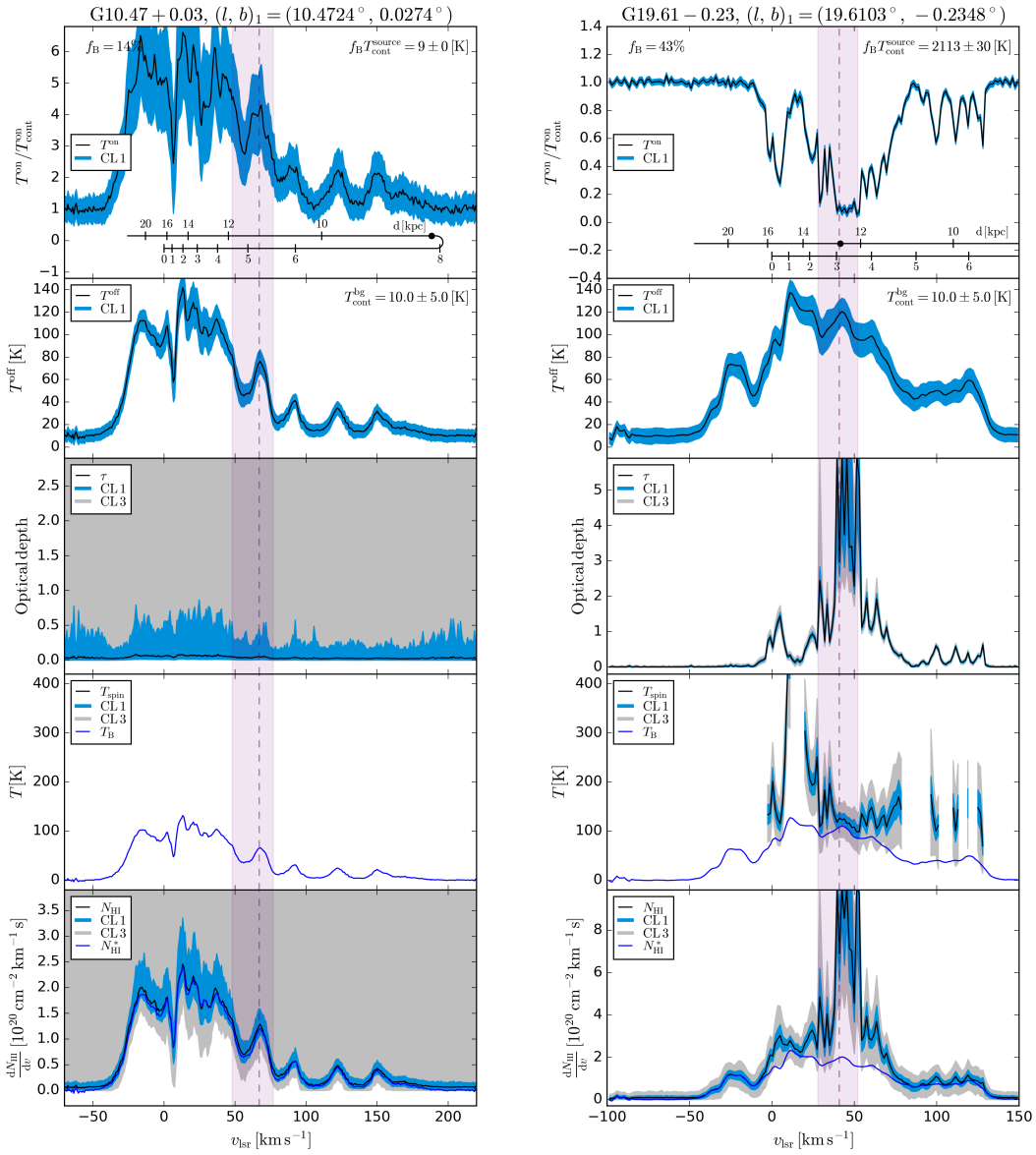

Figure E.1: *From top to bottom*: HI absorption and emission spectra, optical depth, spin temperature, and HI column density toward AG10.472+00.027 (*left*) and AG19.609−00.234 (*right*). The pink dashed line and shaded region mark the systemic velocity of the source and highlight the velocity dispersion of the source.

E.3 Column density profiles

In this Appendix we present the column density profiles for all the species studied in this work except HI (which is already presented in Appendix E.1) toward the entire source sample in this study.

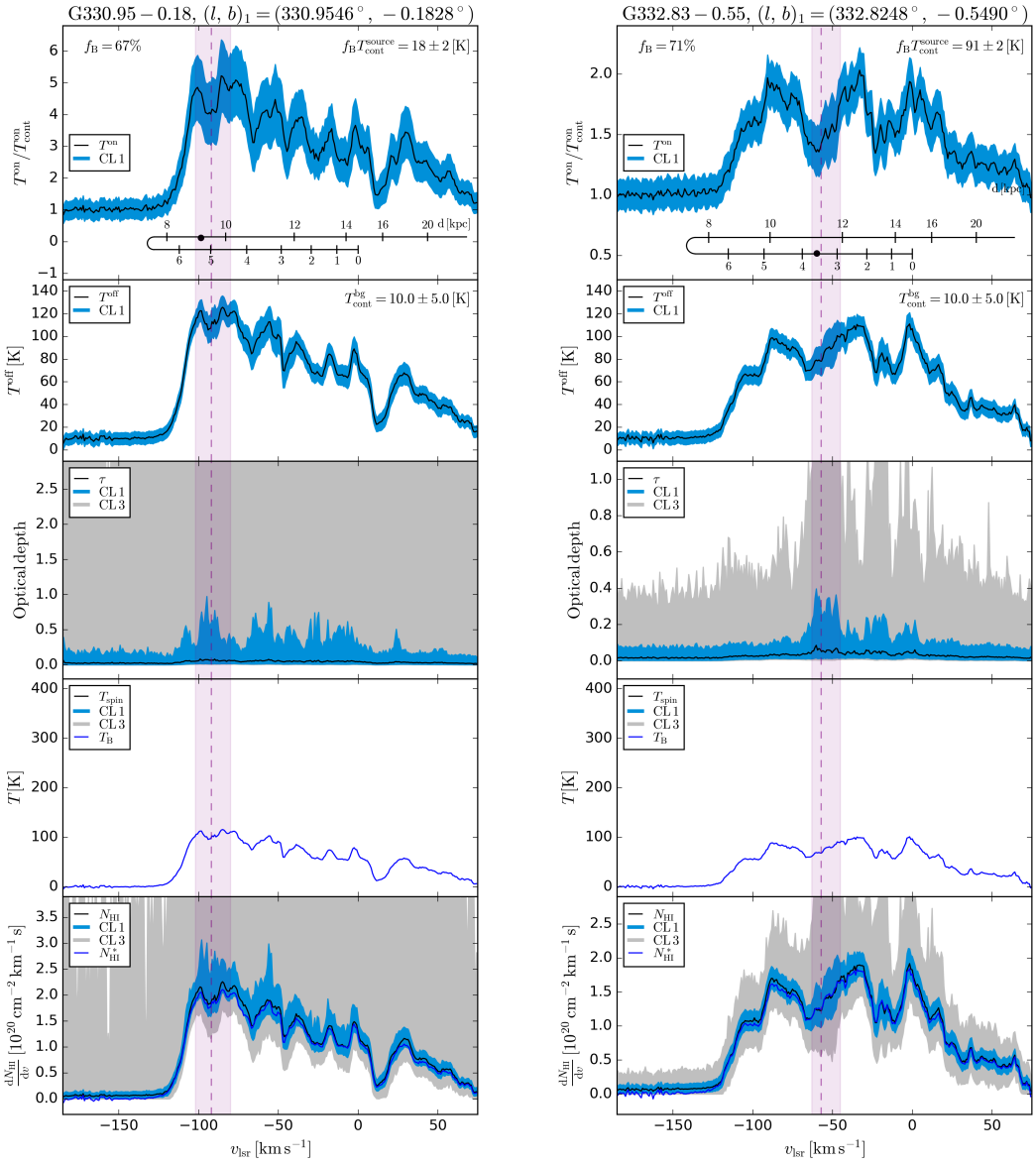

Figure E.2: Same as Fig. E.1 but toward AG330.954−00.182 (*left*) and AG332.826−00.549 (*right*).

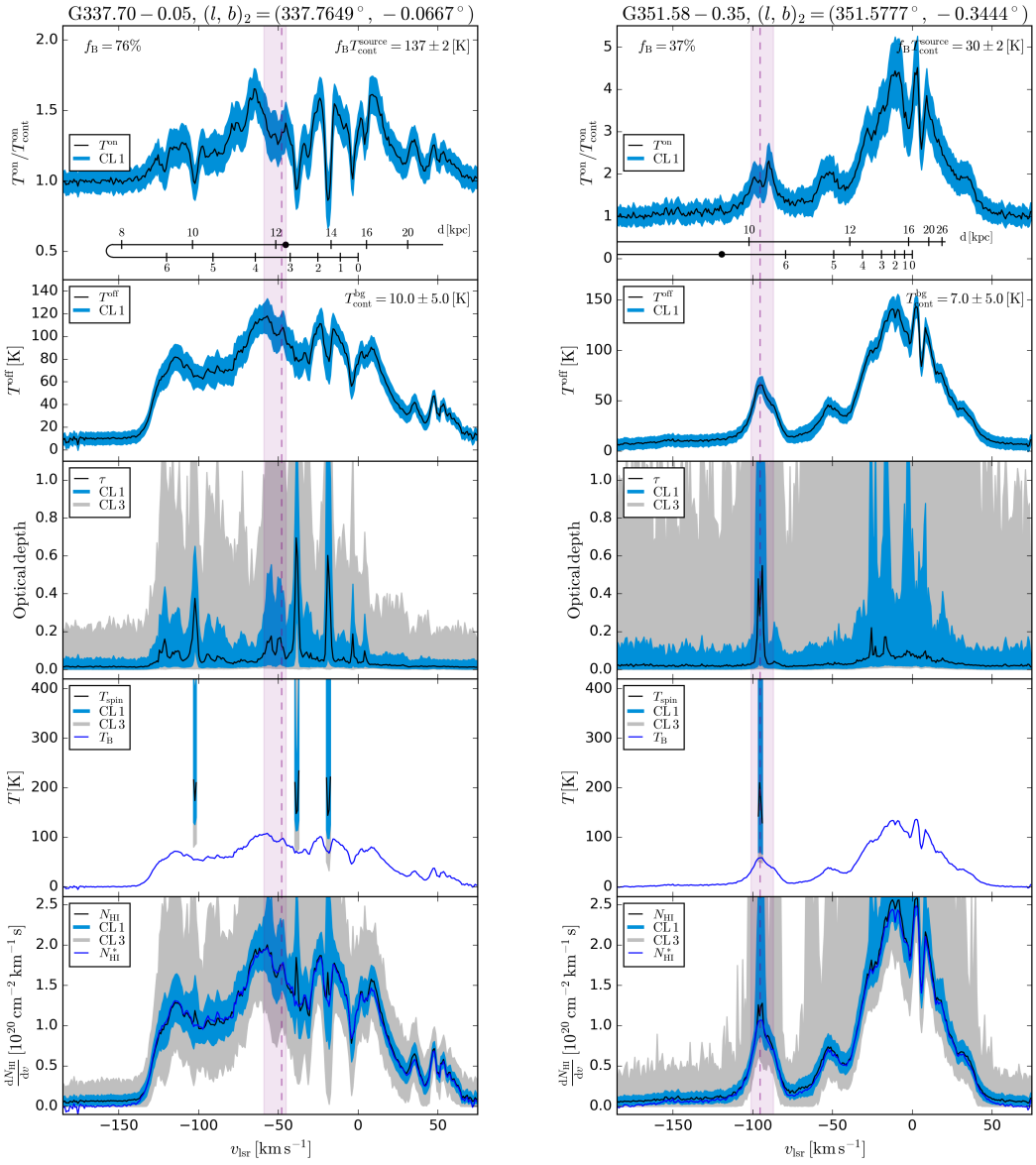

Figure E.3: Same as Fig. E.1 but toward AG337.704−00.054 (*left*) and AG351.581−00.352 (*right*).

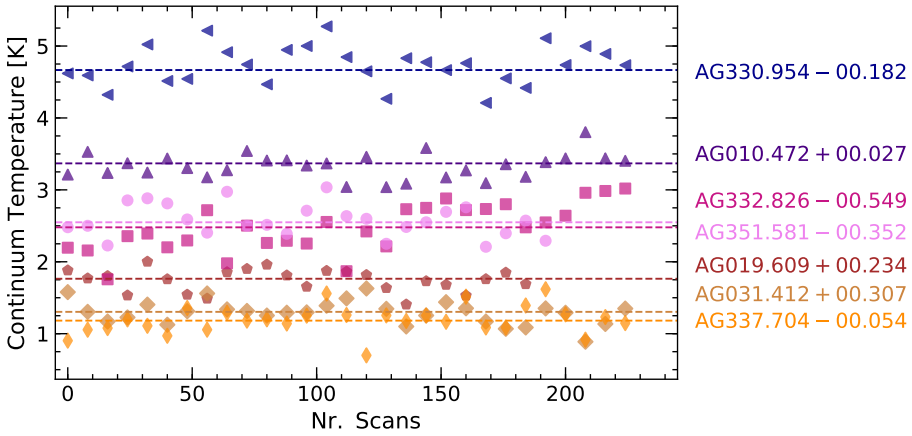

Figure E.4: Continuum fluctuations across scans. The dashed lines represent the median continuum level for each source.

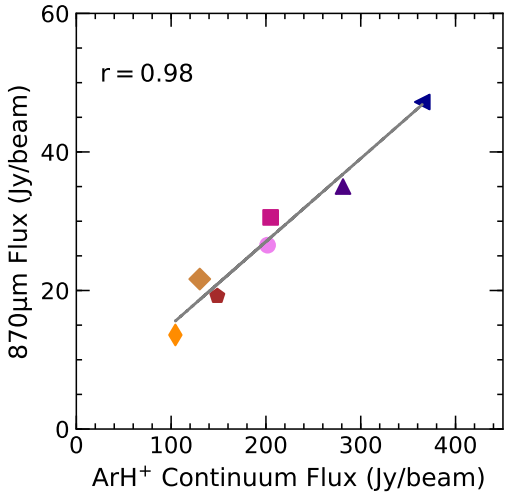

Figure E.5: Correlation between the observed ArH^+ continuum flux and the 870 μm continuum flux.

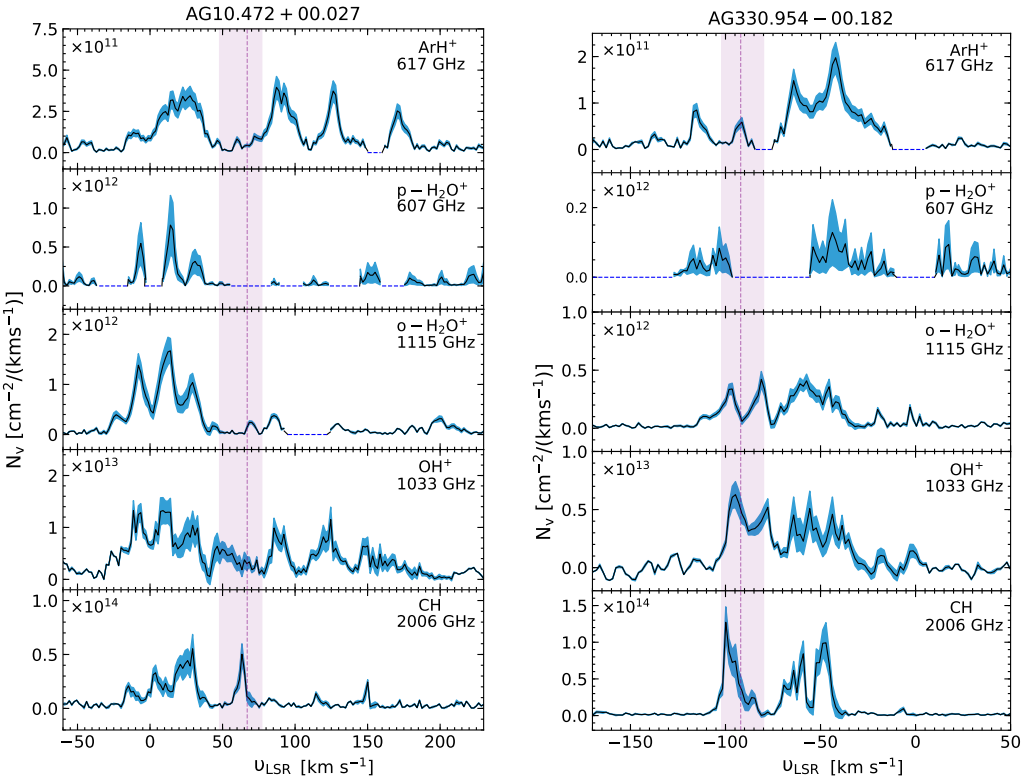

Figure E.6: *Top to bottom*: Column density per velocity channel of ArH^+, p-H_2O^+, o-H_2O^+, OH^+, and CH towards G10.472+00.027 (*left*) and G330.954−00.182 (*right*). The blue shaded region represents the uncertainties while the pink dashed line, and shaded region mark the systemic velocity of the source and highlight the velocity dispersion of the source. The dashed blue lines indicate those velocity intervals that were omitted from the fitting routine due to contamination.

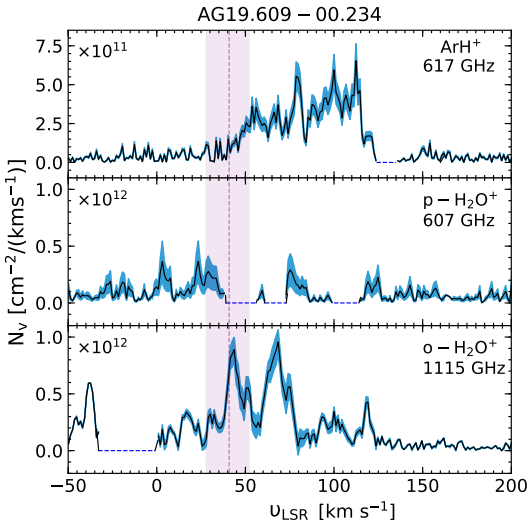

Figure E.7: Same as Fig. E.6 but towards G19.609−00.234. Note that there is no OH^+ and CH spectra of the transitions studied here, available for this source.

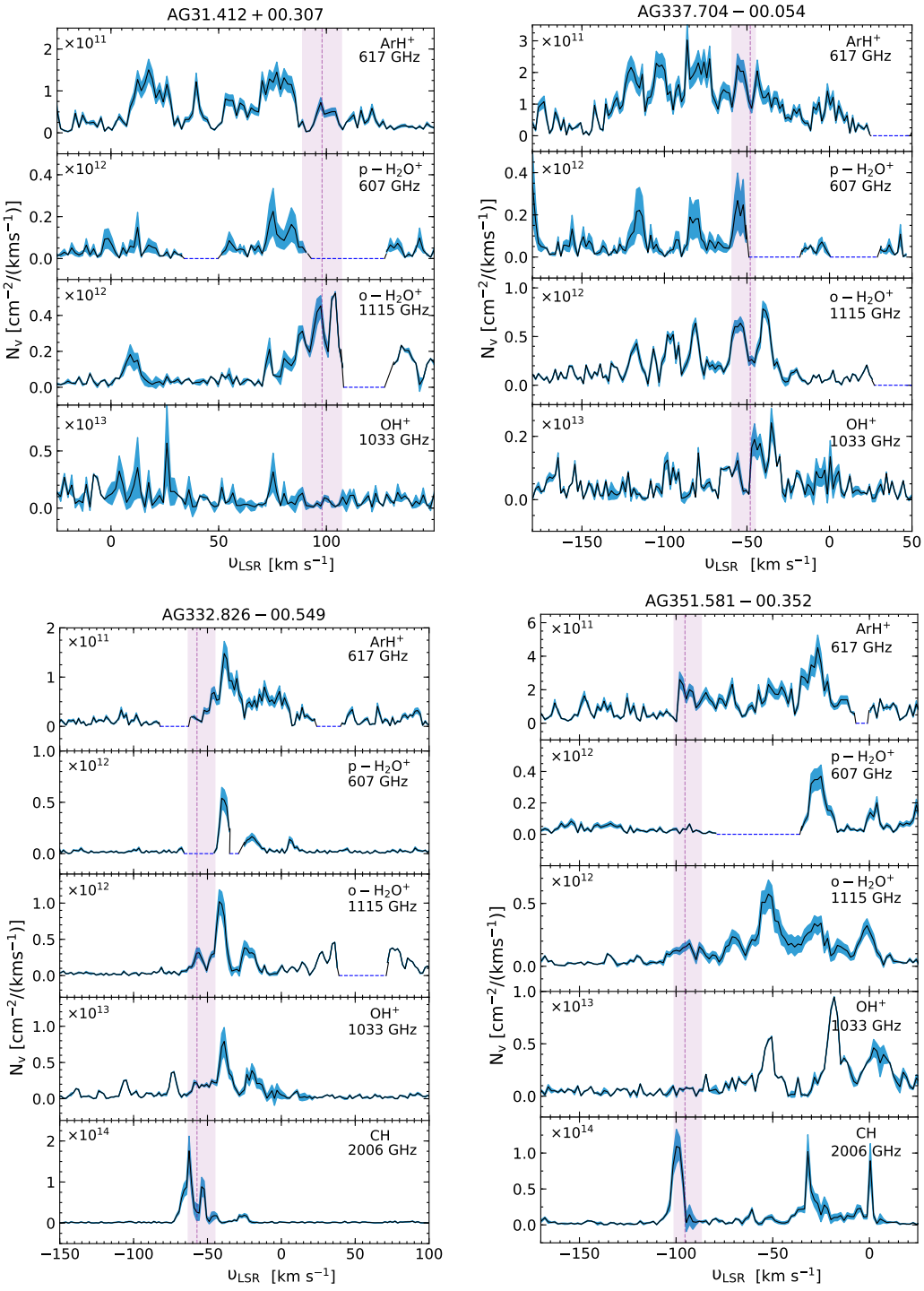

Figure E.8: Same as Fig. E.6 but towards (*clockwise from the top-left*) G31.412+00.307, G337.704−00.054, G351.581+00.352, and G332.826−00.549. Note that there is no CH spectrum of the transitions studied here, available for G31.412+00.307 and G337.704−00.054.

Appendix F

Appendix to Chapter 8

F.1 HI analysis

In this appendix we discuss the HI 21 cm line analysis. The HI absorption ($T_{\rm on}$) and emission spectra ($T_{\rm off}$), along with derived quantities such as the optical depth, spin temperature and column density are presented in Fig. F.1 for NGC 253 and NGC 4945. The solid black curve in the top panel of these figures, represents the continuum normalised on-source absorption profiles ($T^{\rm on,obs}/T^{\rm sou,obs}_{\rm cont}$) smoothed to the resolution of the emission data. The off-source spectrum is taken from a position next to the source of interest (well outside of the beam width). Similar to the Milky Way disk, the HI data toward these galaxies are subject to strong spatial fluctuations and using a single off position would be error prone. Therefore, following Winkel et al. (2017), a spatial filtering technique using a ring (or doughnut-shaped) kernel was applied to obtain an interpolated brightness temperature, as shown in the second panel (black curve). For comparison, in the panel displaying spin temperatures, we also plot the brightness temperature in blue and lastly, the column density panel also displays the uncorrected column density profile, $N^{*}_{\rm HI}$. The blue and grey shaded regions indicate the 1σ (68% percentile) and 3σ (99.7% percentile) confidence intervals, respectively. A detailed description is presented in Winkel et al. (2017). As a caveat in this analysis, we mention here that this filtering technique may not be what is best suited to describe the often observed, 'butterfly'-shaped distribution of gas in these external galaxies and a proper treatment of the same, would require the use of a tilted ring model.

F.2 Continuum level uncertainties

We now briefly assess the reliability of the absolute calibration of the continuum brightness temperatures used in our analysis that were derived from the sub-mm spectra of the ArH^+ and p-H_2O^+ lines taken with the APEX telescope. In Fig. F.2, for both NGC 253 and NGC 4945, we plot the continuum brightness temperatures measured for all individual scans versus time over velocity intervals used to determine the continuum level and baseline. The scatter across different scans displayed is found to lie between 11 and 17% for the two sources with an average value of 14%, thereby yielding a fairly stable continuum level.

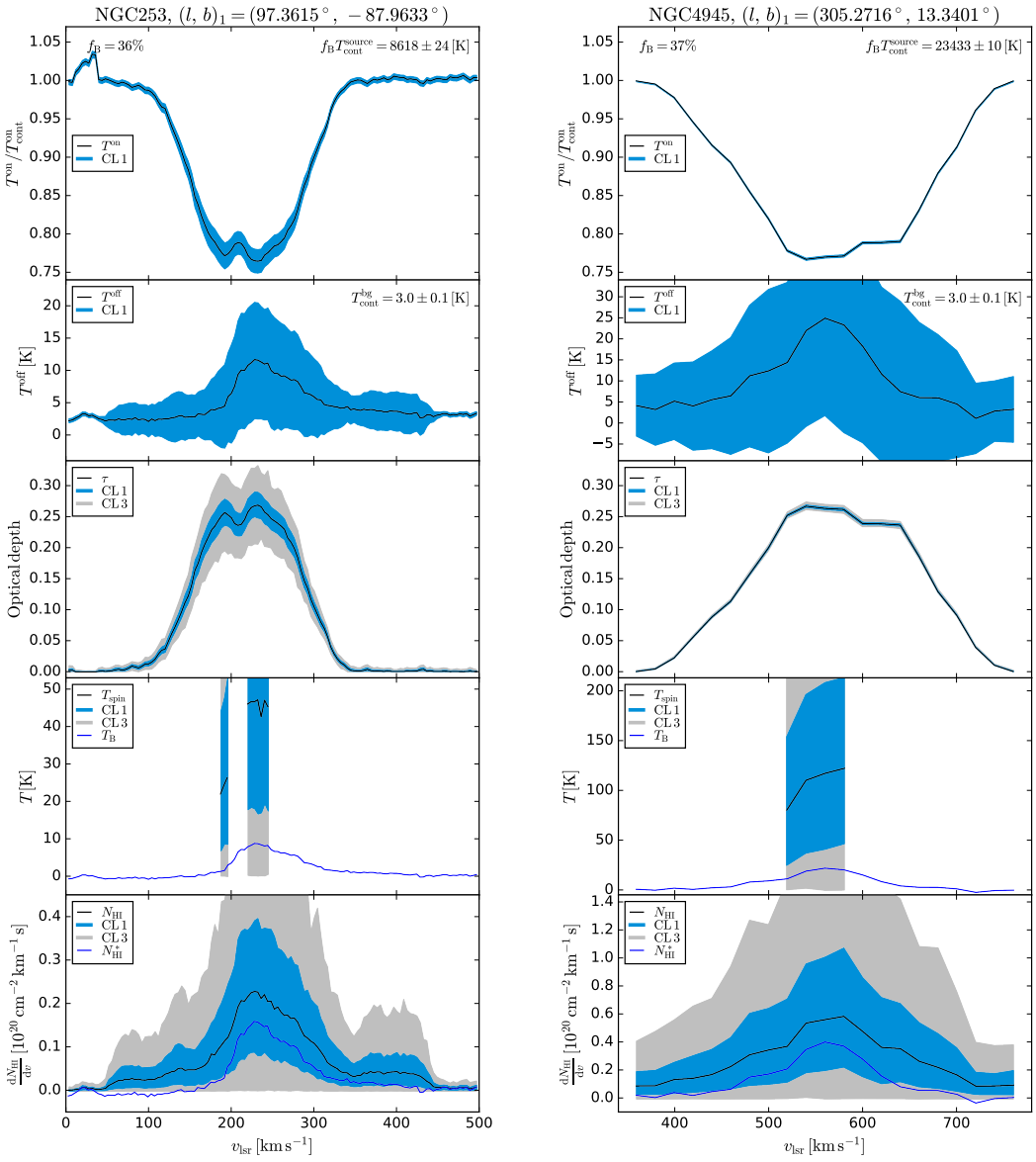

Figure F.1: *From top to bottom:* HI analysis towards NGC 253 (*left*) and NGC 4945 (*right*).

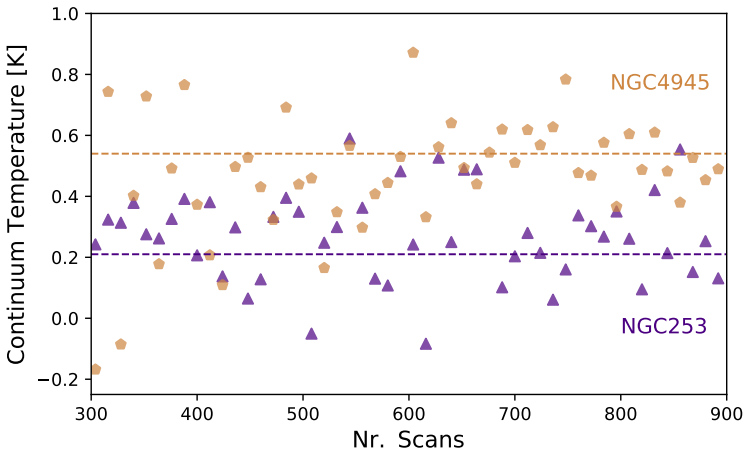

Figure F.2: Continuum fluctuations across scans for NGC 253 (purple triangle) and NGC 4945 (yellow pentagons), with the dashed lines indicating the median continuum levels for each source.

Nomenclature

Frequently used acronyms

ALMA	Atacama Large Millimetre/submillimetre Array
APEX	Atacama Pathfinder Experiment
ATCA	Australia Telescope Compact Array
ATLASGAL	APEX Telescope Large Area Survey of the Galaxy
CMB	Cosmic microwave background
CMZ	Central molecular zone
CNM	Cold Neutral Medium
DMG	Dark Molecular Gas
FIR	Far-infrared
FWHM	Full-width at half maximum
GC	Galactic centre
GMC	Giant molecular cloud
GOTC+	Galactic Observations of Terahertz C+
(up)GREAT	German REciever for Astronomy at Terahertz frequencies
HIFI	Heterodyne Instrument for the Far-Infrared
HEXGAL	Herschel EXtraGALactic
HEXOS	Herschel observations of EXtra-Ordinary Sources
HFS	Hyperfine structure
HIM	Hot ionised medium
HPBW	Half power beam width
HSO	Herschel Space Observatory
ISM	Interstellar medium
ISRF	Interstellar radiation field
JVLA	*Karl G. Jansky* Very Large Array
LABOCA	Large Apex BOlometer CAmera
KP	Kitt Peak
LOS	Line-of-sight
LSB	Lower side band
LSR	Local standard of rest
LTE	Local thermodynamic equilibrium
MC	Molecular clouds
MSE	Mean-square-error
MIR	Mid-infrared
NIR	Near-infrared
OPR	ortho-to-para ratio
OSO	Onsala Space Observatory

PACS	Photodetector Array Camera and Spectrometer
PDR	photodissociation regions
PNe	Planetary Nebulae
PRISMAS	PRobing InterStellar Molecules with Absorption line Studies
PWV	Precipitable water vapor
RMS	Root-mean-square
RRL	Radio recombination lines
SEPIA660	Swedish-ESO PI-instrument
SFR	Star-forming region
S/N	Signal-to-noise
SOFIA	Stratospheric Observatory for Infrared Astronomy
SPIRE	Spectral and Photometric Imaging Receiver
TDR	Turbulent dissipation regions
UCHII	Ultra compact HII
USB	Upper side band
UV	Ultra violet
WF	Wiener Filter
WIM	Warm ionised medium
WNM	Warm neutral medium
WT	Wavelet Transform

Physical Constants

Speed of light (in vacuum)	$c = 2.9979 \times 10^{10}\,\mathrm{cm\,s^{-1}}$
Planck's constant	$h = 6.626 \times 10^{-27}\,\mathrm{erg\,s}$
Boltzmann's constant	$k_\mathrm{B} = 1.381 \times 10^{-16}\,\mathrm{erg\,K^{-1}}$
Mass H atom	$m_\mathrm{H} = 1.673 \times 10^{-24}\,\mathrm{g}$

Astronomical Constants

Astronomical unit	$1\,\mathrm{au} = 1.496 \times 10^{13}\,\mathrm{cm}$
Parcec	$1\,\mathrm{pc} = 3.086 \times 10^{18}\,\mathrm{cm}$
Solar mass	$1\,M_\odot = 1.989 \times 10^{27}\,\mathrm{g}$
Solar luminosity	$1\,L_\odot = 3.9 \times 10^{33}\,\mathrm{erg\,s^{-1}}$
Electronvolt	$1\,\mathrm{eV} = 1.6021 \times 10^{-19}\,\mathrm{J}$
Jansky	$1\,\mathrm{Jy} = 10^{-23}\,\mathrm{erg\,s^{-1}\,cm^{-2}\,Hz^{-1}}$

Bibliography

Adler, D. S., Wood, D. O. S., & Goss, W. M. 1996, ApJ, 471, 871

Aladro, R., Martín, S., Riquelme, D., et al. 2015, A&A, 579, A101

Albertsson, T., Indriolo, N., Kreckel, H., et al. 2014, ApJ, 787, 44

Alekseyev, A. B., Liebermann, H.-P., & Buenker, R. J. 2007, Physical Chemistry Chemical Physics (Incorporating Faraday Transactions), 9, 5088

Alves, J. & Homeier, N. 2003, ApJ, 589, L45

Asensio Ramos, A. & Elitzur, M. 2018, A&A, 616, A131

Auer, L. H. 1987, Acceleration of Convergence (Springer), 101

Baan, W. A. & Haschick, A. D. 1995, ApJ, 454, 745

Baars, J. W. M. & Kärcher, H. J. 2018, Radio Telescope Reflectors, Vol. 447 (Springer)

Bacmann, A., Caux, E., Hily-Blant, P., et al. 2010, A&A, 521, L42

Bally, J., Anderson, L. D., Battersby, C., et al. 2010, A&A, 518, L90

Bally, J. & Langer, W. D. 1982, ApJ, 255, 143

Bally, J., Reipurth, B., Walawender, J., & Armond, T. 2002, AJ, 124, 2152

Barlow, M. J., Swinyard, B. M., Owen, P. J., et al. 2013, Science, 342, 1343

Barrow, D. & Matcheva, K. I. 2011, Icarus, 211, 609

Bartlett, N. & Lohmann, D. 1962, Journal of the Chemical Society (Resumed), 5253

Batria, W., Wilson, T. L., Bastien, P., & Ruf, K. 1983, A&A, 128, 279

Belitsky, V., Lapkin, I., Fredrixon, M., et al. 2018, A&A, 612, A23

Belitsky, V., Lapkin, I., Fredrixon, M., et al. 2015, A&A, 580, A29

Belloche, A., Müller, H. S. P., Garrod, R. T., & Menten, K. M. 2016, A&A, 587, A91

Belloche, A., Müller, H. S. P., Menten, K. M., Schilke, P., & Comito, C. 2013, A&A, 559, A47

Belov, S. P., Winnewisser, G., & Herbst, E. 1995, Journal of Molecular Spectroscopy, 174, 253

Bergin, E. A., Phillips, T. G., Comito, C., et al. 2010, A&A, 521, L20

Bertojo, M., Cheung, A. C., & Townes, C. H. 1976, ApJ, 208, 914

Bethe, H. A. 1939, Physical Review, 55, 434

Beuther, H., Bihr, S., Rugel, M., et al. 2016, A&A, 595, A32

Bialy, S., Neufeld, D., Wolfire, M., Sternberg, A., & Burkhart, B. 2019, ApJ, 885, 109

Bizzocchi, L., Dore, L., Degli Esposti, C., & Tamassia, F. 2016, ApJ, 820, L26

Black, J. H. 1978, ApJ, 222, 125

Black, J. H. 1994, in Astronomical Society of the Pacific Conference Series, Vol. 58, The First Symposium on the Infrared Cirrus and Diffuse Interstellar Clouds, ed. R. M. Cutri & W. B. Latter, 355

Black, J. H., Hartquist, T. W., & Dalgarno, A. 1978, ApJ, 224, 448

Blasi, P. 2014, Nuclear Physics B Proceedings Supplements, 256, 36

Bolatto, A. D., Warren, S. R., Leroy, A. K., et al. 2013a, Nature, 499, 450

Bolatto, A. D., Wolfire, M., & Leroy, A. K. 2013b, ARA&A, 51, 207

Bonfand, M., Belloche, A., Menten, K. M., Garrod, R. T., & Müller, H. S. P. 2017, A&A, 604, A60

Booth, A. J. & Blackwell, D. E. 1983, MNRAS, 204, 777

Bottinelli, S., Wakelam, V., Caux, E., et al. 2014, MNRAS, 441, 1964

Bradford, C. M., Nikola, T., Stacey, G. J., et al. 2003, ApJ, 586, 891

Brock, D., Joy, M., Lester, D. F., Harvey, P. M., & Ellis, H. Benton, J. 1988, ApJ, 329, 208

Brown, R. L., Lockman, F. J., & Knapp, G. R. 1978, ARA&A, 16, 445

Bruderer, S. 2019, PyPDR: Python Photo Dissociation Regions

Brünken, S., Michael, E. A., Lewen, F., et al. 2004, Canadian Journal of Chemistry, 82, 676

Bujarrabal, V., Salinas, F., & Gonzalo, I. 1984, ApJ, 285, 312

Bunn, E. F. & Wandelt, B. 2017, Phys. Rev. D, 96, 043523

Burke, B. F. & Graham-Smith, F. 2014, An Introduction to Radio Astronomy (Cambridge University Press)

Burton, W. B. 1970, A&AS, 2, 291

Butner, H. M., Charnley, S. B., Ceccarelli, C., et al. 2007, ApJ, 659, L137

Campbell, M. F., Butner, H. M., Harvey, P. M., et al. 1995, ApJ, 454, 831

Cannon, C. J. 1985, The transfer of spectral line radiation (Cambridge University Press)

Caprari, R. S., Goh, A. S., & Moffatt, E. K. 2000, Appl. Opt., 39, 6633

Carpenter, J. M. & Sanders, D. B. 1998, AJ, 116, 1856

Carruthers, G. R. 1970, ApJ, 161, L81

Chou, R. C. Y., Peck, A. B., Lim, J., et al. 2007, ApJ, 670, 116

Clegg, P. E., Ade, P. A. R., Armand, C., et al. 1996, A&A, 315, L38

Cooke, R. J., Pettini, M., & Steidel, C. C. 2018, ApJ, 855, 102

Cox, P., Huggins, P. J., Maillard, J. P., et al. 2002, A&A, 384, 603

Coxon, J. A. & Hajigeorgiou, P. G. 2016, Journal of Molecular Spectroscopy, 330, 63

Crutcher, R. M., Hakobian, N., & Troland, T. H. 2010, MNRAS, 402, L64

Csengeri, T., Bontemps, S., Wyrowski, F., et al. 2017, A&A, 601, A60

Csengeri, T., Menten, K. M., Wyrowski, F., et al. 2012, A&A, 542, L8

Csengeri, T., Urquhart, J. S., Schuller, F., et al. 2014, A&A, 565, A75

Cuadrado, S., Goicoechea, J. R., Cernicharo, J., et al. 2017, A&A, 603, A124

Cuadrado, S., Goicoechea, J. R., Pilleri, P., et al. 2015, A&A, 575, A82

Cuadrado, S., Goicoechea, J. R., Roncero, O., et al. 2016, A&A, 596, L1

Dabrowski, I. & Herzberg, G. 1980, in Liege International Astrophysical Colloquia, Vol. 21, Liege International Astrophysical Colloquia, ed. I. Dubois & G. Herzberg, 341–349

Dagdigian, P. J. 2018a, MNRAS, 479, 3227

Dagdigian, P. J. 2018b, MNRAS, 475, 5480

Dame, T. M. & Thaddeus, P. 2008, ApJ, 683, L143

Danks, A. C., Federman, S. R., & Lambert, D. L. 1984, A&A, 130, 62

Davidson, S. A., Evenson, K. M., & Brown, J. M. 2001, ApJ, 546, 330

Davidson, S. A., Evenson, K. M., & Brown, J. M. 2004, Journal of Molecular Spectroscopy, 223, 20

de Graauw, T., Helmich, F. P., Phillips, T. G., et al. 2010, A&A, 518, L6

De Pree, C. G., Mehringer, D. M., & Goss, W. M. 1997, ApJ, 482, 307

De Pree, C. G., Peters, T., Mac Low, M. M., et al. 2015, ApJ, 815, 123

De Pree, C. G., Wilner, D. J., Kristensen, L. E., et al. 2020, AJ, 160, 234

Dicke, R. H. 1946, Review of Scientific Instruments, 17, 268

Dickel, H. R., Dickel, J. R., Wilson, W. J., & Werner, M. W. 1980, ApJ, 237, 711

Dickel, J. R., Dickel, H. R., & Wilson, W. J. 1978, ApJ, 223, 840

Dickman, R. L., Snell, R. L., Ziurys, L. M., & Huang, Y.-L. 1992, ApJ, 400, 203

Dixon, R. N. & Field, D. 1979a, MNRAS, 189, 583

Dixon, R. N. & Field, D. 1979b, Proceedings of the Royal Society of London Series A, 368, 99

Douglas, A. E. & Herzberg, G. 1941, ApJ, 94, 381

Downes, D. & Eckart, A. 2007, A&A, 468, L57

Draine, B. T. 2011, Physics of the Interstellar and Intergalactic Medium (Princeton University Press)

Dreher, J. W., Johnston, K. J., Welch, W. J., & Walker, R. C. 1984, ApJ, 283, 632

Dunham, T., J. 1937, PASP, 49, 26

Egert, A., Waite, J. H., & Bell, J. 2017, Journal of Geophysical Research (Space Physics), 122, 2210

Einstein, A. 1917, Physikalische Zeitschrift, 18, 121

Elitzur, M. 1977, ApJ, 218, 677

Elitzur, M. 1982, Reviews of Modern Physics, 54, 1225

Elitzur, M. 1992, Astronomical masers, Vol. 170 (Springer Science & Business Media)

Elitzur, M. & Asensio Ramos, A. 2006, MNRAS, 365, 779

Elitzur, M. & Watson, W. D. 1978, ApJ, 222, L141

Emprechtinger, M., Monje, R. R., van der Tak, F. F. S., et al. 2012, ApJ, 756, 136

Engel, H., Davies, R. I., Genzel, R., et al. 2011, ApJ, 729, 58

Engelke, P. D. & Allen, R. J. 2018, ApJ, 858, 57

Estalella, R. 2017, PASP, 129, 025003

Etxaluze, M., Goicoechea, J. R., Cernicharo, J., et al. 2013, A&A, 556, A137

Falgarone, E., Godard, B., Cernicharo, J., et al. 2010, A&A, 521, L15

Falgarone, E., Verstraete, L., Pineau Des Forêts, G., & Hily-Blant, P. 2005, A&A, 433, 997

Federman, S. R. 1982, ApJ, 257, 125

Federman, S. R. & Willson, R. F. 1982, ApJ, 260, 124

Field, G. B., Goldsmith, D. W., & Habing, H. J. 1969, in Bulletin of the American Astronomical Society, Vol. 1, 240

Flower, D. 1990, Molecular collisions in the interstellar medium (Cambridge University Press)

Flower, D. R. & Pineau des Forets, G. 1998, MNRAS, 297, 1182

Flower, D. R., Pineau Des Forêts, G., & Walmsley, C. M. 2006, A&A, 449, 621

Frayer, D. T., Maddalena, R. J., Meijer, M., et al. 2015, AJ, 149, 162

Furuya, R. S., Cesaroni, R., & Shinnaga, H. 2011, A&A, 525, A72

Galli, D. & Palla, F. 2013, ARA&A, 51, 163

García-Burillo, S., Martín-Pintado, J., Fuente, A., & Neri, R. 2001, ApJ, 563, L27

Geballe, T. R. & Oka, T. 1996, Nature, 384, 334

Genzel, R., Downes, D., Pauls, T., Wilson, T. L., & Bieging, J. 1979, A&A, 73, 253

Genzel, R., Downes, D., Schneps, M. H., et al. 1981, ApJ, 247, 1039

Gerin, M., de Luca, M., Goicoechea, J. R., et al. 2010, A&A, 521, L16

Gerin, M., Neufeld, D. A., & Goicoechea, J. R. 2016, ARA&A, 54, 181

Gerin, M., Ruaud, M., Goicoechea, J. R., et al. 2015, A&A, 573, A30

Giannetti, A., Wyrowski, F., Brand, J., et al. 2014, A&A, 570, A65

Ginsburg, A., Goddi, C., Kruijssen, J. M. D., et al. 2017, ApJ, 842, 92

Ginsburg, A., Goss, W. M., Goddi, C., et al. 2016, A&A, 595, A27

Glosík, J., Plašil, R., Kotrík, T., et al. 2010, Molecular Physics, 108, 2253

Godard, B., Falgarone, E., Gerin, M., et al. 2012, A&A, 540, A87

Godard, B., Falgarone, E., & Pineau Des Forêts, G. 2009, A&A, 495, 847

Godard, B., Falgarone, E., & Pineau des Forêts, G. 2014, A&A, 570, A27

Goddi, C., Henkel, C., Zhang, Q., Zapata, L., & Wilson, T. L. 2015, A&A, 573, A109

Goldsmith, P. F., Velusamy, T., Li, D., & Langer, W. D. 2010, ApJ, 715, 1370

Gong, Y., Henkel, C., Thorwirth, S., et al. 2015, A&A, 581, A48

González-Alfonso, E., Fischer, J., Bruderer, S., et al. 2018, ApJ, 857, 66

González-Alfonso, E., Fischer, J., Bruderer, S., et al. 2013, A&A, 550, A25

Gordon, M. A. & Sorochenko, R. L. 2002, Radio Recombination Lines. Their Physics and Astronomical Applications, Vol. 282 (Springer Science & Business Media)

Gould, R. J. & Salpeter, E. E. 1963, ApJ, 138, 393

Gray, M. 2012, Maser Sources in Astrophysics (Cambridge University Press)

Greaves, J. S. & Williams, P. G. 1994, A&A, 290, 259

Green, J. A. & McClure-Griffiths, N. M. 2011, MNRAS, 417, 2500

Grenier, I. A., Casandjian, J.-M., & Terrier, R. 2005, Science, 307, 1292

Griffin, M. J., Abergel, A., Abreu, A., et al. 2010, A&A, 518, L3

Guan, X., Stutzki, J., Graf, U. U., et al. 2012, A&A, 542, L4

Güsten, R., Nyman, L. Å., Schilke, P., et al. 2006, A&A, 454, L13

Güsten, R., Wiesemeyer, H., Neufeld, D., et al. 2019, Nature, 568, 357

Gutiérrez, E. M., Romero, G. E., & Vieyro, F. L. 2020, MNRAS, 494, 2109

Halfen, D. T., Woolf, N. J., & Ziurys, L. M. 2017, ApJ, 845, 158

Halfen, D. T., Ziurys, L. M., Pearson, J. C., & Drouin, B. J. 2008, ApJ, 687, 731

Heaton, B. D., Little, L. T., & Bishop, I. S. 1989, A&A, 213, 148

Heiles, C., Koo, B.-C., Levenson, N. A., & Reach, W. T. 1996, ApJ, 462, 326

Henkel, C., Guesten, R., & Gardner, F. F. 1985, A&A, 143, 148

Henkel, C., Whiteoak, J. B., Nyman, L. A., & Harju, J. 1990, A&A, 230, L5

Henkel, C., Wilson, T. L., & Bieging, J. 1982, A&A, 109, 344

Henkel, C., Wilson, T. L., Langer, N., Chin, Y. N., & Mauersberger, R. 1994, Interstellar CNO Isotope Ratios, Vol. 439 (Springer), 72–88

Herbst, E. 2015, in EPJ Web of Conferences, Vol. 84, EDP Sciences, 06002

Herbst, E. & Klemperer, W. 1973, ApJ, 185, 505

Hermsen, W., Wilson, T. L., Walmsley, C. M., & Batrla, W. 1985, A&A, 146, 134

Herwig, F. 2005, Annu. Rev. Astron. Astrophys., 43, 435

Herzberg, G. 1942, ApJ, 96, 314

Herzberg, G. 1990, Journal of Molecular Structure, 217, xi

Hesper, R., Khudchenko, A., Lindemulder, M., et al. 2018, in Proc. 29th Int. Symp. Space Terahertz Technol.

Heyminck, S., Graf, U. U., Güsten, R., et al. 2012, A&A, 542, L1

Heyminck, S., Kasemann, C., Güsten, R., de Lange, G., & Graf, U. U. 2006, A&A, 454, L21

Hierl, P. M., Morris, R. A., & Viggiano, A. A. 1997, J. Chem. Phys., 106, 10145

Ho, P. T. P., Genzel, R., & Das, A. 1983, ApJ, 266, 596

Hoang-Binh, D. & Walmsley, C. M. 1974, A&A, 35, 49

Hocking, W. H., Gerry, M. C. L., & Winnewisser, G. 1975, Canadian Journal of Physics, 53, 1869

Hogness, T. R. & Lunn, E. G. 1925, Physical Review, 26, 44

Hollenbach, D., Kaufman, M. J., Neufeld, D., Wolfire, M., & Goicoechea, J. R. 2012, ApJ, 754, 105

Hollenbach, D. J. & Tielens, A. G. G. M. 1997, ARA&A, 35, 179

Hollis, J. M., Jewell, P. R., & Lovas, F. J. 1995, ApJ, 438, 259

Howe, J. E., Jaffe, D. T., Genzel, R., & Stacey, G. J. 1991, ApJ, 373, 158

Huggins, W. & Huggins, M. 1889, Proceedings of the Royal Society of London Series I, 46, 40

Huggins, W. & Miller, W. A. 1864, Philosophical Transactions of the Royal Society of London Series I, 154, 437

Hunter, J. D. 2007, Computing in Science Engineering, 9, 90

Imai, H., Kameya, O., Sasao, T., et al. 2000, ApJ, 538, 751

Immer, K., Schuller, F., Omont, A., & Menten, K. M. 2012, A&A, 537, A121

Indriolo, N. & McCall, B. J. 2012, ApJ, 745, 91

Indriolo, N., Neufeld, D. A., Gerin, M., et al. 2012, ApJ, 758, 83

Indriolo, N., Neufeld, D. A., Gerin, M., et al. 2015, ApJ, 800, 40

Ivezić, Ž., Connelly, A. J., Vand erplas, J. T., & Gray, A. 2019, Statistics, Data Mining, and Machine Learning in Astronomy (Princeton University Press)

Iwasawa, K., Koyama, K., Awaki, H., et al. 1993, ApJ, 409, 155

Jackson, J. M. & Kraemer, K. E. 1994, ApJ, 429, L37

Jacob, A. M. 2017, Master's thesis, Universität Bonn

Jacob, A. M., Menten, K. M., Gong, Y., et al. 2021, arXiv e-prints, arXiv:2101.02654

Jacob, A. M., Menten, K. M., Wiesemeyer, H., et al. 2020a, A&A, 640, A125

Jacob, A. M., Menten, K. M., Wiesemeyer, H., et al. 2019, A&A, 632, A60

Jacob, A. M., Menten, K. M., Wyrowski, F., Winkel, B., & Neufeld, D. A. 2020b, A&A, 643, A91

Jaffe, D. T., Becklin, E. E., & Hildebrand, R. H. 1984, ApJ, 279, L51

Jakob, H., Kramer, C., Simon, R., et al. 2007, A&A, 461, 999

Johnson, D. R., Lovas, F. J., & Kirchhoff, W. H. 1972, Journal of Physical and Chemical Reference Data, 1, 1011

Jones, E., Oliphant, T., Peterson, P., et al. 2001, SciPy: Open source scientific tools for Python

Kalkofen, W. 1984, Methods in Radiative Transfer. (Cambridge University Press)

Kavak, Ü., van der Tak, F. F. S., Tielens, A. G. G. M., & Shipman, R. F. 2019, A&A, 631, A117

Kennicutt, R. C. & Evans, N. J. 2012, ARA&A, 50, 531

Kester, D., Higgins, R., & Teyssier, D. 2017, A&A, 599, A115

Klein, B. 2017, "A new Fast Fourier Transform Spectrometer for upGREAT and 4GREAT". Spectroscopy with SOFIA: new results & future opportunities. Schloss Ringberg, Germany

Klein, B., Hochgürtel, S., Krämer, I., et al. 2012, A&A, 542, L3

Klessen, R. S. & Glover, S. C. O. 2016, Saas-Fee Advanced Course, 43, 85

Kobayashi, C., Karakas, A. I., & Umeda, H. 2011, MNRAS, 414, 3231

Koley, A., Roy, N., Menten, K. M., et al. 2021, MNRAS, 501, 4825

König, C., Urquhart, J. S., Csengeri, T., et al. 2017, A&A, 599, A139

Koribalski, B., Whiteoak, J. B., & Houghton, S. 1995, PASA, 12, 20

Kounkel, M., Hartmann, L., Loinard, L., et al. 2017, ApJ, 834, 142

Kramer, M., Menten, K., Barr, E. D., et al. 2016, in MeerKAT Science: On the Pathway to the SKA, 3

Kuchar, T. A. & Bania, T. M. 1993, ApJ, 414, 664

Kurayama, T., Nakagawa, A., Sawada-Satoh, S., et al. 2011, PASJ, 63, 513

Lang, K. R. & Wilson, R. F. 1978, ApJ, 224, 125

Langer, W. D. & Penzias, A. A. 1990, ApJ, 357, 477

Larson, R. B. 2003, Reports on Progress in Physics, 66, 1651

Lattanzi, V., Walters, A., Drouin, B. J., & Pearson, J. C. 2007, ApJ, 662, 771

Le Petit, F., Ruaud, M., Bron, E., et al. 2016, A&A, 585, A105

Ledoux, C., Petitjean, P., & Srianand, R. 2006, ApJ, 640, L25

Lee, H. H., Bettens, R. P. A., & Herbst, E. 1996, A&AS, 119, 111

Lequeux, J. 2005, The Interstellar Medium (Springer Science & Business Media)

Li, D., Tang, N., Nguyen, H., et al. 2018, ApJS, 235, 1

Lilley, A. E. & Palmer, P. 1968, ApJS, 16, 143

Liszt, H., Gerin, M., & Grenier, I. 2018, A&A, 617, A54

Liszt, H. & Lucas, R. 2002, A&A, 391, 693

Little, L. T., MacDonald, G. H., Riley, P. W., & Matheson, D. N. 1979, MNRAS, 189, 539

Lodders, K. 2008, ApJ, 674, 607

Lodders, K., Palme, H., & Gail, H. P. 2009, Landolt Börnstein, 4B, 712

Lovas, F. J., Suenram, R. D., & Evenson, K. M. 1983, ApJ, 267, L131

Lyu, C.-H., Smith, A. M., & Bruhweiler, F. C. 2001, ApJ, 560, 865

Magnani, L. & Onello, J. S. 1993, ApJ, 408, 559

Magnani, L., Sandell, G., & Lada, E. A. 1992, A&AS, 93, 509

Mangum, J. G., Wootten, A., & Plambeck, R. L. 1993, ApJ, 409, 282

Marinakis, S., Kalugina, Y., Kłos, J., & Lique, F. 2019, A&A, 629, A130

Mathis, J. S., Mezger, P. G., & Panagia, N. 1983, A&A, 500, 259

Matsushima, F., Matsunaga, M., Qian, G.-Y., et al. 2001, Journal of molecular spectroscopy, 206, 41

Mattila, K. 1986, A&A, 160, 157

McClure-Griffiths, N. M., Dickey, J. M., Gaensler, B. M., et al. 2005, ApJS, 158, 178

McGuire, B. A., Asvany, O., Brünken, S., & Schlemmer, S. 2020, Nature Reviews Physics, 2, 402

McKee, C. F. & Ostriker, J. P. 1977, ApJ, 218, 148

McKellar, A. 1940, PASP, 52, 187

Megeath, S. T., Herter, T., Beichman, C., et al. 1996, A&A, 307, 775

Megeath, S. T., Townsley, L. K., Oey, M. S., & Tieftrunk, A. R. 2008, Handbook of Star Forming Regions, Volume I, 4, 264

Menten, K. M., Reid, M. J., Forbrich, J., & Brunthaler, A. 2007, A&A, 474, 515

Michael, E. A., Lewen, F., Winnewisser, G., et al. 2003, ApJ, 596, 1356

Milam, S., Savage, C., Brewster, M., Ziurys, L. M., & Wyckoff, S. 2005, ApJ, 634, 1126

Mirabel, I. F. 1982, ApJ, 260, 75

Mitchell, J. B. A. 1990, Phys. Rep., 186, 215

Moisés, A. P., Damineli, A., Figuerêdo, E., et al. 2011, MNRAS, 411, 705

Möller, T., Endres, C., & Schilke, P. 2017, A&A, 598, A7

Monje, R. R., Lord, S., Falgarone, E., et al. 2014, ApJ, 785, 22

Mookerjea, B., Casper, E., Mundy, L. G., & Looney, L. W. 2007, ApJ, 659, 447

Moon, D.-S. & Koo, B.-C. 1994, Journal of Korean Astronomical Society, 27, 81

Müller, H. S. P., Muller, S., Schilke, P., et al. 2015, A&A, 582, L4

Müller, H. S. P., Schlöder, F., Stutzki, J., & Winnewisser, G. 2005, Journal of Molecular Structure, 742, 215

Müller, H. S. P., Thorwirth, S., Roth, D. A., & Winnewisser, G. 2001, A&A, 370, L49

Muller, S., Beelen, A., Guélin, M., et al. 2011, A&A, 535, A103

Muller, S., Müller, H. S. P., Black, J. H., et al. 2016, A&A, 595, A128

Müller-Sánchez, F., González-Martín, O., Fernández-Ontiveros, J. A., Acosta-Pulido, J. A., & Prieto, M. A. 2010, ApJ, 716, 1166

Nagy, Z., Ossenkopf, V., van der Tak, F., et al. 2015a, in IAU General Assembly, Vol. 29, 2254241

Nagy, Z., Ossenkopf, V., Van der Tak, F. F. S., et al. 2015b, A&A, 578, A124

Natta, A., Walmsley, C. M., & Tielens, A. G. G. M. 1994, ApJ, 428, 209

Navarete, F., Galli, P. A. B., & Damineli, A. 2019, MNRAS, 487, 2771

Neelamani, R., Choi, H., & Baraniuk, R. 2004, IEEE Transactions on Signal Processing, 52, 418

Neill, J. L., Bergin, E. A., Lis, D. C., et al. 2014, ApJ, 789, 8

Neufeld, D. A., Black, J. H., Gerin, M., et al. 2015a, ApJ, 807, 54

Neufeld, D. A. & Dalgarno, A. 1989, ApJ, 344, 251

Neufeld, D. A., Godard, B., Gerin, M., et al. 2015b, A&A, 577, A49

Neufeld, D. A., Goicoechea, J. R., Sonnentrucker, P., et al. 2010, A&A, 521, L10

Neufeld, D. A., Schilke, P., Menten, K. M., et al. 2006, A&A, 454, L37

Neufeld, D. A. & Wolfire, M. G. 2016, ApJ, 826, 183

Neufeld, D. A. & Wolfire, M. G. 2017, ApJ, 845, 163

Neufeld, D. A., Zmuidzinas, J., Schilke, P., & Phillips, T. G. 1997, ApJ, 488, L141

Ossenkopf, V., Röllig, M., Neufeld, D. A., et al. 2013, A&A, 550, A57

Otarola, A., De Breuck, C., Travouillon, T., et al. 2019, PASP, 131, 045001

Ozeki, H. & Saito, S. 1995, ApJ, 451, L97

Pabst, C., Higgins, R., Goicoechea, J. R., et al. 2019, Nature, 565, 618

Pagel, B. 1997, Nucleosynthesis and Chemical Evolution of Galaxies, Cambridge Univ

Papadopoulos, P. P., Thi, W.-F., Miniati, F., & Viti, S. 2011, MNRAS, 414, 1705

Parise, B., Du, F., Liu, F. C., et al. 2012, A&A, 542, L5

Parsons, H., Thompson, M. A., Clark, J. S., & Chrysostomou, A. 2012, MNRAS, 424, 1658

Pauls, A., Wilson, T. L., Bieging, J. H., & Martin, R. N. 1983, A&A, 124, 23

Pérez-Beaupuits, J. P., Güsten, R., Harris, A., et al. 2018, ApJ, 860, 23

Persson, C. M., Olofsson, A. O. H., Le Gal, R., et al. 2016, A&A, 586, A128

Persson, M. V., Jørgensen, J. K., & van Dishoeck, E. F. 2013, A&A, 549, L3

Pety, J. 2005, in SF2A-2005: Semaine de l'Astrophysique Francaise, ed. F. Casoli, T. Contini, J. M. Hameury, & L. Pagani, 721

Pickett, H. M., Poynter, R. L., Cohen, E. A., et al. 1998, J. Quant. Spec. Rad. Trans., 60, 883

Pineda, J. L., Langer, W. D., Velusamy, T., & Goldsmith, P. F. 2013, A&A, 554, A103

Planck Collaboration, Ade, P. A. R., Aghanim, N., et al. 2016, A&A, 594, A19

Planck Collaboration, Aghanim, N., Akrami, Y., et al. 2020, A&A, 641, A6

Polehampton, E. T., Baluteau, J.-P., Swinyard, B. M., et al. 2007, MNRAS, 377, 1122

Polehampton, E. T., Menten, K. M., Brünken, S., Winnewisser, G., & Baluteau, J. P. 2005, A&A, 431, 203

Prantzos, N., Aubert, O., & Audouze, J. 1996, A&A, 309, 760

Prasad, S. S. & Huntress, W. T., J. 1980, ApJS, 43, 1

Priestley, F. D., Barlow, M. J., & Viti, S. 2017, MNRAS, 472, 4444

Qin, S. L., Schilke, P., Comito, C., et al. 2010, A&A, 521, L14

Radovich, M., Kahanpää, J., & Lemke, D. 2001, A&A, 377, 73

Reber, G. 1944, ApJ, 100, 279

Reid, M. J. & Ho, P. T. P. 1985, ApJ, 288, L17

Reid, M. J., Menten, K. M., Brunthaler, A., et al. 2019, ApJ, 885, 131

Reid, M. J., Menten, K. M., Brunthaler, A., et al. 2014, ApJ, 783, 130

Reid, M. J. & Moran, J. M. 1981, ARA&A, 19, 231

Richter, J. & Tonner, K.-F. 1967, Zeitschrift fur Astrophysik, 67, 155

Risacher, C., Güsten, R., Stutzki, J., et al. 2018, Journal of Astronomical Instrumentation, 7, 1840014

Risacher, C., Güsten, R., Stutzki, J., et al. 2016, A&A, 595, A34

Ritchey, A. M., Federman, S. R., & Lambert, D. L. 2011, ApJ, 728, 36

Roach, A. & Kuntz, P. 1970, Journal of the Chemical Society D: Chemical Communications, 1336

Roberge, W. & Dalgarno, A. 1982, ApJ, 255, 489

Robitaille, T. P. & Whitney, B. A. 2010, ApJ, 710, L11

Rodríguez-Rico, C. A., Goss, W. M., Viallefond, F., et al. 2005, ApJ, 633, 198

Roelfsema, P. R. & Goss, W. M. 1991, A&AS, 87, 177

Roelfsema, P. R., Goss, W. M., & Mallik, D. C. V. 1992, ApJ, 394, 188

Röllig, M. & Ossenkopf, V. 2013, A&A, 550, A56

Roshi, D. A., De Pree, C. G., Goss, W. M., & Anantharamaiah, K. R. 2006, ApJ, 644, 279

Roueff, E., Alekseyev, A. B., & Le Bourlot, J. 2014, A&A, 566, A30

Roueff, E., Loison, J. C., & Hickson, K. M. 2015, A&A, 576, A99

Rugel, M. R., Beuther, H., Bihr, S., et al. 2018, A&A, 618, A159

Rybicki, G. B. 1985, in NATO Advanced Study Institute (ASI) Series C, Vol. 152, Progress in Stellar Spectral Line Formation Theory, ed. J. E. Beckman & L. Crivellari, 199–206

Rybicki, G. B. & Hummer, D. G. 1991, A&A, 245, 171

Rybicki, G. B. & Lightman, A. P. 1979, Radiative processes in astrophysics (John Wiley & Sons)

Rydbeck, O. E. H., Elldér, J., & Irvine, W. M. 1973, Nature, 246, 466

Rydbeck, O. E. H., Kollberg, E., Hjalmarson, A., et al. 1976, ApJS, 31, 333

Sakai, N., Maezawa, H., Sakai, T., Menten, K. M., & Yamamoto, S. 2012, A&A, 546, A103

Sakamoto, K., Wang, J., Wiedner, M. C., et al. 2008, ApJ, 684, 957

Salas, P., Oonk, J. B. R., Emig, K. L., et al. 2019, A&A, 626, A70

Salgado, F., Morabito, L. K., Oonk, J. B. R., et al. 2017, ApJ, 837, 142

Sánchez-Monge, Á., Schilke, P., Schmiedeke, A., et al. 2017, A&A, 604, A6

Sandell, G., Magnani, L., & Lada, E. A. 1988, ApJ, 329, 920

Sanna, A., Reid, M. J., Menten, K. M., et al. 2014, ApJ, 781, 108

Sato, F., Hasegawa, T., Whiteoak, J. B., & Miyawaki, R. 2000, ApJ, 535, 857

Sato, M., Reid, M. J., Brunthaler, A., & Menten, K. M. 2010, ApJ, 720, 1055

Savage, C., Apponi, A. J., Ziurys, L. M., & Wyckoff, S. 2002, ApJ, 578, 211

Schewe, H. C., Ma, Q., Vanhaecke, N., et al. 2015, J. Chem. Phys., 142, 204310

Schilke, P., Comito, C., Müller, H. S. P., et al. 2010, A&A, 521, L11

Schilke, P., Neufeld, D. A., Müller, H. S. P., et al. 2014, A&A, 566, A29

Schmiedeke, A., Schilke, P., Möller, T., et al. 2016, A&A, 588, A143

Schuller, F., Menten, K. M., Contreras, Y., et al. 2009, A&A, 504, 415

Scoville, N. Z., Yun, M. S., & Bryant, P. M. 1997, ApJ, 484, 702

Serabyn, E., Guesten, R., & Schulz, A. 1993, ApJ, 413, 571

Sheffer, Y., Rogers, M., Federman, S. R., et al. 2008, ApJ, 687, 1075

Shull, J. M. & Beckwith, S. 1982, ARA&A, 20, 163

Sievers, A. W., Mezger, P. G., Bordeon, M. A., et al. 1991, A&A, 251, 231

Smith, H. E., Lonsdale, C. J., Lonsdale, C. J., & Diamond, P. J. 1998, ApJ, 493, L17

Snow, T. P. & McCall, B. J. 2006, ARA&A, 44, 367

Sofia, U. J., Lauroesch, J. T., Meyer, D. M., & Cartledge, S. I. B. 2004, ApJ, 605, 272

Sormani, M. C. & Magorrian, J. 2015, MNRAS, 446, 4186

Sorochenko, R. L. & Tsivilev, A. P. 2000, Astronomy Reports, 44, 426

Stacey, G. J., Lugten, J. B., & Genzel, R. 1987, ApJ, 313, 859

Steimle, T. C., Woodward, D. R., & Brown, J. M. 1986, J. Chem. Phys., 85, 1276

Stoerzer, H., Stutzki, J., & Sternberg, A. 1995, A&A, 296, L9

Suutarinen, A., Geppert, W. D., Harju, J., et al. 2011, A&A, 531, A121

Swings, P. & Rosenfeld, L. 1937, ApJ, 86, 483

Swinyard, B. M., Ade, P., Baluteau, J. P., et al. 2010, A&A, 518, L4

Tahani, K., Plume, R., Bergin, E. A., et al. 2016, ApJ, 832, 12

Tanaka, K., Harada, K., & Oka, T. 2013, Journal of Physical Chemistry A, 117, 9584

Tang, N., Li, D., Heiles, C., et al. 2017, ApJ, 839, 8

Tang, X. D., Henkel, C., Menten, K. M., et al. 2019, A&A, 629, A6

Theis, R. A., Morgan, W. J., & Fortenberry, R. C. 2015, MNRAS, 446, 195

Thiel, V., Belloche, A., Menten, K. M., et al. 2019, A&A, 623, A68

Thompson, A. R., Moran, J. M., & Swenson, George W., J. 2017, Interferometry and Synthesis in Radio Astronomy, 3rd Edition (Springer Nature)

Thronson, H. A., J. & Harper, D. A. 1979, ApJ, 230, 133

Tieftrunk, A., Pineau des Forets, G., Schilke, P., & Walmsley, C. M. 1994, A&A, 289, 579

Tielens, A. G. G. M. 2005, The Physics and Chemistry of the Interstellar Medium (Cambridge University Press)

Tosi, M. 1982, ApJ, 254, 699

Townes, C. H. & Schawlow, A. L. 1975, Microwave spectroscopy. (Dover Publications, Inc.)

Tran, T. D., Rednyk, S., Kovalenko, A., et al. 2018, ApJ, 854, 25

Truppe, S., Hendricks, R. J., Hinds, E. A., & Tarbutt, M. R. 2014, ApJ, 780, 71

Turner, B. E. 1988, ApJ, 329, 425

Turner, B. E. & Zuckerman, B. 1974, ApJ, 187, L59

Ulich, B. L. & Haas, R. W. 1976, ApJS, 30, 247

Ungerechts, H., Bergin, E. A., Goldsmith, P. F., et al. 1997, ApJ, 482, 245

Urquhart, J. S., Figura, C. C., Moore, T. J. T., et al. 2014, MNRAS, 437, 1791

Urquhart, J. S., Hoare, M. G., Lumsden, S. L., et al. 2012, MNRAS, 420, 1656

Urquhart, J. S., König, C., Giannetti, A., et al. 2018, MNRAS, 473, 1059

Usero, A., García-Burillo, S., Fuente, A., Martín-Pintado, J., & Rodríguez-Fernández, N. J. 2004, A&A, 419, 897

van der Tak, F. F. S., Black, J. H., Schöier, F. L., Jansen, D. J., & van Dishoeck, E. F. 2007, A&A, 468, 627

van der Tak, F. F. S., Lique, F., Faure, A., Black, J. H., & van Dishoeck, E. F. 2020, Atoms, 8, 15

van der Tak, F. F. S., Weiß, A., Liu, L., & Güsten, R. 2016, A&A, 593, A43

van der Walt, S., Colbert, S. C., & Varoquaux, G. 2011, Computing in Science Engineering, 13, 22

van Dishoeck, E. F., Beaerda, R. A., & van Hemert, M. C. 1996, A&A, 307, 645

van Dishoeck, E. F. & Black, J. H. 1986, ApJS, 62, 109

van Dishoeck, E. F. & Black, J. H. 1989, ApJ, 340, 273

van Dishoeck, E. F., Kristensen, L. E., Benz, A. O., et al. 2011, PASP, 123, 138

Vastel, C., Ceccarelli, C., Caux, E., et al. 2010, A&A, 521, L31

Vastel, C., Spaans, M., Ceccarelli, C., Tielens, A. G. G. M., & Caux, E. 2001, A&A, 376, 1064

Vejby-Christensen, L., Andersen, L. H., Heber, O., et al. 1997, ApJ, 483, 531

Velusamy, T. & Langer, W. D. 2014, A&A, 572, A45

Verschuur, G. L. 1992, S&T, 83, 379

Viti, S., Williams, D. A., & O'Neill, P. T. 2000, A&A, 354, 1062

von Weizsäcker, C.-F. 1938, Physikalische Zeitschrift, 39, 633

Wakelam, V., Bron, E., Cazaux, S., et al. 2017, Molecular Astrophysics, 9, 1

Wakelam, V., Herbst, E., Loison, J. C., et al. 2012, ApJS, 199, 21

Walker, G. W., Kalinauskaite, E., McCarthy, D. N., et al. 2016, in Society of Photo-Optical Instrumentation Engineers (SPIE) Conference Series, Vol. 9914, Proc. SPIE, 99142V

Wallström, S. H. J., Biscaro, C., Salgado, F., et al. 2013, A&A, 558, L2

Walmsley, C. M., Natta, A., Oliva, E., & Testi, L. 2000, A&A, 364, 301

Wan, X., Wang, W., Liu, J., & Tong, T. 2014, arXiv e-prints, arXiv:1407.8038

Wang, M., Henkel, C., Chin, Y. N., et al. 2004, A&A, 422, 883

Wannier, P. G., Andersson, B. G., Morris, M., & Lichten, S. M. 1991, ApJS, 75, 987

Watson, J. K. G. 2001, ApJ, 555, 472

Watson, W. D. 1974, ApJ, 188, 35

Weinreb, S., Barrett, A. H., Meeks, M. L., & Henry, J. C. 1963, Nature, 200, 829

Weiß, A., Kovács, A., Güsten, R., et al. 2008, A&A, 490, 77

Welch, W. J., Dreher, J. W., Jackson, J. M., Terebey, S., & Vogel, S. N. 1987, Science, 238, 1550

Welty, D. E., Sonnentrucker, P., Snow, T. P., & York, D. G. 2020, ApJ, 897, 36

Weselak, T. 2019, A&A, 625, A55

Weselak, T., Galazutdinov, G. A., Beletsky, Y., & Krełowski, J. 2010, MNRAS, 402, 1991

Whiteoak, J. B., Dahlem, M., Wielebinski, R., & Harnett, J. I. 1990, A&A, 231, 25

Whiteoak, J. B., Gardner, F. F., & Hoglund, B. 1980, MNRAS, 190, 17P

Wienen, M., Wyrowski, F., Menten, K. M., et al. 2015, A&A, 579, A91

Wiener, N. 1949, Extrapolation, interpolation, and smoothing of stationary time series, vol. 2

Wiesemeyer, H., Güsten, R., Heyminck, S., et al. 2016, A&A, 585, A76

Wiesemeyer, H., Güsten, R., Menten, K. M., et al. 2018, A&A, 612, A37

Williams, D. 1999, Astronomy and Geophysics, 40, 10

Wilson, T. 1999, Reports on Progress in Physics, 62, 143

Wilson, T. L., Rohlfs, K., & Huttemeister, S. 2012, Tools of Radio Astronomy, 5th edition (Springer)

Wilson, T. L. & Rood, R. 1994, ARA&A, 32, 191

Winkel, B., Wiesemeyer, H., Menten, K. M., et al. 2017, A&A, 600, A2

Wolfire, M. G., McKee, C. F., Hollenbach, D., & Tielens, A. G. G. M. 2003, ApJ, 587, 278

Woosley, S. E., Heger, A., & Weaver, T. A. 2002, Reviews of Modern Physics, 74, 1015

Wootten, A. & Thompson, A. R. 2009, IEEE Proceedings, 97, 1463

Wouterloot, J. G. A. & Brand, J. 1996, A&AS, 119, 439

Wyrowski, F., Güsten, R., Menten, K. M., et al. 2016, A&A, 585, A149

Wyrowski, F., Güsten, R., Menten, K. M., Wiesemeyer, H., & Klein, B. 2012, A&A, 542, L15

Wyrowski, F., Walmsley, C. M., Natta, A., & Tielens, A. G. G. M. 1997, A&A, 324, 1135

Xu, D. & Li, D. 2016, ApJ, 833, 90

Xu, L.-H. & Lovas, F. J. 1997, Journal of Physical and Chemical Reference Data, 26, 17

Xu, Y., Reid, M. J., Zheng, X. W., & Menten, K. M. 2006, Science, 311, 54

Yan, Y. T., Zhang, J. S., Henkel, C., et al. 2019, ApJ, 877, 154

Young, E. T., Becklin, E. E., Marcum, P. M., et al. 2012, ApJ, 749, L17

Zapata, L. A., Schmid-Burgk, J., & Menten, K. M. 2011, A&A, 529, A24

Zhang, B., Reid, M. J., Menten, K. M., et al. 2013, ApJ, 775, 79

Zhang, B., Zheng, X. W., Reid, M. J., et al. 2009, ApJ, 693, 419

Zink, L. R., De Natale, P., Pavone, F. S., et al. 1990, Journal of Molecular Spectroscopy, 143, 304

Ziurys, L. M. & Friberg, P. 1987, ApJ, 314, L49

Ziurys, L. M. & Turner, B. E. 1985, ApJ, 292, L25

Zuckerman, B. & Turner, B. E. 1975, ApJ, 197, 123

Acknowledgements

I tell you Hobbes, it's great to have a friend who appreciates an earnest discussion of ideas.

Calvin (Bill Watterson, July 14, 1992)

As this journey– my doctoral thesis nears its end, much like Calvin I would like to acknowledge the many (Hobbes) friends, mentors, and colleagues with whom I've had the pleasure of exchanging ideas with. These discussions have varied from those questioning the chemistry of the Universe, its complexity, the existence of phosphine on Venus, to debates pondering the distinction of warm potato salad as a salad (we have not arrived at a clear consensus on the latter).

I would like to start by thanking Prof. Dr. Karl M. Menten for giving me the opportunity to not only carry out my doctoral work at the Millimetre and Sub-millimetre group of the Max Planck Institute for Radioastronomy but for also encouraging me to gain first hand observing experiences and participate and contribute in meetings. His continuous guidance, motivation, attention to detail and careful review of my manuscripts have helped me grow as a researcher. Thank you, Karl, for being enthusiastic about my work, for always inspiring me with new ideas and for always letting me know that you are only a Skype call away. I would also like to thank you for introducing me to the British sitcom Fawlty Towers which is quickly becoming a favourite and for our many discussions about the Looney Tunes. To Prof. Dr. Pavel Kroupa I extend my sincerest thanks for agreeing to be the second evaluator and for his constant support as well as to thank Prof. Dr. Simon Stellmer and Prof. Dr. Hubert Schorle who have also kindly agreed to be part of my thesis evaluation committee.

I am also grateful to Dr. Helmut Wiesemeyer for his support and guidance throughout the course of my dissertation. Thank you for the discussions on radiative transfer modelling, for showing me the ropes to the GREAT in-flight data reduction onboard SOFIA with patience and for all your help in preparing the many observing proposals. And a big thank you for reading my manuscripts and this thesis in great detail.

I would like to thank Dr. Friedrich Wyrowski for his constructive feedback, and ideas, which have significantly contributed toward different chapters in my thesis and Dr. Arnaud Belloche for his discussions on astrochemistry, support while observing at APEX, the ice cream runs in San Pedro and interest in my work. I owe a great deal to Dr. Dirk Muders for all his help troubleshooting my many IT related problems (read SOS cries), be it big, small, or silly all whilst having the kindest smile on his face.

I would like to thank both Prof. Dr. Bernd Klein and Dr. Rolf Güsten for their guidance whilst on observing runs with both APEX and GREAT/SOFIA as well as for their comments and support. These experiences have given me new insight and appreciation into the work that goes on behind the scenes of the beautiful data sets (and pretty maps) we acquire. On that note I would like to express my gratitude to the APEX and SOFIA staff and science teams for their continued assistance throughout the course of the observations and after. Moreover, I would like to thank my APEX, and SOFIA families who have made even the most tense of

observing runs fun, with conversations over shared interests in music, games of ‘catcho’, the controversies of banana weizen and cookies at the data reduction table. A special thanks goes out to Dr. Denise Riquelme (Gael Sven and Dr. Esteban Morales), Dr. Rebeca Aladro (and Javi) and Dr. Carlos A. Durán for all the love, laughter and for excusing my Spanish. I would also like to thank the Kitt Peak 12 m telescope operators for their help during the on-site and remote observations, and Dr. Abby Hedden for her invaluable assistance with the observations as well as Dr. Arnaud Belloche and Dr. Ed Polehampton.

I am grateful to Frau Fingas, Frau Schmelmer, Frau Tran, Frau Menten and Frau Mertens for helping me take care of administrative work, be it for travelling abroad or for my visits to the Ausländeramt here in Bonn and also Frau Schneider for starting my mornings with the sweetest, ‘Einen wunderschön guten Morgan, meine Liebe’, which makes my day. I would also like to thank the International Max Planck Research School (IMPRS) for Astronomy and Astrophysics at the Universities of Bonn and Cologne, the Bonn-Cologne Graduate School of Physics and Astronomy (BCGS) and the Collaborative Research Centre (CRC) for their financial support while travelling to attend conferences and workshops.

I once read that the academic equivalent of ‘let’s start a band’ was ‘let’s write a paper’, with that being said I would like to thank my friends turned co-authors and co-authors turned friends, without whose contributions the work presented in this thesis would not have been complete, namely, Dr. Min-Young Lee, Dr. Benjamin Winkel, Prof. Dr. David A. Neufeld, Dr. Maitraiyee Tiwari, Dr. Yan Gong, Dr. Gisela N. Ortiz-León, Prof. Dr. Sandra Brünken, Dr. Per Bergman, Dr. A. O. Henrik Olofsson, Dr. Nirupam Roy, and Prof. Dr. Bärbel Koribalski. I would also like to extend my gratitude to Dr. Paul Dagdigian and Dr. Sarantos Marinakis for the collisional rate coefficients they have provided along with valuable inputs and discussions on the same. I would also like to thank Dr. Marijke Haverkorn for providing us with the SGPS continuum data for AG10.472+00.027. I would also like to express my gratitude to the developers of the many C++ and Python libraries, made available as open-source software, in particular this research has made use of the NumPy (van der Walt et al. 2011), SciPy (Jones et al. 2001) and matplotlib (Hunter 2007) packages.

Of course this work would not have borne fruit without the continued support and encouragement from my colleagues and friends: to Dat and Hans for endless gossip, dinners and game nights, thank you both for all the help debugging codes, for listening and always being ready to give advice, to Henning for being Henry, a comrade in all things silly-billy and for understanding my humour, to Ka Tat senpai for a great time in Vietnam and for always being willing to help, even though we communicate almost exclusively through stickers, to my current and previous office-mates Yuxin, Mélisse and Vivien (and Sebastian by extension), I am grateful for the time we shared and all the cake, Joana for all the fun and taking one for the team, to Rohit for strategizing in Azul, being suspicious of my role in games lime S.H. and for all the help with the uGMRT data, to Fateme my wify for attending 6 am yoga classes with me (even though it lasted only for a week) and for the constant check-ins, to Joey for watching scary movies with me, our American Horror story marathon is far from over but I hope that Pepper will forever remain in our hearts, to my family in the pulsars group- Mary, Eleni, Natasha, Tilemachos and Rob (Yuki) for keeping me updated with all the drama and scientific advancements in the world of pulsars and FRBs, all the food and laughter, to Bree, Lea and Giancarlo (a.k.a Mimi), I am indebted to you all for always reminding me to take

breaks, for keeping up our Karneval traditions and exploring new cuisines with me, to Franzi for connecting with me on a deep and emotional level in a very short span of time and for encouraging me to get back to drawing during the first lockdown, to Anjishnu (Nunu ji) for being family and for always taking care of me and reminding me of my 'padaku bachha' ways, to V.K, Kela and Smaran for being inner circle since 2015 and my Kochi gang for all your love and support since the 90s and of course Laura a.k.a LBU, for all the discussions on the continuum (which almost always start with a pspsps... on either end), for being my quick guide to CLASS commands, for the advice on matplotlib colours and for sharing my love for Disney and the Lion King, thank you, for all your help till the very end. I am also deeply grateful to a number of other friends and colleagues namely, Manali, Laure, Aiyun, Shampa, Maitraiyee, Nina, Yao, Michael, Dario, Veselina (and Chrisy), Rosie, Richa, Parichay, Sac, Sergio (and Coco), Antonio, Leeza, Soorya, Tashina, Jackie, Tasha, Prajwal, Madhuri and Ivalu. It has been a pleasure working with all of you and my apologies in case I have forgotten any names!

To Archishman Pradhan, my best friend, for helping me navigate through difficult times, for always lending a ear and for being the fourth leaf to my lucky clover. Last but not the least this accomplishment would not have been possible without the unconditional love, unfailing support and continuous encouragement from my parents, grand parents and brother. The past year, 2020 has been such a smörgåsbord of unprecedented twists and turns and I couldn't have done it without most people on this list but most of all you.

Telescopes and instrumentation

The contents of this thesis is based on data acquired using a wide array of telescopes and instruments and in the following I would like to acknowledge the support from the different facilities: (1) APEX is a collaboration between the Max-Planck-Institut für Radioastronomie, the European Southern Observatory, and the Onsala Space Observatory, (2) the 100-m telescope at Effelsberg is operated by the Max-Planck-Institut für Radioastronomie (MPIFR) on behalf of the Max-Planck Gesellschaft (MPG), (3) SOFIA Science Mission Operations is jointly operated by the Universities Space Research Association, Inc., under NASA contract NAS2-97001, and the Deutsches SOFIA Institut under DLR contract 50 OK 0901 and 50 OK 1301 to the University of Stuttgart. upGREAT is financed by resources from the participating institutes, and by the Deutsche Forschungsgemeinschaft (DFG) within the grant for the Collaborative Research Centre 956, as well as by the Federal Ministry of Economics and Energy (BMWI) via the German Space Agency (DLR) under Grants 50 OK 1102, 50 OK 1103 and 50 OK 1104 (4) the Onsala Space Observatory for the provisioning of its facilities/observational support. The Onsala Space Observatory national research infrastructure is funded through Swedish Research Council grant No 2017-00648.

Cover page background image: The Orion Nebula star-formation region obtained from the HAWK-I infrared camera on ESO's Very Large Telescope in Chile. (ESO/H. Drass)